

# Lawrence Berkeley National Laboratory

## Recent Work

### Title

THE APPLICATION OF ALGEBRAIC RECONSTRUCTION TECHNIQUES TO GEOPHYSICAL PROBLEMS

### Permalink

<https://escholarship.org/uc/item/95r8w9pz>

### Author

Peterson, J.E.

### Publication Date

1986-04-01



# Lawrence Berkeley Laboratory

UNIVERSITY OF CALIFORNIA

## EARTH SCIENCES DIVISION

RECEIVED  
LAWRENCE  
BERKELEY LABORATORY

JUL 2 1986

LIBRARY AND  
DOCUMENTS SECTION

THE APPLICATION OF ALGEBRAIC RECONSTRUCTION  
TECHNIQUES TO GEOPHYSICAL PROBLEMS

J.E. Peterson, Jr.  
(Ph.D. Thesis)

April 1986

**For Reference**

Not to be taken from this room



LBL-21498  
2.1

## **DISCLAIMER**

This document was prepared as an account of work sponsored by the United States Government. While this document is believed to contain correct information, neither the United States Government nor any agency thereof, nor the Regents of the University of California, nor any of their employees, makes any warranty, express or implied, or assumes any legal responsibility for the accuracy, completeness, or usefulness of any information, apparatus, product, or process disclosed, or represents that its use would not infringe privately owned rights. Reference herein to any specific commercial product, process, or service by its trade name, trademark, manufacturer, or otherwise, does not necessarily constitute or imply its endorsement, recommendation, or favoring by the United States Government or any agency thereof, or the Regents of the University of California. The views and opinions of authors expressed herein do not necessarily state or reflect those of the United States Government or any agency thereof or the Regents of the University of California.

**The Application of Algebraic Reconstruction  
Techniques to Geophysical Problems**

*by*

JOHN EDWARD PETERSON, JR.

(Ph.D. Thesis)

Center for Computational Seismology  
Earth Sciences Division  
Lawrence Berkeley Laboratory  
University of California  
Berkeley, California 94720

This work was supported by the U.S. Department of Energy under Contract Number DE-AC03-76SF00098.

# The Application of Algebraic Reconstruction Techniques to Geophysical Problems

*JOHN EDWARD PETERSON, JR.*

Center for Computational Seismology  
Earth Sciences Division  
Lawrence Berkeley Laboratory  
University of California  
Berkeley, California 94720

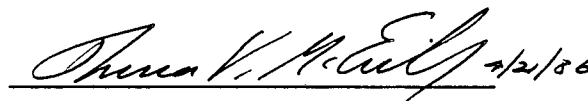
## *ABSTRACT*

Algebraic Reconstruction Techniques (ART), introduced in medical radiology, are extended in this study to seismic travel time data. The algorithms based on these techniques, developed initially for use with X-rays, must be modified for acoustic wave data. Modifications include slight changes in the algorithms themselves and additional weights for specific data types. The convergence properties of these algorithms to an adequate solution and the reliability of this solution are also investigated. The algorithms developed are initially tested on synthetically derived travel time data. Travel time data from simplistic velocity models are used to determine the general behavior of the algorithms and to estimate the reliability of the reconstructed velocity field. More complex models simulate realistic velocity distributions. Results from these studies provide critical guidelines for the inversion of real travel time data. The study also investigates the amount of detail that may be determined by this method with realistic structures.

Two high quality travel time data sets are inverted using ART. The experiments were carried out at the Retsof salt mine in New York and at the underground

radioactive waste repository study site in Sweden (Stripa). The raypaths in the Stripa experiment were short, with the maximum just over 10 meters in length. The Stripa data set is unique in that it consists of two suites of travel time measurements; one taken while the medium was being heated by a simulated waste canister, and the other some months after the heat had been turned off. This tests the use of ART as a monitoring technique using seismic waves. The velocity contrasts detected are small, but the anomalous zones are reconstructed quite well. The Retsof data consist of travel times for ray paths through a complicated structure with velocity contrasts reaching 50 percent. This study shows that ART performs well even in a complex region.

ART algorithms can be shown theoretically to converge to the least squares solution. This convergence is not seen in the application of the method. However, synthetic studies show that ART produces a more realistic reconstruction of the original velocity model than does least squares. These two methods are combined in an effort to increase the effectiveness of the ART algorithms.

A handwritten signature in cursive script, reading "Thomas V. McEvilly", with the date "1/21/86" written to the right of the signature.

Thomas V. McEvilly

For KATHERINE PEÑALOZA PETERSON

## ACKNOWLEDGEMENTS

My deepest appreciation goes to my academic advisor Tom McEvilly for his support and insight throughout my graduate career. I wish also to thank Lane Johnson and Shimon Coen who initiated my interest in tomography.

Many valuable discussions with Phil Cummins, Fred Eastwood, Lee Hirsch, Michael Leonard, Dan O'Connell, Jonathan Scheiner, Mary Templeton, Dave Tralli and Don Vasco have helped me throughout the years.

Without the technical support of the Center for Computational Seismology, Lawrence Berkeley Laboratory, this work could not have been undertaken. I would especially like to thank Ernie Majer for his assistance.

I am indebted to David D. Jackson whose valuable comments and suggestions concerning least squares resulted in Chapter 6. I would also like to thank Bjorn Paulson for providing the Stripa data set and Jerry Nelson of Harding-Lawson Associates for providing the Retsof data set.

This work was supported by the Department of Energy through University of California, Lawrence Berkeley Laboratory.



## Table of Contents

I.	Introduction .....	1
II.	The Method of ART .....	5
	A. Introduction .....	5
	B. The algorithms .....	6
	C. Algorithm modifications .....	14
	1. Smoothing Function .....	15
	2. Velocity Constraints .....	15
	3. Weighting .....	16
	4. Curved Ray paths .....	17
	D. Convergence and reliability .....	17
III.	Application to Synthetic Models .....	23
	A. Introduction .....	23
	B. Generating the data .....	25
	C. Results .....	27
	1. Algorithm performance .....	27
	2. Relaxation parameter .....	29
	3. Stopping criterion .....	29
	4. Smoothing .....	31
	5. Raytracing .....	31
	6. Pixel size .....	32

7. Noise .....	33
8. Limited Coverage .....	34
9. Velocity model B .....	34
D. Discussion and summary .....	35
IV. Application to a Complex Velocity Model .....	64
A. Introduction .....	64
B. Results .....	65
1. Algorithm performance .....	66
2. Smoothing .....	66
3. Curved raypaths .....	67
4. Pixel size .....	67
5. Doubling the number of stations .....	68
6. Noise .....	69
7. Variations on the model .....	69
C. Discussion and Summary .....	70
V. Applications of ART to Crosshole Seismic Data .....	89
A. Introduction .....	89
B. Data .....	90
C. Results .....	91
1. Stripa .....	92
2. Retsoff .....	94
D. Discussion .....	96
VI. ART and the Least Squares Inversion .....	135
A. Introduction .....	135

B. ART as a Generalized Inverse .....	136
C. Inverting the Matrix Using Singular-Value Decomposition .....	137
D. The Use of <i>A priori</i> Information in ART and SVD Inversions .....	141
E. Discussion .....	145
VII. Summary, Conclusions and Recommendations .....	145
A. Summary .....	166
B. Conclusions .....	167
C. Recommendations .....	169
1. S-waves and surface waves .....	170
2. Anisotropy .....	170
3. Amplitude data .....	171
4. Reflection and refraction surveys .....	172
5. Future work .....	172
REFERENCES .....	173
APPENDIX .....	175

## CHAPTER 1

### Introduction

Methods of imaging are commonly used in many sciences, the most familiar being those formed directly by optical or X-ray instrumentation. In many scientific applications it is necessary to determine the distribution of some physical property within an object by indirect measurements. Projections or "strip" integrals of an object formed by X-rays or acoustic waves at particular view angles can be used to estimate this distribution inside the object. This basic idea of image reconstruction was formulated mathematically by Radon (1917) and is now known as the Radon transform. Radon solved the integral equation relating two-dimensional objects to their projections for various geometries. The method introduced by Radon went virtually unused until Bracewell (1956) applied it in an attempt to track down solar sources of radio emission. By then computers had progressed far enough to handle the large amounts of data required by the method.

The method reached the medical field in the 1960s. A large amount of data is necessary for medical imaging and this alone was a major factor in the various techniques developed in the medical field. The work in medical applications produced four major classes of reconstruction algorithms: the summation methods, the convolution methods, the Fourier methods, and the summation expansion methods. Collectively, these algorithms are known as tomographic methods. The convolution and Fourier methods are quite similar to the method introduced by Bracewell (1956). In the

category of summation expansion methods fall the Algebraic Reconstruction Techniques (ART). These algorithms pose the integral equation in a matrix form which is solved using relaxation techniques, taking advantage of the sparse nature of the matrix. ART algorithms tend to be simple and can be modified easily to different data geometries and restricted angular coverage. All methods assume non-refracting, straight paths through the medium and require a full range of penetration angles for completeness. Many variations on the basic ideas have been developed, most of which have advantages in specific problems.

Many imaging techniques have long been used in seismology, the most familiar applications are reflection, refraction and  $p$ - $\tau$  analysis. However, the tomographic reconstruction techniques developed in the medical fields remain almost unused in geophysical applications. A back-projection method introduced by (Bois *et al.*, 1972) is a very simplified form of an algebraic reconstruction, but even this technique has rarely been applied. There are several reasons why ART remains unused in seismology: data acquisition is expensive and in some ways inadequate and the acoustic waves used in seismology not only follow curved paths, but also experience diffraction, reflection, scattering and various forms of attenuation. Data acquisition methods are now at the point where collection of data adequate for reconstruction techniques is becoming feasible. The behavior of seismic waves remains an obstacle in the applicability of these algorithms.

Tomographic techniques have applications in seismology ranging from ultrasonic cross-hole studies of rock properties (Wong *et al.*, 1983) to reflection seismology (Fawcett and Clayton, 1984) to deep earth structure (Clayton and Comer, 1984). In these applications either the slowness field or the attenuation field is determined. In most seismological problems, restrictions on source and receiver locations limit the range of penetration angles through the volume of interest, resulting in irregular sampling. Seismological applications thus are often customized for each experiment,

depending on the available sampling and the source-receiver geometries.

Two characteristics of the wave may be measured as data for tomographic reconstructions: the travel time between the source and receiver and the energy content of the resulting waveform. Travel times provide the velocity structure, but the energy content contains additional information about the medium. However, it is difficult to extract the necessary data from the waveform. A wavelet generally contains energy due to different wavefronts arriving simultaneously along with effects of scattering, geometry, noise and so on. To eliminate the undesirable effects would take considerable computational effort as well as a good *a priori* knowledge of the medium. Travel times are easier to analyze than full waveforms, although they contain information relating primarily to the slowness or velocity of the medium. Velocity information is useful for delineating anomalous zones in a medium caused by fractures, temperature distribution, hydrological features and changes in rock type.

This thesis deals primarily with Algebraic Reconstruction Techniques applied to seismological travel time data. Because of the differences in seismological and medical reconstruction problems, a straight-forward application of the algorithms developed in the medical field cannot be made to seismology. Thus, the primary motivation of this study is to develop algorithms applicable to seismology, based on the algebraic reconstruction techniques used in medical applications. A thorough experimental study with synthetic data from various velocity models is presented in this thesis. Such a study was lacking in the geophysical literature. The algorithms and knowledge gained in these initial studies is then used in reconstructions with real data. Complete studies of this nature were also lacking in the literature.

Basic principals and derivations of ART as applied to seismology are given in Chapter 2. Mathematical detail has been well documented, mostly in the medical and engineering literature and will largely be referenced. A set of synthetic test data is derived in Chapters 3 and 4 for several velocity models of differing complexities. Simple

models are used initially to determine the general behavior of the various algorithms and to supply a basis for comparison with other algorithms which may be developed in the future. The more complex models provide information helpful in predicting the behavior of the algorithms using real data. Velocity models from two real data sets are reconstructed in Chapter 5. Both experiments use cross-hole type geometry, but differ in media and dimensions of the features. The data sets contain very accurate travel time and station location measurements and one contains two suites of measurements taken for the same raypaths one year apart. This provides a unique opportunity to compare changes in travel times due to changes in the media and shows an important application of ART. Chapter 6 deals with the use of ART in conjunction with standard least square inversion methods. The two techniques are compared and an effort is made to combine them to increase the accuracy of the reconstructions. Finally, Chapter 7 is the overall conclusion regarding the applicability of ART to cross-hole seismic data.

## CHAPTER 2

### The Method of ART

#### Introduction

The problem I address is the determination of the velocity and attenuation fields in a region given the travel times and waveforms from distributed seismic sources and receivers. The initial step is to generate algorithms from those described in the medical literature, specifically, the iterative ART algorithms developed in the field of radiology (Gordon, Bender and Herman, 1970; Gilbert, 1972; Gordon, 1974), and to develop methods for determining the reliability of these algorithms. These algorithms are then used for the reconstructions performed in subsequent chapters of this thesis. In this chapter, the basic algorithms are described, along with several useful modifications which may be applied. Also, some mathematical and visual measures of convergence and reliability will be introduced.

The ART algorithms are considered superior to the widely used transform methods described in Scudder (1978) for several reasons:

- 1) ART is easily adaptable to any source-receiver configuration without interpolations to uniform sampling grids. The source-receiver configuration can be any geometry in which the pairs produce ray paths which sample the field of interest.
- 2) the geometrically more accurate curved ray paths may be used



- 3) computation time is fast
- 4) ART is an iterative method in which the rate of convergence may be altered with the use of a damping parameter

The initial point is critical for many geophysical applications where a symmetrical geometry is not feasible. The primary disadvantage of ART relative to the transform methods is the absence of criteria to determine at which iteration the best solution occurs. The transform methods are not iterative, so such criteria is unnecessary.

### The Algorithms

Simplistically, ART is based on a back-projection method. The field of interest is divided into many pixels of constant physical properties. Source-receiver ray paths project across this field as shown in Figure 2.1. As the wave passes through each of the pixels, the properties of the pixel effects its amplitude and velocity. The resultant amplitudes and travel times are thus dependent on the pixel properties and it is assumed that the contribution of each pixel can be deduced by back-projecting the rays. For example, if the data were a single ray the best velocity model would be the average velocity of the ray as determined by its mean slowness (travel time divided by ray length). For two intersecting rays of different slownesses, the pixels common to both rays would have velocities dependent upon some weighted average of both rays. It follows that a data set consisting of many rays crossing at all angles may be back-projected to determine an estimate of the velocities in each pixel needed to produce the travel times. The attenuation of each pixel may be determined in a similar manner.

The method of processing is based on the relation between propagation velocity and the total travel-time, or between attenuation characteristics and received amplitude. For a particular ray path in the  $u$ - $v$  plane, the relation for total travel-time is

$$t_k = \int_{R_k} \frac{ds}{\phi(u, v)} \quad (2.1)$$

where  $\phi(u, v)$  is the velocity of the medium and the integration is along the particular ray path  $R_k$ . The amplitude  $A_k$  at the receiver is related to the attenuation field,  $\alpha(u, v)$  through the equation

$$A_k = A_0 \exp[-\int_{R_k} \alpha(u, v) ds] \quad (2.2)$$

where  $\alpha(u, v) = \frac{\pi f}{\phi(u, v) Q}$  and  $Q$  is dependent on  $(u, v)$ .  $A_0$  has been corrected for the radiation pattern, geometric spreading, and instrument response.  $\alpha(u, v)$ , as determined from this model will be an effect of apparent attenuation, consisting of intrinsic dissipation described in equation (2.2) plus elastic scattering. The projection is then defined as

$$P_k = \ln \frac{A_k}{A_0} = -\int_{R_k} \alpha(u, v) ds \quad (2.3)$$

where  $A_k$  is the received amplitude and  $A_0$  is the source amplitude. In general, the integral equation is written

$$y_k = \int_{R_k} x(u, v) ds \quad (2.4)$$

with  $y_k$ ,  $k = 1, 2, \dots, N$  representing the measured travel-time or amplitude for  $N$  paths and  $x$  representing the slowness or attenuation operator. After discretizing the field, the line integral becomes a finite sum and the problem may be described by a set of linear equations

$$y_k = \sum_{i=1}^I \Delta a_{ki} x_i \quad k = 1, 2, \dots, N \quad (2.5)$$

where  $\Delta a_{ki}$  is the length of the ray  $k$  which penetrates pixel  $i$ , and  $I$  is the total number of pixels, and  $x_i$  is the property of pixel  $i$ .

In matrix notation, this is written as  $\mathbf{y} = \mathbf{A}\mathbf{x}$ , where  $\mathbf{A}$  is an  $N \times I$  matrix with each ray a row of the matrix. Through the use of common inversion techniques, the equations may in principle be solved for  $\mathbf{x}$ , but there are some distinguishing features

which set them apart from an ordinary set of linear equations:

- 1) The matrix  $\mathbf{A}$ , or  $\Delta a_{ki}$ , is quite sparse. If the field is divided into an  $n \times n$  array of pixels then the maximum number of pixels sampled by each ray is  $2n - 1$  and the *maximum* number of zero values for each row  $i$  is then  $n^2 - 2n + 1$ . For  $n = 30$  the matrix is at least 93.44% sparse.
- 2)  $\mathbf{A}$  can be quite large, though not as large as those found in radiology. In practice the number of rays as well as the number of pixels could easily exceed 10,000.
- 3) The equations can be in various degrees either over- or underdetermined for a given data set, because the number of pixels, i.e. the number of columns in matrix  $\mathbf{A}$ , may be changed at will.
- 4) In practice the equations are inevitably inconsistent. Even if the equations were well-determined and a unique solution did exist, it may be as inaccurate as any other "solution". This is due to noise corruption in the data resulting from measurement inaccuracy, discretization of the problem and unknown effects of scattering, diffraction and incomplete data in the form of missing rays or limited angular coverage.

These points eliminate from consideration most of the classical methods of inversion. Sparse matrices have been well-studied in linear algebra, and the techniques developed have been applied to tomography in ART. These techniques are iterative in nature, where one equation, i.e., one ray path, is analyzed at a time. The algorithms require an initial slowness solution  $\mathbf{x}^0$  usually found by specifying a reasonable model, or by performing a simple back-projection of the data:

$$x_i^0 = \frac{1}{N} \sum_{k=1}^N \frac{y_k}{L_k} \quad (2.6)$$

where  $L_k$  is the length of the  $k^{\text{th}}$  ray and  $N$  is the total number of rays. In subsequent iterations an estimate for  $y_k^q$  is calculated along each ray path,

$$\bar{y}_k^q = \sum_{i=1}^I \Delta a_{ki} x_i^q \quad (2.7)$$

where  $x^q$  indicates the estimated slowness after the  $q^{\text{th}}$  iteration. A single iteration includes an analysis of all sets of rays. Most algorithms are based on some minimization of the residual error  $\Delta y_k$ , which is the difference between the observed data  $y_k$  and the calculated data  $\bar{y}_k$

$$\Delta y_k^q = (y_k - \bar{y}_k^q) = \sum_{i=1}^I \Delta a_{ki} \Delta x_{ki}^q \quad (2.8)$$

where  $\Delta x_{ki}^q$  are the set of corrections to the previous slowness values. The determination of these adjustments is the essence of ART algorithms. The correction is then applied to each pixel through which the ray  $k$  passes,

$$x_i^{q+1} = x_i^q + \Delta x_{ki}^{q+1} \quad (2.9)$$

Alternatively, the corrections may be applied after all  $N$  rays have been analyzed by averaging the corrections of each pixel

$$\Delta x_i^q = \frac{1}{M_i} \sum_{k=1}^N \Delta x_{ki}^q \quad (2.10)$$

where  $\Delta x_i^q$  is the total correction for pixel  $i$  and  $M_i$  is the number of rays passing through pixel  $i$ . This latter technique should diminish the effects of noise.

ART was initially used as a reconstruction algorithm in radiology by Gordon, Bender and Herman (1970) and was later found to be similar to algorithms already used in mathematics for solving systems of linear equations. In fact, ART algorithms were being used in radiology before mathematical foundations establishing their validity were produced and, even then, the assumptions were usually too strict to justify their use. Comparative studies by Herman and Rowland (1973), Herman *et al.*, (1973), Herman (1972) and Gilbert (1972) have shown ART algorithms to be quite effective in image reconstruction. Gordon *et al.* (1970) discovered their algorithm in an attempt to

use the projections themselves to solve equation (2.5) without following the transform methods already in use. To take advantage of the sparsity of the matrix and the physical aspects of how it is formed by projections, they suggested an iterative process initiated by some density field. This field is modified in each iteration using information from one ray at a time. The discrepancy in the real projection data and the calculated projection data from the current image is then applied only to those pixels in the field which the ray  $k$  has sampled as shown by equation (2.9). Their initial algorithm simply weighted the residual  $\Delta y_k^g$  by  $\frac{1}{N_{ki}}$ , the number of pixels ray  $k$  has sampled.

In presenting the various algorithms, the mathematics and proofs will not be discussed in detail, but referenced. The reasons for this are two-fold; 1) The algorithms and the mathematics were derived over a decade ago and several papers have been written in various fields presenting the mathematics, and 2) perhaps more importantly, when implementing the algorithms, few of the assumptions necessary for mathematical convergence are usually valid, so the results of these derivations are not applicable to real data. This sobering point will be discussed in detail in the section on convergence and reliability. Presently, four basic algorithms are reviewed.

The first algorithm is thoroughly discussed in Herman *et al.* (1978), Herman *et al.* (1973) and Gaarder and Herman (1972). The algorithm is shown to converge to the minimum norm solution of the equations (2.5) and it is the solution with minimum variance. The convergence is strictly mathematical and may not be applicable to experimental data with inevitable inconsistencies and noise.

*Algorithm 1. ART*

$$x_i^{g+1} = x_i^g + \lambda_k \frac{\Delta y_k^g}{\sum_{i=1}^I \Delta a_{ki}^2} \Delta a_{ki} \quad k = 1, 2, \dots, N \quad (2.11)$$

The rightmost term is the correction term  $\Delta x_{ki}^g$  of equation (2.9) which may be

thought of as the residual  $\Delta y_k$  being redistributed among the pixels with the lengths of the ray through each pixel acting as weights. A relaxation parameter  $\lambda_k$  is also included in this term. These are a sequence of numbers which act as a damping to allow one to control the rate of convergence (Herman *et al.* 1978). Usually a single value is used for all ray paths. In practical implementation of ART, relaxation parameters become extremely important. The consequences of using the "wrong" relaxation parameter can lead to missing the "best" solution by overshooting (under damping) or by slow convergence (over damping) so that the solution is never reached. A slightly different algorithm using just the ray length in the denominator of the weights is shown by Herman *et al.* (1978) to converge similarly to ART, and it has been used in some studies, for example Boyd *et al.* (1974).

*Algorithm 2. ART 1*

$$x_i^{q+1} = x_i^q + \lambda_k \frac{\Delta y_k^q}{\sum_{i=1}^I |\Delta a_{ki}|} \Delta a_{ki} \quad k = 1, 2, \dots, N \quad (2.12)$$

The denominator is now just the total length of the ray path, suggesting that shorter rays hold greater weight. This makes physical sense for two reasons; 1) the shorter rays sample fewer pixels and therefore average fewer velocities, and 2) the  $\Delta y_k^q$  will usually be larger for longer rays, but the correction term should not reflect this purely geometrical characteristic. In crosshole geological applications, the shorter rays will tend to be the more horizontal on average, as are the geological features. This means greater weight will be given to the horizontal features of the velocity field. Of course, this is all dependent on the geometry of the experiment, which should be designed with these ideas in mind. The  $\Delta a_{ki}$  in the numerator gives more weight to the pixel through which the ray segment length is longest. Again, this is intuitively justified because the pixel which the ray samples with the longest path makes the greatest contribution to the total ray value and, therefore, that ray's value should be

weighted relatively more when redistributed to that pixel. Note that the relaxation parameter  $\lambda_k$  is no longer dimensionless and in fact has dimension (length)<sup>-1</sup>. The

choice of  $\lambda_k = \frac{\sum_{i=1}^I |\Delta a_{ki}|}{\sum_{i=1}^I \Delta a_{ki}^2}$  will give equivalent results to ART, but Boyd *et al.*

give it the more practical value of  $w^{-1}$ , where  $w$  is the width of a pixel. They observe some improvement in the reconstructions with this value.

Shepp and Logan (1974) and Dines and Lytle (1979) slightly alter the algorithm to distribute the correction evenly among the pixels sampled using only the ray length as a weight.

*Algorithm 2a. ART 2*

$$x_i^{q+1} = x_i^q + \lambda_k \frac{\Delta y_k^q}{\sum_{i=1}^I |\Delta a_{ki}|} \quad k = 1, 2, \dots, N \quad (2.13)$$

This is just a simple back-projection; the same value is added to each pixel regardless of the length of ray segment which intersects the pixel. The advantage of ART2 is that the segment lengths  $\Delta a_{ki}$  can be ignored, only the ray length and those cells through which the ray passes are needed. This reduces the amount of computer storage space necessary for the computations. The payment for this is the lack of weighting due to greater sampling lengths of pixels, which can produce slightly poorer reconstructions than ART1, but still better than ART in most cases. In this algorithm,  $\lambda_k$  are again dimensionless.

The problem may be approached in terms of entropy optimization (Censor, 1983). This refers to the mathematical problem of maximizing the functional

$$f(\mathbf{x}) = - \sum_{j=1}^m x_j \ln x_j \quad (2.14)$$

over various sets of constraints. In the present case the constraints would be the

collected data in the form of equation (2.1) and the *a priori* information that slowness is positive,  $x_i \geq 0$ . Theoretically, entropy optimization techniques should give better results in situations of information deficiency such as incomplete angular coverage which is common in geophysical applications. As seen from Algorithm 3 below, the corrections are multiplied by, rather than added to, the previous slowness field, giving rise to the term Multiplicative Algebraic Reconstruction Technique (MART). A form of this was originally developed by Gordon *et al.*, (1970).

*Algorithm 3. MART*

$$x_i^{q+1} = \left( \frac{y_k^q}{\sum_{i=1}^I \Delta a_{ki} x_i} \right)^{\lambda_k \Delta a_{ki}} \cdot x_i^q. \quad (2.15)$$

Here the  $\lambda_k$  are relaxation parameters such that  $0 \leq \lambda_k \leq 1$ . Note that they are no longer dimensionless and again have the dimension  $(\text{length})^{-1}$  which becomes very important when determining their values. To be mathematically complete, the slowness field  $\mathbf{x}^0$  must be initialized as  $e^{-1}$  where  $e$  is the base of the natural logarithms. The behavior of this algorithm in practical situations with the presence of noise is unknown.

As an alternative to the ART algorithms, Gilbert (1972) proposed a Simultaneous Iterative Reconstruction Technique (SIRT) which he claimed gave a smoother image than the somewhat "peppered" reconstructions given by ART. The name is derived from the idea of performing the iterative adjustments based on data from all rays simultaneously. This differs from ART which uses information obtained one ray at a time, but is similar to applying the averaged sum of the corrections (equation 2.10). As with equation (2.10) an advantage of SIRT is that it is less susceptible to noise in the data. The mathematical properties of SIRT reconstructions were demonstrated by Lakshminarayanan and Lent (1975). They show that SIRT may be considered an attempt to obtain a least squares reconstruction by identifying it with the Richardson least squares algorithm.



*Algorithm 4. SIRT*

$$x_i^{q+1} = x_i^q + \frac{\sum_{k=1}^N y_{ki}}{\sum_{k=1}^N L_k} - \frac{\sum_{k=1}^N R_{ki}}{\sum_{k=1}^N N_k} \quad (2.16)$$

where the subscript  $ki$  denotes those rays  $k$  which pass through pixel  $i$ .  $y_{ki}$  is the observed data,  $L_k$  is the length of ray  $k$ ,  $R_{ki}$  is defined as the sum of the values in each pixel that ray  $k$  samples and  $N_k$  is the number of pixels that ray  $k$  samples.

A computational advantage to SIRT is that the segments  $\Delta a_{ki}$  need not be calculated, saving a large amount of storage space and computation time. The price is that these segments usually act as weights and improve reconstructions for seismological data where the ray lengths are variable. To make use of these segments, SIRT may be modified rather heavily to obtain

*Algorithm 4a. SIRT (modified)*

$$x_i^{q+1} = x_i^q + \frac{\sum_{k=1}^N \lambda_k \Delta y_k^q \frac{\Delta a_{ki}}{L_k}}{\sum_{k=1}^N \Delta a_{ki}} \quad (2.17)$$

This turns out to be very similar to ART2 using the average corrections by equation (2.10) and in practice the results are indeed similar. This modification has no real mathematical basis and the results of Lakshminarayanan and Lent as well as those found by Gilbert are probably not applicable to this algorithm.

**Algorithm Modifications**

An advantage of ART algorithms is that the basic algorithms, as described in the previous section, can be easily modified. These modifications are usually in the form of weights and can be applied to individual or groups of rays and pixels. The purpose of

these “tricks”, as they are sometimes called in the medical literature, is to provide a means of de-emphasizing certain less reliable rays, or for constraining certain pixels to reasonable values. This is important in seismological applications where some travel times are more reliable than others and velocity bounds for the medium can be determined.

#### A. *Smoothing function*

In the presence of noise or with a highly oscillatory solution a smoothing function may be incorporated in the algorithm to inhibit “peppered” reconstructions. A window which averages the slownesses of the nine adjacent pixels into the central pixel in some manner will greatly improve reconstructions. This can be done by performing the following operation between each iteration:

$$x_{ij}^{q+1} = \frac{\sum_{k=i-1}^{i+1} \sum_{l=j-1}^{j+1} W_{kl} x_{kl}^{q+1}}{9} \quad (2.18)$$

where  $x_{ij}^{q+1}$  is the slowness value in the  $i^{th}$  row and  $j^{th}$  column of the slowness grid for the  $q+1$  iteration. The nine specified weights,  $W_{kl}$ , are usually determined by the relative positions to the central pixel,  $x_{ij}$ . For example, the central pixel will be given the greatest weight while the corner pixels receive the least. The improved reconstruction produced by smoothing will be at the expense of resolution, but in many cases this sacrifice is reasonable, if not necessary.

#### B. *Velocity constraints*

Another modification used to improve reconstructions constrains the solution to reasonable values or to known velocity limits. In radiology it is common to set any negative densities to zero. In seismology this is analogous to constraining the slownesses to values reasonable for the region of study. Greater constraints may be applied in

regions of poor ray coverage or a general constraint model may be applied to the entire field. The constraints are applied after every iteration using the following algorithm:

$$\text{For all } x_{ij} : x_{ij} = \begin{cases} U_{ij} & \text{if } x_{ij} > U_{ij} \\ V_{ij} & \text{if } x_{ij} < V_{ij} \\ x_{ij} & \text{otherwise} \end{cases} \quad (2.19)$$

where  $U_{ij}$  and  $V_{ij}$  are respectively the upper and lower velocity limits for pixel  $ij$ . Care must be taken since over-zealous constraints will tend to render the reconstructed values useless.

### C. Weighting

The algorithms are modified by weighting primarily for two reasons; certain travel times are less reliable than others, and the variable path lengths should be taken into account. Weights are incorporated into the algorithm by forming a matrix  $\mathbf{W}$  of weights corresponding to each element of matrix  $\mathbf{A}$ . These weights are applied as each correction  $\Delta x_{ki}^q$  is calculated

$$x_i^{q+1} = x_i^q + W_{ki} \Delta x_{ki}^q \quad k = 1, 2, \dots, N \quad (2.20)$$

Now each ray  $k$  may be weighted for travel time reliability by assigning to each  $W_{ki}$  a value between 0 and 1. Another weighting scheme, based on the ray length, weights according to the ratio of the length of ray path  $k$  through pixel  $i$  to the total path length

$$W_{ki} = \frac{\Delta a_{ki}}{\sum_{i=1}^I \Delta a_{ki}} \quad (2.21)$$

The purpose of these weights is to give the longer ray paths lower weights while giving those pixels with longer ray segments greater weights. This can help to reduce the problem of "smearing" which will be discussed in the next chapter. Virtually any other weighting scheme may be used, but this study uses only equation (2.21).

#### D. Curved raypaths

The presence of an inhomogeneous velocity field leads to ray paths which violate the assumption of straight rays. Depending on the velocity distribution, the Fermat path will be curved to a certain degree. The flexibility of the ART algorithms allows these curved paths to be easily incorporated through ray tracing (with a substantial increase in CPU time). The ray segments  $\Delta a_{ki}$  are simply a digitization of the ray path. Therefore the ray may be traced through any given velocity model and the resulting curved ray path discretized into the  $\Delta a_{ki}$ . These ray segments can then be used in the algorithms. A detailed description of this process will be given in the following chapter.

#### Convergence and Reliability

The ART algorithms are iterative, so some criteria must be specified to stop the process. An added difficulty is introduced because the solution is non-unique, especially in the presence of noise, so that the convergence may not be to the actual slowness distribution. In fact, it has been found that the solution initially converges toward a plausible slowness model then diverges from this model after some number of iterations (Herman *et al.*, 1973). This presents a problem in determining the reliability of the solution at any given time, which in turn makes the determination of a relaxation parameter and estimating the optimal number of iterations very difficult. Optimizing these values will improve computation time, and more importantly, will help ensure the calculation of the solution closest to the actual slowness field. The question is then; How can the reliability of the solution be evaluated and by what criteria is the best solution determined? To answer this question some mathematical measures and visual inspection criteria are presented in this section. These measures are used with synthetic data in the next chapter to determine their behavior and usefulness with real data. Most experiments presented in the medical literature are performed on test data so

that problems with convergence and reliability have been discussed at length for solutions with known images. With an unknown image the analysis becomes much more difficult and no rigid criteria has been developed to test the solution of real data.

The most commonly used mathematical measures used to measure reliability and resolution, and to determine stopping criteria (Gordon, Bender and Herman, 1970) are the distance between the measured and calculated projection values (RMS residual)

$$r^q = \sqrt{\frac{1}{N-I} \sum_{k=1}^N (\Delta y_k)^2} \quad , \quad (2.22)$$

the variance

$$V^q = \frac{1}{I} \sum_{i=1}^I (x_i^q - \bar{x})^2 \quad , \quad (2.23)$$

where  $\bar{x}$  is the mean slowness of the field, and the entropy

$$S^q = \frac{-1}{\ln n} \sum_{i=1}^I \left( \frac{x_i^q}{\bar{x}} \right) \ln \left( \frac{x_i^q}{\bar{x}} \right) \quad . \quad (2.24)$$

If equations (2.5) are complete and consistent,  $r^q$  will tend to zero while  $V^q$  will tend to decrease and  $S^q$  to increase with increasing  $q$ . The purpose of minimizing variance (or maximizing entropy) is to find the "smoothest" possible image, i.e. the one closest to the mean, while still satisfying the data. In real applications the starting model is often excessively smooth, so that the variance will actually increase (and entropy decrease) to satisfy the data.  $r^q$ ,  $V^q$  and  $S^q$  measure convergence to a solution, but not closeness of the solution to the actual slowness distribution. In fact, these measures may continue to "converge" while the solution may be diverging unacceptably from the actual distribution. For synthetic experiments in which the true slowness field is known, the closeness of the solution to the actual field may be measured. This "distance" between the original slownesses and the reconstructed slownesses is

$$\delta^q = \left[ \frac{1}{NV^q} \sum_{i=1}^N (x_i^q - x_{0i}) \right]^{\frac{1}{2}} \quad (2.25)$$

where  $x_{0i}$  is the original slowness model and  $V^q$  is the variance for the  $q^{\text{th}}$  iteration (Lakshminarayanan and Lent, 1979). The distance is used in the synthetic studies to determine the accuracy of the algorithms and to study the behavior of other measures as the solution converges to the original model. It is hoped that some consistent behavior is exhibited by the other measures so they can be useful in analysis of real data.

To study the characteristics and reliability of the measures themselves, the distance given by equation (2.25) must be assumed an accurate measure of the goodness of fit to the solution. This allows, using synthetic data, the study of the behavior of the different measures in the vicinity of the solution closest to the actual model using synthetic data. If consistent patterns of the measures are seen in the vicinity of the optimal solution, these measures may be used with real data, with the optimal image selected as that in which some measure shows similar patterns as it did with the synthetic data. For example, after looking at many examples, Herman *et al.* (1973) adopted the following methodology using variance. An estimation of the optimum number of iterations is the smallest number  $q$  such that

$$| V^{q+1} - V^q | < \frac{1}{100} V^q \quad (2.26)$$

That is, the process is stopped at that iteration when the change in variance is less than 1% of the variance. While this method may be consistent in radiology, it is found in this study the optimum percent value of variance is not constant, depending on relaxation, geometry, number of rays and size of pixels, making a standard value difficult to obtain. However, the idea remains helpful in determining the optimum number of iterations.

Along with the above mathematical measures, the solution may be inspected visually for some obvious inconsistencies which may not be readily determined mathematically. For example, real data will form solutions with a decreasing RMS residual while

the image can be visibly oscillating. This signifies a need for a smaller relaxation value; more damping. For real data visual inspection is a subjective measure of reliability; one assumes he has a good idea of what the image should look like and judges the solutions accordingly. A visual evaluation of a solution begins with a check for large oscillations of velocity in adjacent pixels. This oscillation is caused by overshooting the solution, particularly for poorly determined problems, and it may be controlled by decreasing the relaxation parameter or the number of iterations. Two-dimensional spatial Fourier transforms are used to help measure the nature of the oscillation in the image. The velocity variations are expected to be relatively long wavelength, occurring over several pixels, while the variations due to improper parameters occur at wavelengths of only one or two pixels. Therefore, in wavenumber space (reciprocal wavelength) the unwanted oscillations appear as large amplitudes at values of  $C^{-1}$ , where  $C$  is the pixel width. These will be at the high wavenumber end of the spectrum while the physical velocity variation will more likely be at the low or intermediate wavenumber. By performing a Fourier transform the relative amplitude values may be measured and those solutions with a smoother transform, i.e. lower values at high wavenumbers, will generally be the most reliable.

After a reconstructed velocity distribution is chosen, it can then be inspected for significant deviations from plausible models, both in location of the anomalous zones and the actual velocity values in the field. Of course the actual velocity distribution is unknown, but a systematic procedure may be followed to ensure that a feature of the reconstructed distribution is real (Gordon, 1974). The method essentially measures the sensitivity of the solution to the starting model  $x_i^0$  by running the program with different starting models. There may be some features which are consistent among the final solutions, others appear only for a few starting models, and thus are suspect. Another procedure consists of changing the values of anomalous zones in a solution and then using this model as the initial slowness field in a new iteration. If the zone does

not appear in the new reconstruction its significance is questionable. If it does remain, some confidence is gained in its reality, since its presence apparently is required by the data.



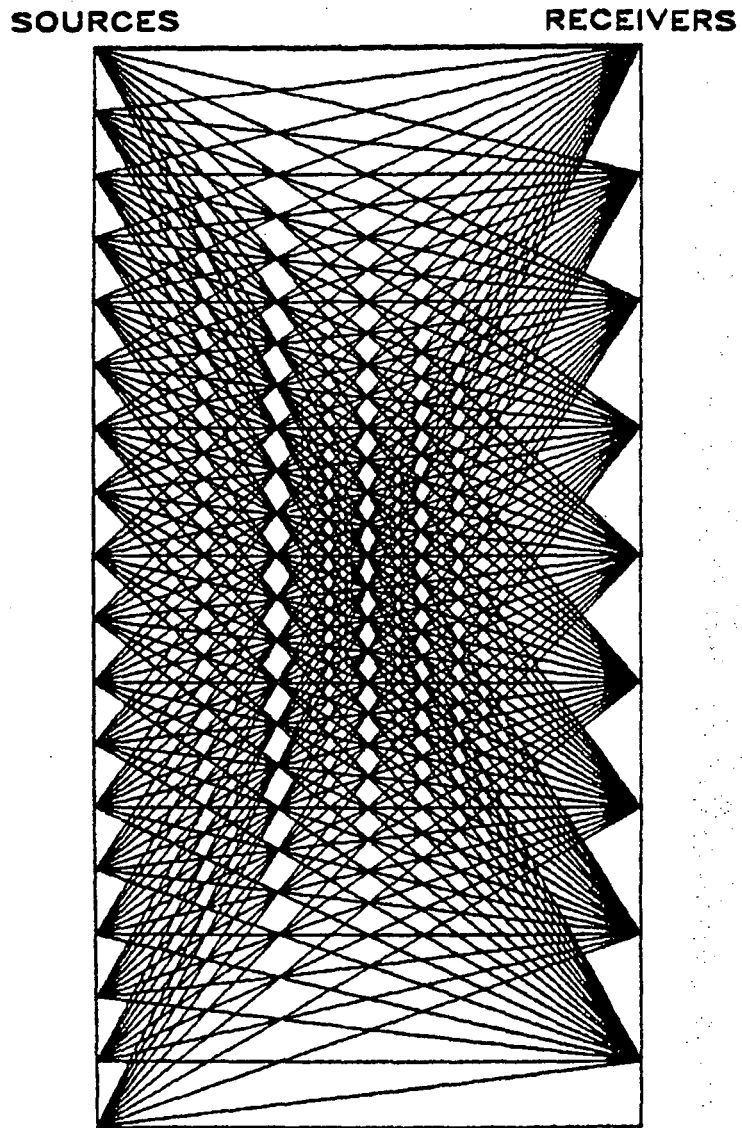


Figure 2.1. The raypaths for a typical crosshole experiment.

## CHAPTER 3

### Application to Synthetic Models

#### Introduction

The ART algorithms are applied to several velocity models of varying complexity to determine the reliability and behavior of the algorithms. Such studies should be done in practice to determine the source-receiver configuration needed in an experiment. A modeling study may be performed with existing data to determine resolution and the types of anomalies that can be seen (Ivansson, 1985). Valuable insight can be gained by studying reconstructions over a suite of parameter values and pixel sizes on various velocity models. None of this can be determined mathematically because of the number of parameters involved and more importantly because of the lack of a firm mathematical base in the presence of noise and other irregularities. Resolution matrices can be calculated (Menke, 1984 and Chapter 6, this thesis), but they only show expected resolution for specific geometries and not how well the ART methods reconstruct an area.

This chapter makes use of a simple velocity model to study the general reliability and behavior of ART with travel time data. Several factors are analyzed individually. The velocity model is initially reconstructed using each one of the algorithms to give an idea how they perform. A representative algorithm will then be chosen for the following analyses:

- 1) The relaxation parameter is varied to determine the effect of damping on the convergence rate and the distance  $\delta$  (as defined in equation (2.25)).
- 2) Some criteria must be developed to determine when to stop the algorithm if ART is to be effective in reconstructing real data. Synthetic data enables  $\delta$  to be calculated and behavior of visual and statistical measures around the minimum  $\delta$  can be noted and quantified.
- 3) One of the common problems with ART methods is the "peppered" reconstructions often produced. These are results with high velocity oscillations between adjacent pixels. The most effective technique available to eliminate peppering is the application of the smoothing function of equation (2.18) to invert the travel time data.
- 4) A common criticism of tomographic inversions is that an assumption of straight ray paths is usually made in practical applications. Mathematically, straight rays are not necessary in ART, the integral in equation (2.1) is over any curve  $R_k$ , but are used because of practical convenience. Curved ray paths are incorporated into the algorithm and used in the inversion of the velocity model.
- 5) It is desired that the pixel size used in the inversion be small so that small velocity features can be recovered. However, if pixels are too small the results deteriorate; a trade-off exists. A sequence of inversions are performed on a suite of 11 different pixel sizes using the same travel times. The optimal pixel size can then be deduced from these results.
- 6) Even the best data will have some noise due to measurement errors, diffractions and scattering. Therefore, random Gaussian noise is added to the travel time data to study its effect on the reconstructions.
- 7) At times the range of projection angles available in a survey will be limited. This is true for surface data where noise and the near-surface weathered layer greatly

affects the quality of the signals. An example is given to show how this can change the results.

8) Finally, a slightly more complex model will be reconstructed.

Comparisons between reconstructions are made throughout this chapter. Factors compared are the distance,  $\delta$ , to the original model, visual observations of the smoothness of the result and how well it represents the model.

Another goal of this chapter is to present a graphic catalog of problems that are encountered with ART inversions and the effect of variations in the algorithms on the reconstruction. Such a catalog is helpful when problems arise in processing real data. In fact, a separate study should be done before any experiment to anticipate problems and suggest solutions.

### **Generating the Data**

In radiology model studies, a "true" projection is defined as the actual value for the projection along a certain ray. A "pseudo" projection is the approximate value calculated by the summation of the pixel densities along each ray (Herman *et al.*, 1973). The two projections are in general different. Early studies calculated true projection data in units of density by integrating along a ray path through some test pattern usually in the form of a photograph (Gordon *et al.*, 1970; Gilbert (1972); Herman (1972); Herman and Rowland (1973)). Initially this integration was carried out over the same grid used for the inversion, yielding the pseudo projections. Gilbert (1972) showed the error in this procedure by integrating analytically along the ray path and finding poor quality reconstructions. Integrating analytically along each ray path limits the suitable test patterns studied and takes unreasonable time, so most studies simply sum along a much finer pixel grid than that reconstructed (Herman and Rowland, 1973).

A similar situation occurs in seismology where the curved ray paths and scattering of acoustic waves makes the forward calculation more critical. Most studies have used straight rays for both the generation of the synthetic data and the inversion (McMechan, 1983) giving far better reconstructions than can be expected in real situations. Tracing rays through a test model to obtain travel times, while not totally realistic, gives errors similar to the noise in real data. A program capable of ray tracing through any reasonable two-dimensional velocity model is used for data generation in this thesis. Using horizontal layers and velocity gradients between vertical interfaces, the program can provide travel times for direct, reflected and refracted rays. A shooting method is used to find the correct ray path. The required takeoff angle is calculated based on the difference between the receiver coordinates and the previous ray end point. The method uses a fair amount of computation time and, due to shadow zones, some rays cannot "hit" the receiver within the error value allotted for convergence.

The rays can be determined for most reasonable velocity models and source-receiver configurations. At least three parameters must be evaluated; the type of data being considered, the geometry of the model, including the source-receiver locations and the velocity heterogeneity. The types of data usual in tomographic reconstructions with seismic waves are cross-borehole, borehole-mine, surface wave, reflection profiles, refraction surveys or earthquake data at any scale. This chapter tests only borehole-to-borehole or borehole-to-surface-to-borehole data. The geometry of the borehole data will be a rectangular area varying with borehole spacing and depth. Sources will be down one borehole and receivers down another, with an option for a surface array. The test velocities are homogeneous fields, simple gradients with few layers, and single low- or high-velocity anomalies. More realistic models are studied in the next chapter. The goal here is a basic understanding of the algorithms and their behavior, which is seen more clearly with simple models.

## Results

Velocity model A consists of a simple rectangular low velocity zone (5.5 km/s) in a constant velocity (6.0 km/s) field (Figure 3.1). Stations are located 0.5 units apart down the 10-unit boreholes and 0.5 units apart for the surface array, a total of 1081 rays. The algorithms studied will be:

ART - Algorithm 1, equation (2.11)

ART1 - Algorithm 2, equation (2.12)

ART2 - Algorithm 2a, equation (2.13)

MART - Algorithm 3, equation (2.15)

WART - weighting scheme, equation (2.21), applied to ART

SIRT - Algorithm 4a, equation (2.17)

For each of these algorithms the image was corrected after each ray was analyzed. Equation (2.10) was used to correct the image after each iteration (signified by an "A", e.g. ARTA). The same starting model used to initiate the algorithms, calculated by a simple back-projection (equation 2.6), is the same throughout the chapter. Also, a 35x35 pixel grid and straight ray paths are used except where specified.

### A. Algorithm performance

The performance of each algorithm can be best determined by a visual comparison of the velocity model and the reconstruction. The mathematical distance between the two given by equation (2.25) is less important. All algorithms take about 200 seconds of CPU time on the VAX 11/780, VMS, for 30 iterations, so none have a computation time advantage. Figure 3.1 shows velocity model A and the shading scheme which will be used in all the figures. The convergence rate was altered by damping each algorithm so that the solution closest to the model was achieved after 14 to 22 iterations. This eliminates the effect of convergence rate on the final solution.

The best reconstruction of the velocity model for each algorithm are shown in Figure 3.2. The similarity between results is immediately apparent. The low velocity zone is adequately recovered in each case, but with smearing extending from the corners of the low-velocity rectangle. This common "smearing" is due to incomplete or limited projection angles and the use of straight rays in the inversion. Smearing is prevented toward the surface due to the presence of the surface array creating a more complete set of rays than found at the bottom of the field. The WART weighting scheme (Figure 3.2) does not eliminate this smearing. Figure 3.3 displays the results of using averaged corrections applied after each iteration (equation 2.10). SIRT is included with these algorithms since it uses all rays simultaneously. Except for SIRT, the reconstructions, as expected, are noticeably smoother than in Figure 3.2. This result suggests that it is better to use ART with correction procedures than the SIRT algorithm. Although the reconstructions are smoother, improvement over Figure 3.2 is minimal and the smearing persists.

The algorithms are also compared mathematically. Figure 3.4 shows the convergence of each algorithm by plotting the distance found by equation (2.25) versus the number of iterations. The iteration at which the smallest distance occurs was used for Figures 3.2 and 3.3. Again, the similarity between algorithms is apparent. The distance initially drops quickly then levels off until the minimum at about 16 iterations where it begins a slow increase. The value of the minimum point is shown in Table 1. This value is dependent on the relaxation parameter as shown in the next section. The oscillations shown by the -A algorithms (Figure 3.4B) occurs because such low damping (high  $\lambda$ ) is needed for a minimum distance to occur before 30 iterations.

From such a simple velocity model only a general comparison between algorithms can be made. Visually, the algorithms using averaged corrections give slightly smoother reconstructions, while ART2 and ART2A give the closest mathematical distance to the original model. Based on these findings and numerical studies using other

velocity models, ART2 will primarily be used in the following studies.

### B. *Relaxation parameter*

The relaxation parameter,  $\lambda$ , is used to damp the convergence rate of the algorithms. A greater  $\lambda$  corresponds to lesser damping. Table 1 shows the wide range of values necessary for the algorithms to converge at the same rate. The effect of the relaxation parameter on convergence rate for ART2 is illustrated in Figure 3.5. The number of iterations to the "best" picture, defined as that reconstruction corresponding to the smallest  $\delta$ , increases with decreasing relaxation. This suggests that the target relaxation parameter is that one which gives the best reconstruction after a few iterations. This is not always true in practice, for several reasons. First, one usually wishes to see the reconstruction developing when the distance cannot be measured to get a better feel for the optimal result. Also, damping that gives the "best" reconstruction after 10 iterations will give a better solution than that damping which gives the best reconstruction after only two or three iterations (Figure 3.5B). This is expected, increased damping by lower relaxation values will change the solution less for each iteration and the solution will converge slower with less chance of overshooting the best solution. Figure 3.6 shows this more clearly. For increased damping, the curves reach a lower minimum and also become smoother. The lower damping causes oscillations in the curve and shows no true minimum.

### C. *Stopping criterion*

Figure 3.6 also illustrates an important convergence characteristic of ART. Note that for each relaxation value,  $\delta$  begins to increase after passing through a minimum, i.e. the solution will ultimately diverge from the original model as the number of iterations continues to increase. One reason for this is that the distance is measured to velocity model A, but because the inversion uses straight rays the algorithm will try to fit the data, produced using traced rays, to an unknown model. The point is that



criteria must be developed to determine when to stop the algorithm when real data are being used. Several such criteria are developed in this section through the use of modeling.

The quality of a solution is usually indicated by the extent of oscillation in the velocities. High oscillations indicate that the damping is too low or the algorithm was not stopped soon enough. A visual assessment of the reconstructions is the simplest means of determining the extent of the oscillation. This is not very quantitative, but is the quickest means of approximating the iteration at which the algorithm should have been terminated.

Another general rule for stopping the algorithm makes use of the RMS residual (equation (2.22)). This value is a measure of the accuracy at which the reconstructed velocity distribution fits the travel time data. Therefore, if the value is below the accuracy of the travel time measurements the algorithms should be stopped. For example, if the travel times are measured to 0.01 second the algorithm is stopped when the RMS residual drops below this value. If the algorithm is continued it will be trying to find a solution that fits the noise, producing unreliable results.

A stopping procedure similar to that found by Herman *et al.* (1973) which was discussed in Chapter 2 provides a more quantitative method of stopping the algorithm (equation (2.26)). Their stopping criteria of 1% of the variance is not useful, because it is variable, dependent on relaxation parameter, geometry, number of rays and size of pixels. However, the basic idea remains helpful. Figures 3.7, 3.8 and 3.9 show the behavior of the variance (equation (2.23)), entropy (equation (2.24)) and RMS residual (equation (2.22)), respectively, versus iteration using the same data and parameters as Figure 3.4. The arrow indicates the point where  $\delta$  from Figure 3.4 reaches a minimum. These curves are characterized by large initial increases or decreases in values and a gentle bend developing after a few iterations reducing the slope just before the arrow. This graphically illustrates the Herman *et al.* stopping criterion where they assume

the arrow will occur at the same slope for every inversion. Inversion of several velocity models shows this not to be the case. However, the optimal iteration always occurs after a similar bend in the curves. Thus, a simple plot of these values can give a good approximation of the optimal iteration. The exact value for this iteration is not necessary as shown by Figure 3.10.

#### D. *Smoothing*

One of the problems inherent in the ART methods is oscillation of the velocities between adjacent pixels, causing peppered reconstructions. Smoothing algorithms may be incorporated into ART to eliminate some of this oscillation. Smoothing would also help eliminate the "legs" of the low velocity zone or in general, any scattered low or high velocity pixels that are not real. A consequence of smoothing is that the resolution of smaller features is reduced.

The smoothing algorithm given by (equation (2.18)) was performed on Model A after every iteration of ART2. There is obvious visual improvement over the unsmoothed reconstruction (Figure 3.11). The distance,  $\delta$  is also reduced (Figure 3.12). The objective of the smoothing function is realized; the oscillatory behavior in the reconstructed velocity distribution is effectively removed. However, a more complex model must be used to determine the resolvability of smaller features when smoothing is applied.

#### E. *Raytracing*

Curved ray paths are incorporated into the algorithm by tracing the rays through the velocity reconstruction at every iteration to get the true pixel sublenghts  $\Delta a_{ki}$ . There are several reasons why this has not been done. First, it would take a prohibitive amount of computing time to set up a velocity model and trace through it after every iteration. Another reason is that an anomalous pixel can severely distort a ray, so that raytracing would have to be performed on a smoothed version of the

solution. Also, noise will produce anomalous pixels and ultimately the curved ray paths can become more erroneous than straight rays. Careful thought must be given to the question of how accurately the raytracing finds the actual path and the travel time. The most practical way of incorporating raytracing into the algorithms is to trace the rays through some general velocity model, and then use these calculated sub-lengths in the inversion. The general velocity model may be determined by a straight ray inversion, or by *a priori* information on the area, or by a combination of them. The model may be updated and traced again after the inversion is completed.

The raytraced sublengths  $\Delta a_{ki}$  are calculated for velocity model A and then used with ART2 to obtain Figure 3.13. The comparison with the unraytraced result (Figure 3.11B) shows no visual improvement. Smearing may be slightly reduced, but velocity oscillations increase. A subtle, yet important difference is that the velocities of the anomalous zone in the raytraced reconstruction are closer to the original model than the unraytraced velocities. This is reflected in the  $\delta$  values given in Figure 3.14. Figure 3.13 also includes the results of the smoothing algorithm applied with the raytraced program. The results are visually impressive and the velocity values are almost identical to the original model. Again, this is reflected in  $\delta$  (Figure 3.14). The price of the raytraced inversion is a 10-fold increase in CPU time.

#### F. Pixel size

The size of the pixels used in the inversion effectively determines the limiting size of the velocity feature which can be recovered. A trade-off results because the solution becomes unstable with decreasing pixel size. Therefore, the optimal pixel size is small enough to recover the desired velocity features without resulting in peppered reconstructions. Of course the design of the experiment plays a large role in the trade-off; the pixel size may be reduced with a greater number of rays. The optimal pixel size for model A is determined by running ART2 on the velocity model for an increasing

number of pixels beginning with a 10x10 array. Straight ray paths are used.

The reconstructions for the series from a 10x10 array to a 60x60 array are shown in Figures 3.15. Good reconstructions are obtained throughout the sequence, though some deterioration results after the 45x45 array. The reconstructions become rather peppered for pixel arrays greater than this. Therefore, the inversion is performed with smoothing on the 60x60 array (Figure 3.16). The reconstruction is visually better than the 35x35 array (Figure 3.15) used throughout this chapter showing that the pixel size may be reduced through the use of the smoothing function. These results indicate that a 2 to 1 ratio of station spacing to pixel size is possible without smoothing and a 3 to 1 ratio is possible with smoothing. These ratios are higher than expected, but a more complex velocity model must be studied to determine if these ratios can be achieved with real data.

#### *G. Noise*

Synthetic data does not contain the noise inherent in real data which should affect the results of an inversion. Noise can be modeled by random Gaussian additions to the travel times. In this section variable amounts of random Gaussian noise are added to the model A travel times which are then inverted using ART2 and straight rays.

Initially, Gaussian noise with a mean of 0.0 seconds and a standard deviation of 5% of the total travel time was added to the travel times (Figure 3.17). Deterioration of the reconstructions results in the form of increased velocity oscillations and increased smearing. The oscillations are of high amplitude, 0.25 to 0.50 km/s between adjacent pixels, and are scattered randomly about the image. Smearing becomes more dominant in the presence of noise. The effect is to decrease the size of the low velocity zone by smearing it toward the lower corners. When 10% Gaussian noise is added (Figure 3.17) the oscillations and smearing increase. The smoothing algorithm was

applied to ART2 to diminish these effects of noise on the reconstructions (Figure 3.18). Smoothing has the anticipated effect of eliminating virtually all of the scattered oscillations produced by the 5% noise and most of those produced by the 10% noise. Smearing has not been eliminated, but its extension had been limited. However, the effect of low velocity "leaking" into the legs is more dramatic with the oscillations removed.

#### H. *Limited coverage*

ART2 has been applied to a simple velocity model with good station coverage. In real situations the ambient seismic noise and the presence of a weathered layer will reduce the quality of surface data. This will cause a reduction in the effective distance between source and receiver at which onset times can be read accurately. To model this, the surface array of model A is eliminated and the effect on the reconstructions studied. This reduces the number of travel times to 400. The angular coverage is also diminished which effectively reduces horizontal resolution (Menke, 1984), i.e. horizontal extension of the low velocity zone should result.

The result does show extension of the low velocity zone toward the boreholes (Figure 3.19). The reconstructions also suffer from oscillating velocities in this area and higher velocity values in the low velocity rectangle. It is possible that this behavior is partially due to the number of pixels being too large for the reduced number of rays. Therefore, the grid is reduced to a 20x20 array. This has the obvious effect of smoothing the oscillations, but generally gives poor reconstructions. The oscillations can be removed more effectively by smoothing on a 45x45 pixel array. The smearing and horizontal extension of the low velocity rectangle remain unaffected by this smoothing.

#### I. *Velocity Model B*

Velocity model A provides a simplistic velocity distribution convenient for studying the behavior of ART2. The next chapter provides results for a more complex

model. In this section velocity model B (Figure 3.20) is constructed to give an indication of how ART2 will perform with a more complicated structure. Model B consists of a linear velocity gradient from 5.5 km/s to 6.5 km/s with an anomalous rectangular low velocity zone (5.5 km/s) similar to that of model A (Figure 3.20). Stations are located 0.5 units apart down the 20-unit boreholes spaced 10 units apart, and 0.5 units apart for the surface array, giving a total of 3003 rays. The 2:1 ratio of well depth to distance between wells increases the angular coverage of model A. ART2 is used to reconstruct the model B velocities using straight rays on a 30x60 pixel grid.

A visual assessment of the resulting inversion (Figure 3.20) shows that model B is reconstructed quite well; the horizontal layering is clear and the bounds of the low velocity rectangle are accurate. Smearing toward the bottom of the velocity field provides the biggest source of error. This simple test indicates that more complex structures may be adequately reconstructed with smearing providing some problems.

### **Discussion and Summary**

The reconstruction of a simple velocity model was analyzed using ART algorithms. The simple model was used so that the general behavior of the algorithms could be studied. A result of such a simplistic model is that all algorithms reconstruct the velocity model quite well, making comparisons between them difficult, while making the study of weighting, smoothing, pixel size, noise and stopping criteria much easier. Outstanding features of the reconstructions include the accuracy of the bounds of the low velocity zone, the overall velocity values, velocity oscillations and the effects of smearing.

The biggest problem with ART algorithms is that it is difficult to determine when to stop the iterative procedure. It is found that the procedure initially converges to the original model, but ultimately it will drift from it. It is not critical to obtain exactly the optimal iteration, but the general point where this drifting begins must be

found for reliable reconstructions. Several criteria were developed in this chapter and it seems all of them should be used in the analysis of real data to find a reasonably accurate optimum iteration.

Problems with real data can emerge from noise or from limited station coverage. The effects of limited station coverage depend on the extent of this limitation; a few missing source-receiver pairs will have virtually no effect on the reconstruction. A surface array will usually provide the least precise travel time data, and in noisy environments data acquisition will not even be attempted at the surface. This decreases the horizontal resolution for the reconstruction of velocity model A. Smearing and oscillating velocities dominate the area between the low velocity zone and boreholes. This is an important result because angular coverage is commonly limited even in boreholes due to the longer paths traveled by the steep-angled rays. Noise was also modeled using random Gaussian additions to the travel times. The result was an increase in the oscillations and smearing effects. The basic velocity model may be retrieved from the reconstructions, but it is evident from this study that more complex velocity distributions can not be recovered reliably in the presence of even 5% random Gaussian noise unless a smoothing function is employed.

The effects of smearing and velocity oscillations may be reduced by smoothing the reconstructions between each iteration. This will also tend to increase the overall quality of the picture. Smoothing is also helpful, if not necessary, in the presence of noise or limited station coverage. Using the true curved ray path also reduces the smearing, but perhaps not enough to justify the 10-fold increase in CPU time. Further studies with more complex velocity distributions are necessary to determine how smoothing affects smaller velocity features and whether raytracing can produce greater improvement in the reconstructions in the presence of larger velocity contrasts.

Finally, the study showed that smaller pixels may be used if the smoothing algorithm is incorporated. Smaller pixel sizes mean that smaller velocity features may be

recovered, because each pixel assumes a constant velocity area. In real situations the pixel size should be as small as possible without resulting in unstable solutions.

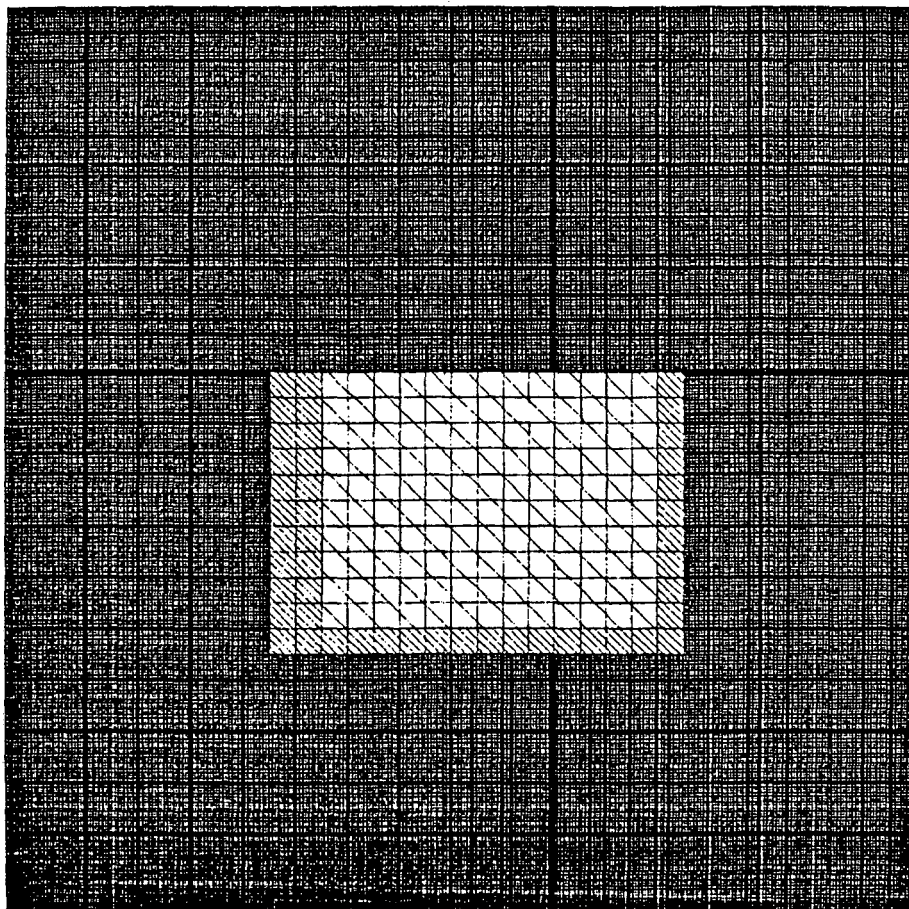
In general, the results from the study are encouraging. Model A was reliably reconstructed using ART algorithms and the results of model B indicate that reconstructions of more complex velocity distributions will have similar success. The presence of noise and limited station coverage diminished the accuracy of the results, but these obstacles were overcome through the use of the smoothing function. The results of this chapter lead to a continuation of the study using a more complex velocity model, in the following sections.





Algorithm	$\lambda$	Iter to Min	Minimum Distance (km/s)
ART	0.14	14	0.7419217
ART1	0.50	14	0.7418688
ART2	0.10	14	0.7283480
WART	4.50	16	0.7352613
MART	0.50	14	0.7369022
ARTA	2.20	23	0.7408047
ART1A	8.50	23	0.7409949
ART2A	2.00	20	0.7278879
WARTA	58.00	23	0.7454458
MARTA	8.00	23	0.7367257
SIRT	0.60	12	0.7427554

**Table 3.1.** The relaxation parameters,  $\lambda$ , required to produce minimum distance,  $\delta$ , at 12 to 22 iterations. The number of iterations to the minimum and the value of that minimum are also given.



## MODEL A

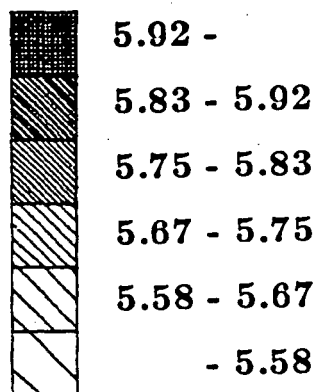
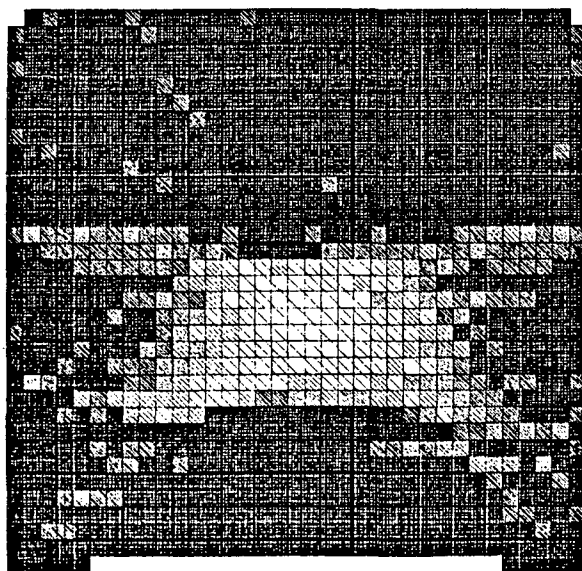
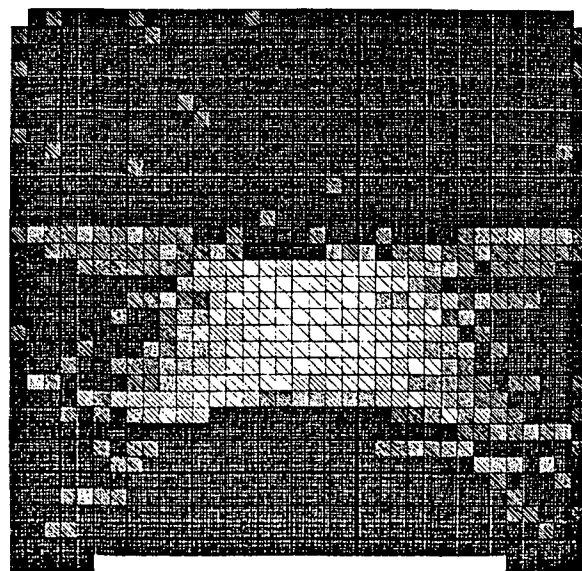


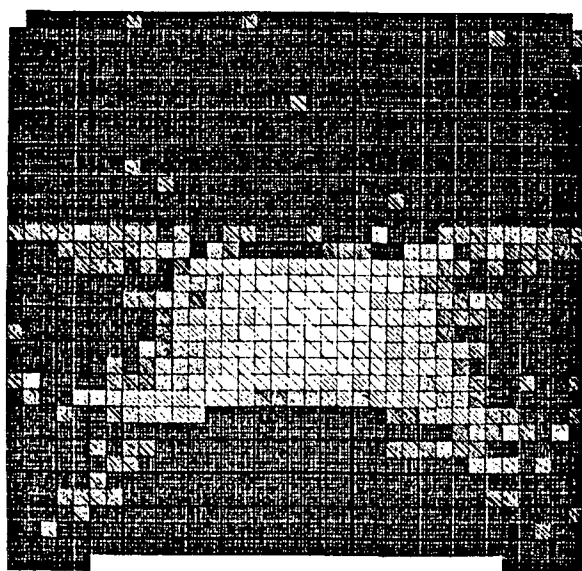
**Figure 3.1.** Velocity model A and the shading scheme used in the following plots; velocities are in units of kilometers per second.



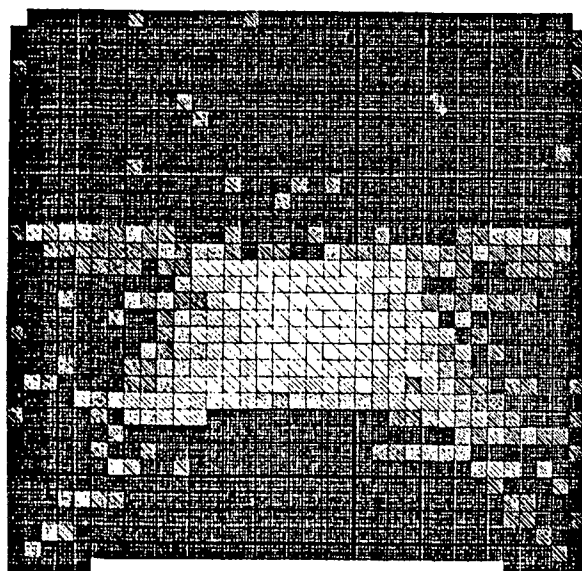
ART



ART1

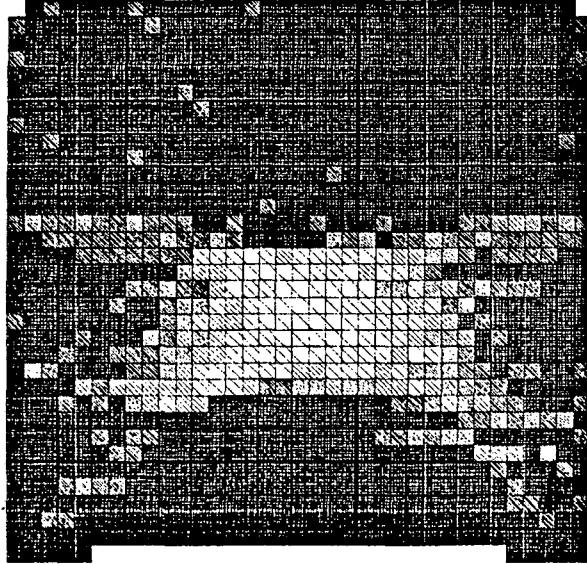


ART2



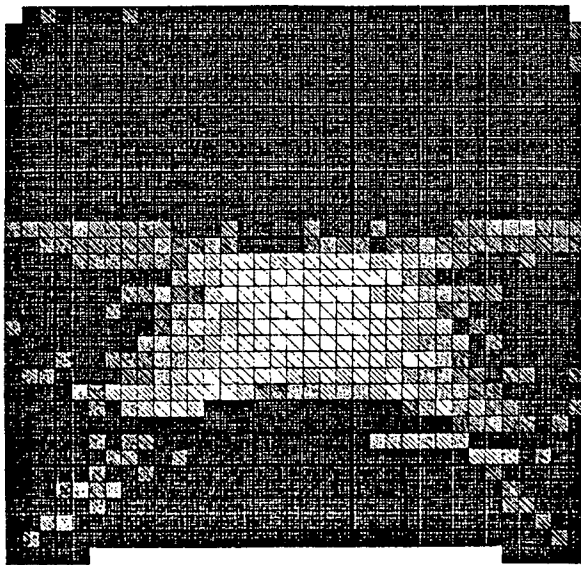
WART

**Figure 3.2.** The best reconstructions of the velocity model for each algorithm. Refer to Chapter 2 for a discussion of the algorithms. The inversion was performed using straight rays and a damping parameter that gave the minimum distance  $\delta$  to model A at about iteration 14. The algorithms tend to produce similar results.

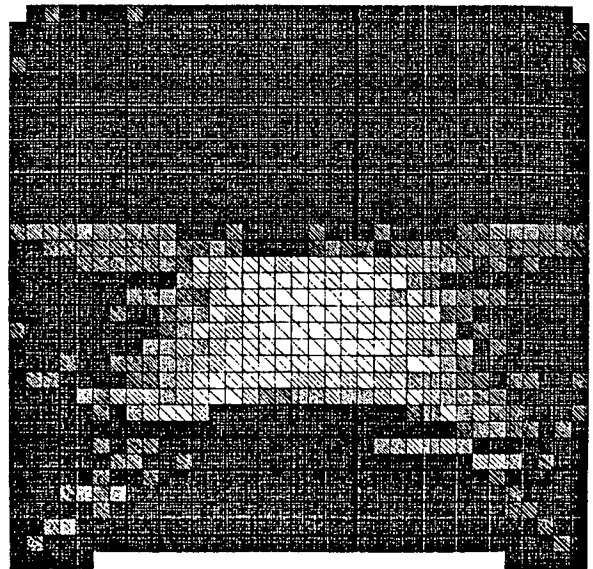


MART

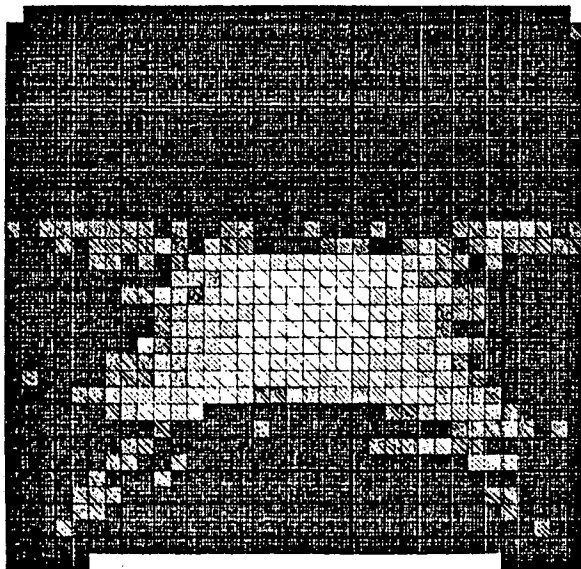
Figure 3.2 (continued).



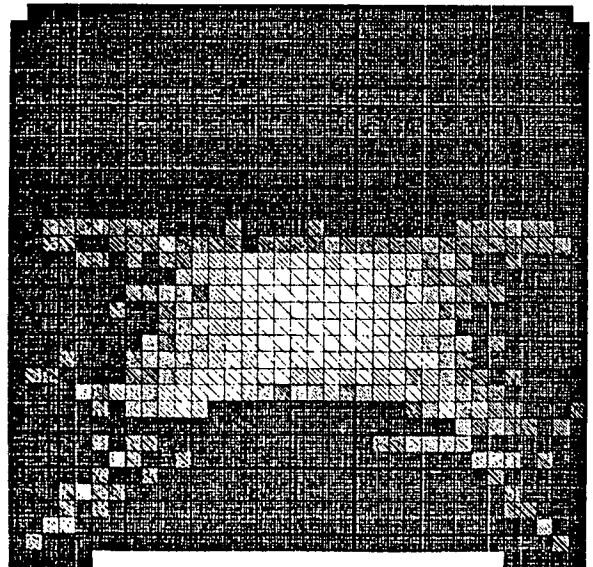
ARTA



ART1A

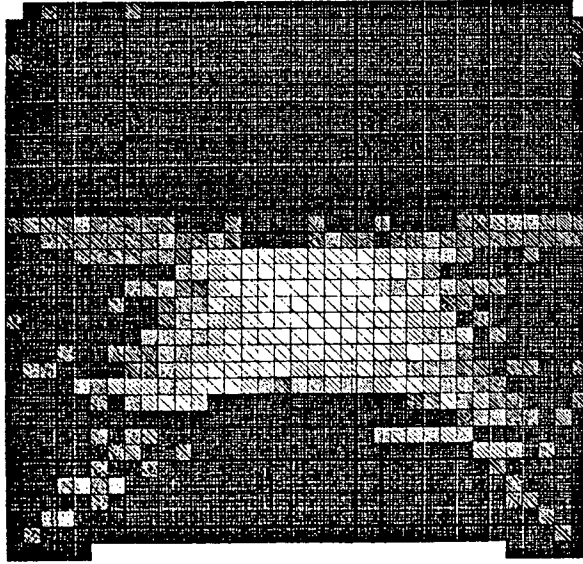


ART2A

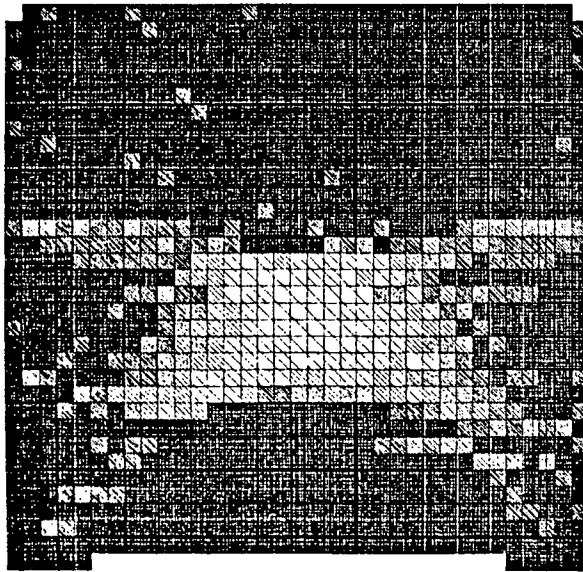


WARTA

Figure 3.3. Same as Figure 3.2, but for the “-A” algorithms. Smoother reconstructions result from these algorithms.

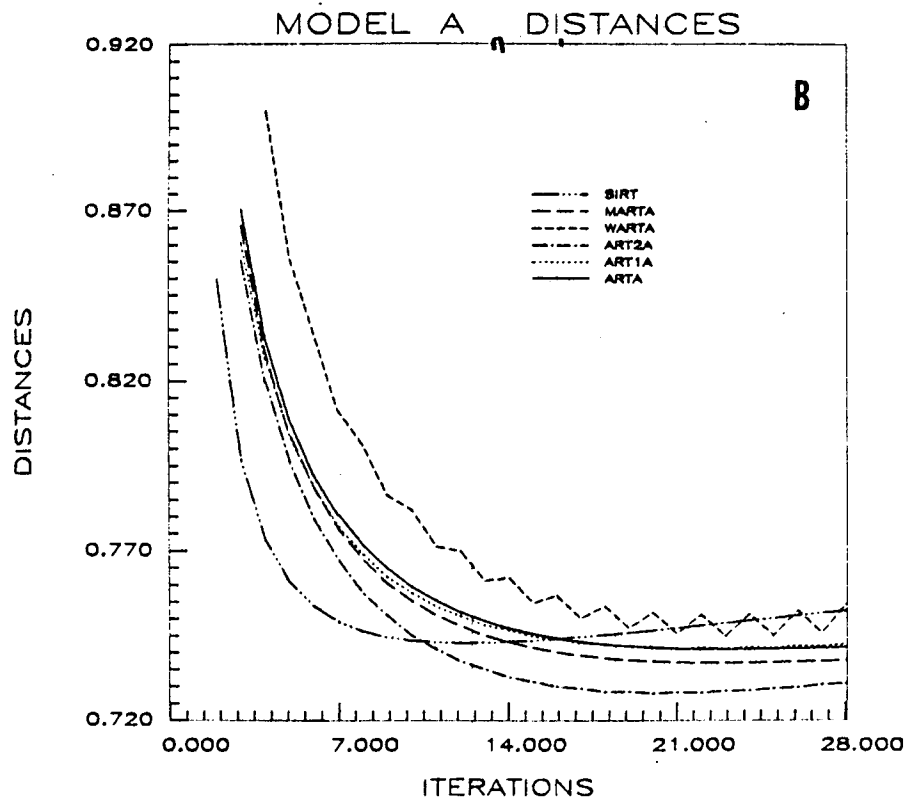
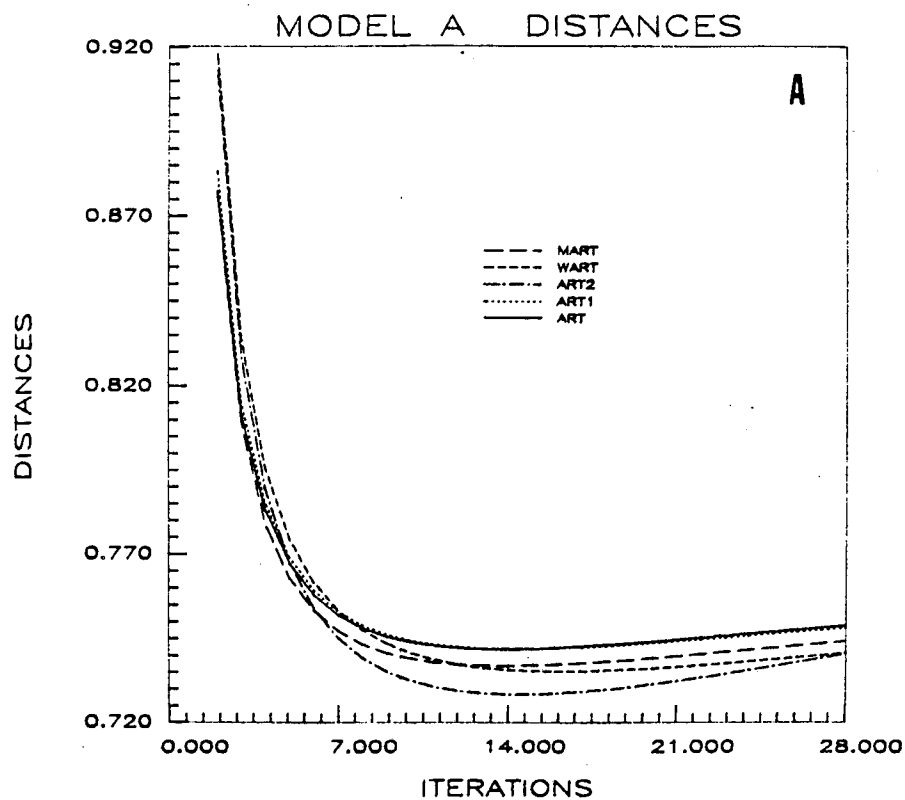


MART



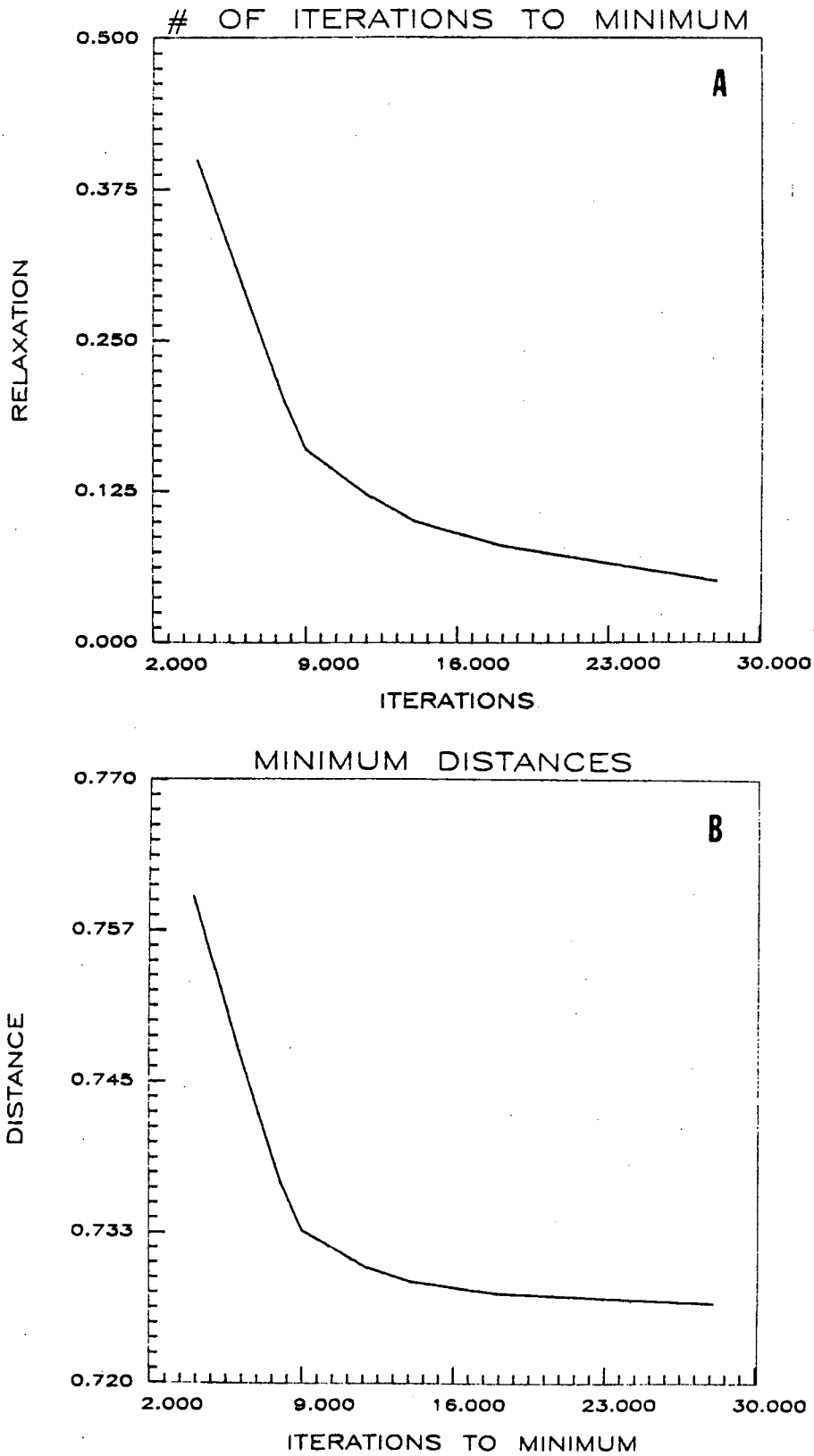
SIRT

Figure 3.3 (continued).



**Figure 3.4.** The distance  $\delta$  to model A calculated by equation 2.25 for A) Figure 3.2 and B) Figure 3.3. Note the initial sharp decline to a minimum, then a slow increase. The algorithms with the smallest minimum value are ART2 and ART2A. The minimum values are given in Table 3.1.





**Figure 3.5.** The effect of the relaxation parameter on the convergence rate for ART2. A) The number of iterations required to reach the minimum distance for various damping values. As damping increases the number of iterations decreases. B) The distance to the original model at the optimal iteration. As the number of iterations to minimum increases, the minimum distance decreases.

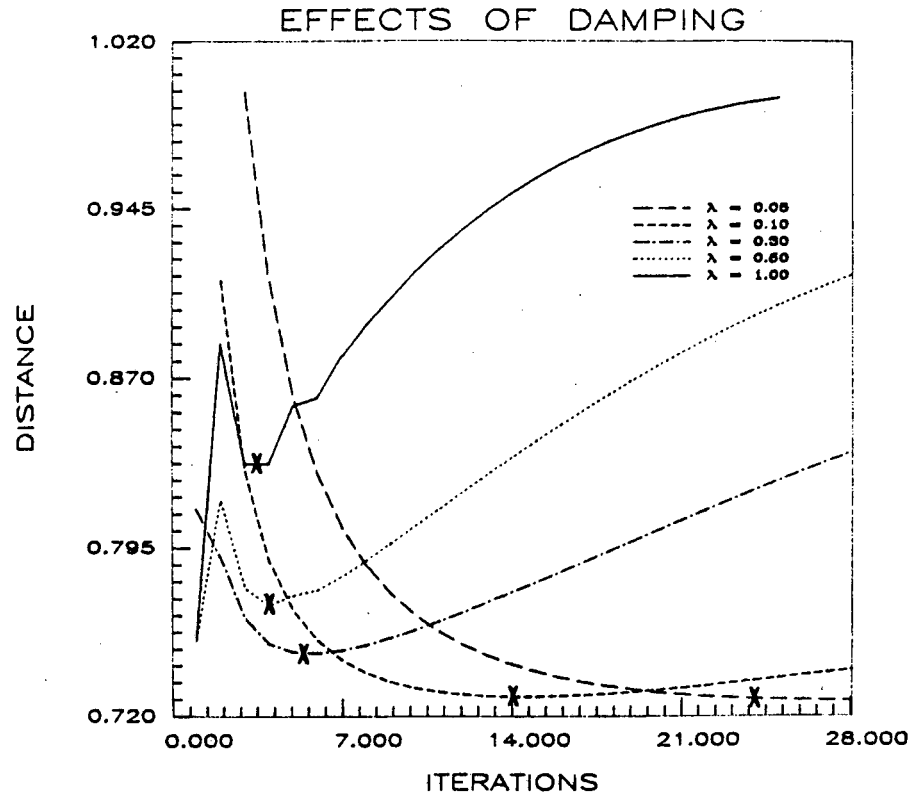


**Figure 3.6.** Effect of damping on convergence rate for ART2. This shows the actual convergence curves for various relaxation parameters,  $\lambda$ ; the greater  $\lambda$ , the smaller the damping. The "X's" refer to the minimum  $\delta$ ; the closest point to model A.

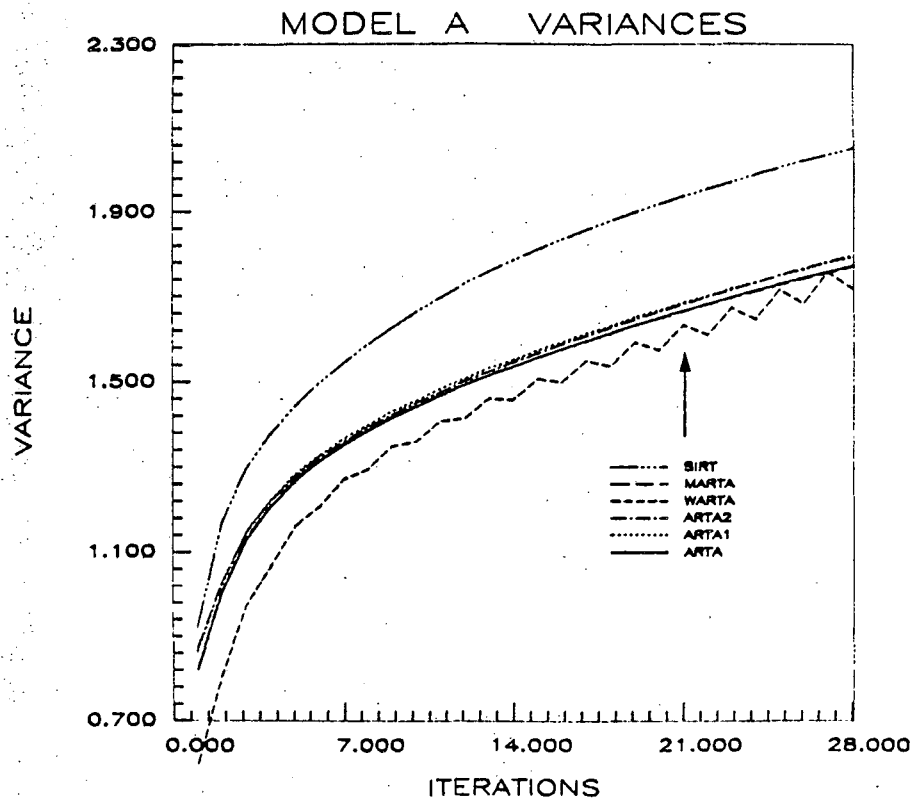
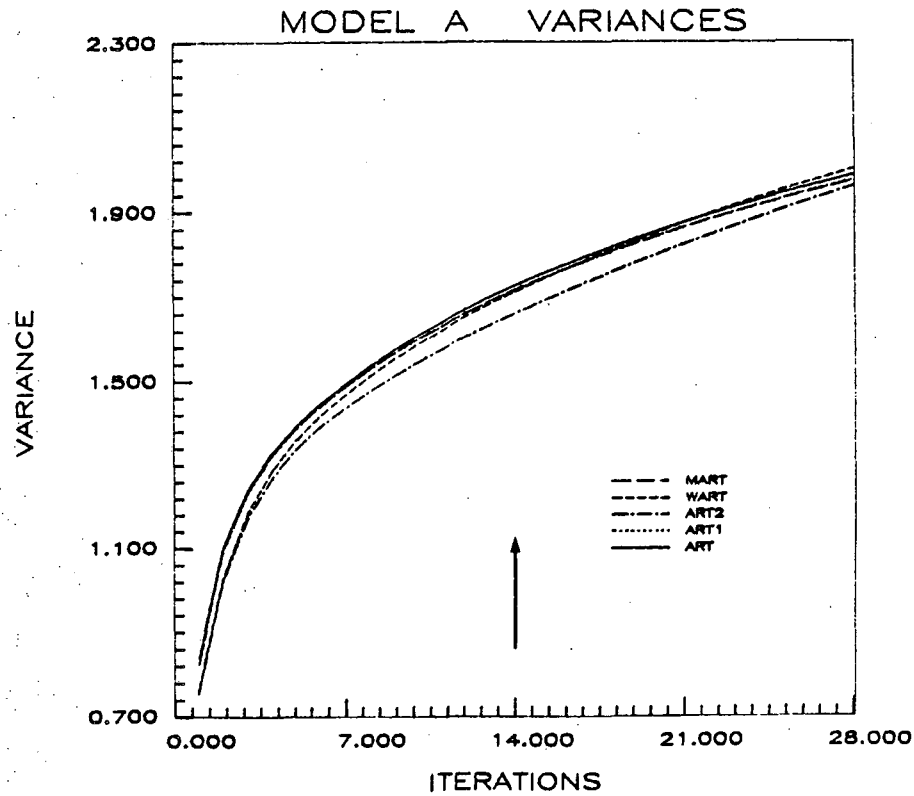


**Figure 3.7.** Variances from equation 2.23 plotted with iterations for each of the algorithms in Figure 3.2 and Figure 3.3. Note the sharp rise in values giving way to gentle slope after a few iterations. This behavior can be used to determine the optimal iteration to stop the algorithm in the absence of  $\delta$ . The arrows refer to the point where the minimum  $\delta$  value occurs.

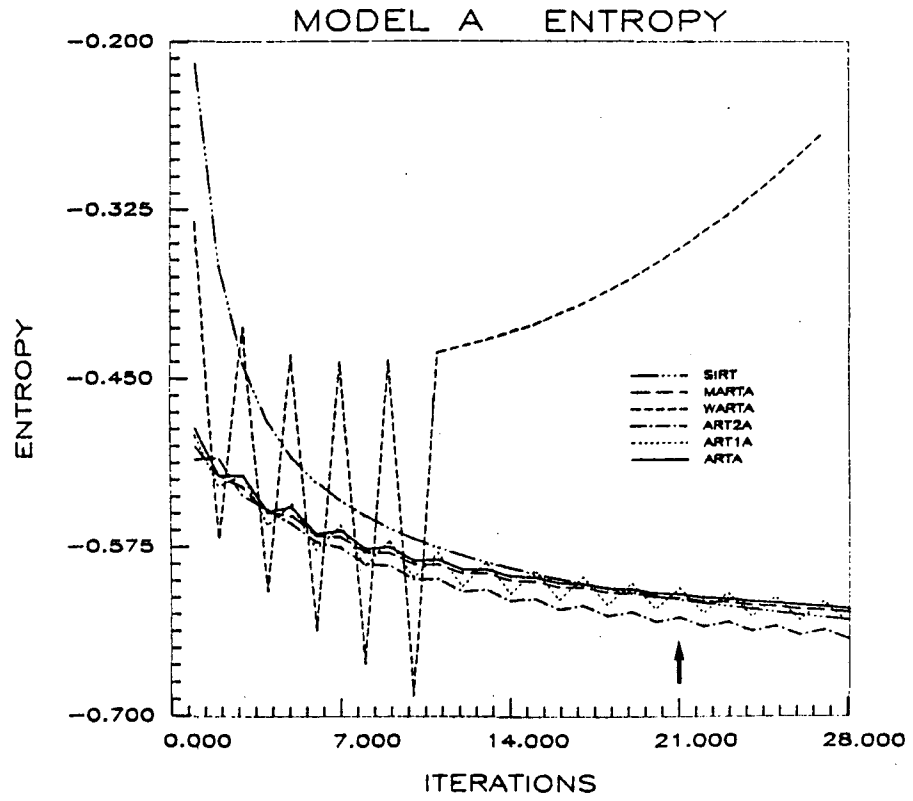
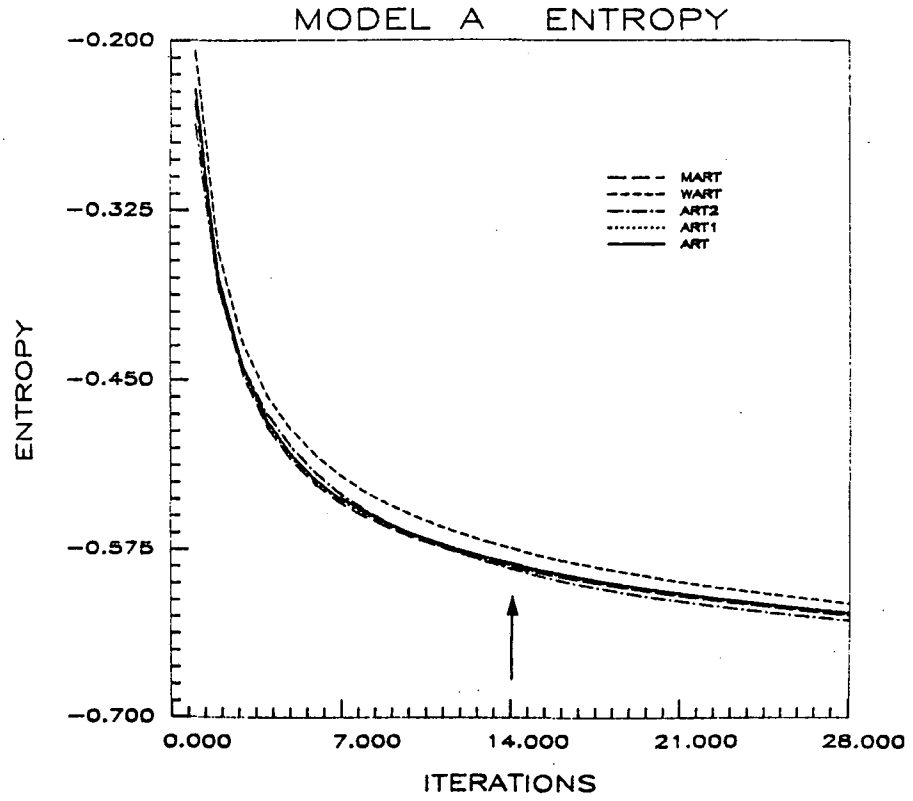


Figure 3.8. Entropy from equation 2.24. See Figure 3.7

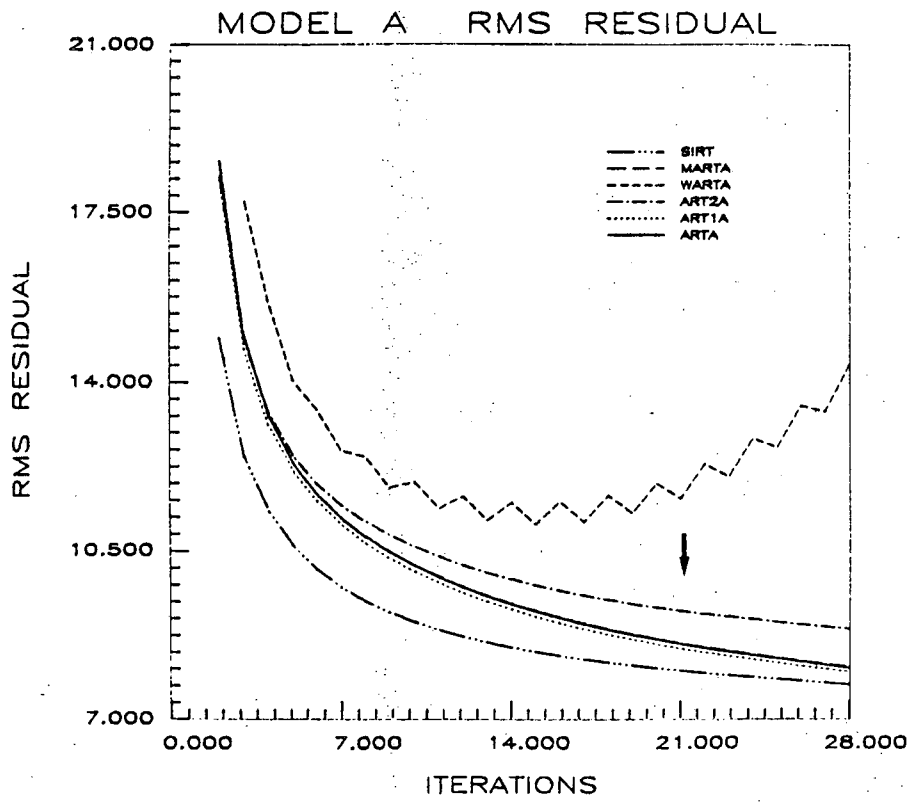
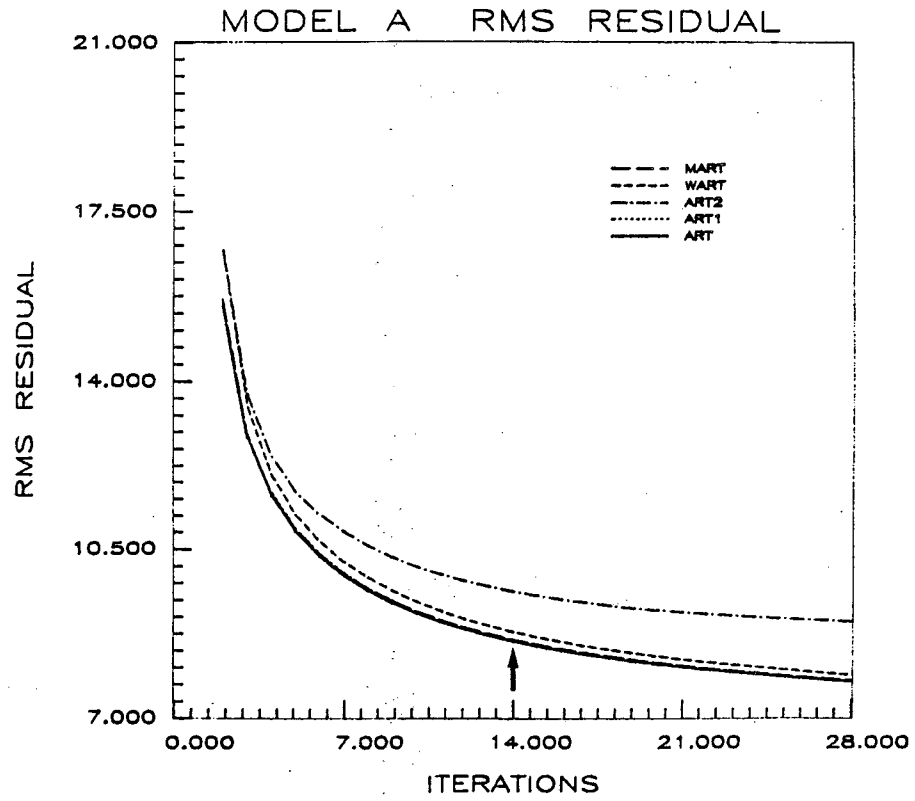
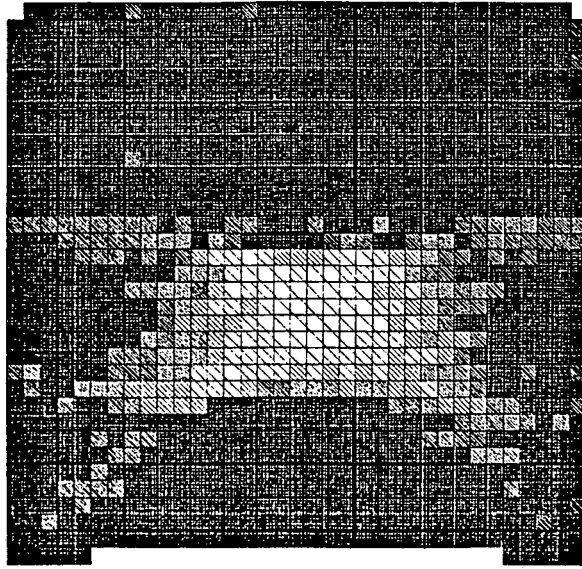
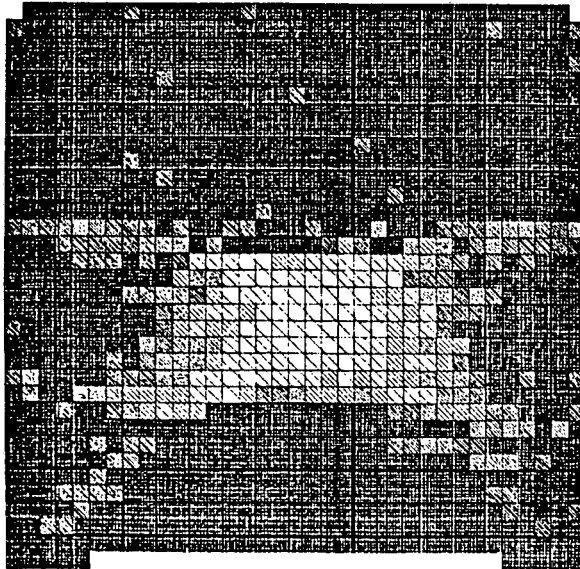


Figure 3.9. RMS residuals from equation 2.22. See Figure 3.7

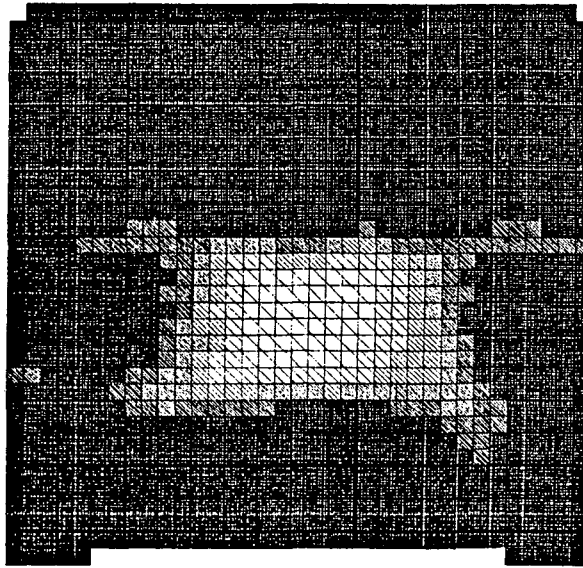


12 ITERATIONS

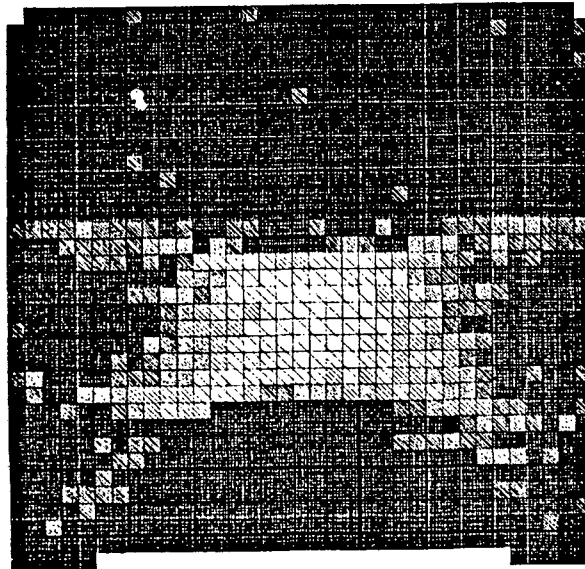


16 ITERATIONS

**Figure 3.10.** Reconstructions at different iterations of ART2 for model A showing that it is not critical to obtain the exact optimal iteration. The minimum  $\delta$  occurred at iteration 14.



SMOOTHED



UNSMOOTHED

**Figure 3.11.** The smoothing function of equation (2.18) is applied after every iteration in ART2 resulting in this reconstruction. This is compared to the unsmoothed result from Figure 3.2.

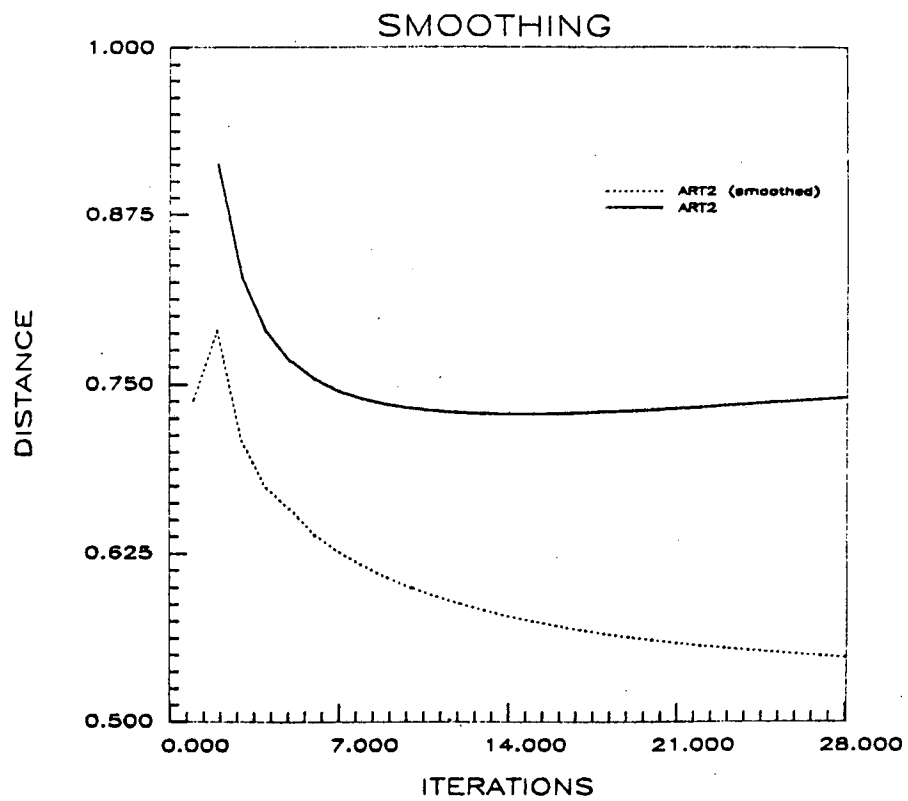
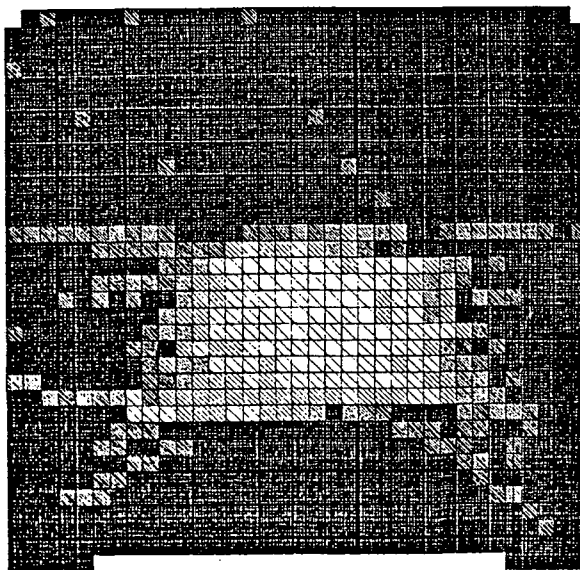
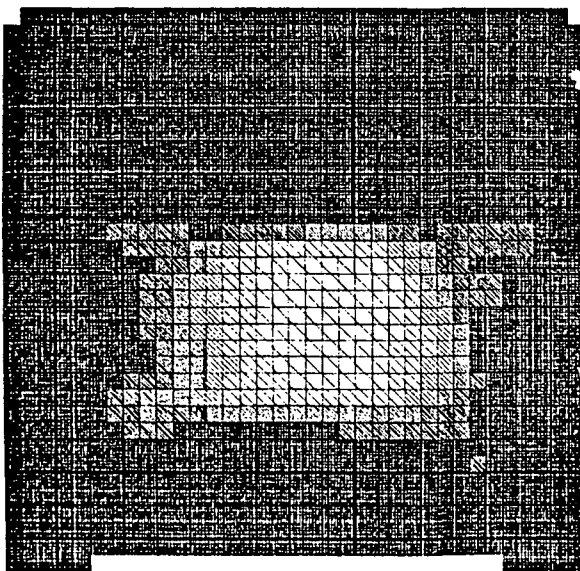


**Figure 3.12.** Smoothing also reduces  $\delta$ , as shown here. Note that the values for smoothed ART2 never begin to increase in the latter iterations.



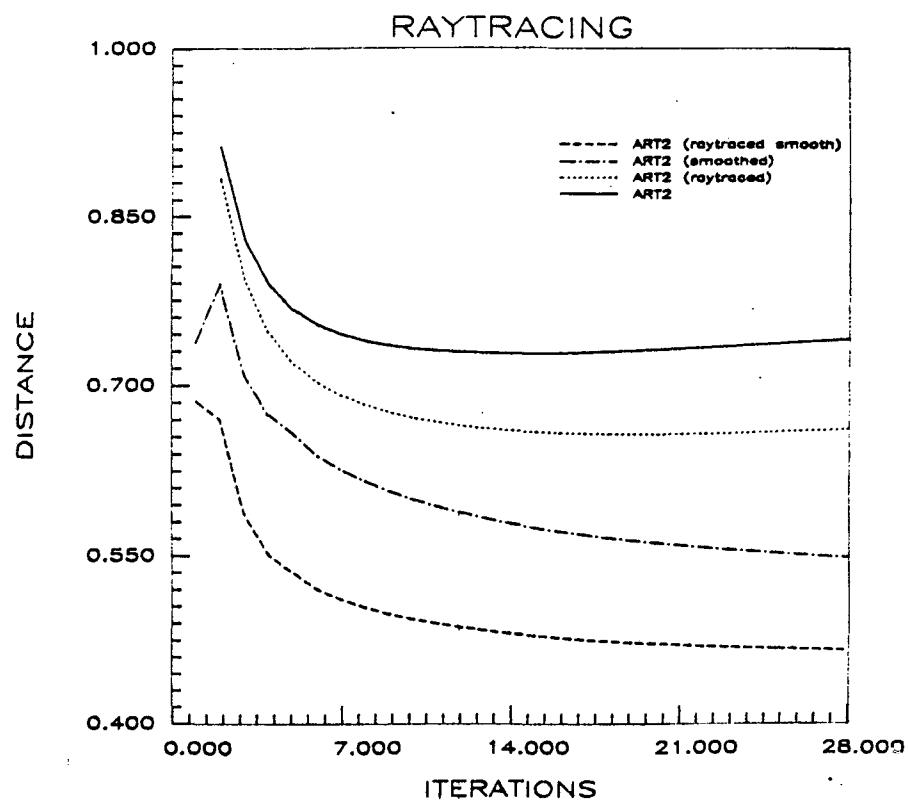


RAYTRACED

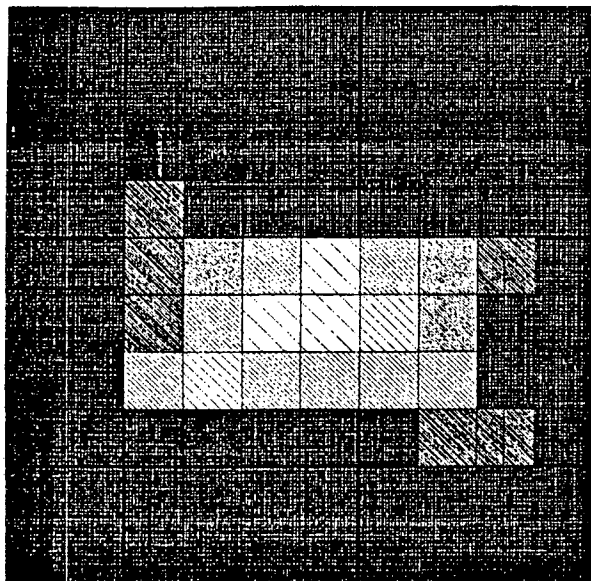
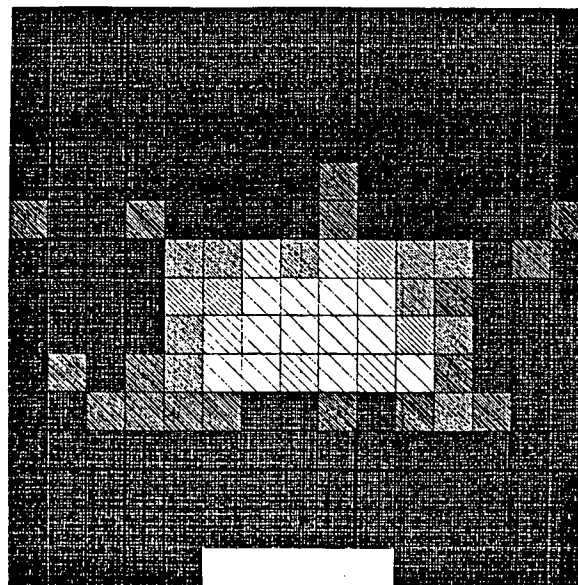
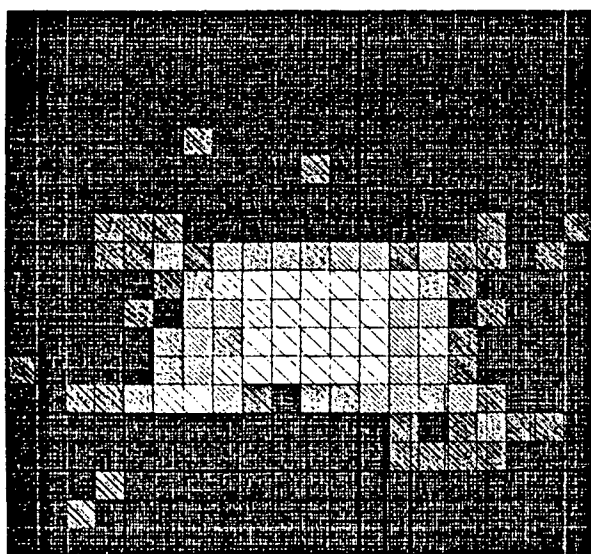
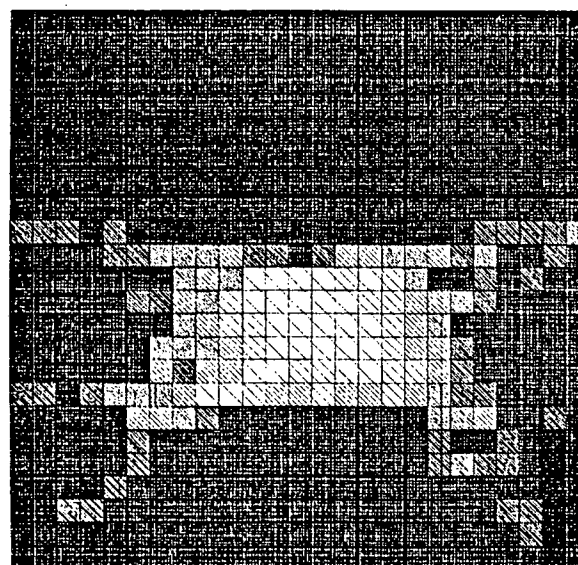


RAYTRACED - SMOOTHED

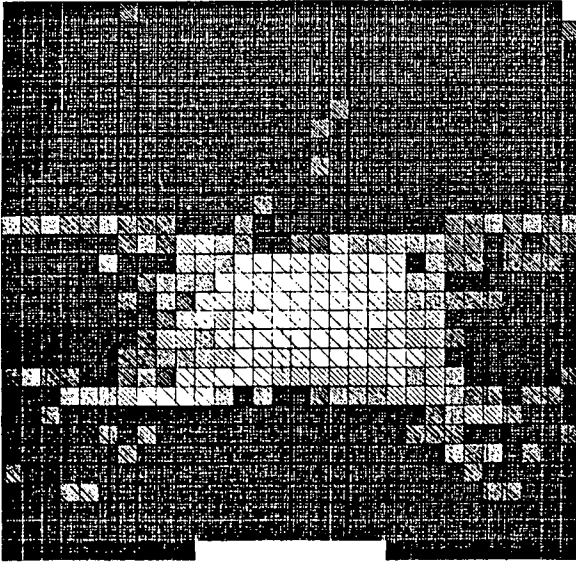
**Figure 3.13.** Instead of using straight rays in the ART2 inversion, the paths may be traced through the velocity model. This is shown to have little effect on the reconstruction of model A. The results are visually impressive when combined with the smoothing function.



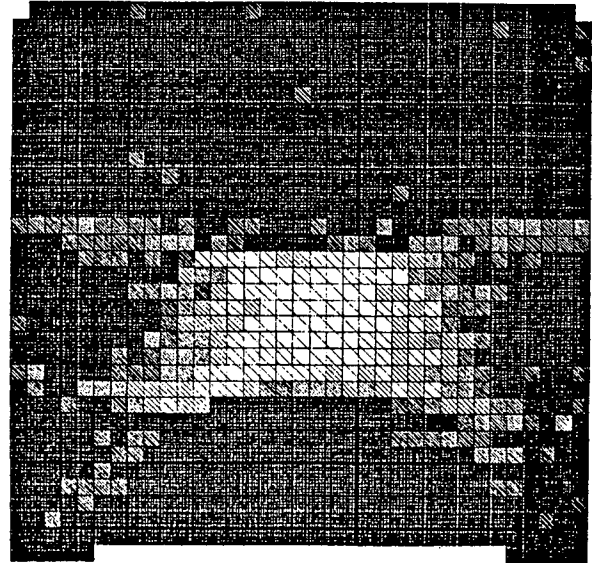
**Figure 3.14.** The high quality results from Figure 3.13 are reflected in the distance  $\delta$  shown here.

**10 x 10****15 x 15****20 x 20****25 x 25**

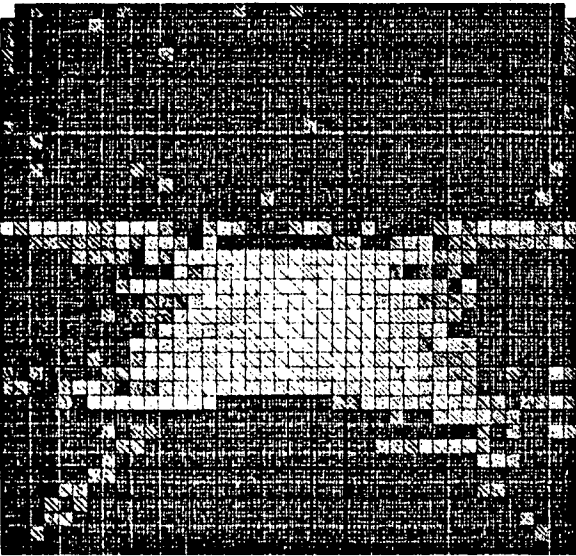
**Figure 3.15.** A sequence of array sizes are used in the ART2 inversion with straight rays. Good reconstructions are obtained throughout the series, though some deterioration occurs after the 45x45 array.



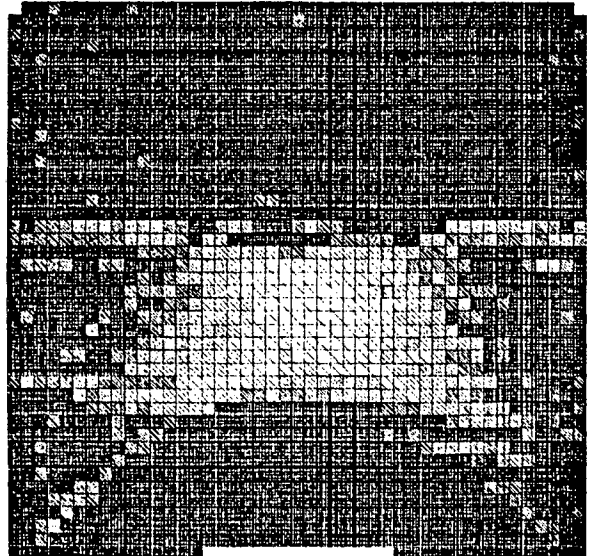
30 x 30



35 x 35

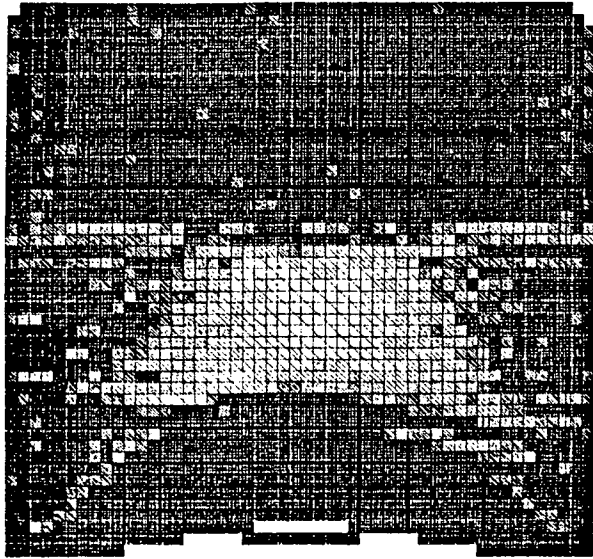


40 x 40

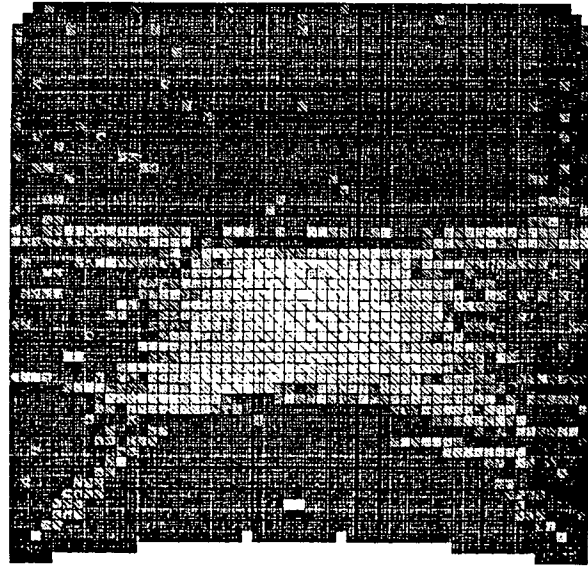


45 x 45

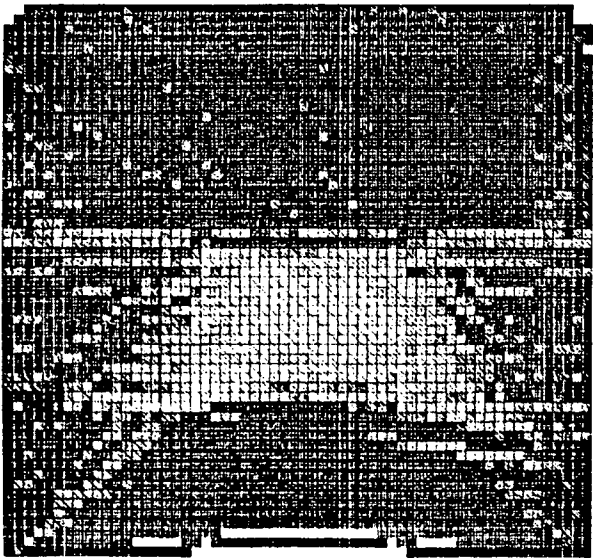
Figure 3.15 (continued).



50 x 50

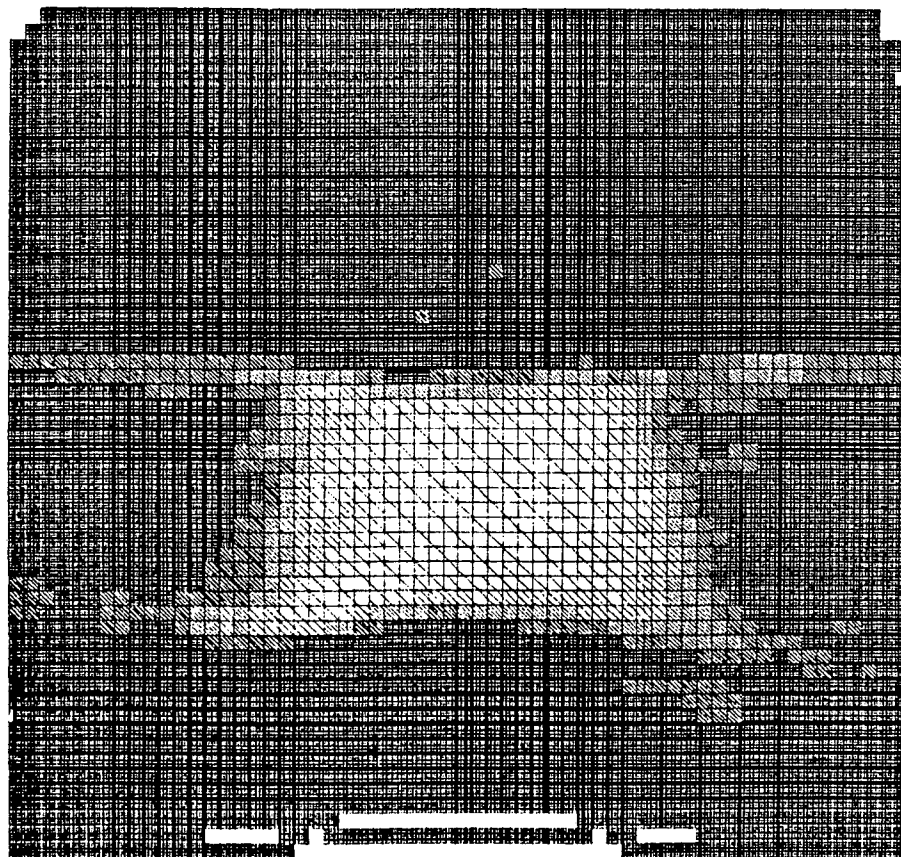


55 x 55



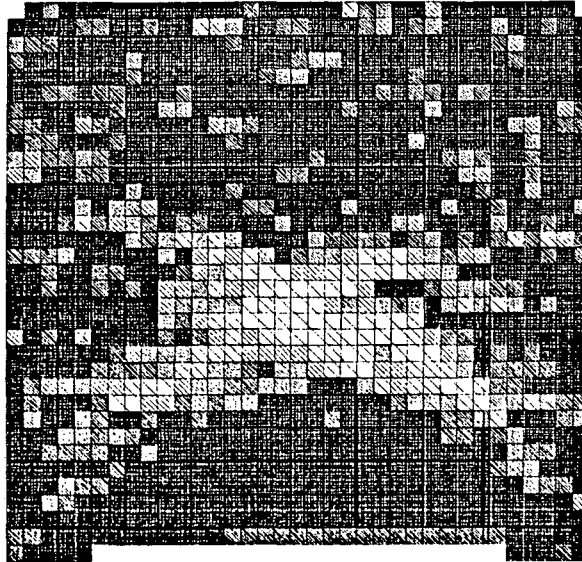
60 x 60

Figure 3.15 (continued).

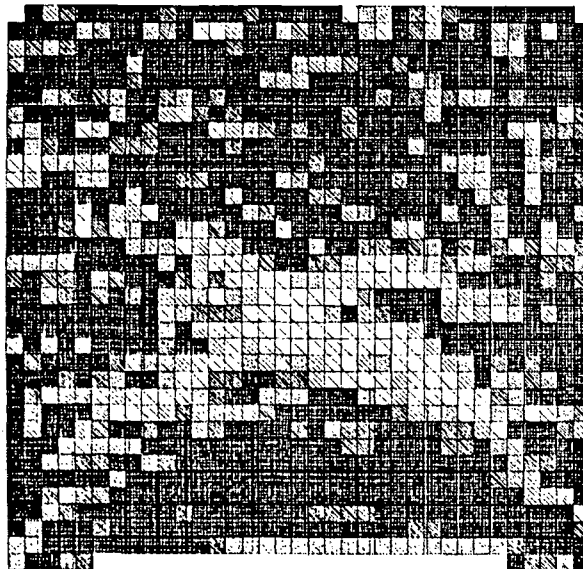


60 x 60 SMOOTHED

**Figure 3.16.** The smoothed version of ART2 performed with a 60x60 array showing that the pixel size can be reduced through the use of the smoothing function.

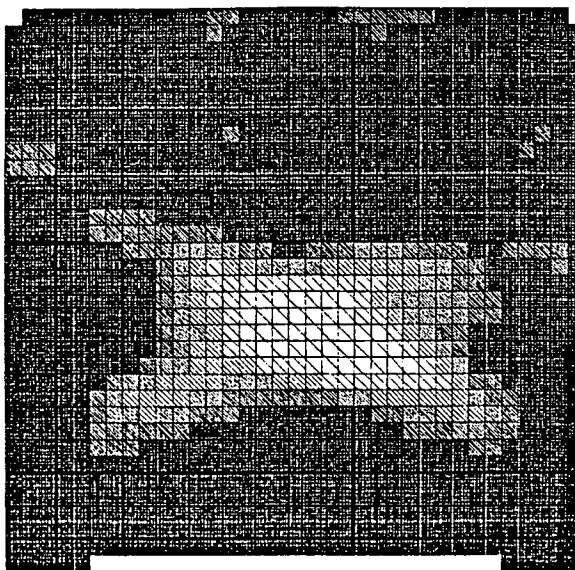


5% NOISE

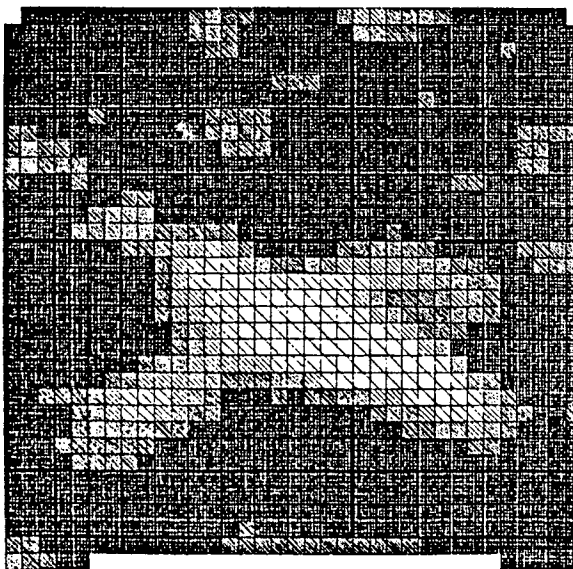


10% NOISE

**Figure 3.17.** The results of adding 5% and 10% noise to the travel times and inverting with ART2. Virtually no velocity structure can be recovered from these reconstructions.



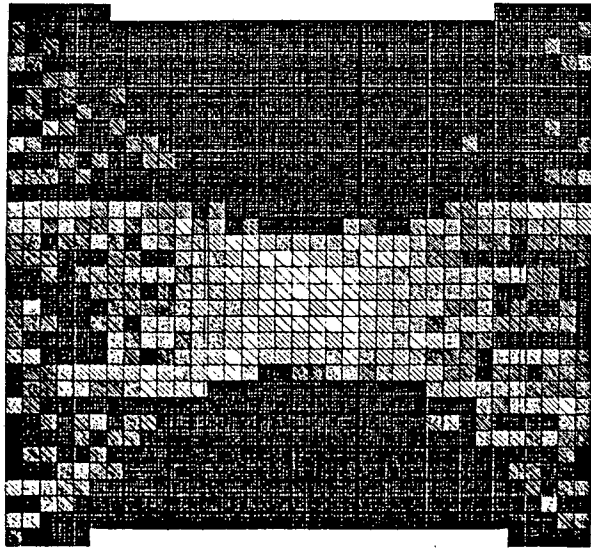
5% NOISE SMOOTHED



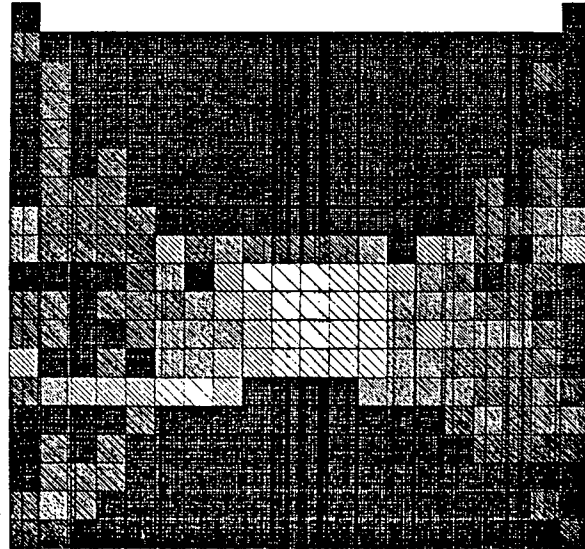
10% NOISE SMOOTHED

**Figure 3.18.** Application of the smoothing function provides visual improvement to the results, but the smearing persists.

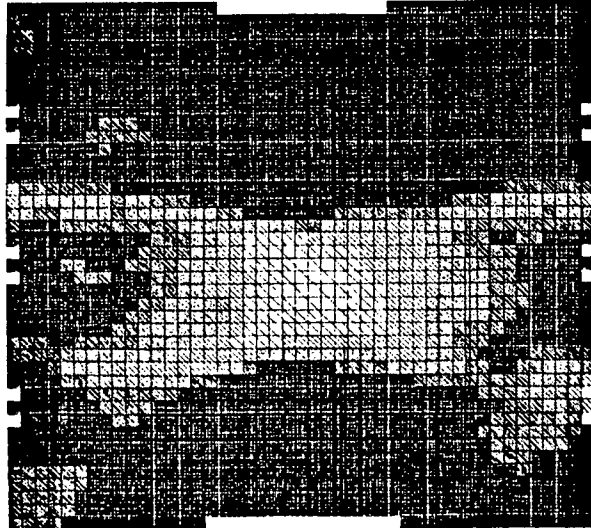




35 x 35

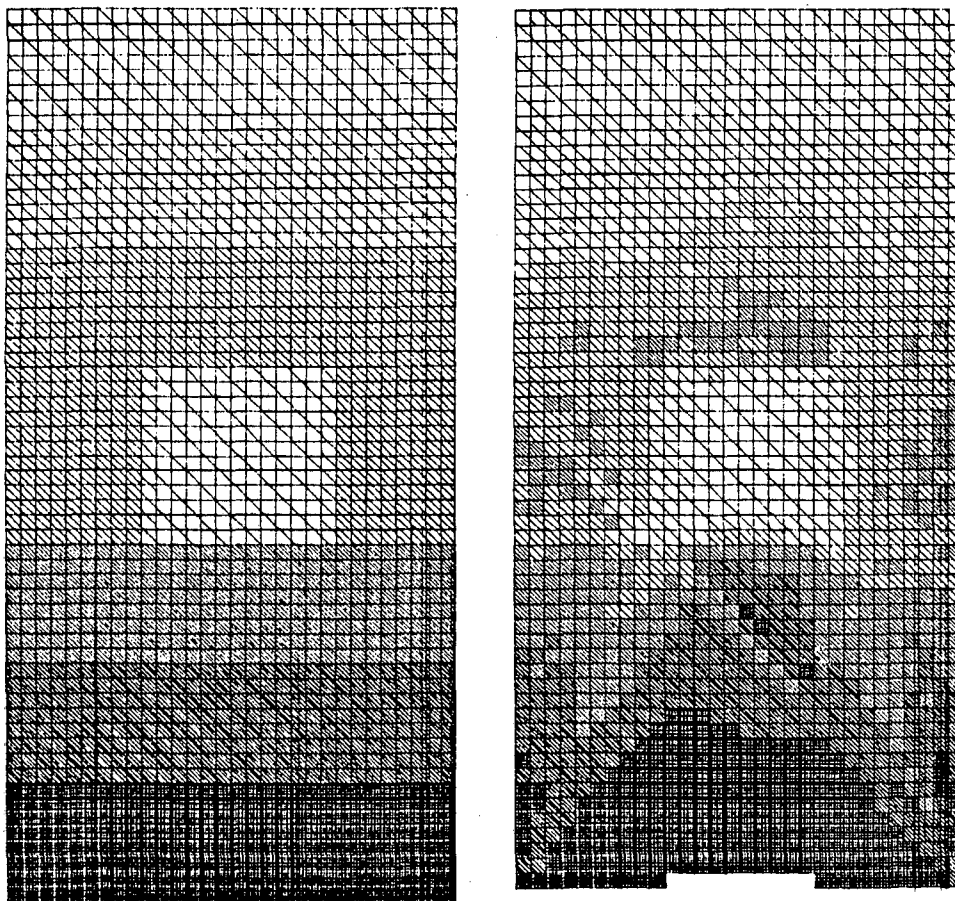


20 x 20



45 x 45 SMOOTHED

**Figure 3.19.** Model A is reconstructed by ART2 without the use of the surface array which decreases the horizontal resolution. This results in a strong smearing effect and velocity oscillations between the low velocity zone and the boreholes. Smoothing eliminates the oscillations, but the smearing persists.



## VELOCITY MODEL B

**Figure 3.20.** Velocity model B is reconstructed using ART2 with straight rays on a 30x60 array. The model is slightly more complex than model A, but is well reconstructed.

## CHAPTER 4

### The Application of ART to a Complex Velocity Model

#### Introduction

The general behavior of the ART algorithms and the effect of various parameters and modifications were described in the preceding chapter. The study used a simple velocity model so that the effects of individual factors could be easily seen. This proved effective for the goals of that chapter, but it was concluded that a complex model should be used for a realistic study. Therefore, a complex velocity distribution is developed in this chapter to study the behavior of ART under more realistic conditions than those used in Chapter 3.

Velocity model 4A simulates a flat-layered structure between two wells, as might be found in an oilfield. Stations are located 10 units apart down the 1000-unit wells which are 100 units apart, giving 10,000 ray paths. In this geometry no surface array is necessary and the ray lengths will vary from 100 units to about 1000 units. The velocity profile consists of 14 layers with velocity values ranging from 1.35 km/s to 2.44 km/s. Table 4.1 gives the layer velocities and depths. Raytracing through this model would result in some critically refracted first arrivals, but the synthetic travel time data will only consist of direct arrival times; refracted arrivals and head waves are ignored. Due to the high velocity contrasts between layers and resulting shadow zones some source-receiver paths cannot be traced successfully for travel times, so the number of rays will be less than 10,000.

The purpose of this velocity model is to investigate the possibility that small low-velocity zones corresponding to steam floods in oil-producing layers can be identified and monitoring in secondary oil recovery operations. Steam injected into an oil sand will lower the velocity of seismic waves in the rock and a cross-well survey can be performed before injection and at various times afterward. If the resolution is sufficient the advance of steam fronts may be monitored.

The results of Chapter 3 showed smoothing functions to be beneficial in eliminating velocity oscillations and, for the simple model used, that raytracing provided little improvement to the solution. The complexity of model 4A will allow further study of differences in the algorithms, of smoothing effects on resolvability of small features, and of raytracing in a more heterogeneous velocity field. Pixel size, survey geometry and noise are also studied. Small, high-contrast, low-velocity zones in some layers of model 4A, simulating the steam floods, are inverted to study the possibility of observing such zones in real situations.

## Results

The algorithms studied in this chapter are:

ART - Algorithm 1, equation (2.11)

ART1 - Algorithm 2, equation (2.12)

ART2 - Algorithm 2a, equation (2.13)

WART - weighting scheme, equation (2.21), applied to ART

WART1 - weighting scheme, equation (2.21), applied to ART1

SIRT - Algorithm 4a, equation (2.17)

For each of these algorithms the image is corrected after each ray was analyzed. The starting model, calculated by a simple back-projection (equation 2.6), is the same throughout the chapter. Also, a 10x100 pixel grid and straight ray paths are used

except where specified. The reconstructions are represented by constant velocity pixels according to the shading scheme in Figure 4.1.

#### A. Algorithm performance

The reconstructions of model 4A (Figure 4.2) show greater difference among the algorithms than was observed in the previous chapter (compare to Figures 3.2). Several characteristics of ART reconstructions described in the previous chapter are seen in these results. The general attributes of model 4A are recovered, but the reconstructions show extensive smearing and peppering. SIRT and ART tend to reduce the peppering, but increase smearing.

Greater distinction between algorithms is also observed in the distance,  $\delta$  (Figure 4.3). The curves show the characteristic behavior described in Chapter 3; an initial decline followed by a leveling and slight increase. Note that SIRT gives the highest values while ART2 again produces small distances to the original model. This consistency of ART2 is important for use in general applications. For this reason and to be consistent with Chapter 3, ART2 will be used for the inversions performed in the remainder of this chapter.

#### B. Smoothing

Chapter 3 showed that the application of the smoothing function (equation 2.18) enhances picture aesthetics, virtually eliminating velocity oscillations. Velocity model 4A enables the effect of smoothing on the resolvability of small velocity features to be studied. The reconstruction produced by the smoothing function and ART2 (Figure 4.4) shows the oscillations are eliminated and the  $\delta$  values are reduced (Figure 4.5). Smoothing does have some effect on the resolvability of the layers. Instead of the sharp bounds seen in the unsmoothed result, there exists an intermediate pixel layer at

the interface with an averaged velocity value of the two layers. Note, however, that this intermediate layer occurs even at some interfaces of the unsmoothed reconstruction.

### C. *Curved raypaths*

To incorporate curved ray paths into the algorithms, the exact ray paths used in the generation of the travel time data from model 4A are used to calculate the pixel sublengths  $\Delta a_{ki}$ . These sublengths are then used in the ART2 inversion. Since the same ray paths are used for the forward and inverse problems, the effect of raytracing on the reconstructions should be eliminated. Figure 4.6 shows the raytraced inversion produces little improvement over the unraytraced result. The small improvements consist of a slightly smoother reconstruction and a tendency toward more constant layer velocity values. These improvements are slight and generally would not warrant the use of the raytracing algorithm. The reason for such a small impact by raytracing on the results may be due to the geometry of the experiment. Most of the rays are horizontal (Figure 4.7), with short paths that do not deviate much from the straight line. The longer rays have almost vertical incidence, and again do not deviate much from the straight line. Another consequence of the near-horizontal ray paths and high contrast velocity layers is that shadow zones are formed in areas critical to the reconstruction of the original velocity model. This lack of complete ray coverage provides an explanation for the "bleeding" outward of the high velocity layers.

### D. *Pixel size*

An effort should be made to determine a pixel size small enough to recover the velocity features at the optimal resolution of the problem, i.e., without resulting in peppered reconstructions. A series of array configurations from 8x80 to 15x150 are used in the ART2 inversions to determine the optimal pixel size. Smaller arrays

average out the thin layers and a larger 15x150 array produces visual deterioration of the image. Larger arrays exceed the storage capacity of the VAX 11/780.

The general velocity distribution is recovered for all arrays (Figure 4.8). The 8x80 array results in a reconstruction that smooths the velocities, while the 15x150 array shows signs of deterioration, such as velocity oscillations and extensive smearing along the diagonals from the top of one borehole to the bottom of another. The 10x100 and 12x120 array reconstructions are similar and both give acceptable results. The smoothing function (Figure 4.9) increases the quality of the reconstructions for all pixel sizes.

#### *E. Doubling the number of stations*

The most obvious way to improve the reconstructions is to reduce the distance between stations, producing more rays and higher resolution. In the next exercise, the distance between stations is halved to 5 units, effectively doubling the number of receiving stations to 200 down each borehole. This quadruples the number of rays to 40,000. Unfortunately, this large amount of data limits the availability of memory on the VAX 11/780, so that the number of pixels may not be increased for the entire data set.

The expanded number of rays were traced through model 4A. The inversion results in improvement to the reconstructions (Figure 4.10); the velocities are more constant throughout each layer and less oscillations are seen. The number of rays may be increased in a specified region of interest, for example, in a steam flood zone. In such cases the station spacing may be reduced in the neighborhood of interest to improve resolution, while the remaining stations are kept to maintain the angular coverage and to give the general velocities in the surrounding areas. The process fine-tunes the data to the specified region without large increases in data acquisition and processing time. Reconstructions of an example of a specified region of interest in model A are shown in Figure 4.11. Results of inverting a 20x200 pixel array produces a

sharper definition of the central low-velocity zone and a generally smoother image.

#### *F. Noise*

In Chapter 3 a simple velocity distribution was used to show that noise increased smearing and velocity oscillations between pixels in the reconstructions. This suggested that the effect on a more complex model could prove intolerable. Random Gaussian noise was added to the travel time data of model 4A and inverted using ART2. The inversion results in very little change in the reconstructions for 5% or 10% noise (Figure 4.12). This surprising result may be due to the highly overdetermined problem here, as opposed to the underdetermined problem of the last chapter. For the model 4A inversion there are 10,000 knowns and 1000 unknowns which helps with the stability of the solution. These results are very encouraging for reconstructions of real data containing measurement errors.

#### *G. Variations on the model*

Two velocity models based on model 4A were analyzed to study velocity anomalies that can be anticipated in real situations. Model 4B incorporates a low velocity zone (1.50 km/s) into one of the high velocity layers (layer 13, 2.26 km/s) to simulate a steamed zone (Figure 4.13). Model 4C (Figure 4.14) is similar to model 4B, but has a slightly higher velocity zone (1.50 km/s) in a low velocity layer (layer 9, 1.35 km/s), giving a lower velocity contrast than in model 4B. The zone is in the form of a gradient from the center of the layer outward, with the higher velocities toward the center. The inversion of each of these models uses the same parameters and starting model as used for model 4A.

The inversion of model 4B reveals a similar reconstruction as for model 4A with a region of oscillating velocity values (Figure 4.13). A comparison with the model 4A result shows an anomalous low velocity zone exists in model 4B, but the extent of this zone cannot be determined. This is an unsatisfactory result for a monitoring process.



The purpose of a monitoring study is to determine the velocity differences between two successive surveys. Therefore, the reconstructions of model 4A and model 4B are subtracted to produce this difference. The proper form of the low-velocity zone, now in the dark shades, is easily distinguishable from the background. Heavy smearing extends from the edges of the zone, but it is obviously an artifact and can be eliminated visually.

The results of model 4C are similar to those of model 4B (Figure 4.14). Not much difference can be seen between the model 4A and model 4C inversions, mainly because of the low velocity contrast produced by the anomaly in model 4C. When taking the difference between the two, the anomaly shows up quite well. The peppering is primarily due to the low velocity contrast making the difference in shading values small. This can be partially eliminated by inverting with the smoothing function (Figure 4.15), resulting in a clear high velocity zone running vertically through the layer and grading linearly outward toward the boreholes.

### **Discussion and Summary**

The use of a complex velocity distribution results in a greater differences among the reconstructions produced by the different algorithms. The SIRT and ART algorithms produce smooth reconstructions with strong smearing effects. The other algorithms produce reconstruction that are more peppered, but less smeared. ART2 and WART give the lowest  $\delta$  values and good visual results. WART does much better on model 4A than it did on model A because of the flat-layered velocity distribution and the high (10:1) borehole distance to depth ratio. The algorithm gives greater weight to the shorter rays, which are the most important in a flat-layered model with such close boreholes. ART2 is recommended for general applications and initial analysis; it gives consistently good results, and when applied with the smoothing function, gives better results than SIRT and ART and provides an option for smoothing. It is not as

dependent on the geometry as are the weighted algorithms.

The smoothing function has proved a useful modification to the algorithms by eliminating velocity oscillations in the reconstructions due to noise or unstable inversions. Model 4A, with thin layers, provides a means to test the effect of the smoothing function on the resolvability of small velocity features. The results show that these small layers are resolved, but with a lack of sharp boundary definition. However, velocity features encountered in real applications generally will not exhibit such sharp interfaces.

For models tested here, incorporating raytracing into the algorithm offers little improvement to the reconstructions. The reason may be due to the model geometry, velocity distribution, and the exclusion of critical rays due to the existence of shadow zones, so a final evaluation of raytracing cannot be made based on this study. Also, in real applications the first arrivals may include refractions and head wave arrivals, in which case raytracing may prove more valuable.

The geometry of the experiment plays a large role in the resolution and optimal size for the pixels. A suggested pixel size based on this study is one station per pixel down the borehole. The number of pixels per station may change for different geometries, but this is a good rule of thumb. Increasing the number of stations to obtain higher resolution can be done in a specified area where greater detail is needed, e.g., at a steam flood zone.

The use of ART2 for monitoring the advance of a steam front requires that the changes in the velocity distribution of two successive surveys be distinguishable. The inversions of models 4B and 4C show that relative velocity changes can be determined by differencing the successive reconstructions. This suggests an important technique for use with real data and in field studies.

The study of model 4A provided many answers to questions resulting from the analysis of model A. The results offer further encouragement to the application of the technique to real data sets, as will be done in the following chapter.

VELOCITY MODEL 4A		
LAYER	DEPTH (M) to boundary	VELOCITY (KM/S) above boundary
1	250.00	1.45
2	290.00	1.97
3	340.00	1.60
4	360.00	1.91
5	400.00	1.52
6	420.00	1.42
7	450.00	1.74
8	500.00	1.42
9	570.00	1.35
10	650.00	1.74
11	670.00	2.26
12	700.00	1.69
13	760.00	2.26
14	800.00	1.69
15	1000.00	2.24

**Table 4.1.** Velocity model 4A used throughout this chapter.

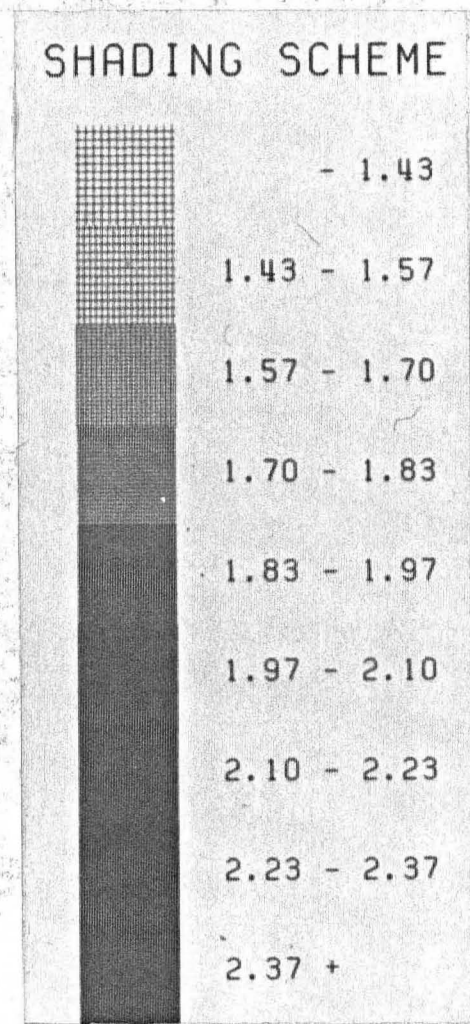


**Figure 4.1.** The shading scheme used in subsequent plots; velocities are in units of kilometers per second.

XBB 850-8279

## MODEL 4A



## ART



## ART1



## ART2



## WART



## WART1



## SIRT



**Figure 4.2.** The best reconstructions of the original velocity model 4A for each algorithm. Straight rays and a pixel array of 10 x 100 are used in the inversions. The boreholes are 100 units apart and 1000 units deep with station spacings of 10 units in each borehole. The general attributes of the model are recovered. Note that SIRT and ART tend to reduce the peppering, but increase smearing.

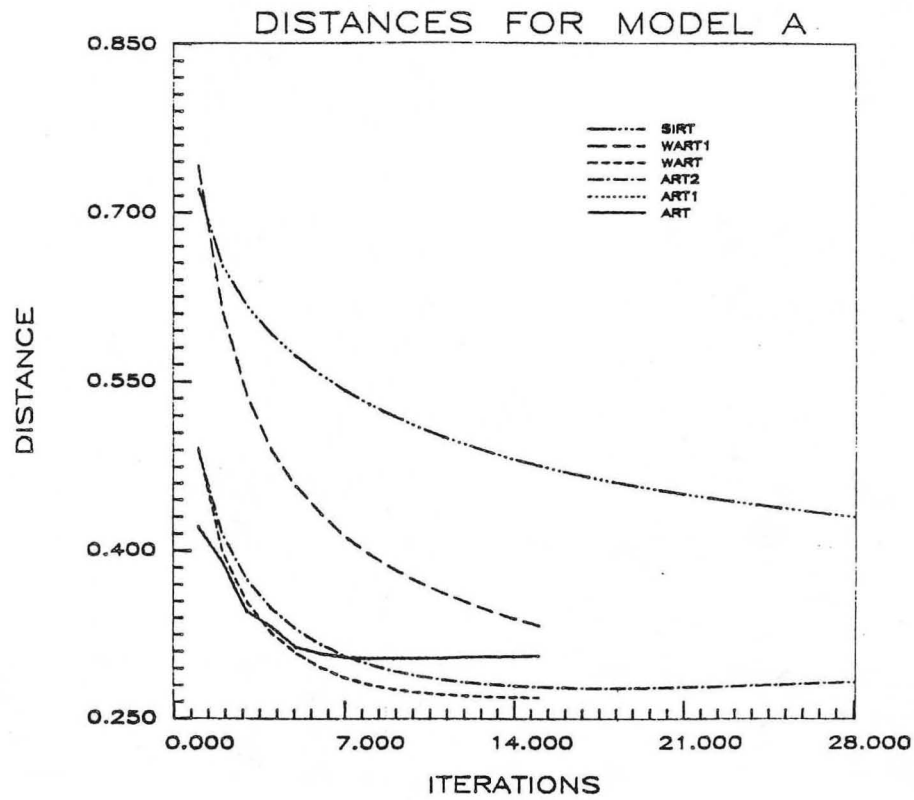


**Figure 4.3.** Distance,  $\delta$  (equation 2.25) to velocity model 4A. Some inversions were only taken to 15 iterations and the shorter curves result. WART and ART2 produce images closest to the original model.

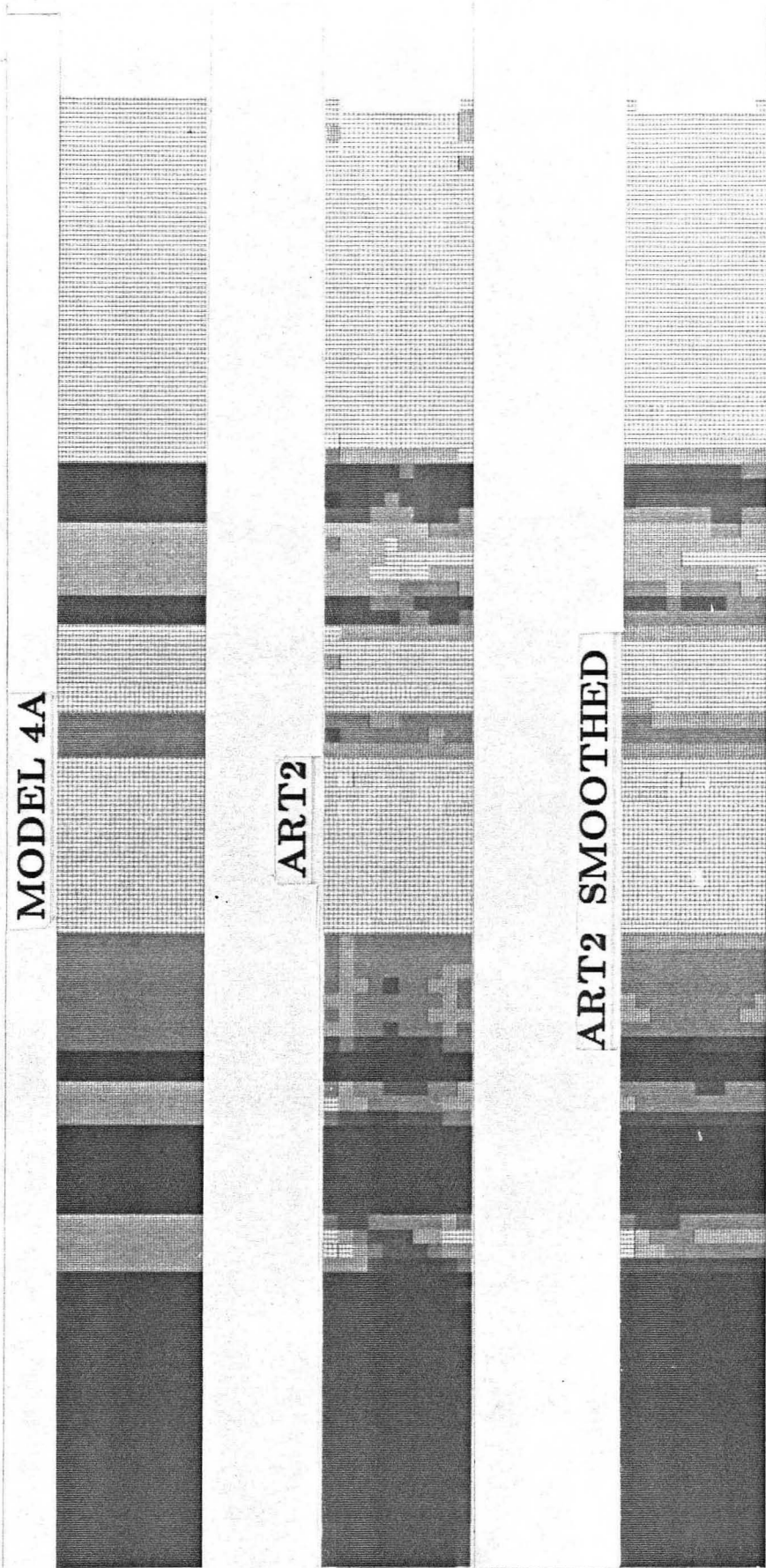
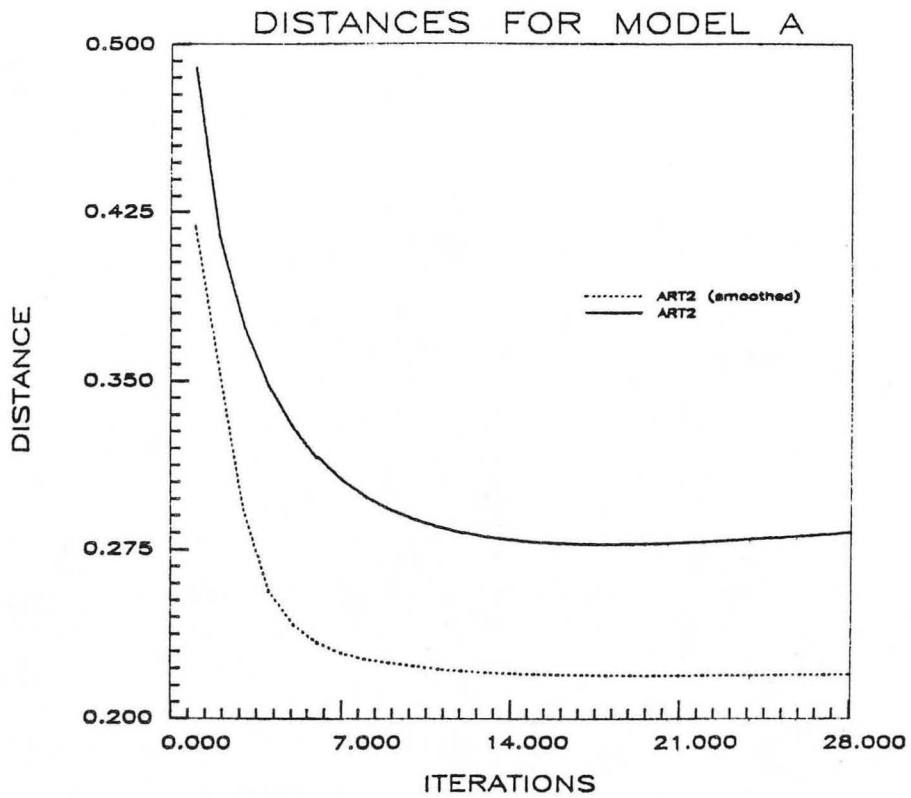


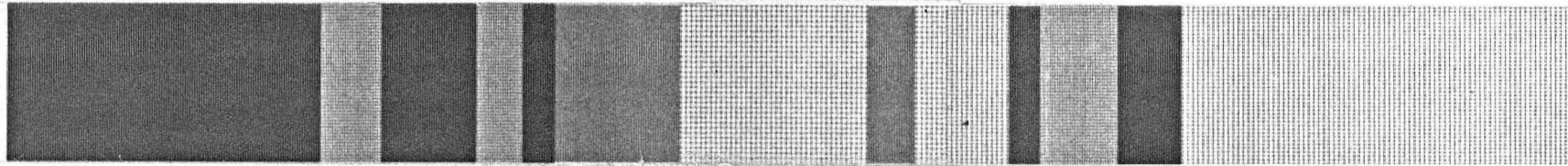
Figure 4.4. Smoothed inversion of velocity model 4A using ART2. For some layers the smoothing results in less distinct some boundary layers.





**Figure 4.5.** Smoothing also reduces the distance to the original model. Note that the initial drop in value is sharper for smoothed ART2 and the  $\delta$  curve levels without increasing at the later iterations as the ART2 curve does.

MODEL 4A



ART2



ART2 RAYTRACED



**Figure 4.6.** The ART2 results compared to the raytraced inversion. Using curved rays through the model produces a slightly smoother reconstruction and a tendency toward more constant velocity layers.

XBB 850-8290

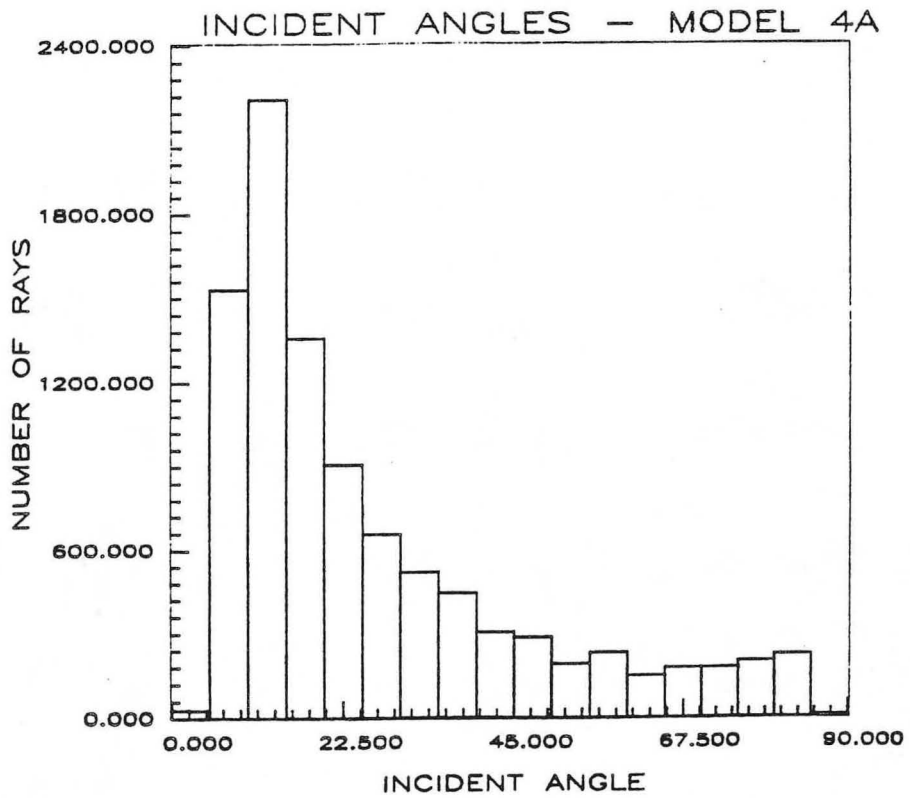


**Figure 4.7.** A histogram showing that a majority of the ray paths have nearly horizontal ( $< 25^\circ$ ) incident angles. This results in many refracted ray paths. The incident angles are absolute values and taken from the horizontal.

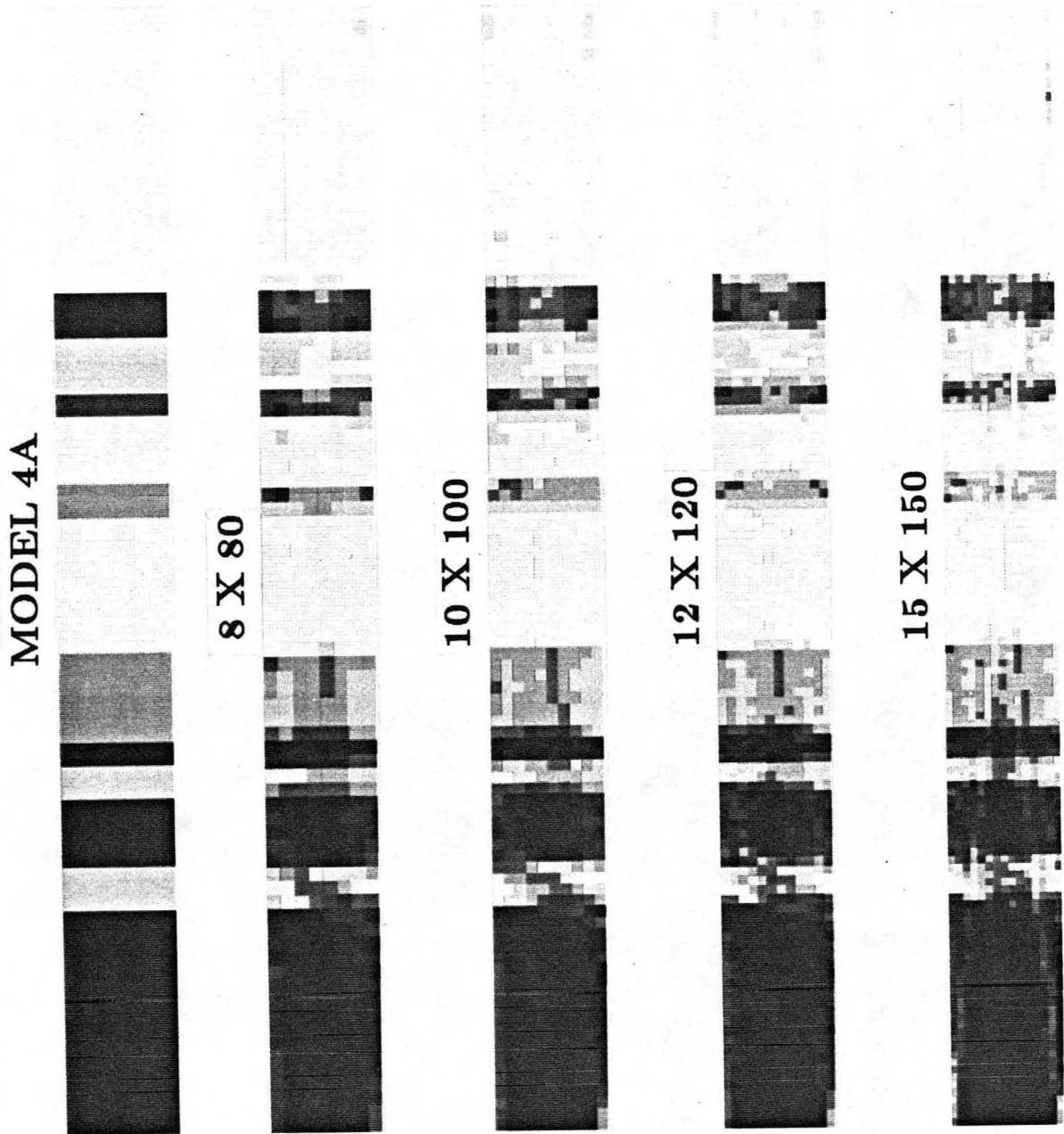


**Figure 4.8.** A sequence of pixel array sizes are used in the inversion to determine the optimal pixel size. These figures show that the 8X80 array produce pixel sizes that are too large to resolve the thin layers, while the 15x150 array produces excess smearing.

XBB 850-8286

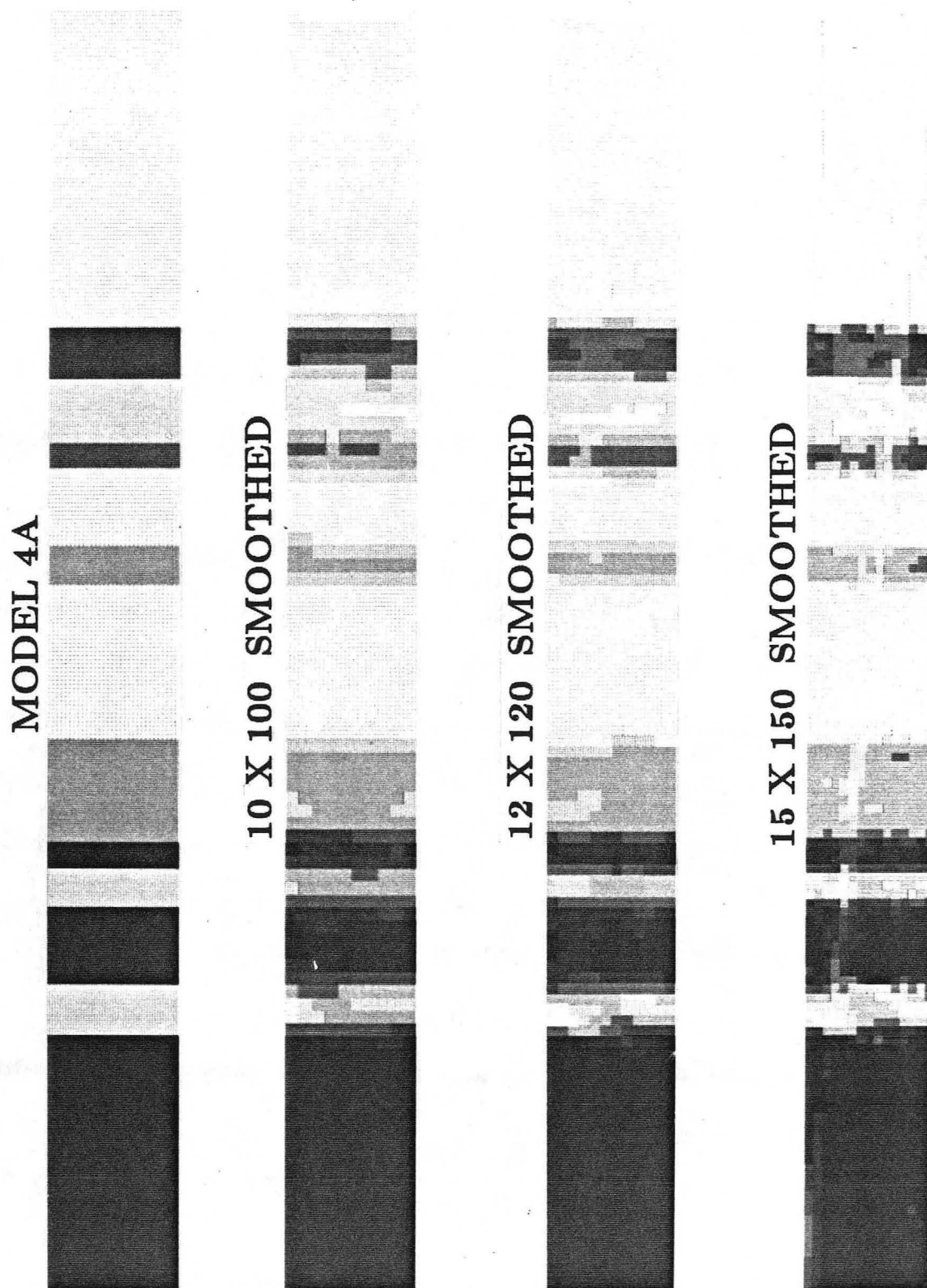


**Figure 4.9.** The applications of the smoothing function helps improve the reconstructions, but smearing remains with the 15x150 array.

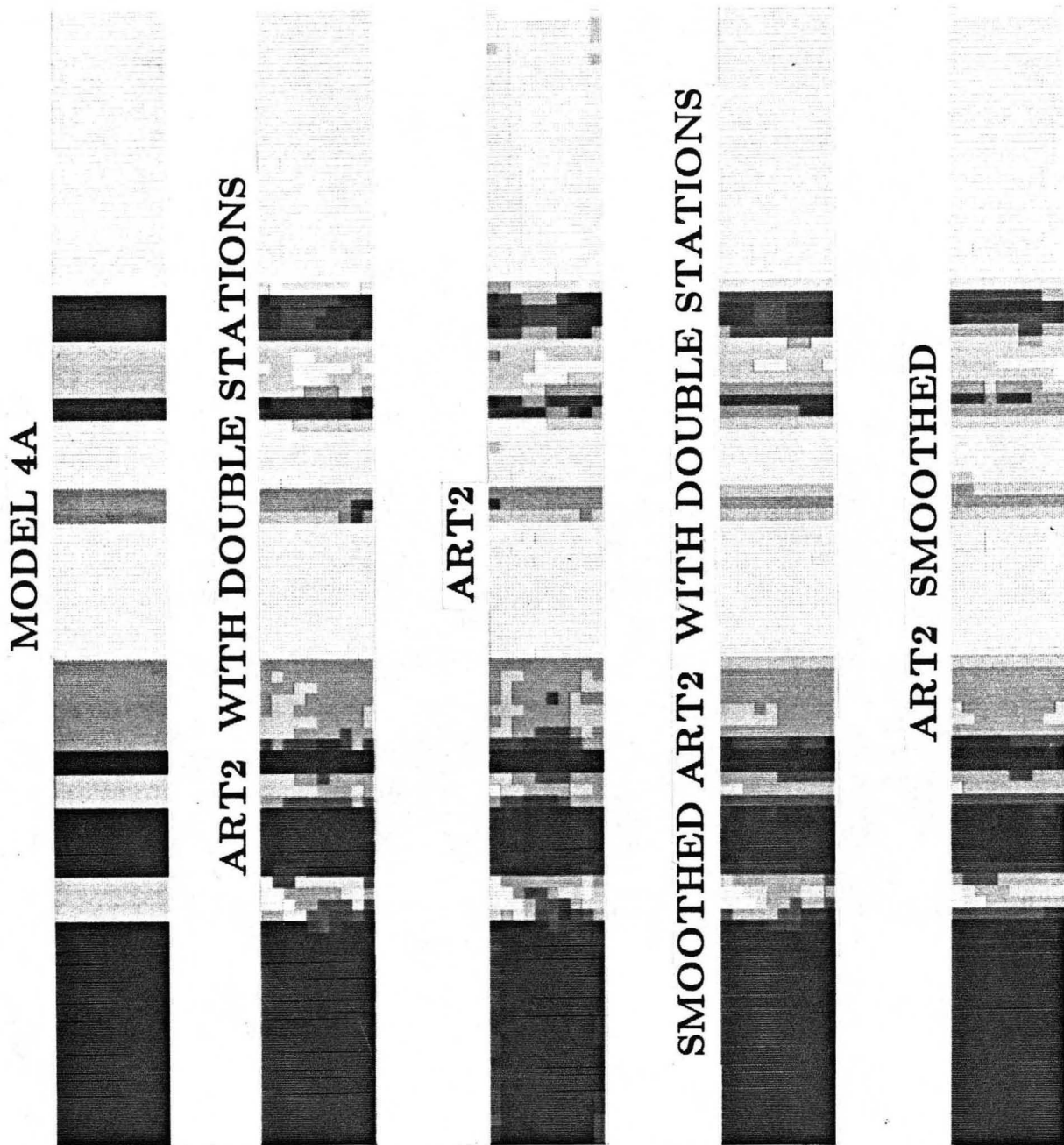


**Figure 4.10.** The number of stations is doubled by decreasing the station spacing from 10 units to 5 units. This quadruples the number of rays with the normal station spacing. The ART2 inversions of model 4A with the different station spacings are compared. The velocities are more constant throughout each layer and less oscillations are seen. XBB 850-8285

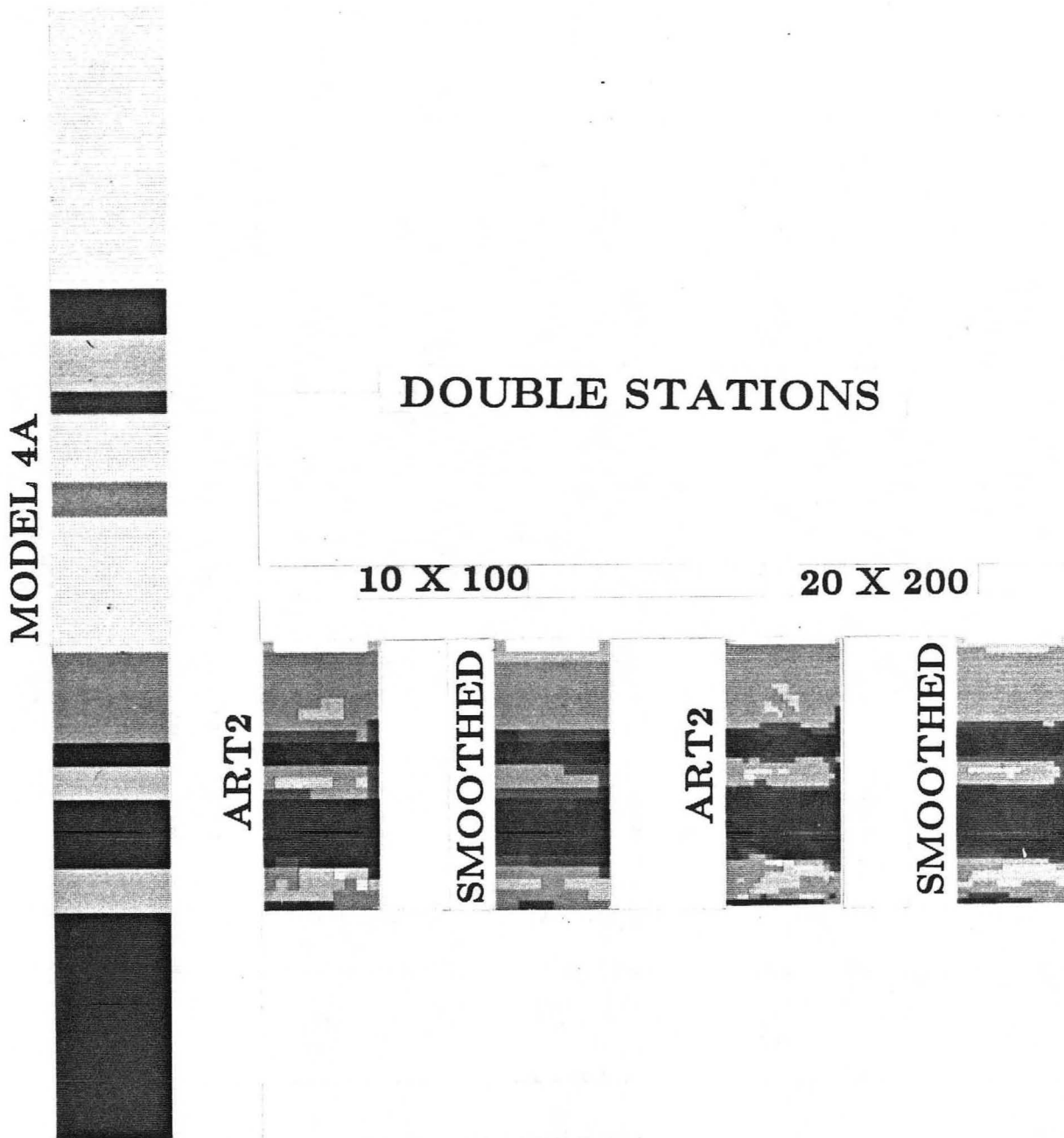


**Figure 4.11.** Focusing on a region of interest. ART2 is used on a region of velocity model 4A. This illustrates the effect of increasing the number of stations in a particular region of interest to save acquisition and computation costs. The 20x200 array reconstructions are smoother and show sharper boundary definition than the 10x100 array results.

XBB 850-8284

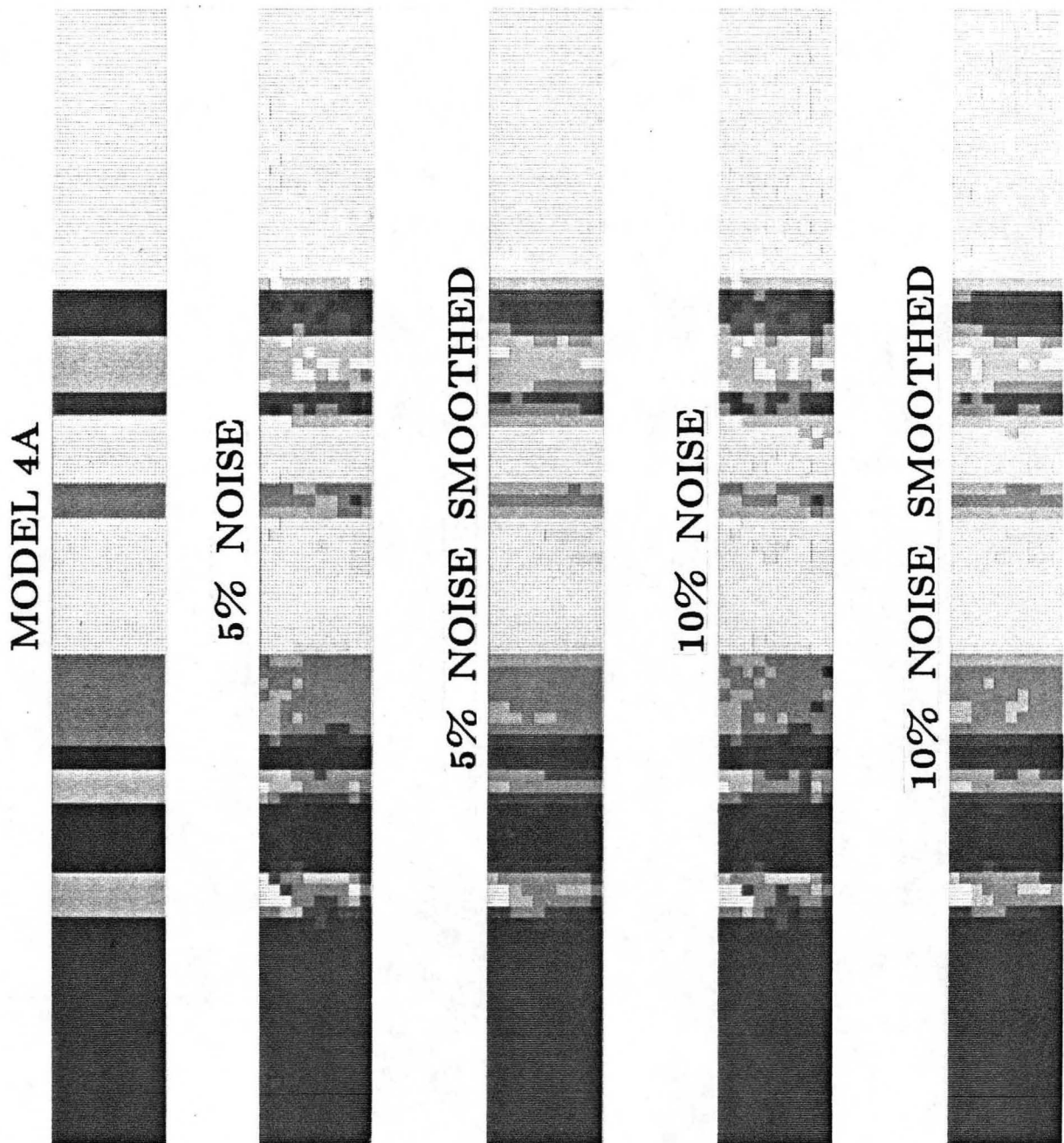


**Figure 4.12.** The effect of noise on the data. 5% and 10% random Gaussian noise is added to the travel time data for model 4A. The noise produces little effect on the reconstructions showing the stability of the inversion, which is an overdetermined problem. XBB 850-8299



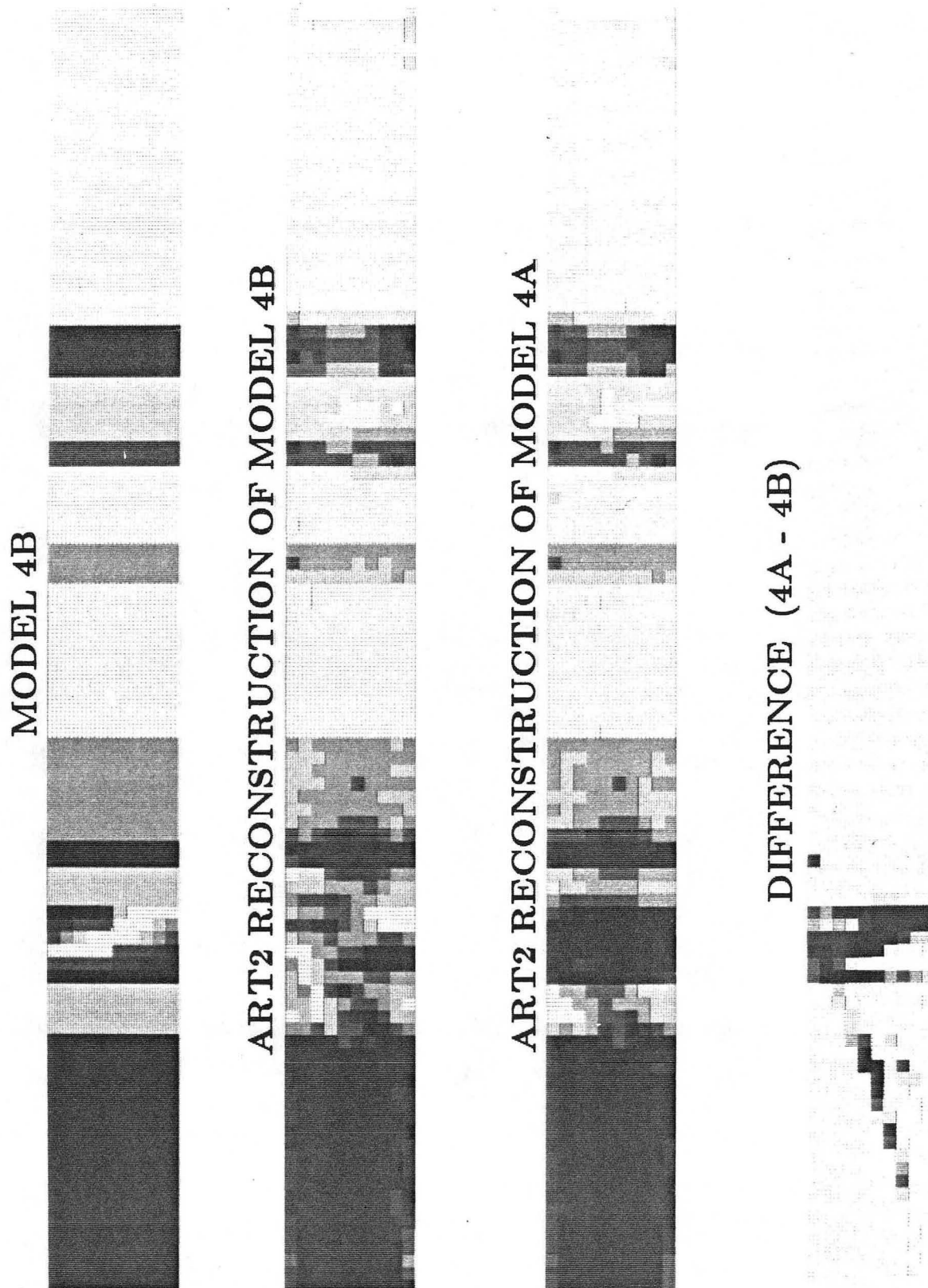


**Figure 4.13.** Reconstruction of velocity model 4B using ART2. The reconstruction is similar to that of model 4A with a zone of anomalous low-velocity values. The bounds on this zone can not be distinguished unless the difference is taken. The darker shades of the difference plot correspond to higher positive values.

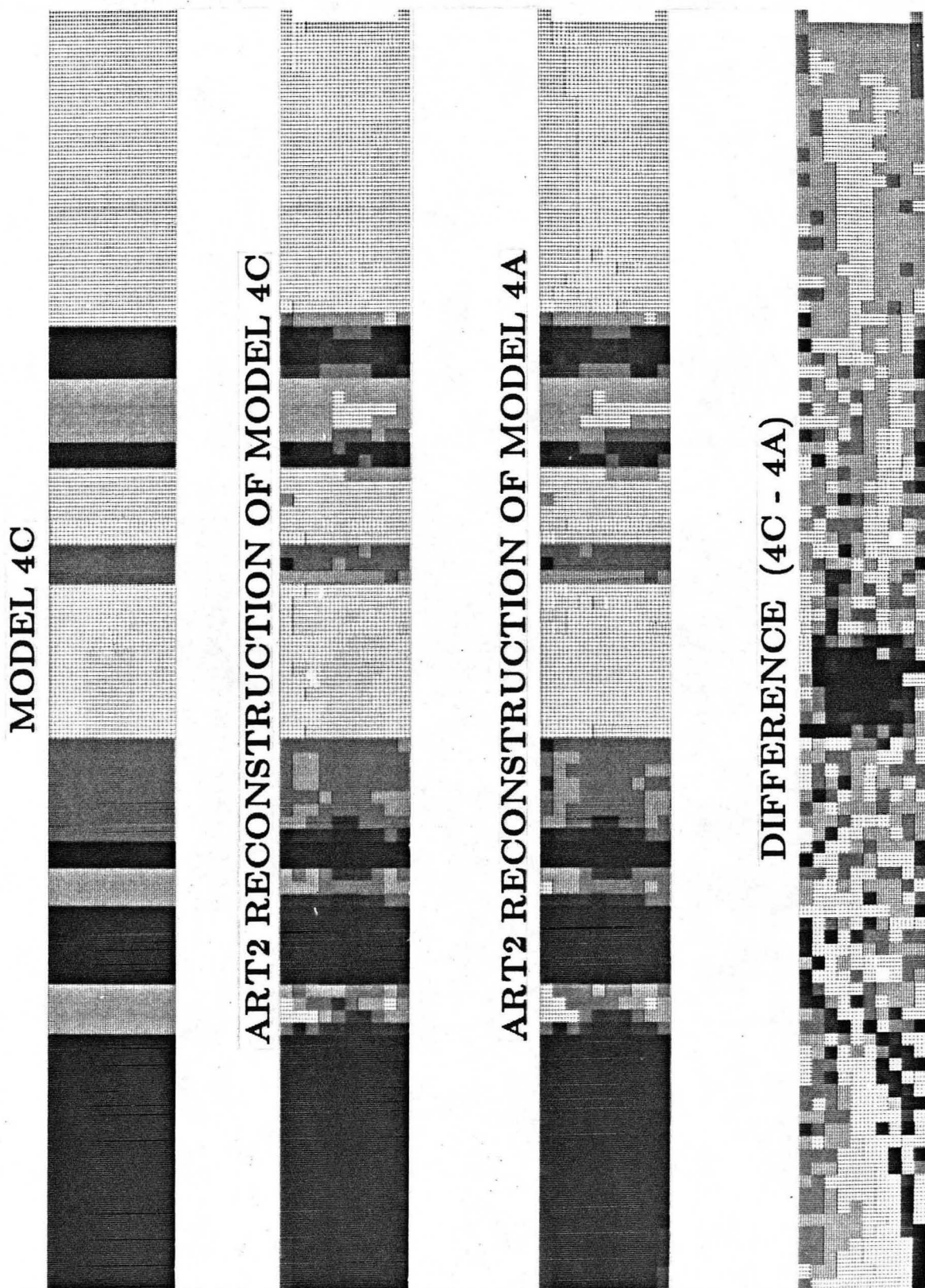


**Figure 4.14.** Reconstruction of velocity model 4C using ART2. The high velocity zone can be distinguished even without taking the difference. The difference plot is noisy because the velocity values of the zone are only 0.15 km/s higher than the surrounding layer. The darker shades in the distance plot correspond to larger negative values.

SMOOTHED RECONSTRUCTION OF MODEL 4A



SMOOTHED RECONSTRUCTION OF MODEL 4C



SMOOTHED DIFFERENCE (4C - 4A)



Figure 4.15. The smoothing function is applied to the ART2 inversion of model 4C to eliminate the noise in the difference plot.

## CHAPTER 5

### Applications of ART to Crosshole Seismic Data

#### Introduction

The previous chapters have shown that Algebraic Reconstruction Techniques perform well on synthetically derived data, even with the inclusion of noise. The critical test lies in the analysis of a real data set. For this test, two data sets (Stripa and Retsof) with crosshole source-receiver geometry were available. In both cases the data consist of high quality travel-times obtained from reasonably dense networks.

The data are inverted using algorithms introduced in Chapter 2. The stopping criteria described in Chapter 3 must be used to stop the iterative process since the distance,  $\delta$ , is not available. These criteria include a visual evaluation of the reconstructions and the change in slope of the RMS residual and variance curves. The relaxation parameter is chosen with the same criteria. The pixel size is selected to correspond to the distance between stations, as suggested in the last chapter. The smoothing function is not applicable to the Stripa data because of the small (9 x 9) grid used, but it should prove helpful in reconstructing the Retsof data, which has variable sampling and limited angular coverage.

The emphasis of this chapter is placed equally on the apparent reliability of the ART reconstructions and the physical interpretation of the results. Reliability is based on the degree to which the reconstructed velocity distribution, the velocity values and bounds of anomalous zones, is consistent with what is known about the media. The

interpretation will address the primary purpose of these two experiments: a search for the effects of heating granitic rocks, and an attempt to outline an anomalous low-velocity zone expected to be caused by dissolution of overlying carbonate rocks by ground water flow into a mineshaft.

### Data

Two appropriate data sets are available from crosshole-type experiments. The experiments were carried out at the underground radioactive waste study site at the Stripa mine facility in Sweden and at the Retsof salt mine in New York, where the anticipated anomalous velocities are due to heating in the former case and to solution processes in the latter.

The Stripa experiment investigated the behavior of a granitic rock mass heated by an electrical heater simulating a radioactive waste canister, emplaced in a large diameter borehole in the floor of an underground drift. The seismic data set consists of P- and S-wave travel-times and amplitudes measured along 162 ray paths between two boreholes. Eighteen sources were located at 0.5 meter intervals in a 10 meter borehole and nine geophones at 1.0 meter intervals located in a parallel borehole approximately 4 meters away, as shown in Figure 5.1. This study uses two suites of measurements, the first taken after the heater had been turned on for several weeks (Data Set 1) and the second several days after the heater had been turned off (Data Set 2). The objective was to determine the degree to which the reconstructions could detect slowness or attenuation changes due to changes in stresses and fractures caused by the heating. The geometry of the experiment is conventional crosshole so that the range of angles through the area of interest is limited, though reasonable ( $-66^\circ$  to  $66^\circ$  at the heater location), and the sampling was at regular intervals. Source and receiver locations were measured to 1.0 mm and travel-times were read to 1.0  $\mu\text{sec}$ .

The Retsof mine data set consists of some 400 P-wave travel-times measured along intersecting ray paths between three sets of explosion sources and geophones; on a 400m long surface line, in a borehole to a depth of 260m and in the mine at a depth of 320m. The resulting array of ray paths is shown in Figure 5.5. The area of interest is almost entirely encircled by this geometry, but the field is not regularly sampled. The paths do not lie within a plane, since the mine is offset approximately 25m from the plane of the boreholes and surface arrays. This sampled region contains a collapse zone apparently due to dissolution of overlying carbonate rocks by groundwater flow into a shaft at a location of a previous explosion. It was hoped that the reconstruction would define zones of major dissolution and provide guidance on possible remedial engineering steps. The number of rays is such that the field may be discretized into 25m square cells.

The symmetrical ray paths and highly accurate measurements make the Stripa problem quite stable. The two data sets can serve as a check of consistency, since pre-existing anomalous zones should show up in both inversions. The inversion of the Retsof data is difficult, because the unsymmetrical station configuration results in varying ray lengths and sampling. The sampling of pixels will be highly variable and the angular coverage will differ between regions of the field.

## Results

Seven different algorithms were used to analyze the two data sets. These include:

ART - Algorithm 1, equation (2.11)

ART1 - Algorithm 2, equation (2.12)

ART2 - Algorithm 2a, equation (2.13)

MART - Algorithm 3, equation (2.15)

WART - weighting scheme, equation (2.21), applied to ART

WART1 - weighting scheme, equation (2.21), applied to ART1

SIRT - Algorithm 4a, equation (2.17)

For each of these algorithms the image was corrected after each ray was analyzed. For these same algorithms the image was also corrected using equation (2.10) (specified by an "A", e.g. ARTA). In general, determining the proper relaxation parameter and stopping criteria, for reasonable solutions required considerable manipulation.

### I. *Stripa*

In the *Stripa* experiment dimensions were small and the ray lengths are similar. Preliminary studies indicate that the velocity contrasts are small, with only 0.3 - 0.5 km/s separating the highest and lowest values (Paulsson, 1983). The region was divided into a  $9 \times 9$  field of rectangular pixels giving 81  $1.0 \times 0.5$ m pixels (Figure 5.1). The one-meter separation between receiver locations limits the minimum cell dimension. A finer vertical division will decrease the number of rays per cell, giving many unsampled pixels near the edges. The coverage is vertically symmetric about the center line with the ray density greatest toward the center of the region where the angular range of sampling is as much as  $130^\circ$ .

A similar solution is obtained from all methods applied to a common starting model. Good detail is recovered, and consistent solutions are obtained even if as many as half the rays are ignored. Figure 5.2 shows plots of the velocity fields at full heating and after heater deactivation. Solutions from the various algorithms are all quite similar. While the heater was on, a constant velocity field of about 5.95 km/s was maintained, though slightly lower velocities occur toward the upper left corner of the field. After the heat source was removed, a low velocity zone of 5.6 - 5.7 km/s developed in the location of the heat source and extending to the upper right and to the upper left

of the section, where the low velocity from Data Set 1 existed. The co-existence of this zone between the data sets suggests the existence of some pre-heating fracturing in this area, possibly due to drilling. Some smearing of the central zone seems to take place, especially on a diagonal extending from the lower left corner toward the upper right. There is some suggestion of low velocity zones toward the lower left and upper right corners of the field, which would tend to accentuate the smearing along that diagonal. Synthetic models of this data set (Figure 5.3) have shown that the smearing also has the effect of reconstructing slightly higher velocities in the low velocity zones than actually exist. The model shows slight smearing only in the horizontal direction, which is expected due to the source-receiver configuration. The weighted algorithms, designed to reduce the smearing effect, fail to do much toward this end. In fact, all algorithms give remarkably similar results. An encouraging observation is the existence of the low velocity zone where it is expected to be. Due to the smearing, the horizontal extension of the zone is not resolvable.

Relaxation parameters and stopping criterion were determined from visual assessment of variance, entropy and RMS residual which are plotted versus the number of iterations in Figures 5.4. The purpose of these plots is to determine of the relaxation parameters for which the curves have the form found in the previous chapters where the best solution was found to exist at about 10 iterations. The form is usually a rapid increase or decrease in value and then leveling off. The best reconstruction is usually found where this leveling off begins. The resulting relaxation parameters and other values are given in Table 5.1.

Figure 5.4 and Table 5.1 also show the consistency of the algorithms. Only small differences are seen between the different statistical values. It also shows that Data Set 1 (Table 5.1A) gives much smaller residuals than Data Set 2. This is due to the absence of any large velocity contrasts in Data Set 1 in contrast to those found in Data Set 2.



## II. Retsof

The Retsof data set is an example of noisy data; the sources and receivers do not lie in a plane, the dimensions are fairly large (hundreds of meters), the travel-times must be corrected for topography, the range of projection angles through each cell is limited, the ray lengths are highly variable, and the velocity contrasts can be large, causing problems with curved rays. The ray path configuration and the number of rays through each box are depicted in Figure 5.5. The drawbacks to the geometry can be easily seen in this figure; there are areas of very low and very high density coverage, with poor angular coverage in some areas and many almost redundant rays. A swath of reasonable coverage with rays penetrating from many directions runs from the mine toward the borehole-surface intersection (lower right to upper left in the figure). The least resolvable area will be toward the right where the ray coverage is poor and the angular coverage is limited.

The area of interest is initially divided into an  $18 \times 14$  field of pixels ( $I = 252$ ) giving a pixel dimension of about 25m on a side. The pixel size was chosen to correspond to the station spacing, as suggested in the last chapter. Despite the apparent limitations in the data, the reconstruction was successful. Figure 5.6 shows the velocity field determined by each of the variations on the algorithms. The various solutions differ only slightly in detail, and two general features are consistent in all of the reconstructions: there is a very low velocity zone (about 2.75 km/s) at the base of the field below a V-shaped zone of intermediate velocities (4.00 km/s). This low-velocity field is bounded by two zones where velocity increases with depth. These features, which show velocity contrasts as high as 40%, are consistent with expected solution patterns.

Oscillation in the solution may be measured by its 2-D spatial Fourier transform. In wavenumber space, the oscillations appear as large amplitudes at values of  $k = C^{-1}$ , where  $C$  is the pixel width. Generally, the smoother the Fourier transform, the

less oscillation is present in the reconstruction. In Figure 5.7, sample k-k plots are shown for reconstructions with the Retsof data using ART2. 2-D spatial Fourier transform for  $\lambda=0.01$  and 0.05 are shown. The plots indicate that most of the velocity variation seen is in the low-wavenumber region (upper left hand corner) and virtually no short wavelength oscillation (high  $k_x$ ) in the horizontal direction, which indicates a smooth reconstruction. Note that for the 0.05 damping value short wavelength oscillations in the vertical direction (large  $k_z$ ) develop, as seen in the lower left portion of the plot. Most oscillations occur in areas of low ray density or low angular coverage toward the upper right and lower left of the velocity field in Figures 5.6.

The stopping criteria were determined as for Stripa. Relaxation parameters were used to control the rate of convergence. The convergence of some of the weighted algorithms was very slow, so a high damping was necessary (Table 5.2). This occurred almost exclusively for algorithms in which the relaxation value had units of length, e.g. WART. The convergence criteria and residuals given in Table 5.2 and Figure 5.8 show small differences among the various algorithms. Therefore, one algorithm can not be deemed better than another on the basis of these values. In general, the RMS residual,  $r^q$ , initially decreased very quickly, leveling off after several iterations. The variance,  $V^q$ , gradually increased without ever leveling off. This behavior would usually indicate that a larger relaxation parameter should be used, but in this case a higher value leads to oscillatory results. Figure 5.9 shows the reconstruction using ART2 with  $\lambda = 0.05$ , somewhat higher than the value of 0.01 used for the results in Figure 5.2. This solution is more oscillatory than Figure 5.6.

The size of the pixels used in the inversion effectively determines the limiting size of the velocity feature which can be recovered. The ART2 inversion is performed with a 26x21 pixel array (Figure 5.10), increasing the station spacing to pixel size ratio to 3:2. The results show improvement over the 18x14 array used in Figure 5.6. A smoother velocity gradient is reconstructed near the collapsed zone and the zone itself

is better defined due to the smaller pixels. The pixel size may be further reduced if the smoothing function is used in the inversion. An array of 40x32 pixels with ART2 (Figure 5.11) results in further improvement over any other Retsof reconstruction. The resolution is improved with more continuity in the velocity gradients and anomalous zones. It is also more aesthetically pleasing. Retsof is a good example of a data set which seems to need smoothing in the inversion.

### Discussion

The two data sets were analyzed to compare various ART algorithms in processing real geophysical data sets for good and average quality. The reconstructions of both data sets are quite consistent with the known structures and expected velocity fields. In the Stripa experiment fairly uniform velocities were seen during heating (Figures 5.2), apparently due to the closure of fractures by thermal expansion (Paulsson *et al.*, 1985; King and Paulsson, 1981). Velocities decreased upon heater removal, due to fracture opening, giving a maximum velocity contrast of about 8%. Some permanent damage (thermal fracturing) was seen in the central region where the heat was greatest and where previous calcite fracturing was evident. This zone is also near the area of maximum ray coverage which can bias the results, but the feature is off-center enough to distinguish itself from such bias. Horizontal extension of the central low velocity zone to the sides of the figure is evident, as expected, based on the studies in Chapters 2 and 3 (see Figure 5.3). The diagonal line of low velocity extending from the bottom left to upper right is due possibly to numerical smearing of actual low velocities created by minimal calcite fracturing at its upper right terminus and by drilling damage at the bottom of the left borehole. Strong evidence is suggested for these conditions from fracture mapping. Note that the smearing takes place primarily toward the surface. This illustrates the importance of using the proper geometry for experiments. Due to the lack of surface sources or receivers, the number of ray paths

between the heater and the surface boreholes were not sufficient to eliminate this smearing. There are enough rays below the heater to eliminate most of the smearing. The single diagonal may be due to existing fracture zones. Some problems of ART are encountered in these inversions, but a reasonably accurate picture of the change in velocity field is achieved. The reconstructions are good enough that reliable velocity values may be determined and the existence of anomalous zones resolved with reasonable bounds on their locations.

The important features revealed in the Retsof mine experiment are the V-shaped low-velocity zone through the center of the picture, the extremely low velocities at the collapsed end of the mine, and the general increase in velocity with depth, from about 4.00 km/s to 5.5 km/s, probably equivalent to the velocity field before the collapse and alteration. A velocity contrast of 40% is indicated. The large low-velocity zone is interpreted as being due to ground water flow and resulting alteration and dissolution of the carbonate rocks. This low-velocity zone intersects the mine where major alteration and collapse of material into the mine is occurring. The reconstruction shows this structure in detail. Possible artifacts in the reconstruction include smearing to the lower left of the picture and a probably anomalous high velocity zone at the upper right both of which may be due to poor coverage and resulting oscillations in the data. Despite the apparent limitations in the data, the reconstruction gives a usable picture of the structure.

In general, all the algorithms give consistent, apparently reliable reconstructions of the Retsof and Stripa velocity fields. The low velocity zones at both Stripa and Retsof are determined to the size of the pixels in the analysis. The largest expected problem with the inversions is distortion due to the straight-ray assumption. While some image distortion inevitably occurs, it does not seem a substantial problem. The anomalous zones at Stripa are so small and the path lengths so short that the curved ray paths do not significantly deviate from the straight line. The problem with the

Retsof data is that the geometry of the velocity and station distributions and the positioning of the low velocities of the collapsed zone tend to severely bend several important rays just before they hit the receivers so that they never can be traced accurately, so the curved-ray algorithm was not performed. Since this occurs just at the end of the rays which enter the failed zones near the mine, it will have little effect on the results. This is not to say that a curved ray algorithm should not be used; if the collapsed zone were located near the middle of the field, the distortion due to the use of straight rays would be greater.

Most of the image distortion in the Stripa and Retsof reconstructions appears to be due to incomplete data in the form of low ray density and, more importantly, incomplete angular coverage. These problems could have been reduced by optimizing the experiments in terms of source and receiver locations. The increased resolution resulting from the "filling in" of a few essential rays would have justified the added effort involved in acquiring the data. Large improvement in the Retsof geometry would come from the addition of sources or receivers down a borehole or shaft at the right of the picture to obtain the low-angle rays from the surface and across the field to the other boreholes. The Stripa experiment used the more classic cross-hole situation of parallel boreholes. Greater resolution, especially toward the top of the region could have been achieved with a line of surface receivers and a greater borehole depth to increase the angular coverage and better determine the horizontal extent of the low velocity zone. Of course, increasing the number of source/receiver pairs is suggested, until more pairs give less improvement than economically justified. The Stripa experiment had 18 sources, but just 9 receivers. An increase to 18 receivers would have allowed a 9x18 configuration to be inverted, and an 18x18 array could be possible with surface sources.

STRIPA - DATA SET 1				
Algorithm	Variance (s <sup>2</sup> /km <sup>2</sup> )	RMS residual (sec)	Optimal Iter	$\lambda$
ART	$3.560 \times 10^{-6}$	$4.224 \times 10^{-3}$	10	0.04
ART1	$3.100 \times 10^{-6}$	$4.394 \times 10^{-3}$	10	0.06
ART2	$3.713 \times 10^{-6}$	$4.211 \times 10^{-3}$	10	0.04
WART	$3.660 \times 10^{-6}$	$4.255 \times 10^{-3}$	10	0.40
WART1	$3.415 \times 10^{-6}$	$4.384 \times 10^{-3}$	10	0.40
MART	$2.709 \times 10^{-6}$	$4.636 \times 10^{-3}$	10	0.05
ARTA	$2.878 \times 10^{-6}$	$4.883 \times 10^{-3}$	10	0.50
ART1A	$2.542 \times 10^{-6}$	$4.961 \times 10^{-3}$	10	0.80
ART2A	$4.419 \times 10^{-6}$	$4.032 \times 10^{-3}$	10	0.80
WARTA	$3.398 \times 10^{-6}$	$4.658 \times 10^{-3}$	10	6.00
WART1A	$3.198 \times 10^{-6}$	$4.804 \times 10^{-3}$	10	6.00
MARTA	$3.092 \times 10^{-6}$	$4.556 \times 10^{-3}$	10	1.00
SIRT	$3.257 \times 10^{-6}$	$4.503 \times 10^{-3}$	10	0.50

**Table 5.1A.** The values for variance and RMS residual for Stripa Data Set 1 reconstructions shown in Figure 5.2. The damping is varied to produce the "best" iteration at about 10 iterations.

STRIPA - DATA SET 2				
Algorithm	Variance (s <sup>2</sup> /km <sup>2</sup> )	RMS residual (sec)	Optimal Iter	$\lambda$
ART	$1.503 \times 10^{-5}$	$0.968 \times 10^{-2}$	10	0.04
ART1	$1.393 \times 10^{-5}$	$0.978 \times 10^{-2}$	10	0.06
ART2	$1.531 \times 10^{-5}$	$1.022 \times 10^{-2}$	10	0.04
WART	$1.536 \times 10^{-5}$	$0.972 \times 10^{-2}$	10	0.40
WART1	$1.430 \times 10^{-5}$	$1.007 \times 10^{-2}$	10	0.40
MART	$1.243 \times 10^{-5}$	$1.023 \times 10^{-2}$	10	0.05
ARTA	$1.288 \times 10^{-5}$	$1.096 \times 10^{-2}$	10	0.50
ART1A	$1.209 \times 10^{-5}$	$1.090 \times 10^{-2}$	10	0.80
ART2A	$4.419 \times 10^{-5}$	$1.014 \times 10^{-2}$	10	0.80
WARTA	$1.444 \times 10^{-5}$	$1.060 \times 10^{-2}$	10	6.00
WART1A	$1.368 \times 10^{-5}$	$1.091 \times 10^{-2}$	10	6.00
MARTA	$1.382 \times 10^{-5}$	$1.031 \times 10^{-2}$	10	1.00
SIRT	$1.436 \times 10^{-5}$	$1.022 \times 10^{-2}$	10	0.50

**Table 5.1B.** The values for variance and RMS residual for Stripa Data Set 2 reconstructions shown in Figure 5.2.

RETSOFF DATA				
Algorithm	Variance (s <sup>2</sup> /km <sup>2</sup> )	RMS residual (sec)	Optimal Iter	$\lambda$
ART	$0.418 \times 10^{-3}$	$7.850 \times 10^{-3}$	10	0.01
ART1	$0.443 \times 10^{-3}$	$7.723 \times 10^{-3}$	10	0.50
ART2	$0.491 \times 10^{-3}$	$7.559 \times 10^{-3}$	10	0.01
WART	$0.611 \times 10^{-3}$	$7.519 \times 10^{-3}$	10	0.25
WART1	$0.605 \times 10^{-3}$	$7.493 \times 10^{-3}$	10	0.25
MART	$0.446 \times 10^{-3}$	$7.742 \times 10^{-3}$	10	0.50
ARTA	$0.618 \times 10^{-3}$	$7.756 \times 10^{-3}$	10	0.50
ART1A	$0.658 \times 10^{-3}$	$7.613 \times 10^{-3}$	10	25.00
ART2A	$0.630 \times 10^{-3}$	$7.903 \times 10^{-3}$	10	0.40
WARTA	$0.752 \times 10^{-3}$	$7.850 \times 10^{-3}$	10	10.00
WART1A	$0.763 \times 10^{-3}$	$7.828 \times 10^{-3}$	10	10.00
MARTA	$0.678 \times 10^{-3}$	$7.610 \times 10^{-3}$	10	25.00
SIRT	$0.629 \times 10^{-3}$	$7.868 \times 10^{-3}$	10	0.40

**Table 5.2.** The values for variance and RMS residual for the Retsoff data reconstructions shown in Figure 5.2. Again, the damping is varied to produce the "best" iteration at about 10 iterations.



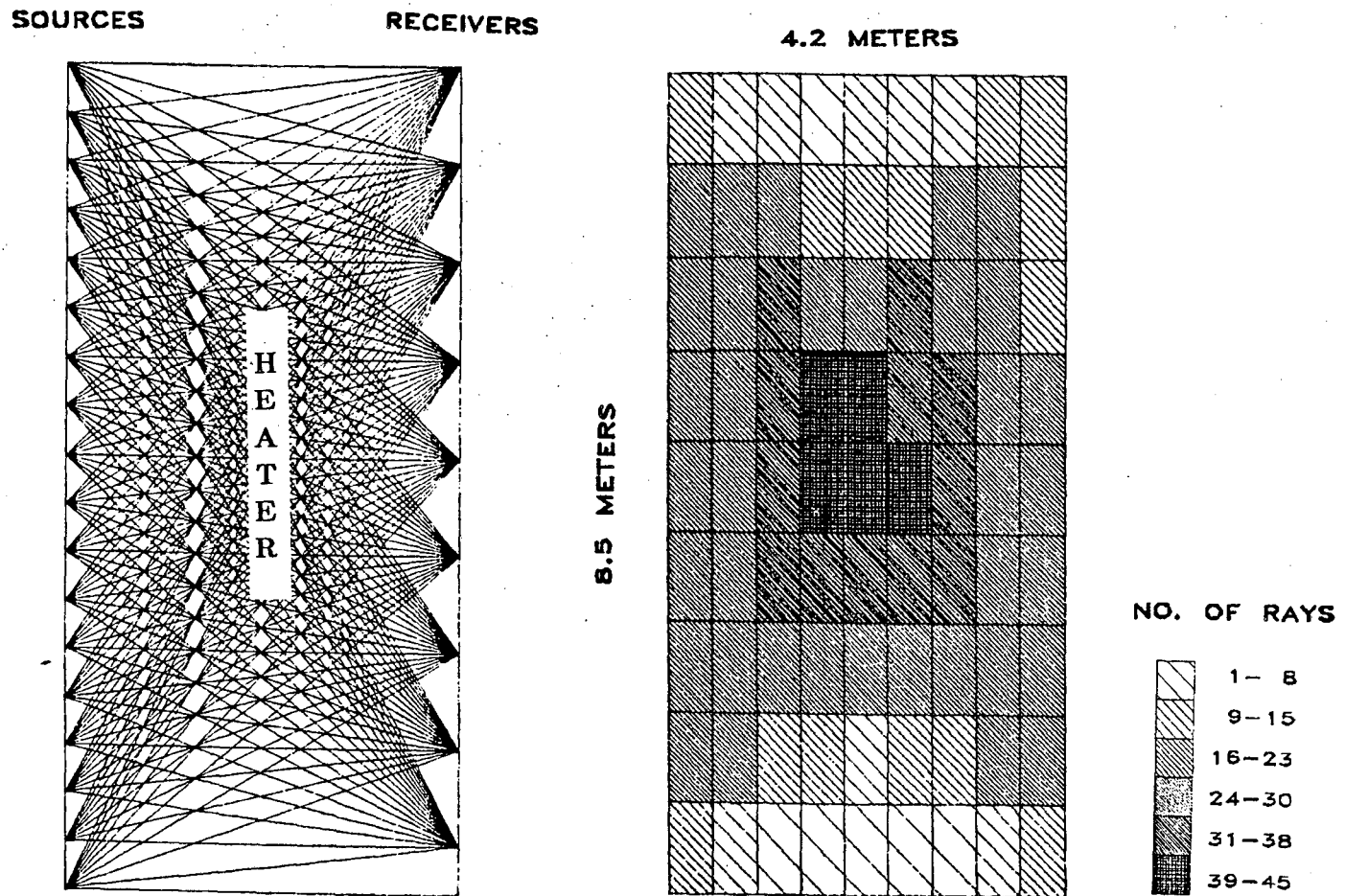
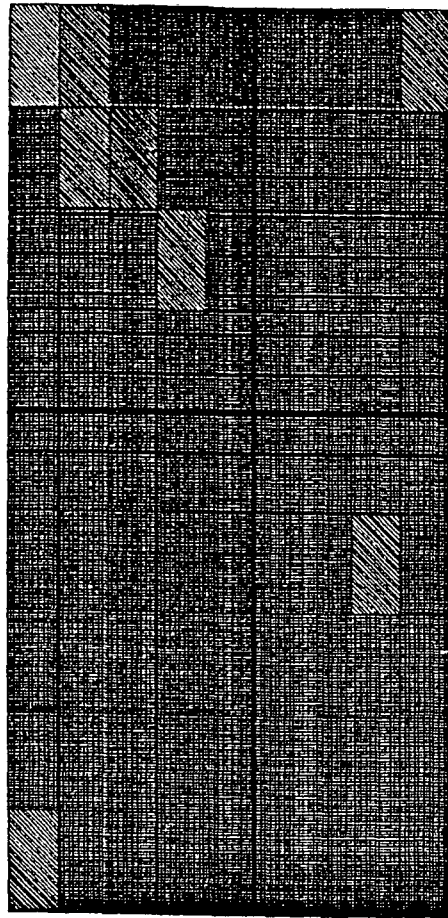
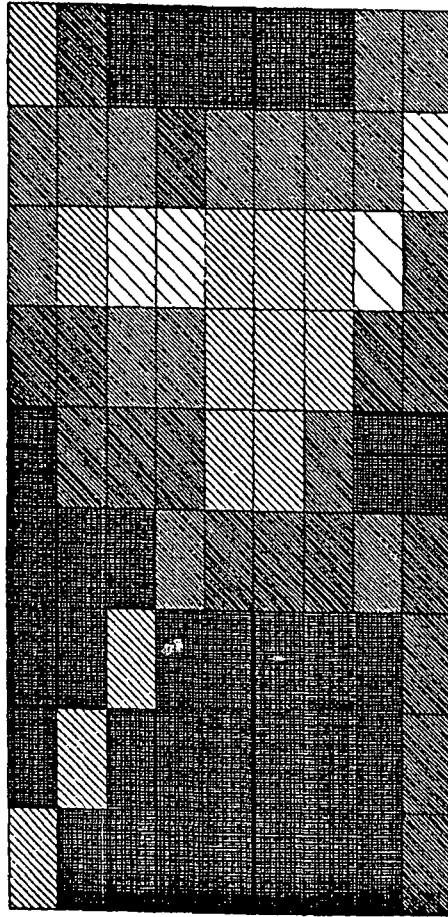


**Figure 5.1.** The raypaths and the ray density for the Stripa data. This geometry provides high symmetry in the sampling.

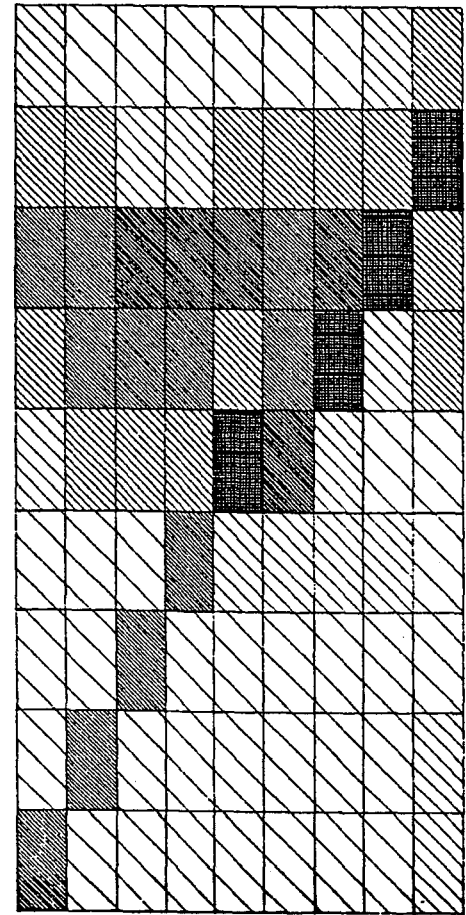
# ART



DATA SET 1



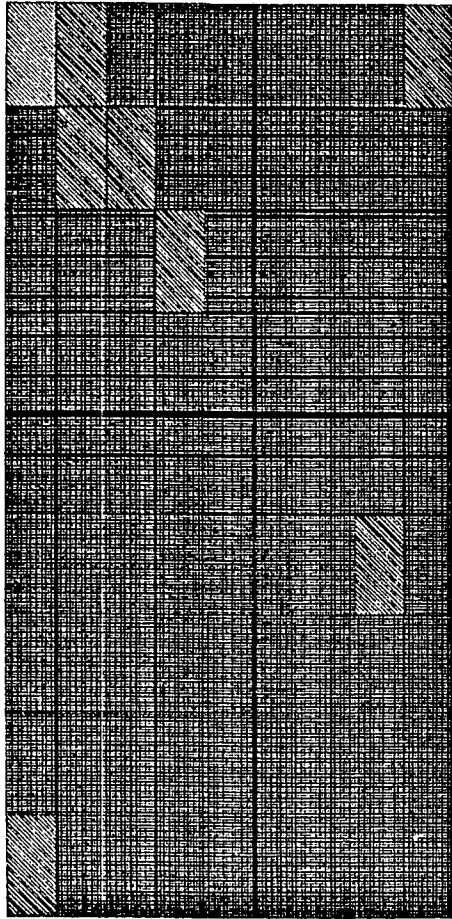
DATA SET 2



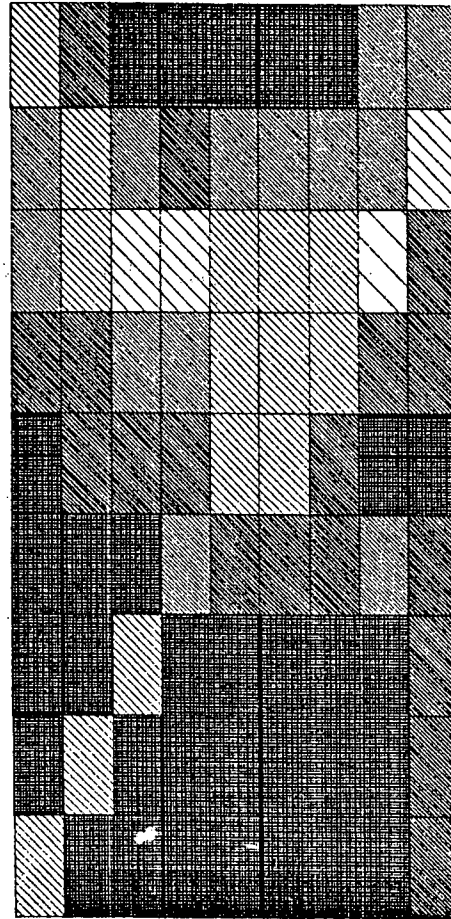
DIFFERENCE

Figure 5.2. Compressional velocity field reconstructions for the Stripa data for the geometry shown in Figure 5.1 using straight ray paths. The data sets correspond to the velocity field during heating (Data Set 1) and the velocity field after cooling (Data Set 2). The difference between these two data sets is also shown. The darker shades correspond to higher velocities and larger velocity differences. The velocity range is from 5.6 km/s to 6.0 km/s for Data Set 1 and 2 and 0.0 to 0.3 km/s for the differences.

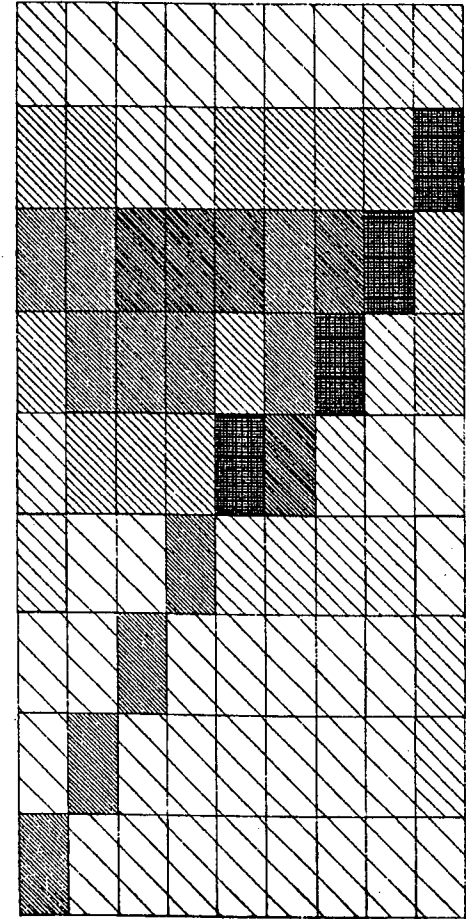
ART1



DATA SET 1



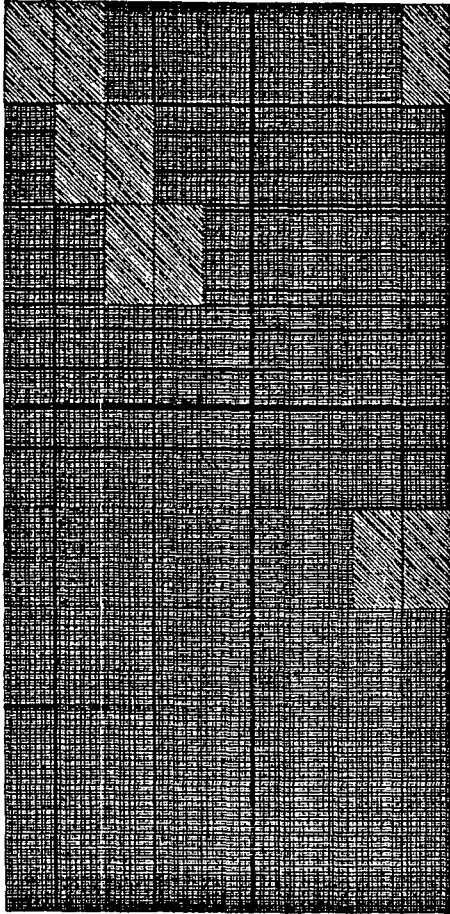
DATA SET 2



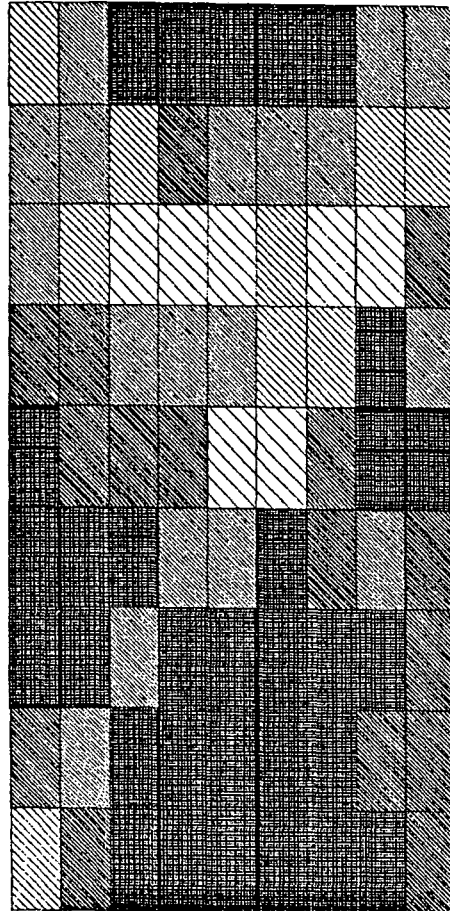
DIFFERENCE

Figure 3.2 (continued).

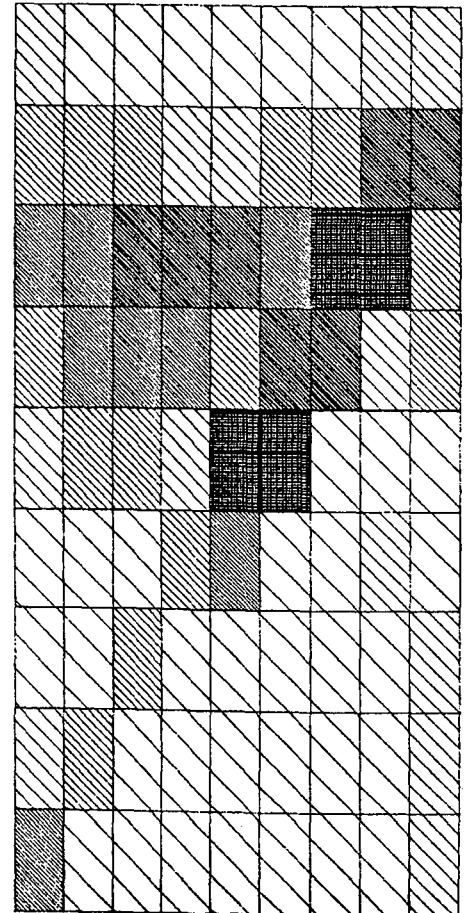
ART2



DATA SET 1



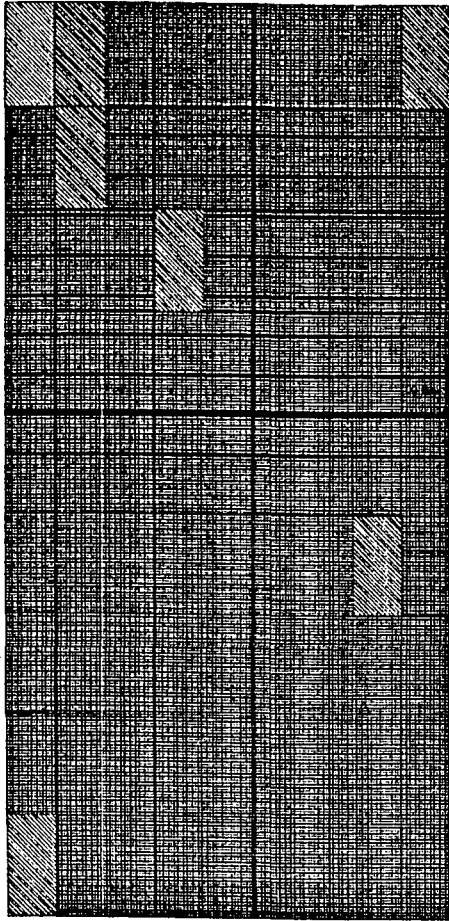
DATA SET 2



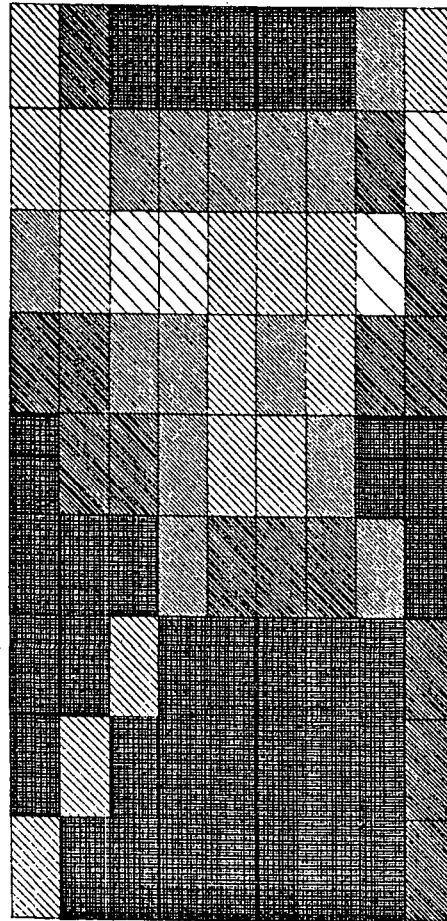
DIFFERENCE

Figure 3.2 (continued).

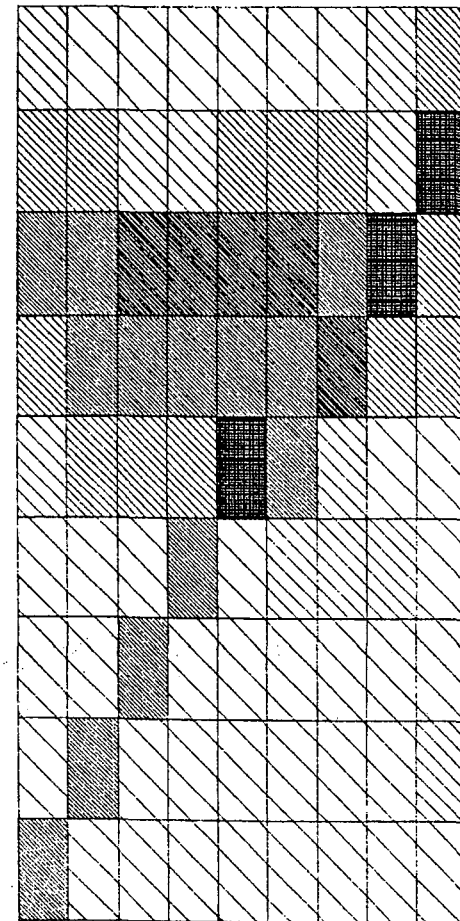
# WART



DATA SET 1



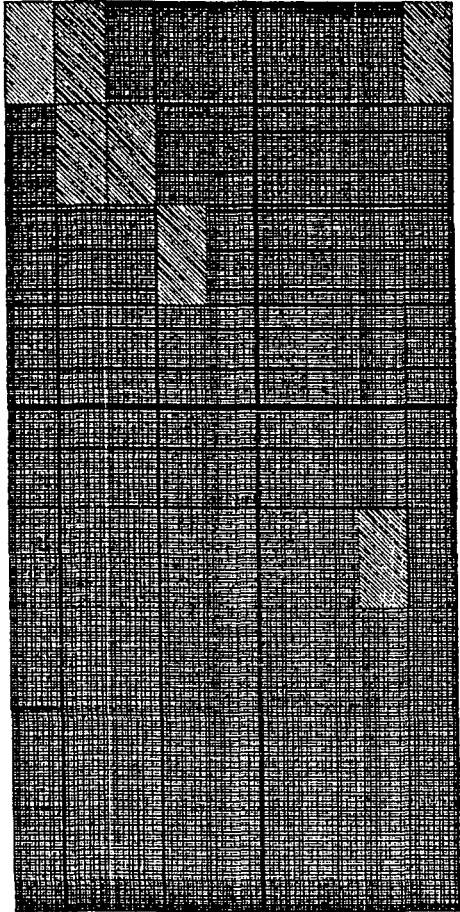
DATA SET 2



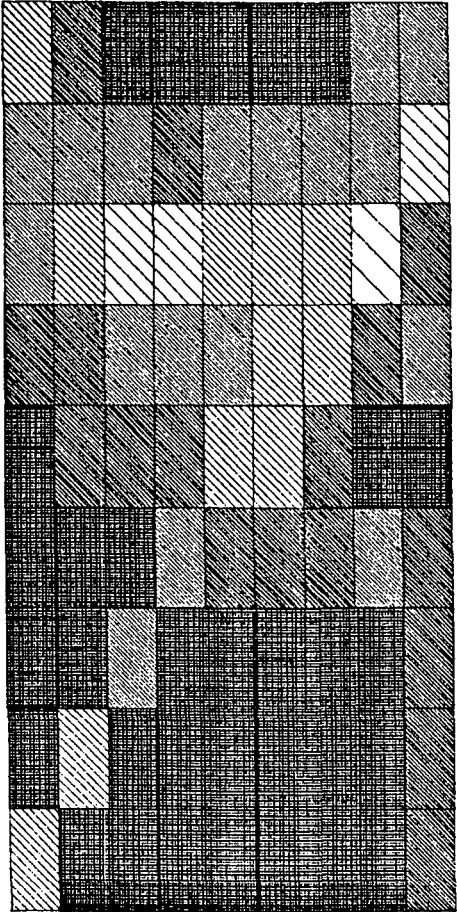
DIFFERENCE

Figure 3.2 (continued).

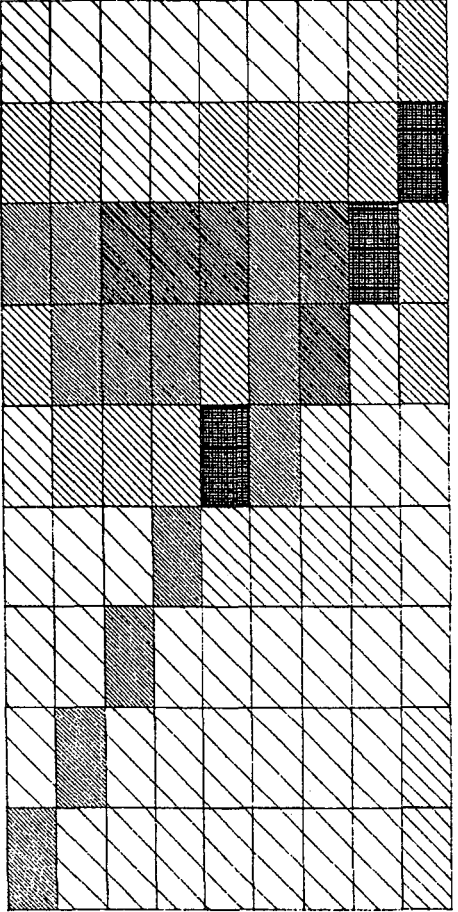
WART1



DATA SET 1



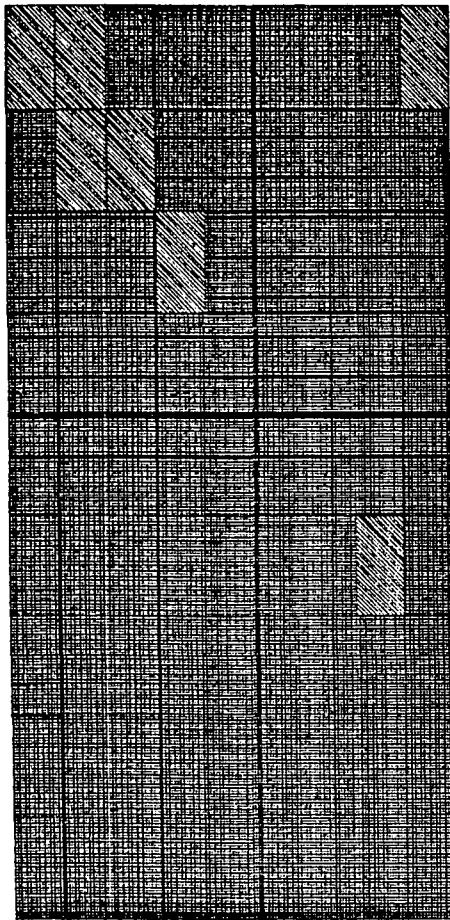
DATA SET 2



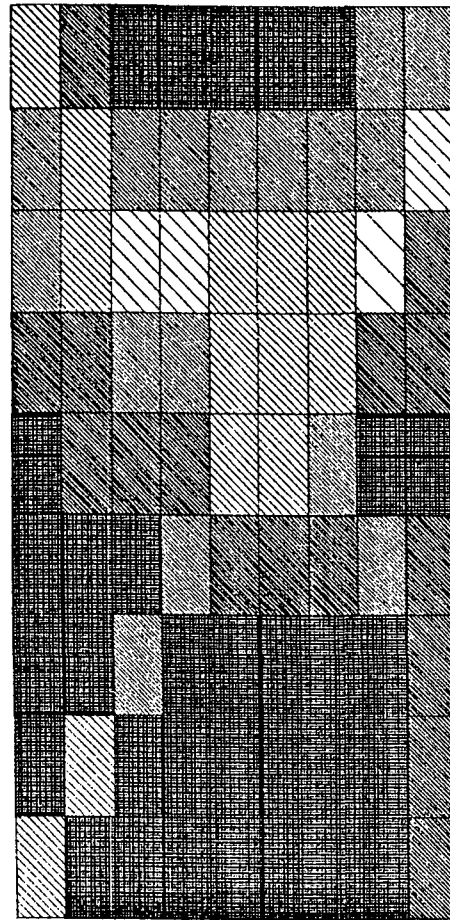
DIFFERENCE

Figure 3.2 (continued).

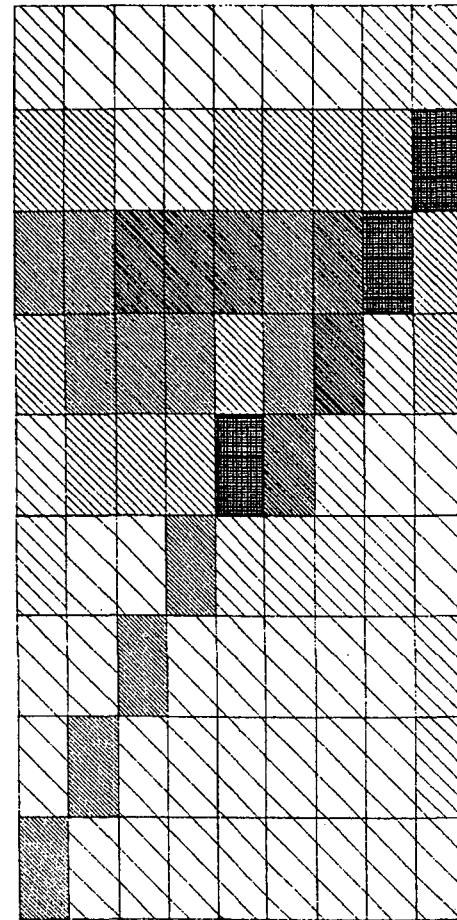
# MART



DATA SET 1



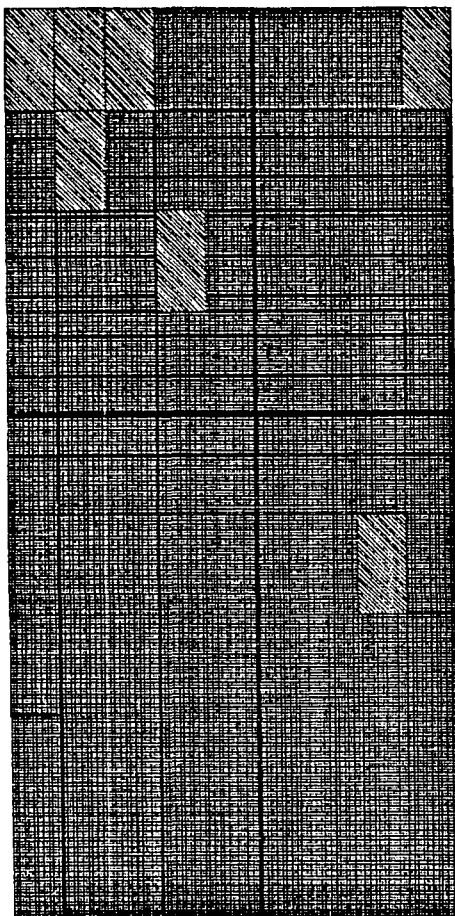
DATA SET 2



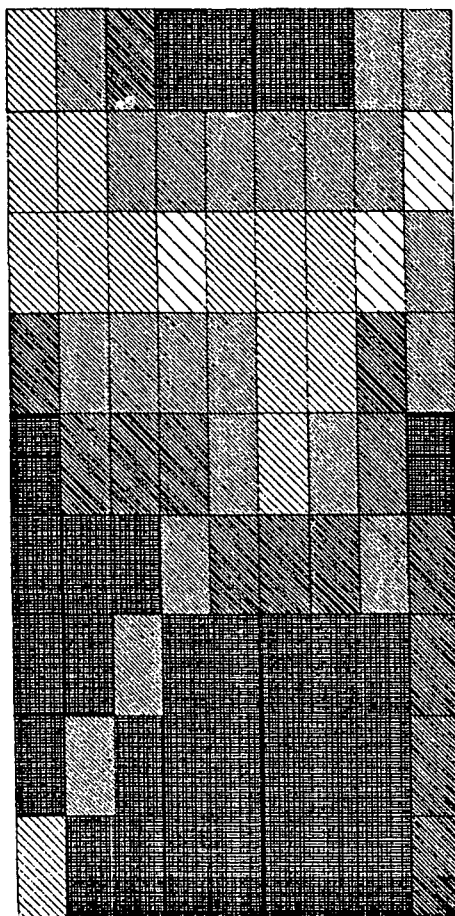
DIFFERENCE

Figure 3.2 (continued).

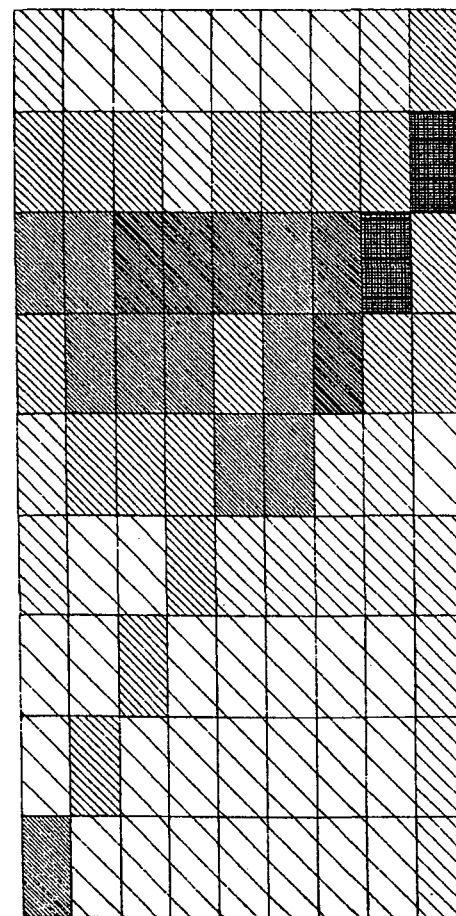
ARTA



DATA SET 1



DATA SET 2

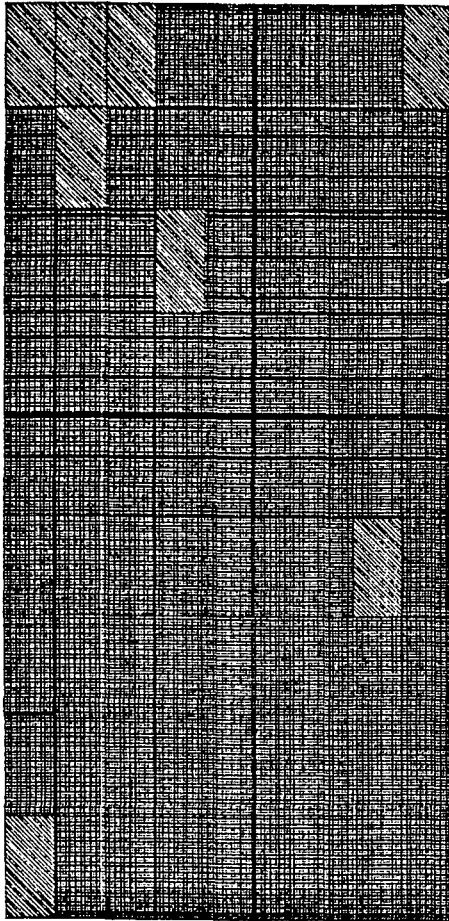


DIFFERENCE

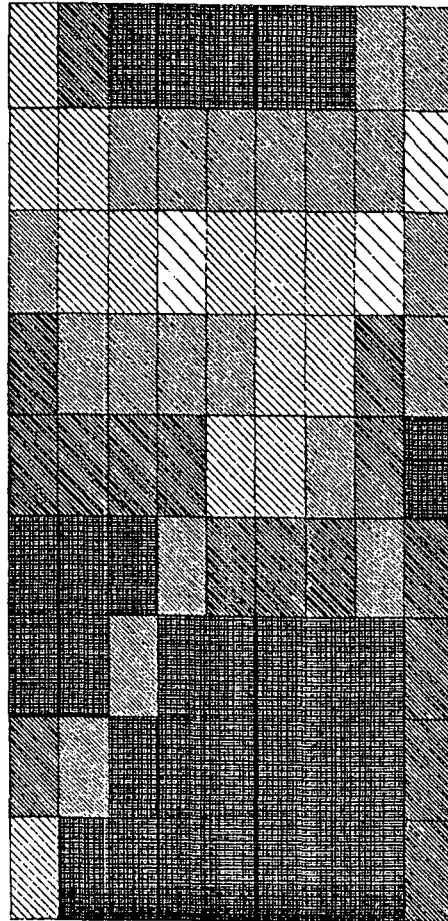
Figure 3.2 (continued).



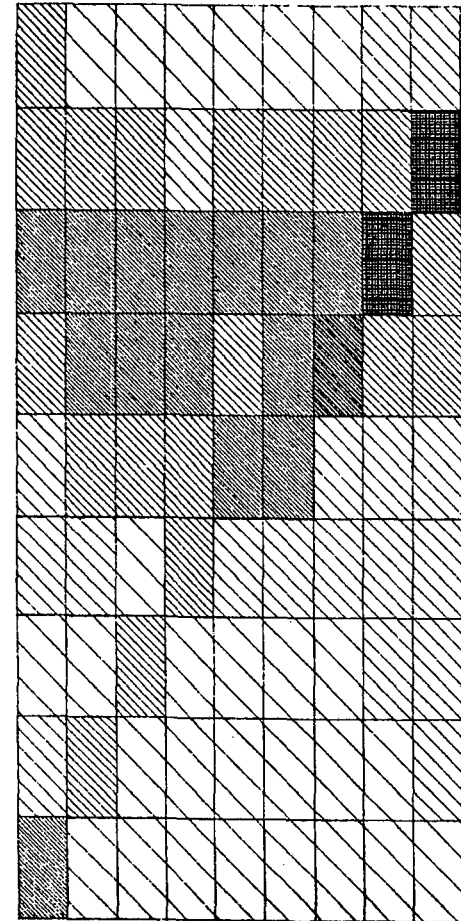
ART1A



DATA SET 1



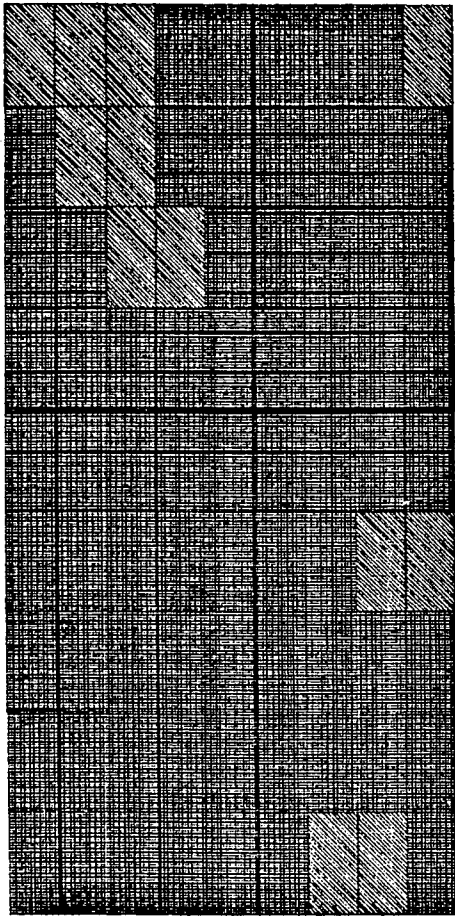
DATA SET 2



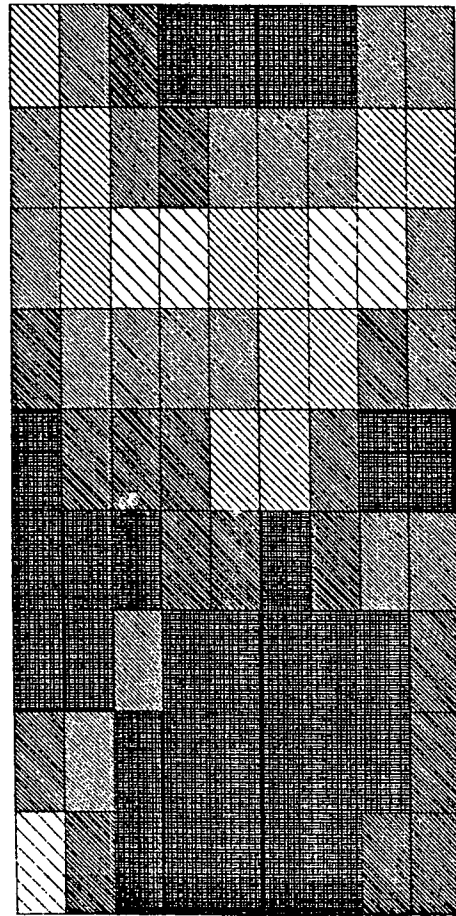
DIFFERENCE

Figure 3.2 (continued).

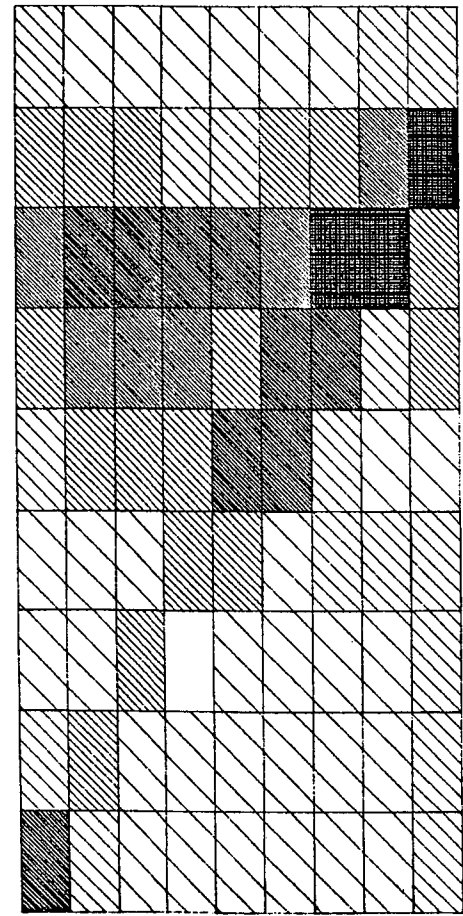
ART2A



DATA SET 1



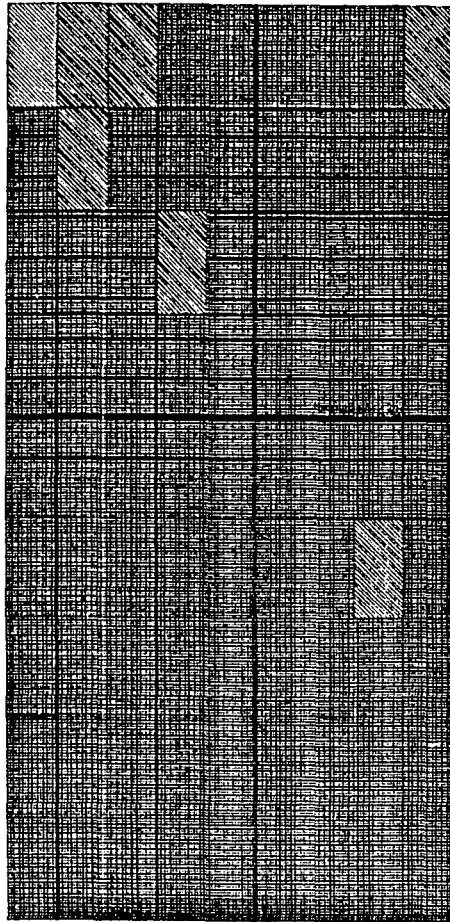
DATA SET 2



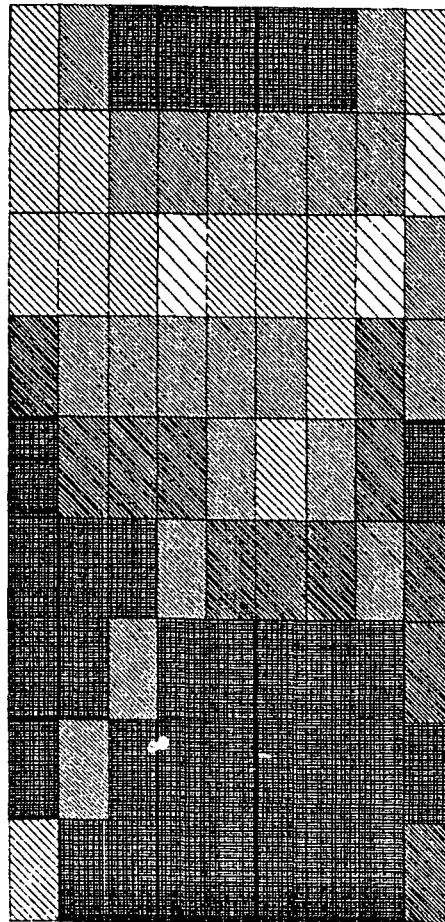
DIFFERENCE

Figure 3.2 (continued).

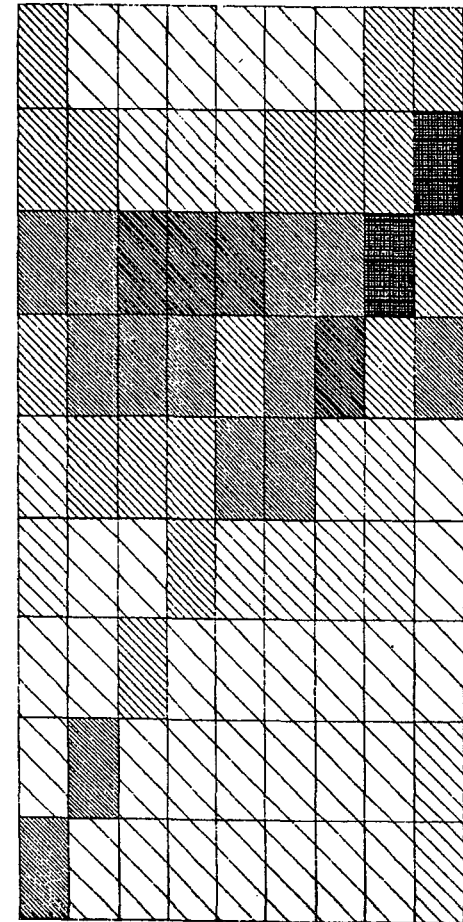
# WARTA



**DATA SET 1**



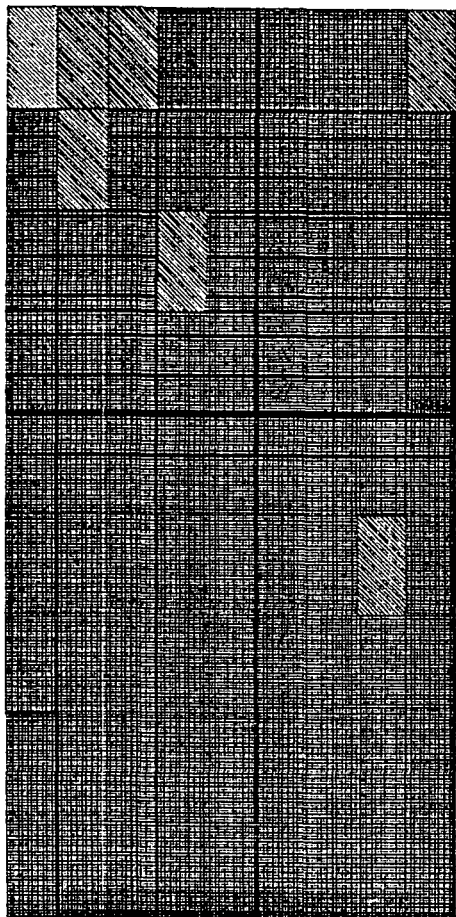
**DATA SET 2**



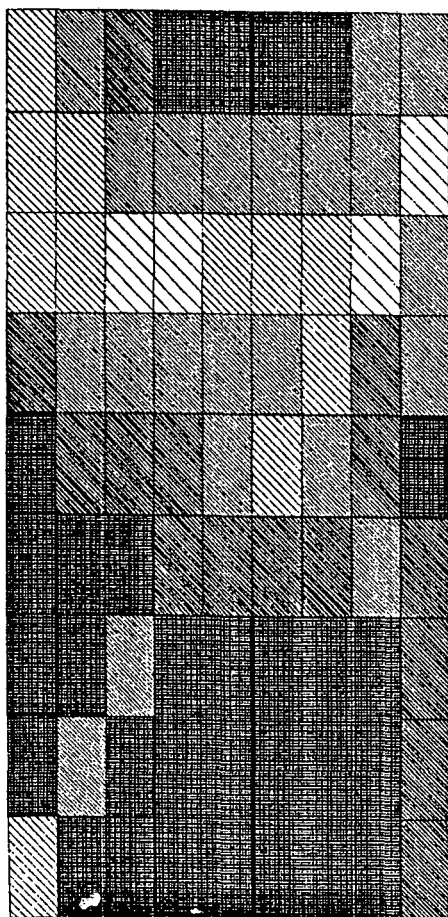
**DIFFERENCE**

Figure 3.2 (continued).

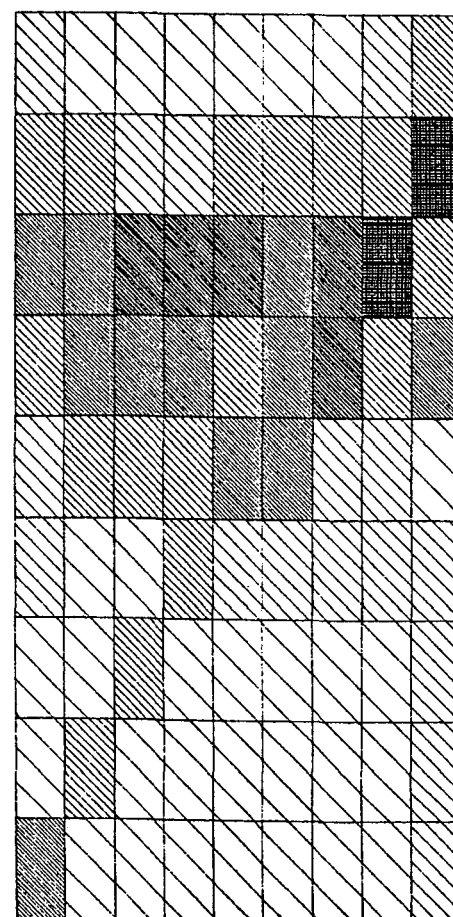
WART1A



DATA SET 1



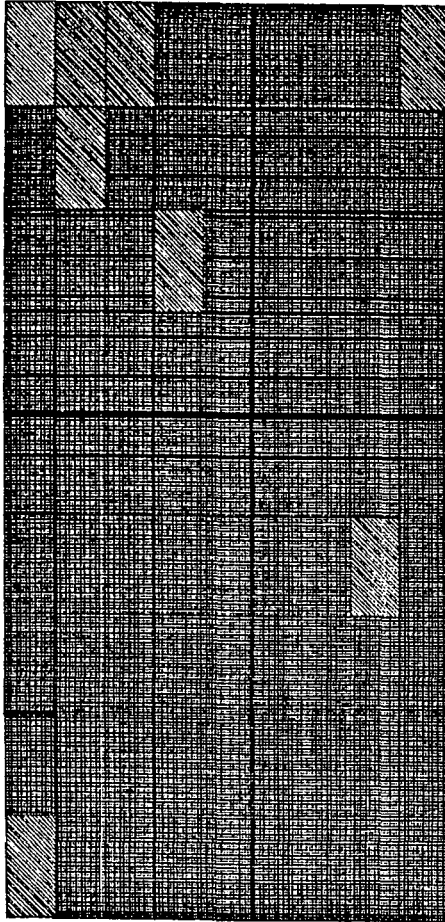
DATA SET 2



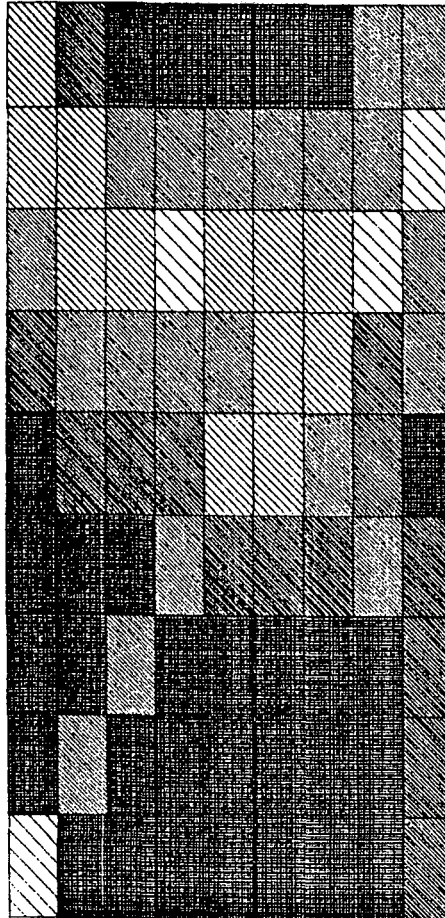
DIFFERENCE

Figure 3.2 (continued).

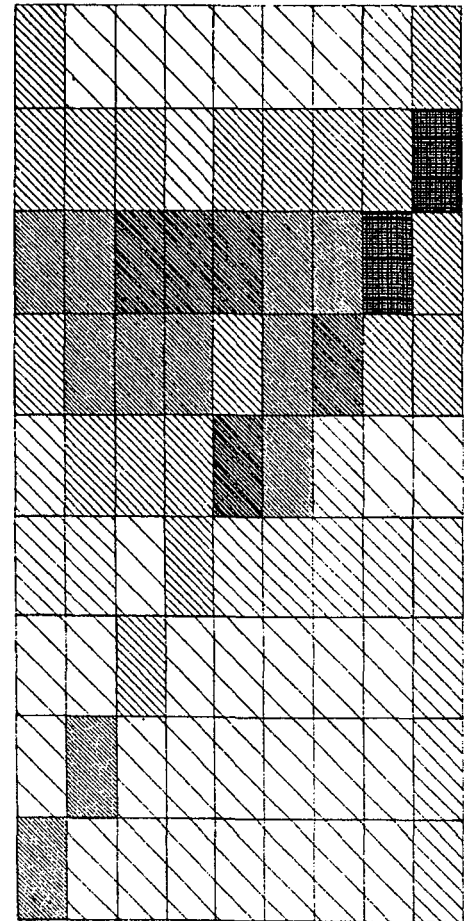
# MARTA



DATA SET 1



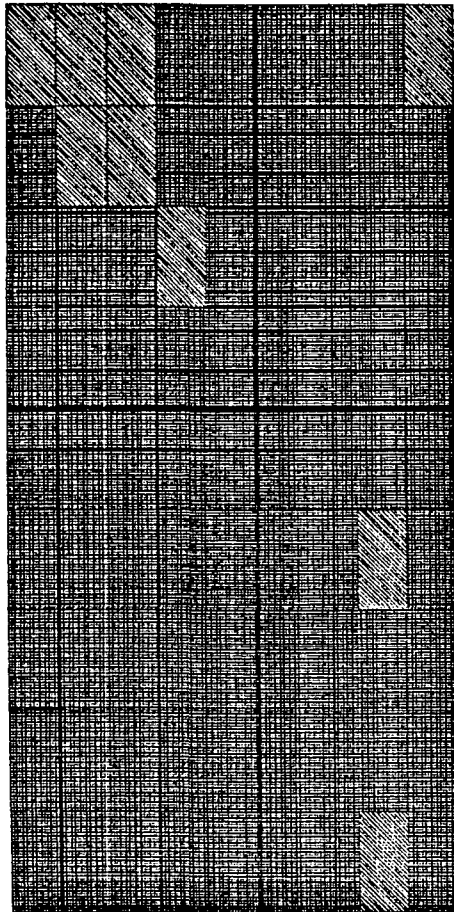
DATA SET 2



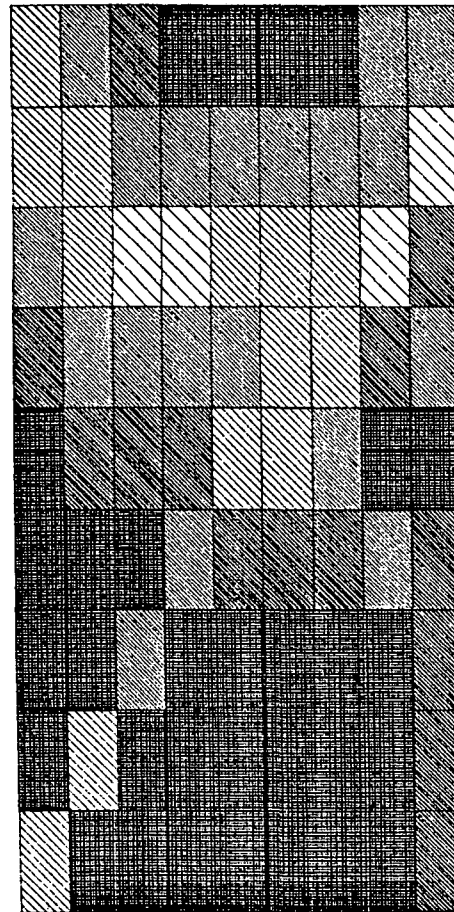
DIFFERENCE

Figure 3.2 (continued).

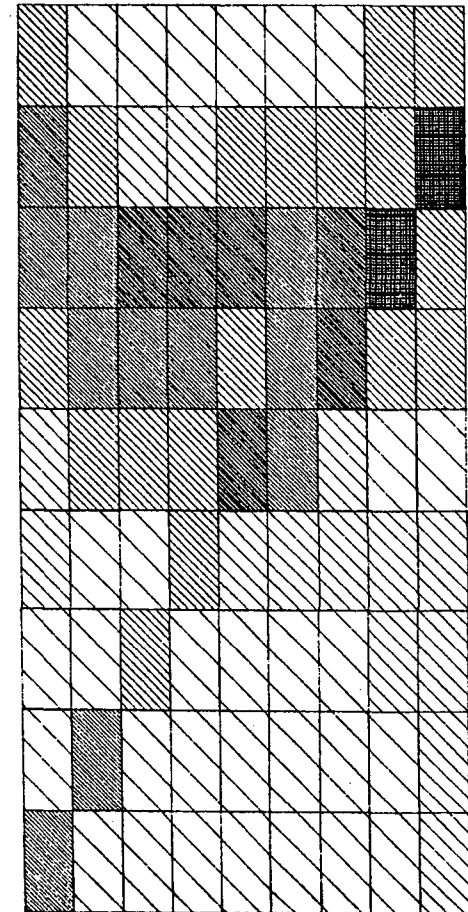
**SIRT**



**DATA SET 1**



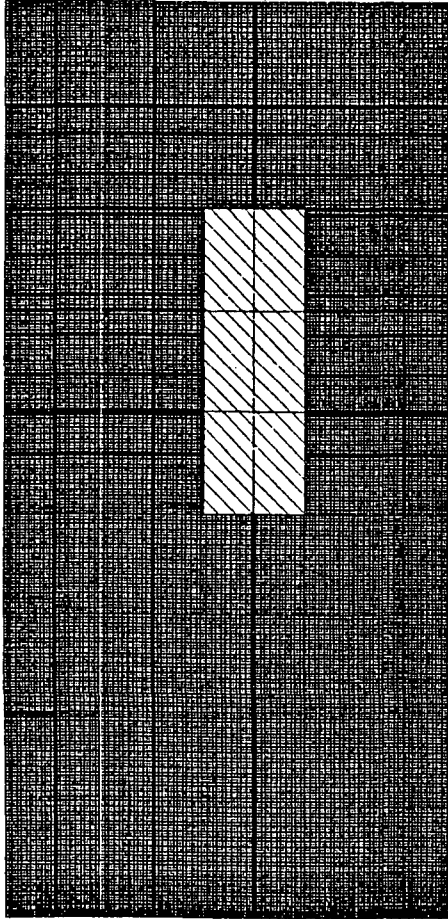
**DATA SET 2**



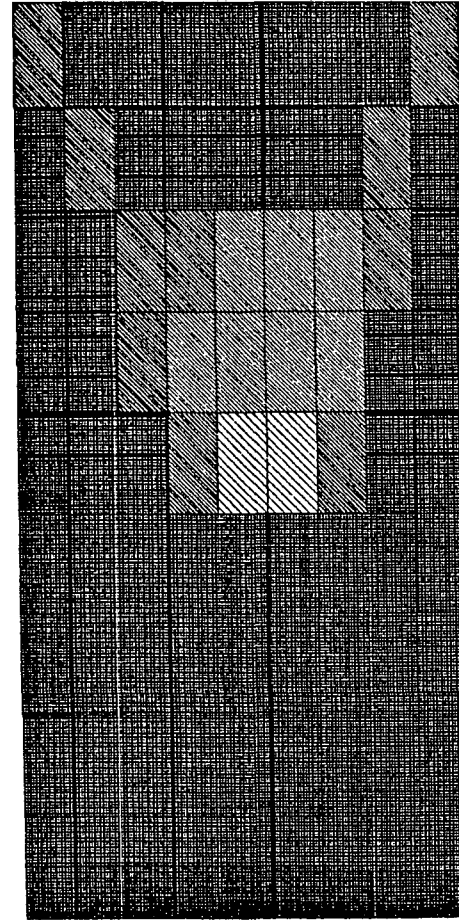
**DIFFERENCE**

Figure 3.2 (continued).

## MODEL



## ART2 RECONSTRUCTION



**Figure 5.3.** Results of a synthetic study done on a simplistic model of Stripa. The input model consists of a background velocity of 6.0 km/s (dark) and an anomalous zone of 5.5 km/s (light). The reconstruction uses ART2 and  $\lambda = 0.05$  with straight ray paths. The smearing in the result is similar to that seen in the real Stripa data.

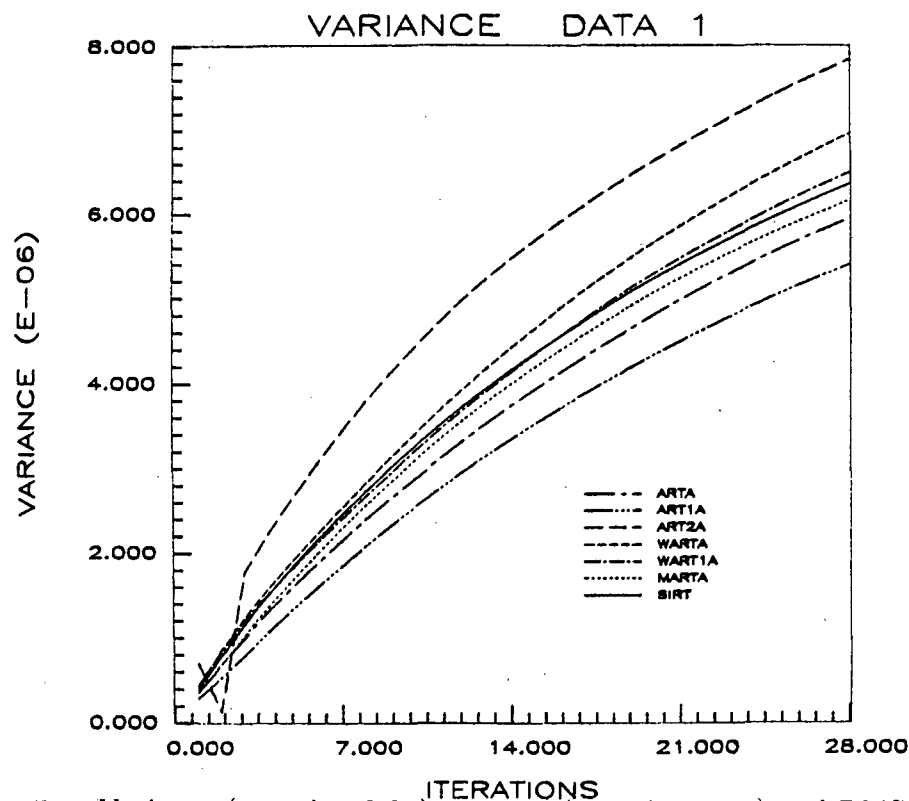
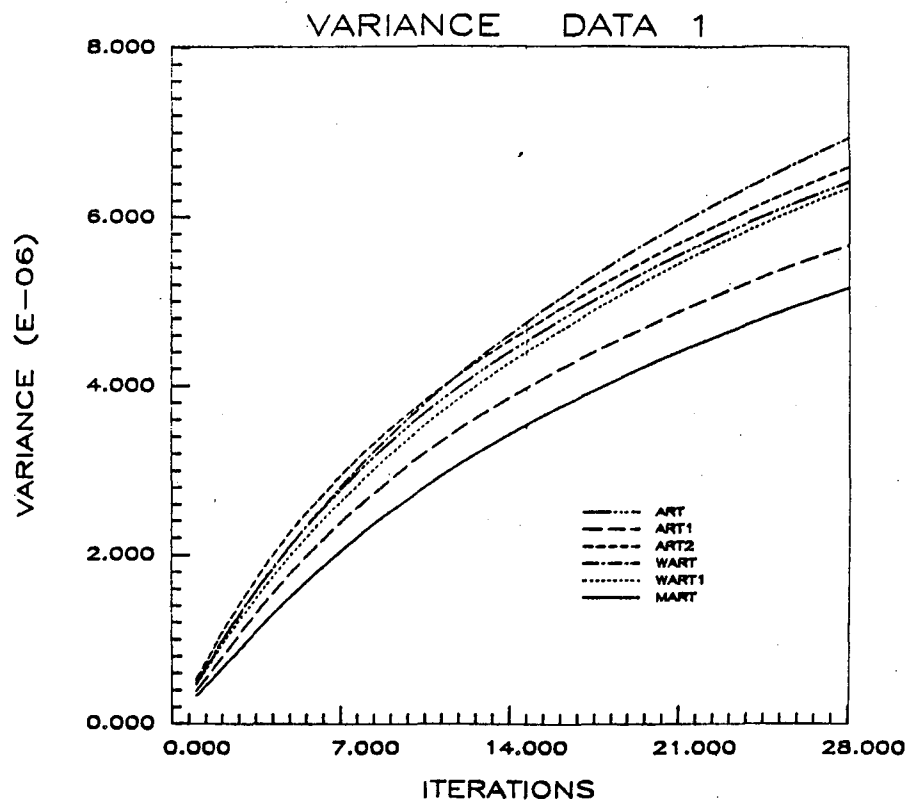


**Figure 5.4.** Variance (equation 2.21), entropy (equation 2.22) and RMS residual (equation 2.20) versus number of iterations for the algorithms of Figure 5.2 with Data set 1 and Data set 2. The curves are similar to those found in the synthetic models. The optimal iteration is taken at about iteration 10, just after the bend in the RMS residual plots.



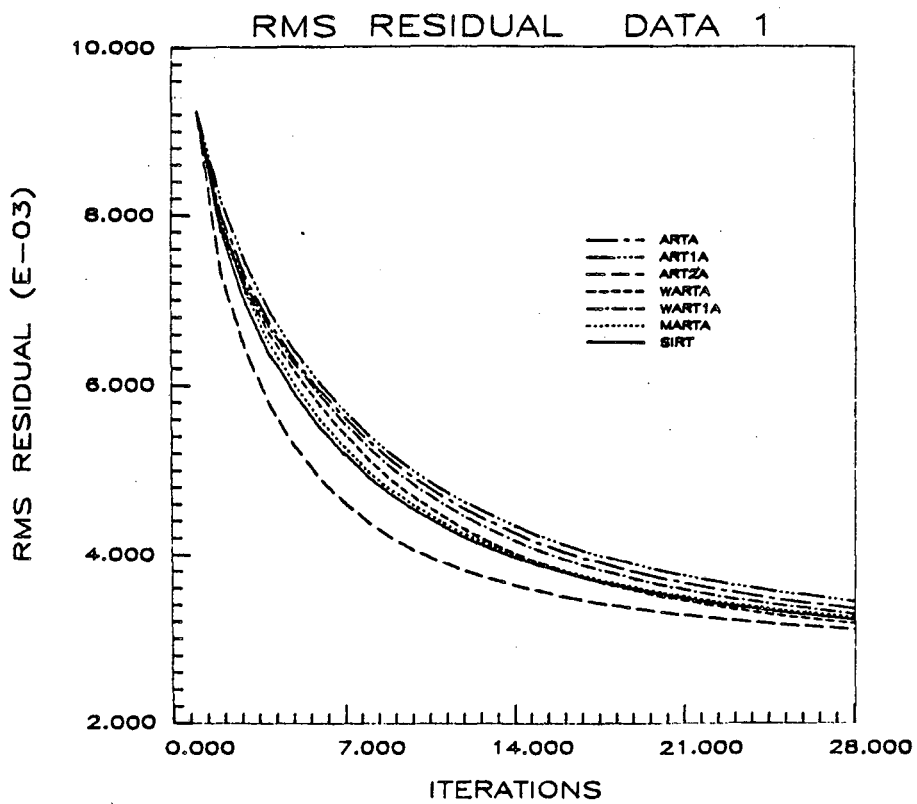
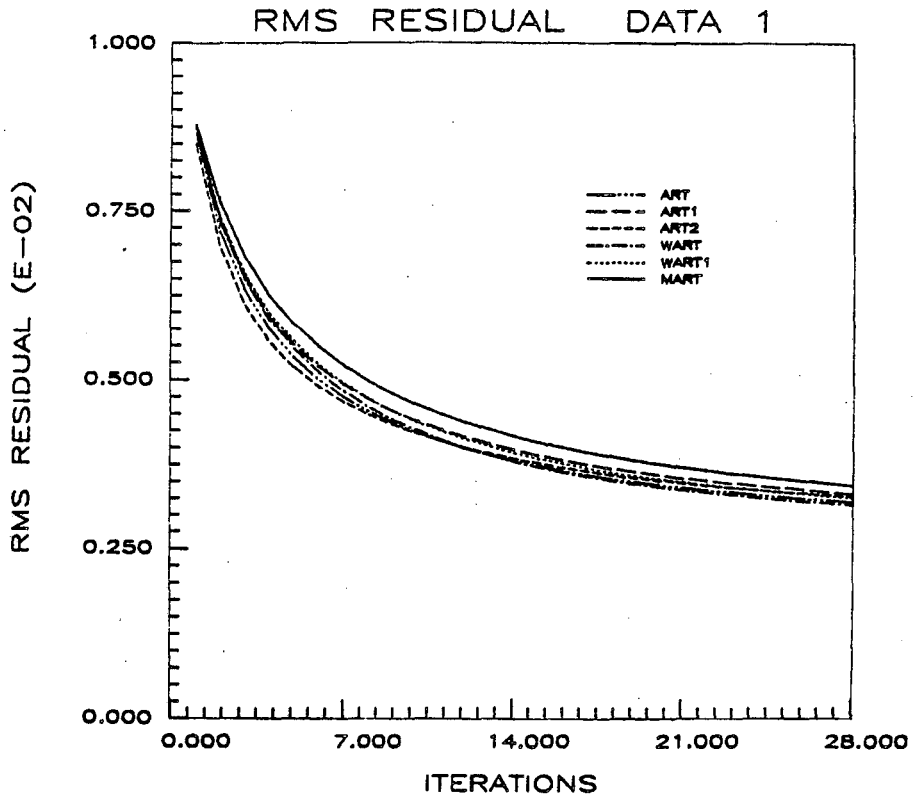


Figure 3.4 (continued).

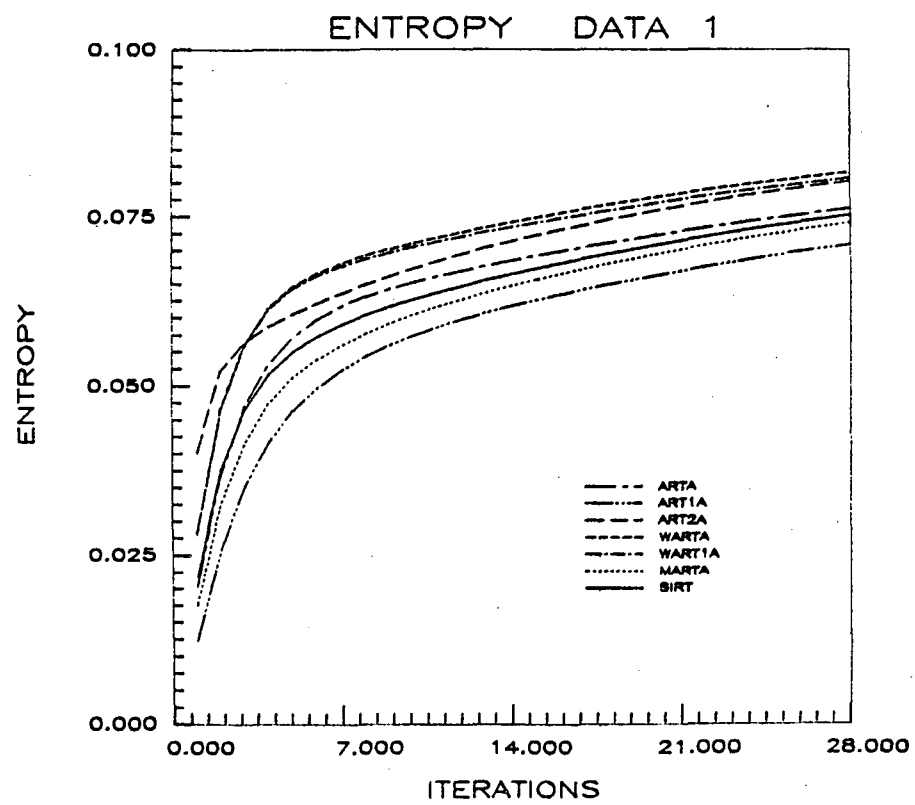
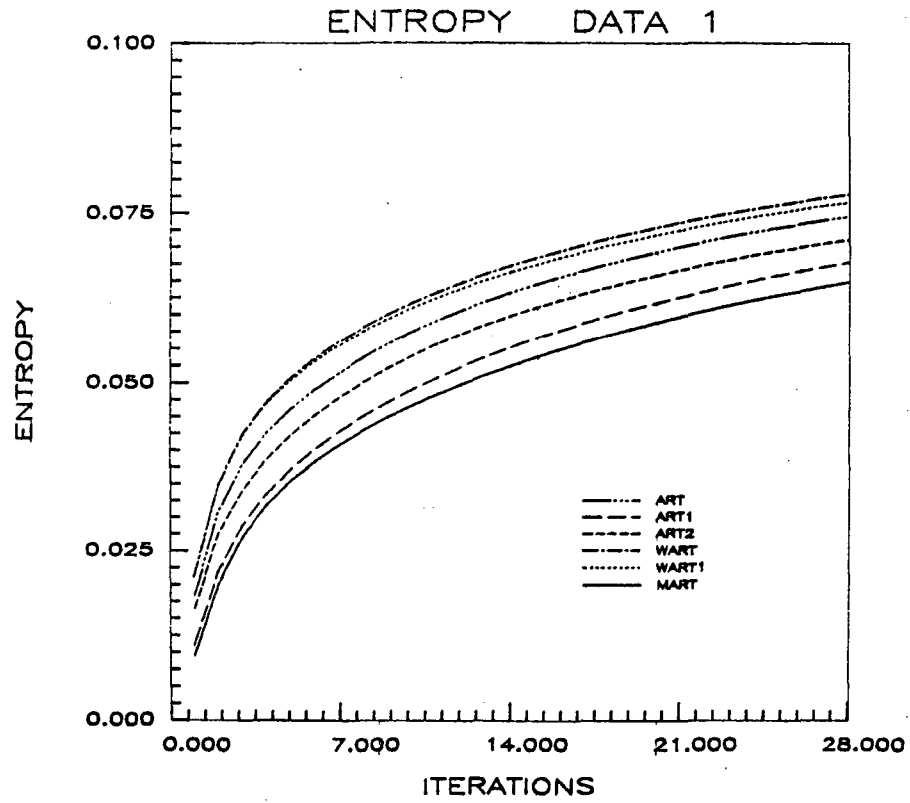


Figure 3.4 (continued).

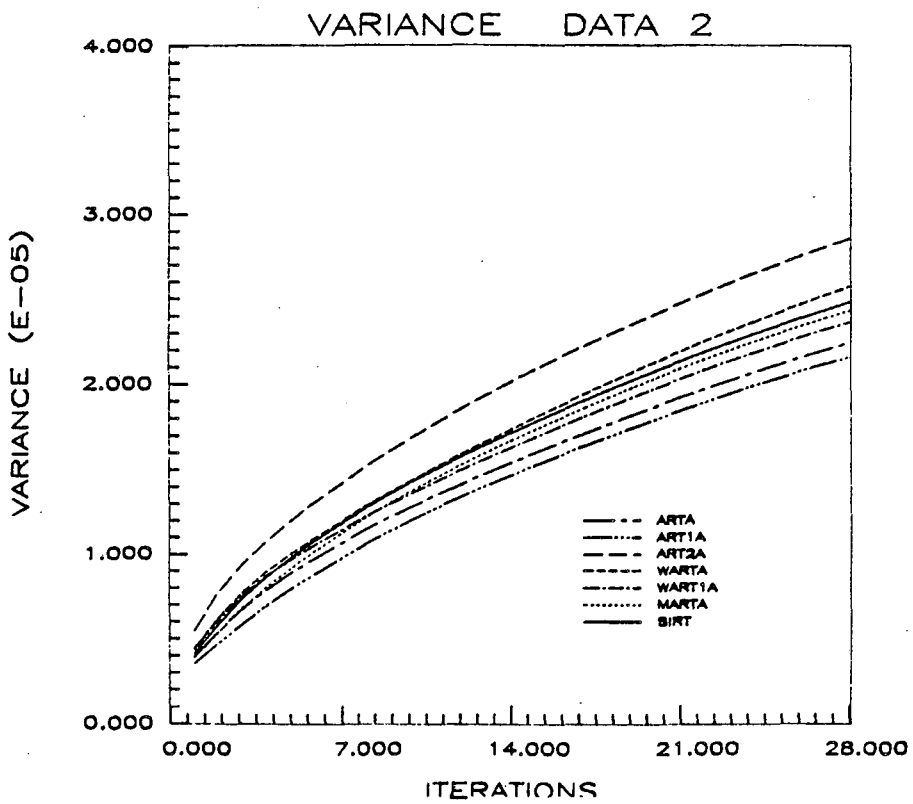
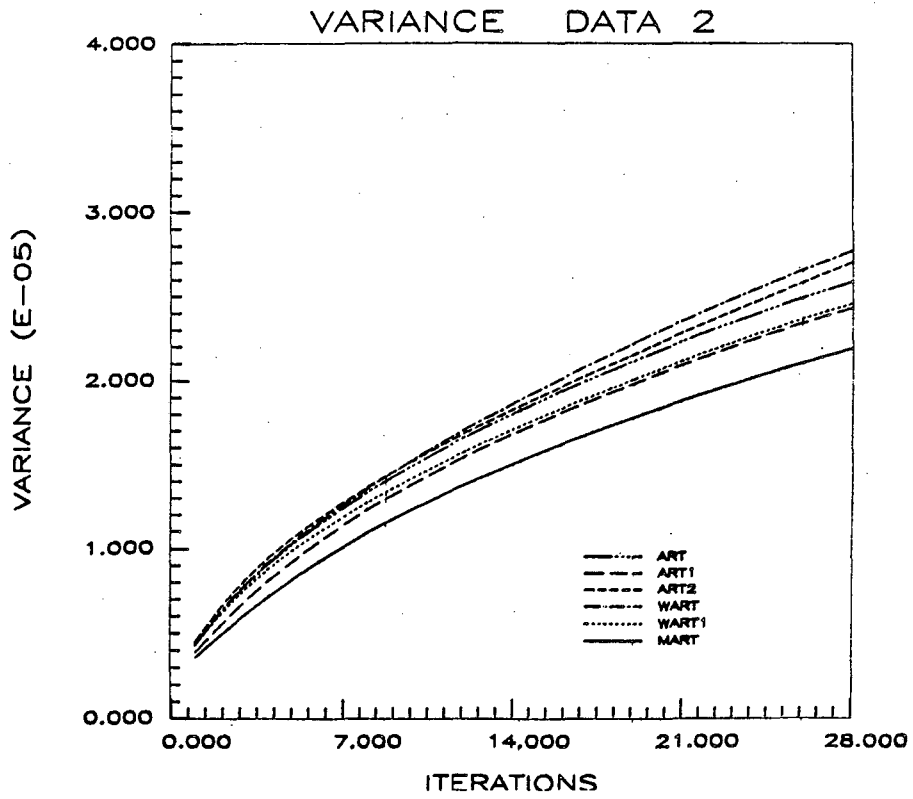


Figure 3.4 (continued).

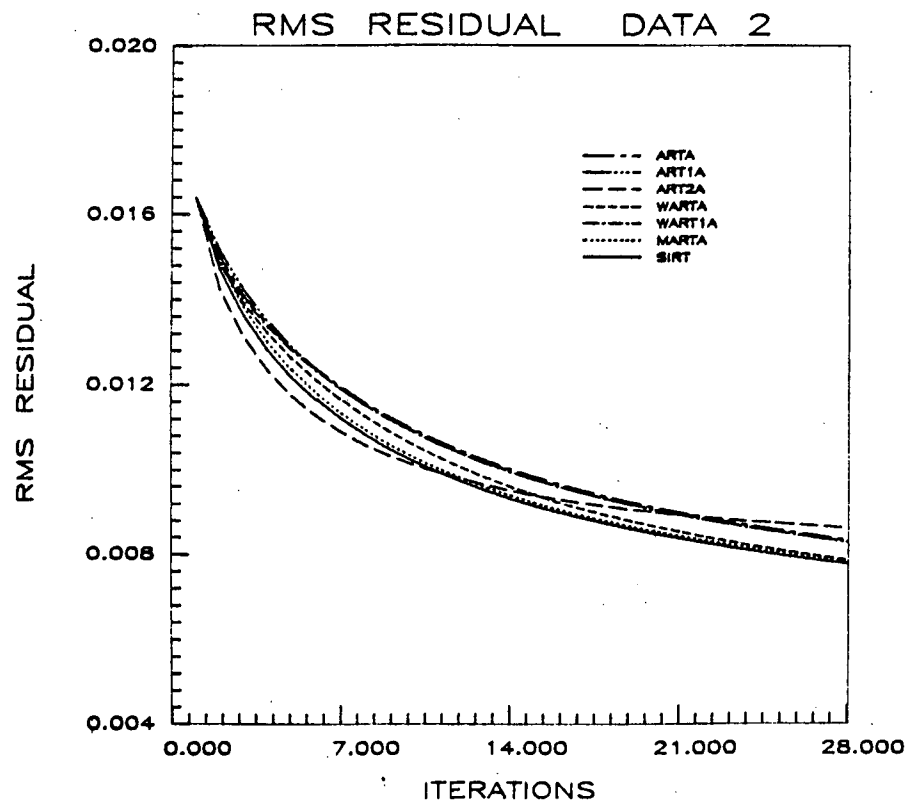
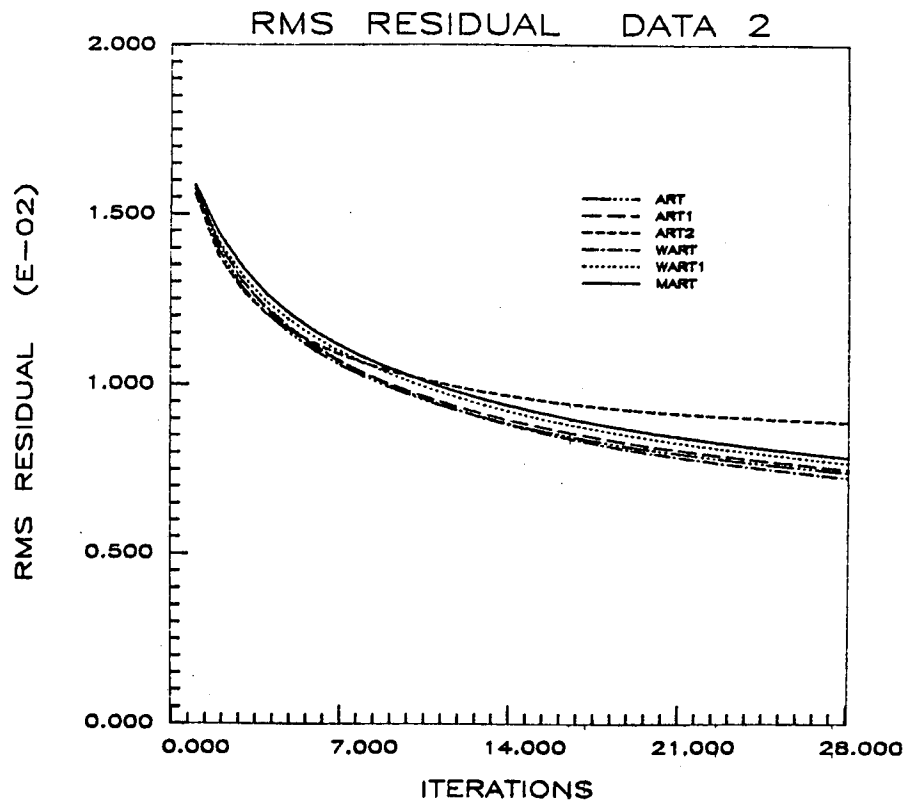


Figure 3.4 (continued).

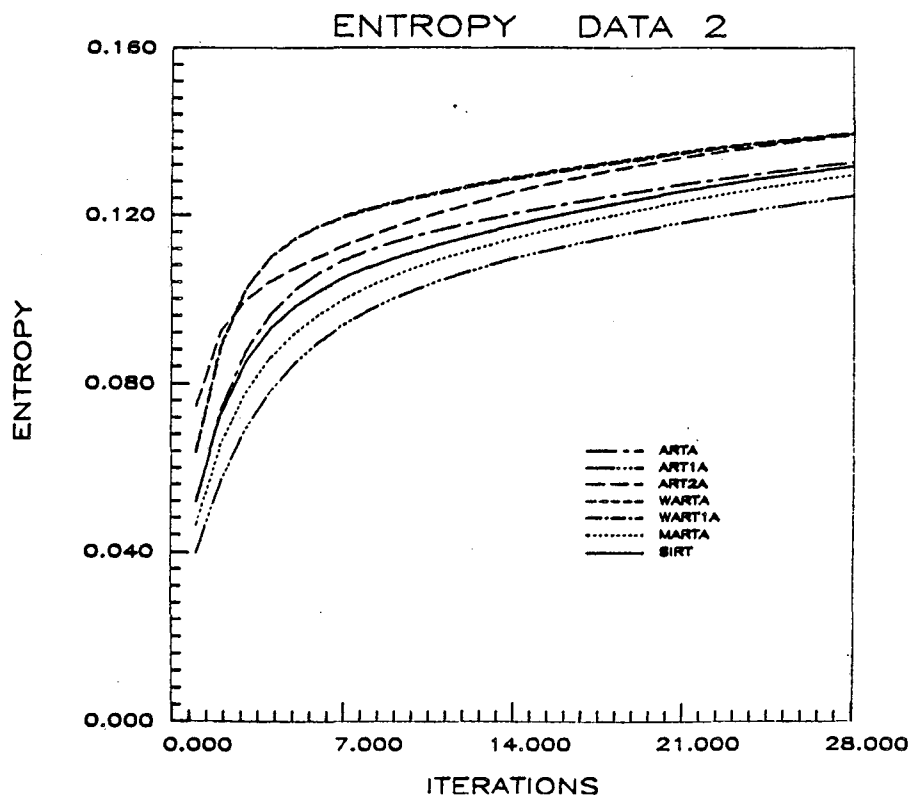
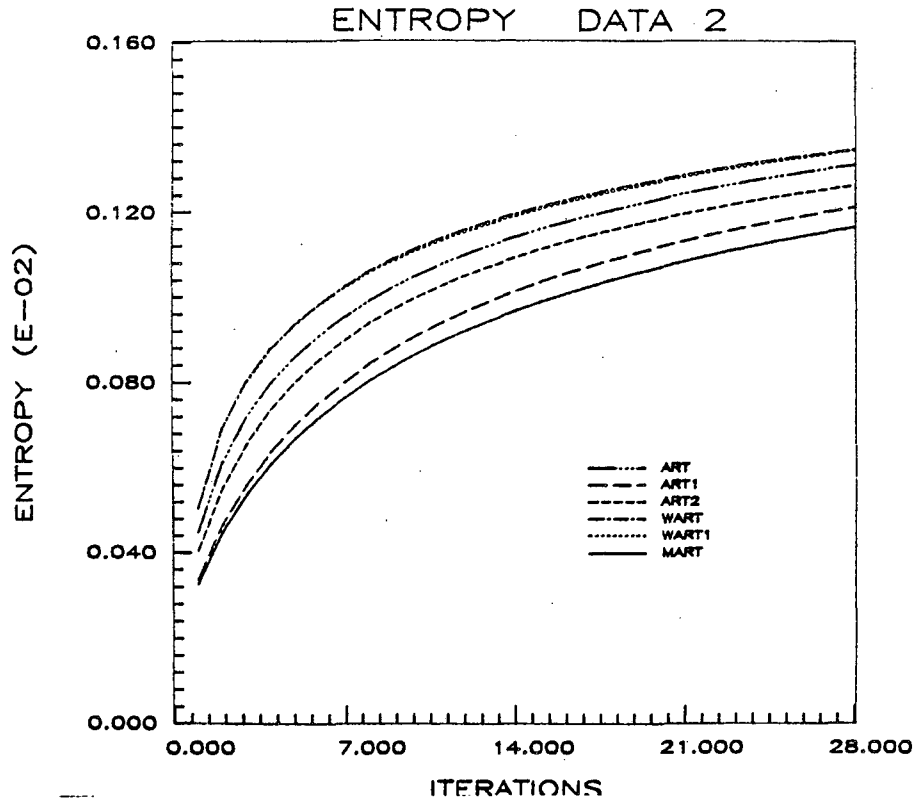


Figure 3.4 (continued).

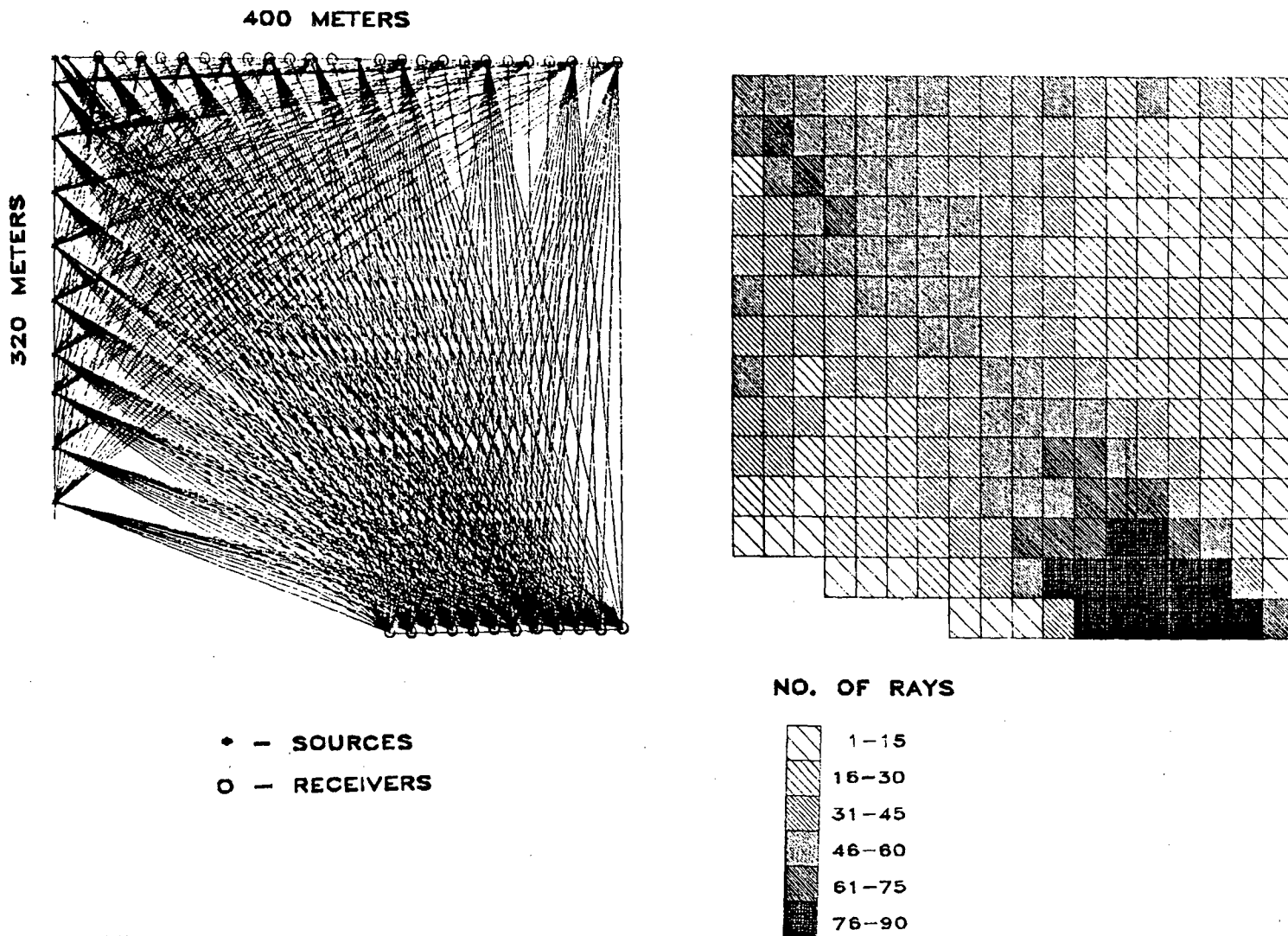
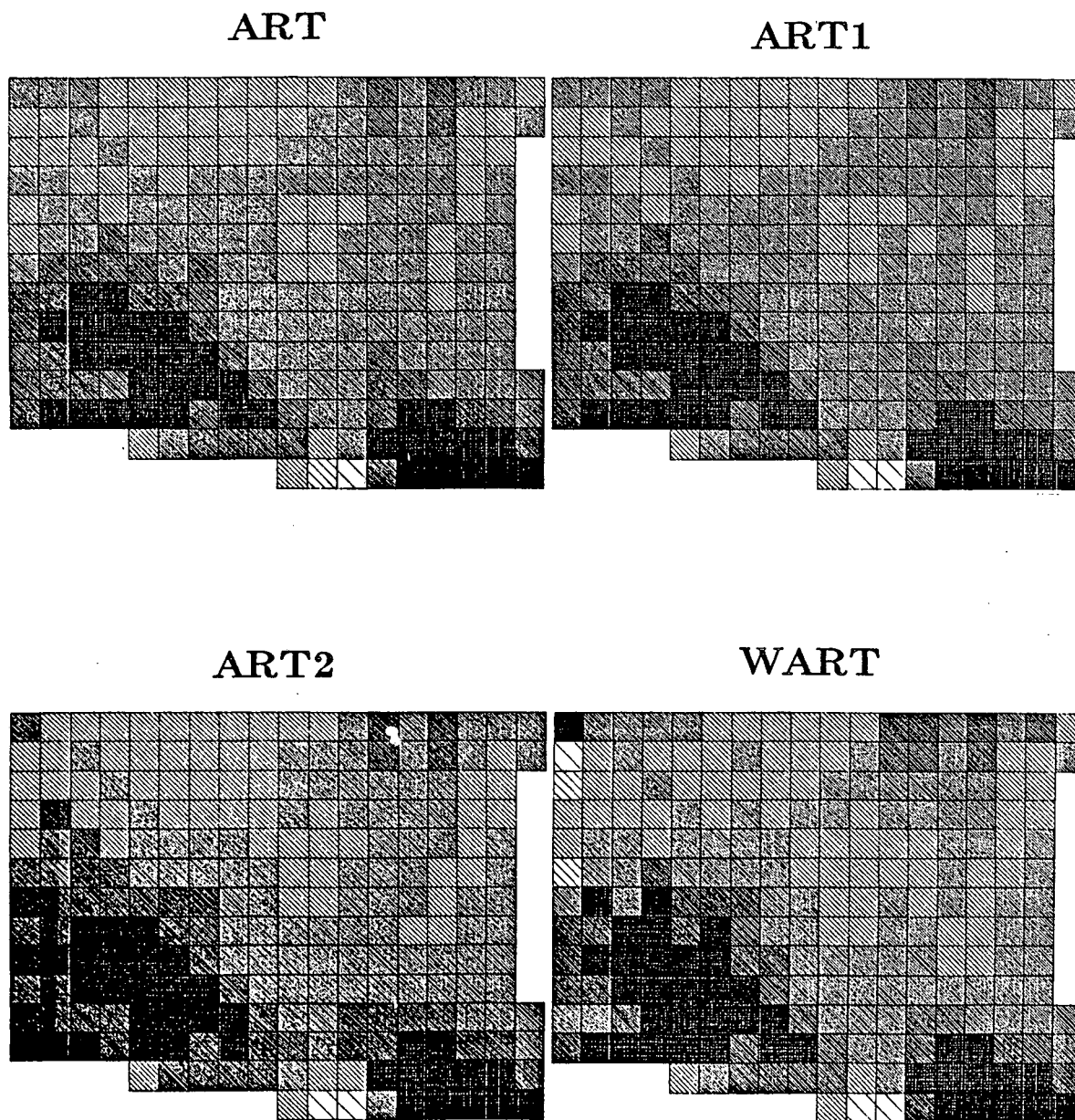
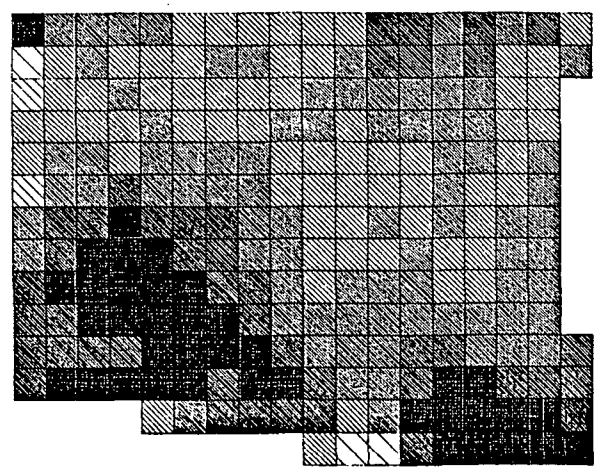


Figure 5.5. The raypaths for the Retsoff data showing arrays on the surface, in the borehole to the left and in the mine at the bottom and the ray density for each pixel. Darker rays are represent greater sampling. The sampling is dominated by paths from the mine to the upper left of the plot.



**Figure 5.6.** Compressional velocity field reconstructions for the Retsoff data using the geometry of Figure 5.5. The darker shades correspond to higher velocities with the velocities ranging from 3.0 km/s to 5.0 km/s. The reconstructions are dominated by a central V-shaped low-velocity region terminating at the collapsed portion of the mine.

### WART1



### MART

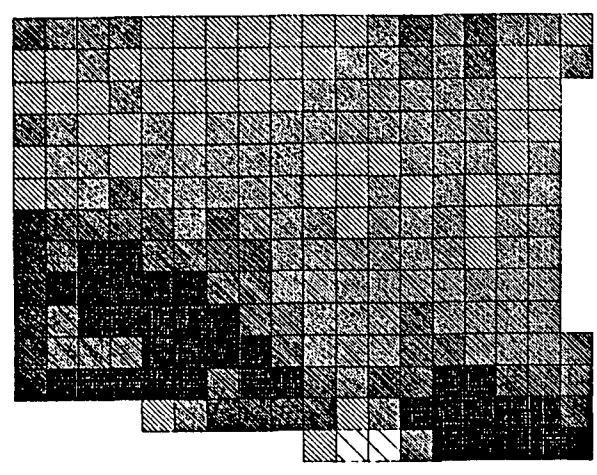
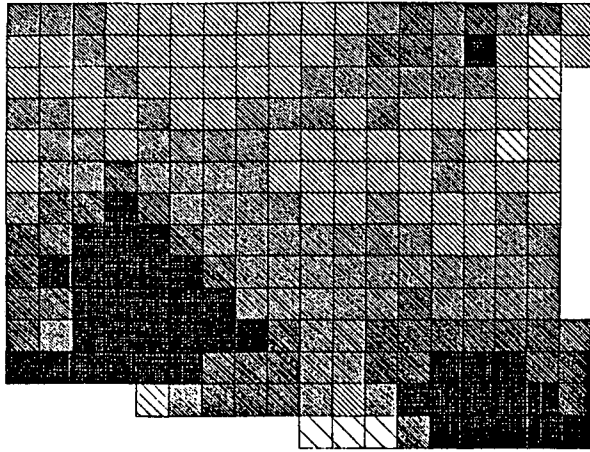


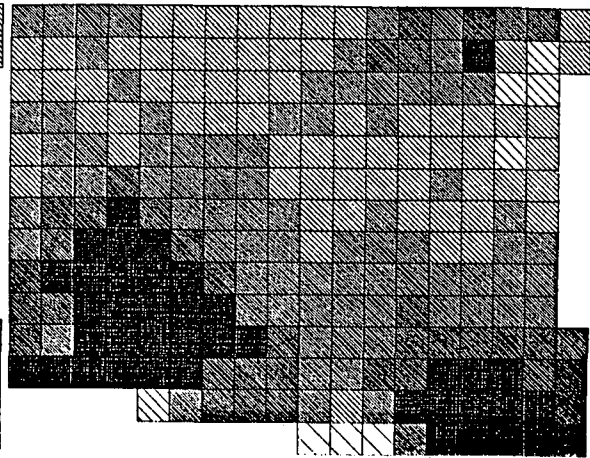
Figure 3.6 (continued).



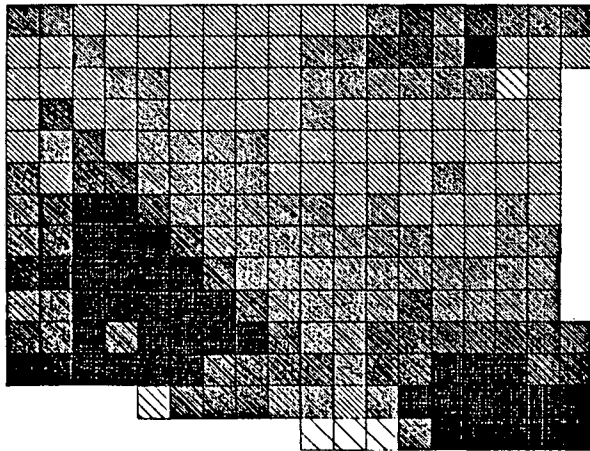
ARTA



ART1A



ART2A



WARTA

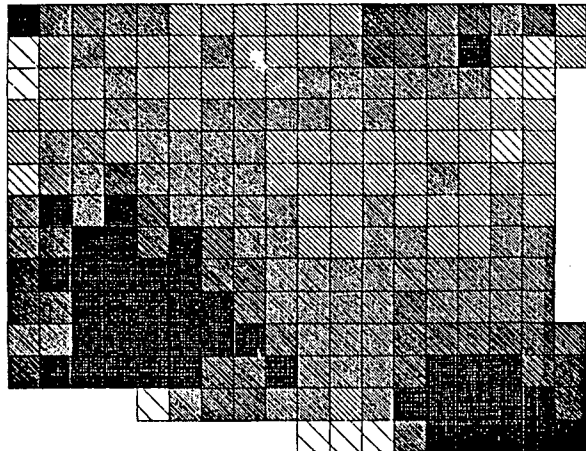
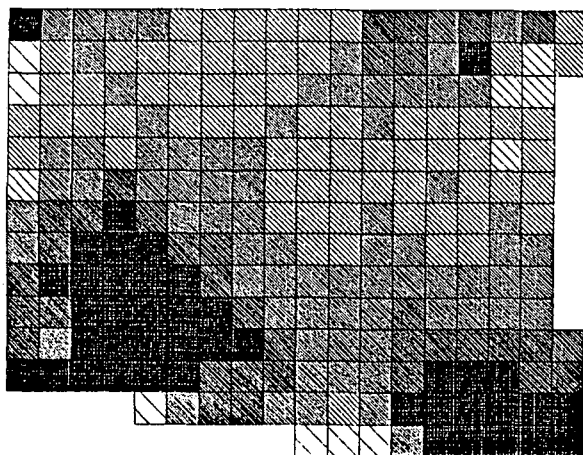
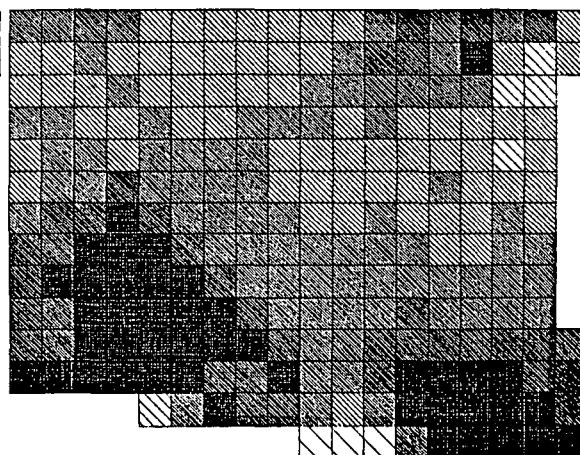


Figure 3.6 (continued).

WART1A



MARTA



SIRT

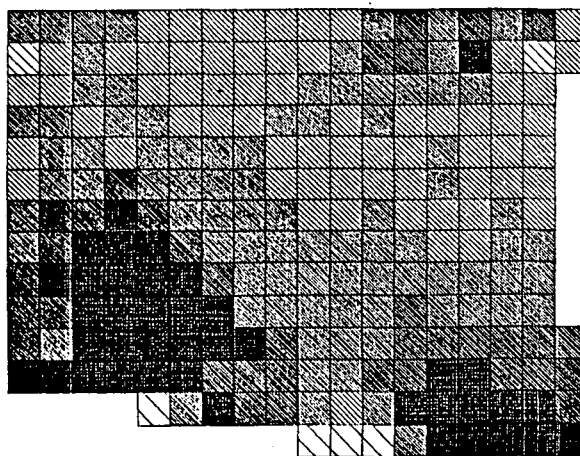
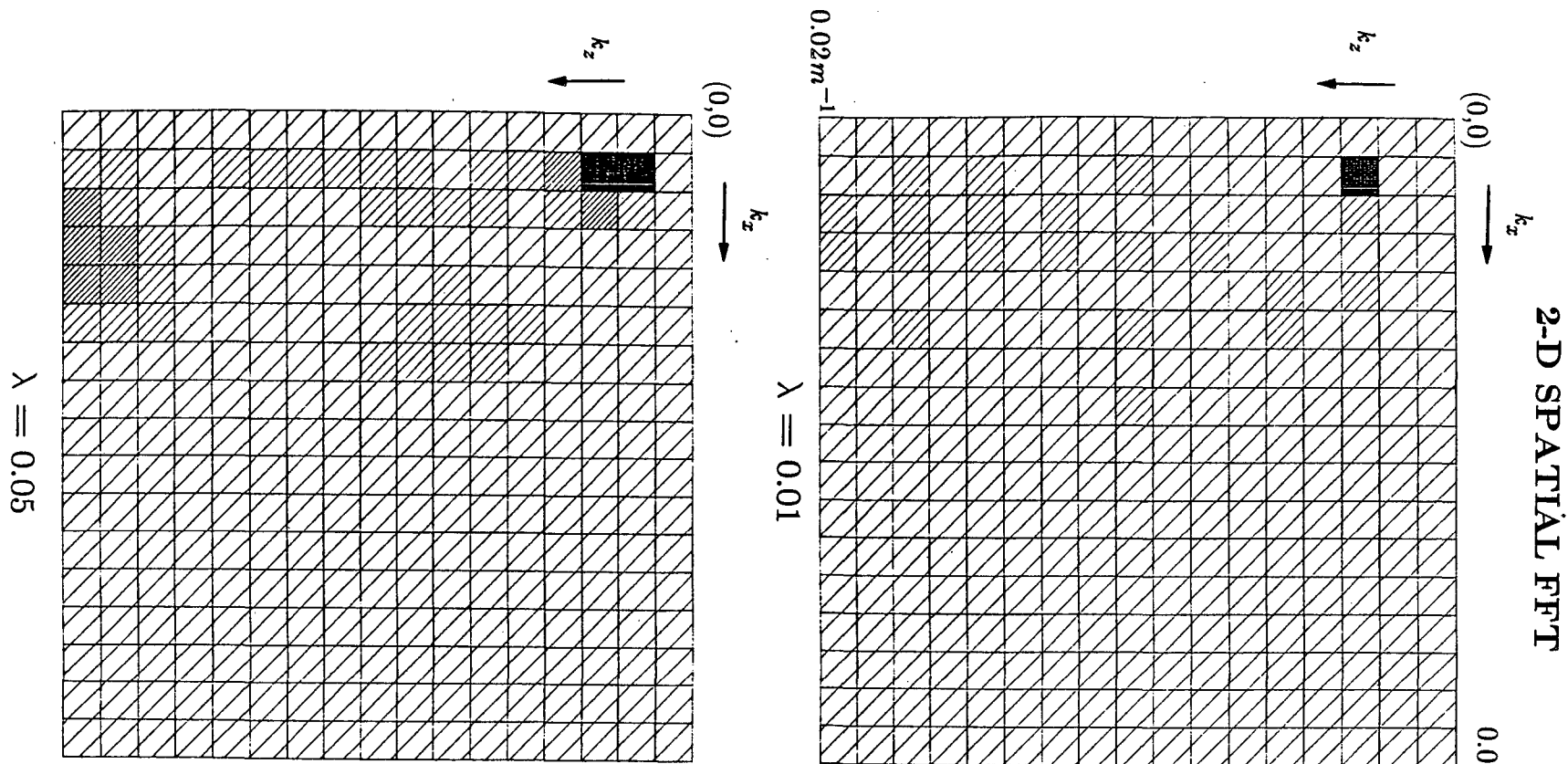


Figure 3.6 (continued).



**Figure 5.7.** Sample  $k$ - $k$  plots using ART2 in units of meters<sup>-1</sup>. The origin ( $k_x = k_z = 0.0$ ) is to the upper left with the horizontal wavenumber ( $k_x$ ) increasing to the right to a value of  $C^{-1} = 0.02m^{-1}$  and the vertical wavenumber ( $k_z$ ) increasing downward to the same value. The darker shades correspond to higher amplitudes showing that most of the energy is in the longer wavelengths and low-oscillating images will have small amplitudes at the higher ends of the spectra. In the upper figure  $\lambda = 0.01$  with the reconstruction given in Figure 5.6, and in the lower figure  $\lambda = 0.05$  with the reconstruction is given in Figure 5.9.

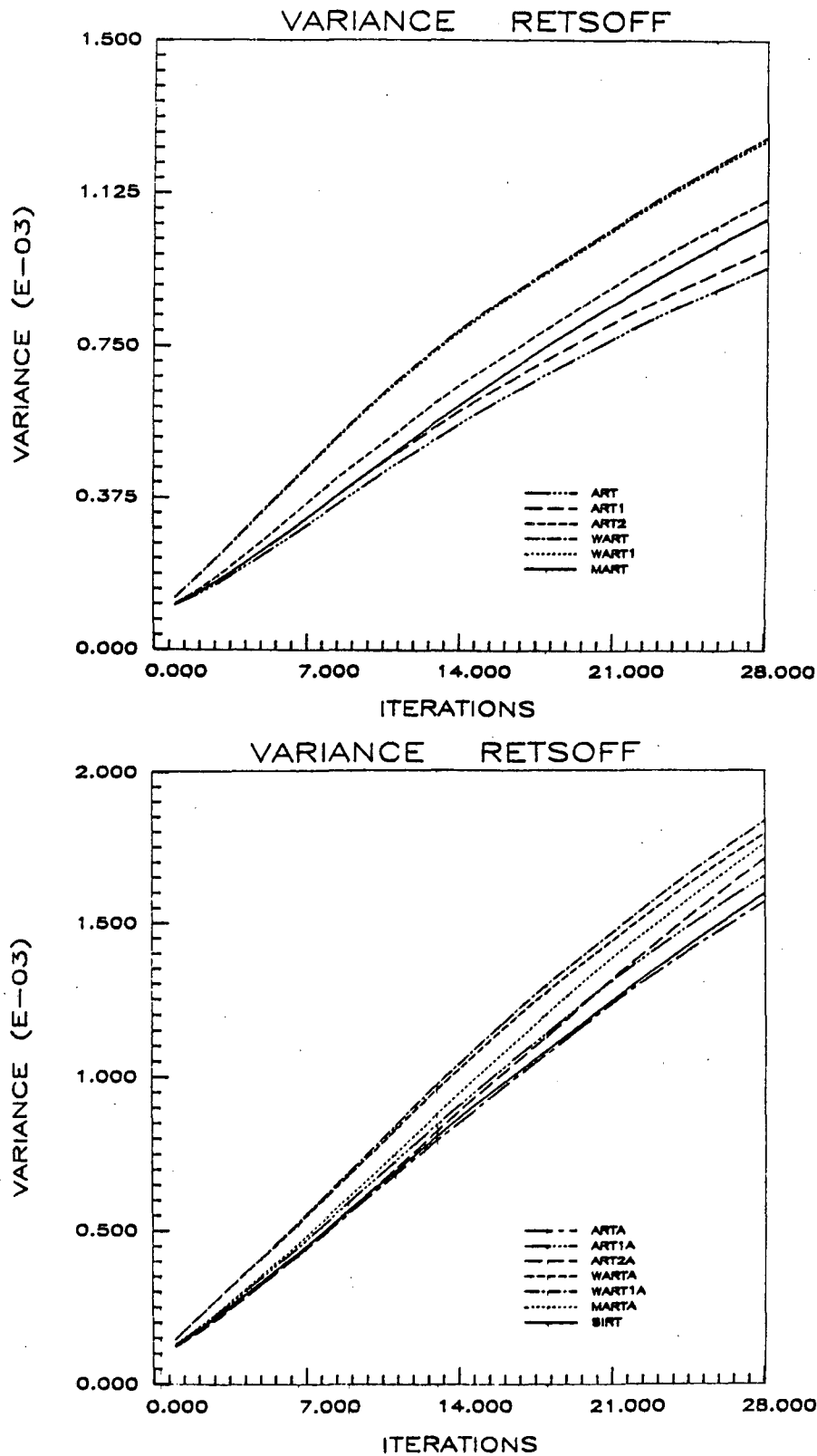


Figure 5.8. Variance (equation 2.21), entropy (equation 2.22) and RMS residuals (equation 2.20) versus iterations for algorithms shown in Figure 5.6. The curves are similar to those for the Stripa data and the synthetic data sets.

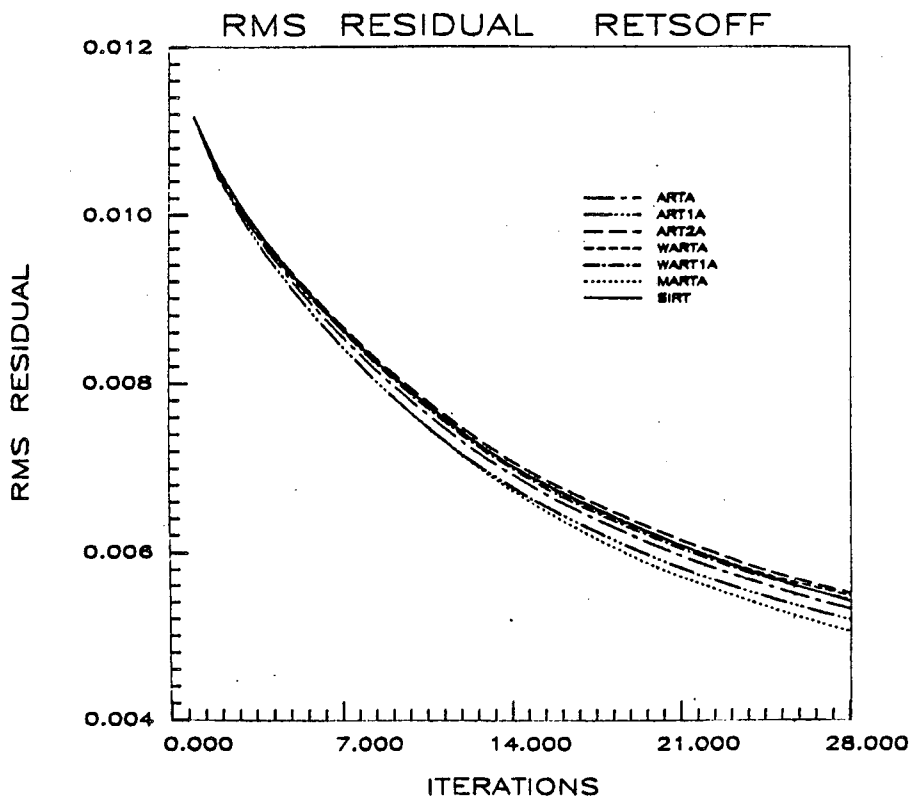
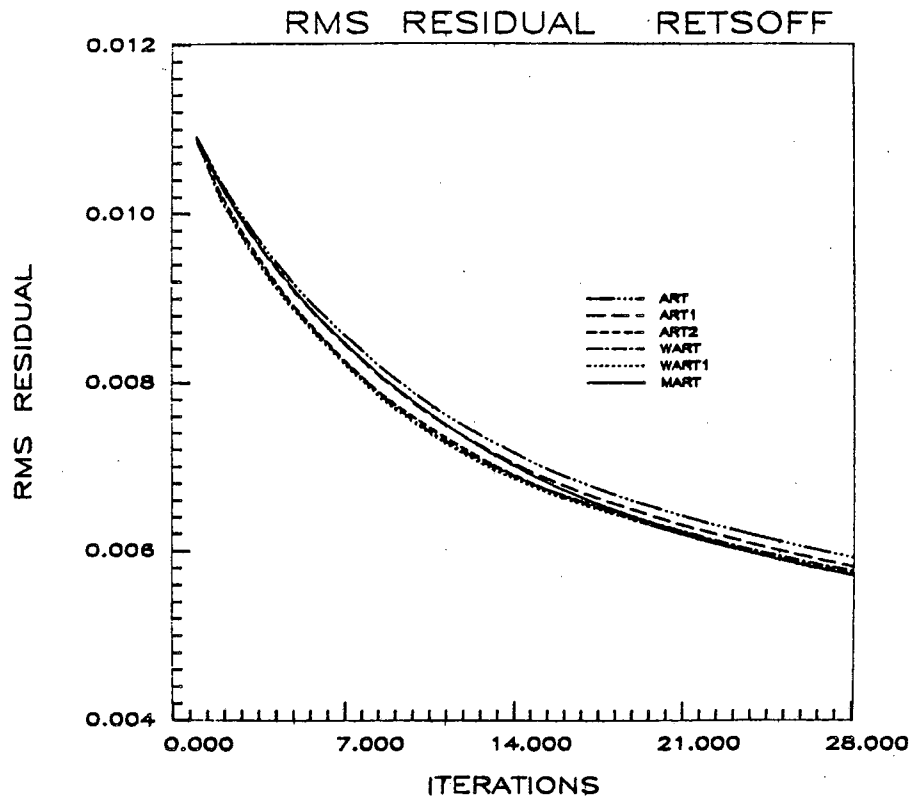


Figure 3.8 (continued).

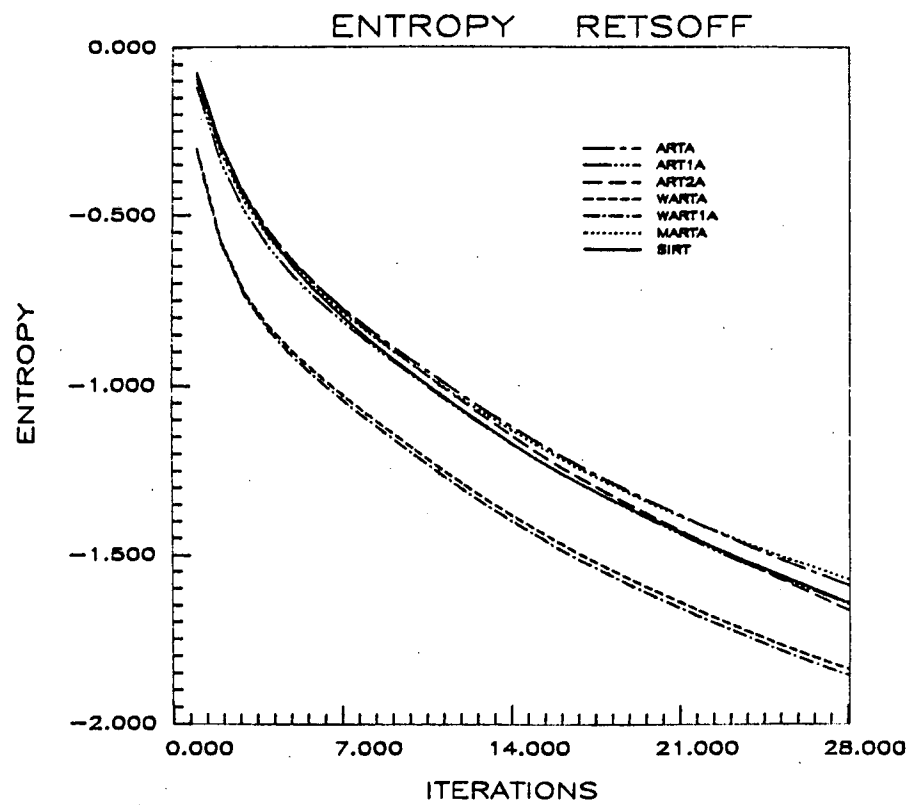
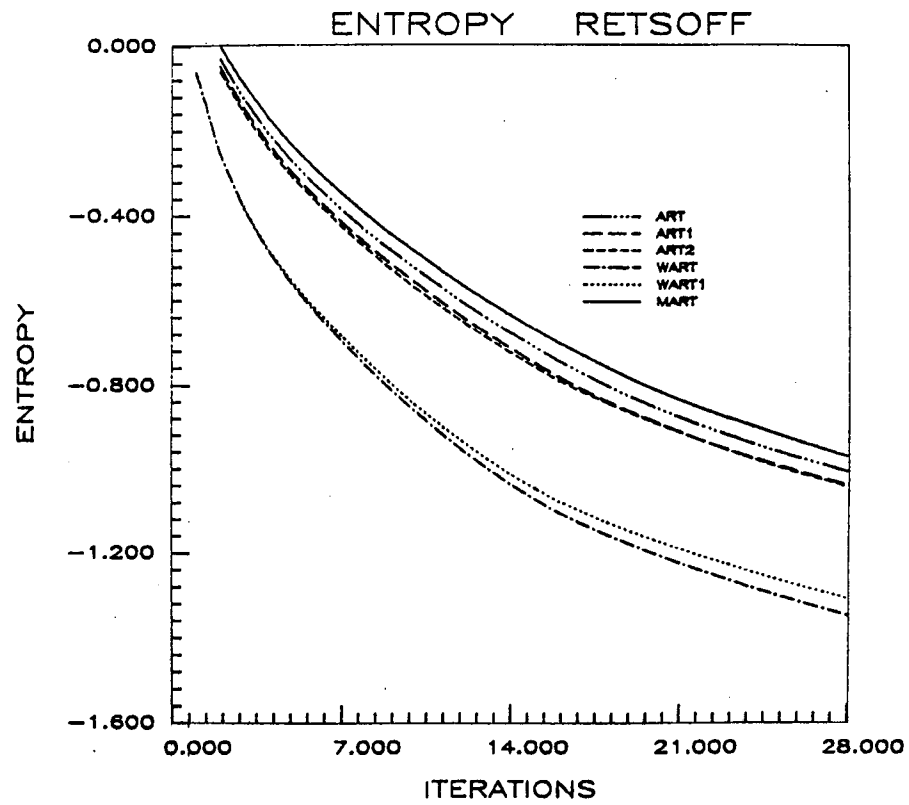
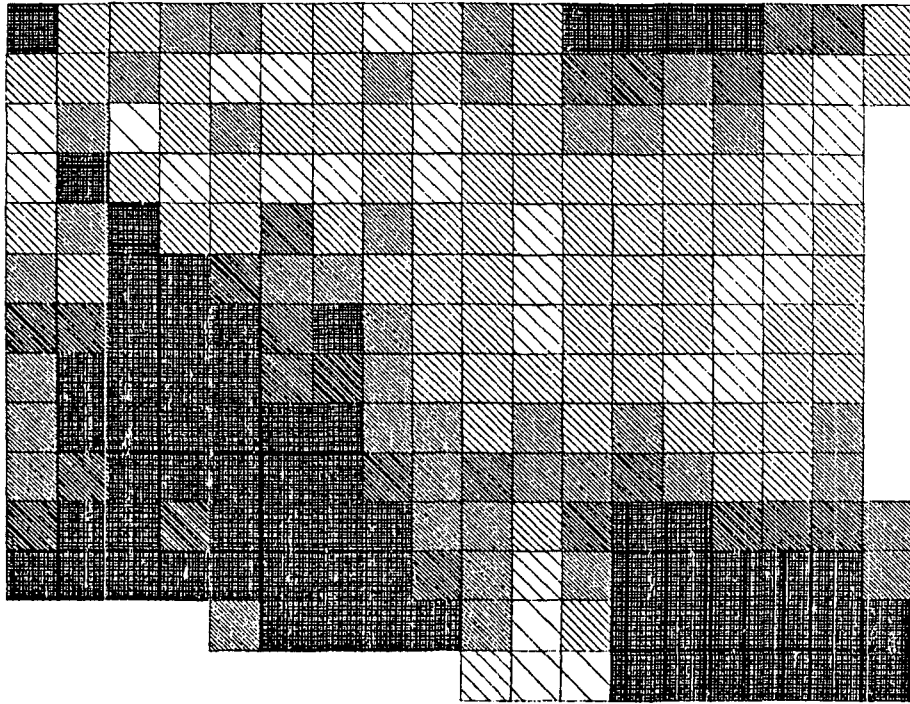
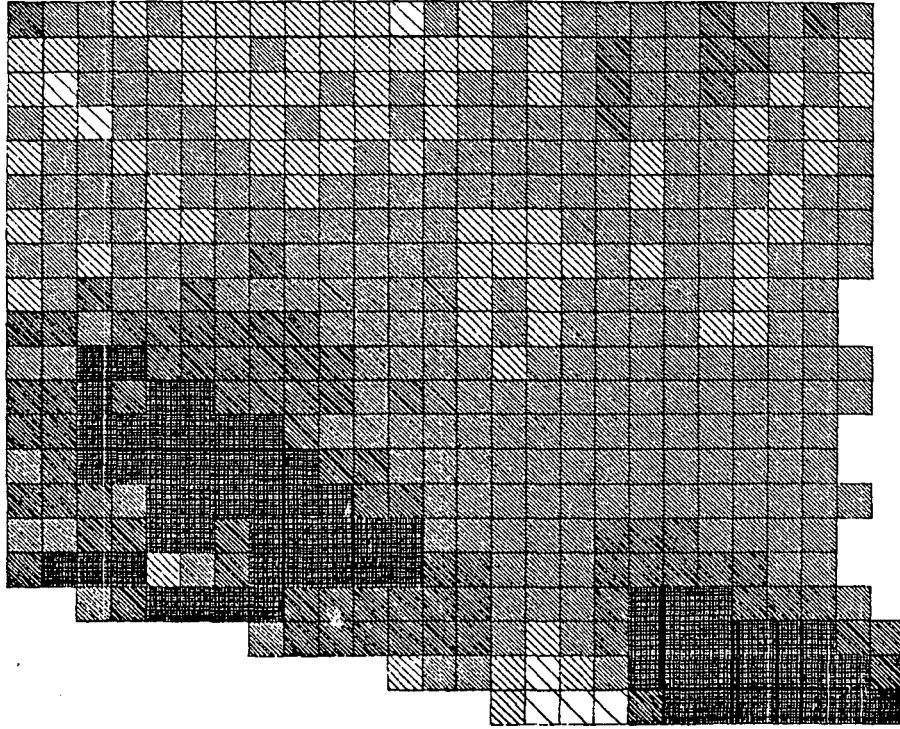


Figure 3.8 (continued).



18 X 14 PIXEL ARRAY

**Figure 5.9.** The ART2 reconstruction using an 18x14 array and  $\lambda = 0.05$ . The result is more oscillatory than the  $\lambda = 0.01$  reconstruction shown in Figure 5.6.



**26 X 21 PIXEL ARRAY**

**Figure 5.10.** The ART2 reconstruction of a 26x21 array of pixels. The result is smoother and show better definition of the gradient around the collapsed zone than the 18x14 array in Figure 5.6



## SMOOTHED ART2 RECONSTRUCTION

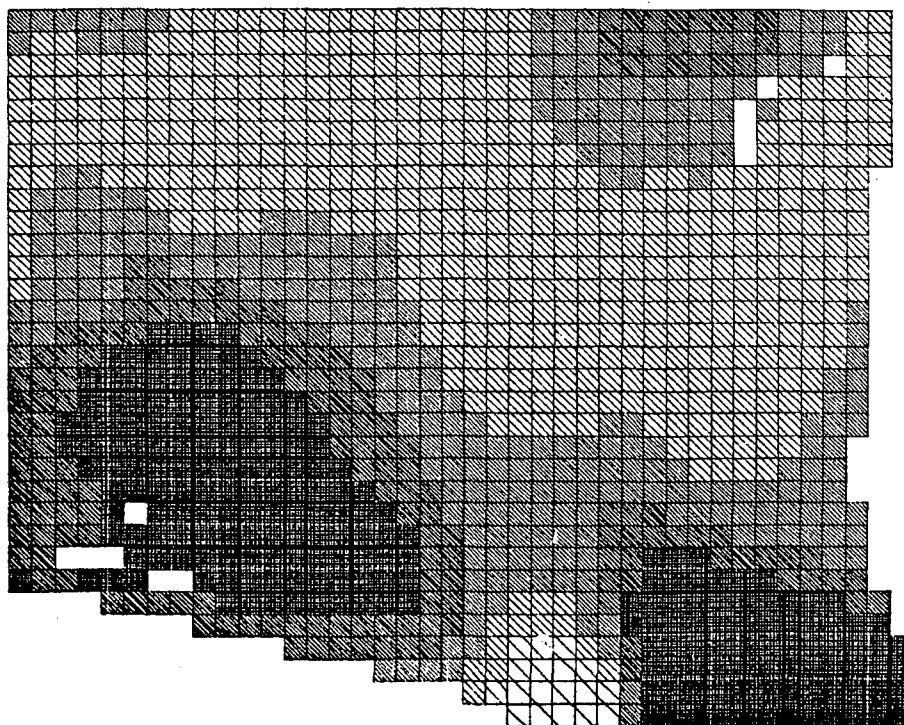


**Figure 5.11.** The pixel array can be increased to a 40x32 grid with the incorporation of smoothing in the ART2 algorithm. The reconstruction shows better definition than the 26x21 array shown in Figure 5.10.

## CHAPTER 6

### ART and the Least Squares Inversion

#### Introduction

In the development of the ART procedure (Chapter 2) the problem was shown to be described by a set of linear equations (equation 2.3). At this point it was determined that the resulting matrix would, in general, be very large and sparse and therefore difficult to invert. Now, ART will be formulated from this point in least squares terminology emphasizing the basis for ART in the least squares method. This formulation helps in identifying a resolution matrix for ART and facilitates a comparison with true least squares inversion.

For small problems the matrix in equation (2.3) can be inverted quite easily using singular-value decomposition (SVD) and the problem may be solved directly in this manner. For larger problems the inverse may still be calculated by using advanced machine-language programming procedures and much CPU time. This may be worthwhile if the direct least squares method produces better results than ART. Here, the two methods are compared using a simple velocity model and the Stripa and Retsof data. Typical ART reconstructions contain artifacts and it is assumed that the SVD inversions will be similar. A combination of the two methods is also attempted on the assumption that improvement to both methods may occur if the positive qualities of the reconstructions can be combined.

A general knowledge of generalized inverse theory will be assumed throughout this chapter. The matrix will be inverted using SVD, but the details of matrix

decomposition will not be discussed thoroughly.

### ART as a Generalized Inverse

In Chapter 2 it was shown that the line integral relating travel times to slownesses could be discretized and described by a set of linear equations

$$y_k = \sum_{i=1}^I \Delta a_{ki} x_i \quad k = 1, 2, \dots, N \quad (2.3)$$

where  $y_k$  are the travel times,  $x_i$  is the slowness of pixel  $i$ ,  $\Delta a_{ki}$  is the length of ray  $k$  which penetrates pixel  $i$ , and  $I$  is the total number of pixels. In matrix notation, this is written

$$\mathbf{y} = \mathbf{A}\mathbf{x}$$

where  $\mathbf{A}$  is an  $N \times I$  matrix with each ray a row of the matrix.

Therefore, ART may be thought of as a generalized inverse technique with the perturbations in travel time inverted for the perturbations in the slowness field. The slowness field is corrected with the addition of these values and the resulting travel time perturbations can again be inverted for new slowness corrections. This process may continue until some stopping criteria is met. For ART, equation (2.9) may be written as follows to invert for the slowness corrections:

$$x_i^{q+1} - x_i^q = \lambda_k \frac{\Delta a_{ki}}{\sum_{i=1}^I \Delta a_{ki}^2} \Delta y_k^q \quad k = 1, 2, \dots, N \quad (6.1)$$

In matrix form this is

$$\Delta \mathbf{x}^{q+1} = \mathbf{H} \Delta \mathbf{y}^q \quad (6.2)$$

where

$$\mathbf{H} = \lambda_k \frac{\Delta a_{ki}}{\sum_{i=1}^I \Delta a_{ki}^2} \quad (6.3)$$

is the generalized inverse matrix. Similar values of  $\mathbf{H}$  are determined from the other ART algorithms.

The purpose of relating ART to the generalized inverse in for the most part illustrative, but also has some practicality with the determination of  $\mathbf{H}$ . The knowledge of this matrix may be used to determine the resolution matrix

$$\mathbf{R} = \mathbf{H}\mathbf{A} \quad (6.4)$$

for each iteration of ART. The matrix  $\mathbf{A}$  as well as its generalized inverse  $\mathbf{H}$  have elements with units of distance. These elements will not change with each iteration, therefore  $\mathbf{R}$  will be constant for all iterations. The diagonal elements of the resolution matrix are the most important values of the matrix and are easily determined in this way.

### Inverting the Matrix Using Singular-Value Decomposition

The eigenvalue analysis used in SVD was originally developed by Lanczos (1961). The results of his work show that any  $m \times n$  matrix  $\mathbf{A}$  can be written

$$\mathbf{A} = \mathbf{U}\mathbf{\Lambda}\mathbf{V}^T \quad (6.5)$$

where  $\mathbf{U}$  is an  $n \times n$  rotation matrix with

$$\mathbf{U}^T\mathbf{U} = \mathbf{U}\mathbf{U}^T = \mathbf{I} \quad (6.6)$$

$\mathbf{V}$  is an  $m \times m$  rotation matrix with

$$\mathbf{V}^T\mathbf{V} = \mathbf{V}\mathbf{V}^T = \mathbf{I} \quad (6.7)$$

and  $\mathbf{\Lambda}$  is a  $n \times m$  matrix of eigenvalues that is zero except for nonnegative elements on the diagonal.  $\mathbf{\Lambda}$  will have at most  $\min(m, n)$  positive values. Equation 2.3 can now be written

$$\mathbf{y} = \mathbf{A}\mathbf{x} = \mathbf{U}\mathbf{\Lambda}\mathbf{V}^T\mathbf{x} \quad (6.8)$$

Using the above properties of  $\mathbf{U}$  and  $\mathbf{V}$  the generalized inverse becomes

$$\mathbf{x} = \mathbf{V}\mathbf{A}^{-1}\mathbf{U}^T\mathbf{y} = \mathbf{H}\mathbf{y} \quad (6.9)$$

with the covariance matrix

$$\mathbf{C} = \sigma_0^2\mathbf{H}\mathbf{H}^T = \sigma_0^2\mathbf{V}\mathbf{A}^{-2}\mathbf{V}^T \quad (6.10)$$

The resolution matrix becomes

$$\mathbf{R} = \mathbf{H}\mathbf{A} = \mathbf{V}\mathbf{V}^T \quad (6.11)$$

The calculation of the generalized inverse  $\mathbf{H}$  is done by the routine LSVDF of the IMSL library. The routine inputs the matrix  $\mathbf{A}$  and outputs the matrices  $\mathbf{V}$  and  $\mathbf{U}^T$  as well as a vector containing the ordered singular values of  $\mathbf{A}$ . From this output the solution vector, the covariance matrix and the resolution matrix may then be easily determined.

The inversion is initially performed on a synthetic data set derived from the velocity model shown in Figure 6.1. The dimensions of the model simulate the geometry of the Stripa experiment with a simple low velocity zone of 5.5 km/s encompassed by a background velocity of 6.0 km/s. Travel times are generated by the raytracing method described in Chapter 3. The image resulting from the SVD inversion shows the near perfect reconstruction of the original model (Figure 6.2), while the image produced by ART gives an averaged value of the low velocity zones with loose bounds. The value of the low velocity zone in the ART inversion is a bit higher than the model and the background velocities vary to about 0.1 km/s, the latter being negligible in the shading scheme. The SVD inversion can be improved through the elimination of some small eigenvalues. While this is not necessary in the present case it is of interest to show the results, since this technique will be used later. The eigenvalues range from about 0 to 8. Figure 6.3 shows the results of eliminating eigenvalues less than 0.1, 0.3, 0.5, and 0.7. In this case the reconstructions become progressively worse as more

eigenvalues are eliminated.

The present study would seem to indicate that the SVD inversion gives results far superior to any ART reconstruction and warrants the added expense for the calculations. Unfortunately, the inversion is not very stable. A very small amount of random Gaussian noise (1% of the total travel time) is added to the travel time data as was done in Chapter 3. Even this small amount of noise causes a great deal of oscillation of velocity values in the SVD reconstruction (Figure 6.4), while the effect is very small on the ART reconstruction. The SVD image can be improved by the elimination of eigenvalues (Figure 6.5), but the final result remains quite unsatisfactory. The SVD inversion does give near perfect reconstructions for near perfect data, but the instability shown by this addition of 1% noise diminishes its effectiveness for use in realistic situations.

The resolution matrix for both techniques is calculated for this test data; the ART matrix calculated using equations 6.3 and 6.4. The diagonals of the matrix show the resolvability of each pixel and are printed out in shaded form (Figure 6.6), The darker pixels corresponding to higher values. The resulting values are similar and seem reasonable. The values for ART reveal a pattern similar to that found by the ray density map (see Figure 5.1). They show greater resolvability toward the center where there is high ray density and low values at the top and bottom where only a few rays sample. The values are similar for the SVD inversion, but show greater resolution along the boreholes. The resolution matrix for the Retsof data is calculated by both methods for completeness (Figure 6.7). The two plots have greater differences than for the Stripa geometry due to the complexities of the Retsof data, but the general features are consistent. The resolution matrices for both data sets show low resolvability in areas corresponding to high velocity oscillation and other features that indicate instabilities. This is important in that these matrices can be used to give the resolution of a given experiment before the data is even collected. The resolution matrix

calculated from the SVD inversion is the most accurate, because it uses the true generalized inverse matrix  $\mathbf{H}$  and should be used when possible; the ART-derived matrix is a good estimate.

Despite the stability problems the Stripa data set will be inverted using SVD. The procedure and geometry is the same as for the test model above. The Stripa data set is fairly clean, but the noise is still about 1% of the travel time, suggesting rather unsatisfactory results. This is borne out in the reconstructions (Figures 6.8, 6.9 and 6.10). The reconstruction of Stripa Data Set 1 (Figure 6.8) shows substantial zones of low velocity and high oscillatory behavior of the velocities. The picture improves as the lower eigenvalues are removed, but the reconstruction remains poor. There is always some amount of doubt to the accuracy of any reconstructions when the true velocity field is unknown, but knowledge from previous trials can be used to determine the reliability of images.

Comparisons of the best SVD inversions with the ART reconstructions show substantial differences. The best SVD inversions, those with eigenvalues below 0.3 eliminated, are plotted with the ART reconstructions in Figure 6.11. For Stripa Data Set 1 the SVD inversion produces a fairly smooth image with a slight low velocity zone toward the upper center near the heater location. This would be a reasonable result by itself, but there are anomalous zones to the lower right and upper left corners of the reconstruction. The same anomalies occur for Data Set 2 suggesting that they may be artifacts of the geometry. Despite these unrealistic anomalous zones, the Data Set 2 reconstruction shows many of the same characteristics found in the ART image, the low velocity zone near the heater location and the smearing from there to the lower left corner. However, the highly oscillatory values, the unrealistic velocity anomalies, and the results of the synthetic analysis signify the unreliability of the SVD inversions.

The results of this analysis show that the ART reconstructions are superior to the SVD inversions, at least for this data. The SVD inversions do have some

advantageous characteristics, the most important being the lack of smearing. It would therefore be productive to combine the two methods in some way to get the advantages from both techniques. The best way may be to use the reconstruction from one method as *a priori* information for the other.

### **The Use of A priori Information in ART and SVD Inversions**

*A priori* information can easily be incorporated into both the ART and SVD inversion methods. For ART, the *a priori* information is simply contained in the starting model. Normally, a starting model is generated automatically in the program by a simple back-projection of the travel times (equation 2.6). This usually gives a smooth field and the corrections are applied to this model. If a general velocity field is already known, it can be substituted as the starting model and the corrections applied to it. Therefore, an initial model can be generated by an SVD inversion and then corrected by ART.

It may be desired to reverse this process and generate an initial model using ART and then use this as *a priori* information to an SVD inversion. One way to do this is to use the initial model to produce travel time residuals and invert the residuals as perturbations of this model. This is a very practical method, but one which does not let the contribution of the prior data be altered.

Unfortunately, these methods will not work in the strict sense. The slownesses produced by the ART, or SVD, inversion will give minimum travel time residuals  $\delta t$ . The result is already at a local minimum so that any correction based on  $\delta t$  will be negligible. Therefore, the only way this process will work is if an averaged model based on the SVD, or ART, result is used as the prior data. In this way, a substantial correction term can be produced and the solution will be a small perturbation upon this model.



There is a method of using an averaged ART model as *a priori* data for SVD which allows one to alter the contribution of the prior data. It requires a re-derivation of the inversion method. Beginning with equation (6.8),

$$\mathbf{y} = \mathbf{Ax} = \mathbf{U}\mathbf{\Lambda}\mathbf{V}^T\mathbf{x}$$

premultiply by  $\mathbf{U}^T$  and use the orthogonality of  $\mathbf{U}$

$$\begin{aligned}\mathbf{U}^T\mathbf{y} &= \mathbf{U}^T\mathbf{U}\mathbf{\Lambda}\mathbf{V}^T\mathbf{x} \\ &= \mathbf{\Lambda}\mathbf{V}^T\mathbf{x}\end{aligned}\tag{6.12}$$

Now make the substitutions

$$\mathbf{y}' = \mathbf{U}^T\mathbf{y}\tag{6.13}$$

$$\mathbf{x}' = \mathbf{V}^T\mathbf{x}\tag{6.14}$$

The primed quantities are the projections of the unprimed vectors onto the eigenvectors of  $\mathbf{U}$  and  $\mathbf{V}$  respectively. The transformations are uniquely invertible because  $\mathbf{U}$  and  $\mathbf{V}$  are orthonormal. The result is

$$\mathbf{y}' = \mathbf{\Lambda}\mathbf{x}'\tag{6.15}$$

This looks much like the original problem with matrix  $\mathbf{A}$  replaced by the quasi-diagonal eigenvalue matrix  $\mathbf{\Lambda}$  which can be easily inverted

$$\mathbf{x}' = \mathbf{\Lambda}^{-1}\mathbf{y}'\tag{6.16}$$

Previously, the equation was returned to the unprimed system (equation (6.9)) at this point. Now the solution will be written to incorporate *a priori* data as follows:

$$\mathbf{x}' = \mathbf{M}\mathbf{y}' + \mathbf{N}\mathbf{x}'_0\tag{6.17}$$

where  $\mathbf{x}'_0$  contains the prior information in the form of an initial guess. The new matrices  $\mathbf{M}$  and  $\mathbf{N}$  are quasi-dimensional eigenvalue matrices dependent on the solution method. These matrices are used to determine the contribution of the prior data to the solution. One method is to set the values

$$\mu_i = \frac{\lambda_i}{\lambda_i^2 + \lambda_0^2} \quad (6.18)$$

$$\nu_i = \frac{\lambda_0^2}{\lambda_i^2 + \lambda_0^2} \quad (6.19)$$

where  $\mu_i$ ,  $\nu_i$  and  $\lambda_i$  are the elements of  $\mathbf{M}$ ,  $\mathbf{N}$  and  $\mathbf{\Lambda}$  respectively and  $\lambda_0$  is the eigenvalue cutoff criterion. The idea of these values is if the prior data is noisy or unreliable  $\lambda_0$  can be made very small. Conversely, if the *a priori* information is strong and only slight adjustments to this model are needed, then  $\lambda_0$  can be made large. Therefore, the eigenvalue cutoff  $\lambda_0$  is the critical factor in determining the amount of prior data to be used. Previously, the values below this number were simply eliminated, now this vacancy is filled with *a priori* data.

Putting this solution back into unprimed coordinates use equations (6.14) and (6.17),

$$\begin{aligned} \mathbf{x} &= \mathbf{V}\mathbf{x}' \\ &= \mathbf{V}\mathbf{M}\mathbf{y}' + \mathbf{V}\mathbf{N}\mathbf{x}_0' \\ &= \mathbf{V}\mathbf{M}\mathbf{U}^T\mathbf{y} + \mathbf{V}\mathbf{N}\mathbf{U}^T\mathbf{x}_0 \end{aligned} \quad (6.20)$$

This may seem a drawn out process, but actually requires only minor adjustments to the SVD inversion program. The synthetically derived data above will be used to initially test this new algorithm.

The travel times are derived from raytracing through the model shown in Figure 6.1 with 1% random Gaussian noise added. The initial reconstructions for ART and the SVD inversion are shown in Figures 6.4 and 6.5. The best result for SVD occurs with the elimination of eigenvalues less than 0.3, or  $\lambda_0 = 0.3$  in equations (6.18) and (6.19). This amounts to throwing out just less than a quarter of the values. For the *a priori* data the true velocity values were used to illustrate the effect on the solution. The velocities obtained by equation (6.20) (Figure 6.12) show a great improvement

even with a relatively small contribution from prior information. The fact that this prior data is known to be perfect probably has some effect on the amount of improvement.

A more realistic situation can be simulated by obtaining an initial model from ART to use as the prior data. It is hoped that the inversion will extract the positive contributions from each method, that is the SVD inversion will try to narrow the bounds of the low velocity zone in the ART reconstruction, while eliminating its own "scattering" of low velocities. The results of the inversion continue to show some trade-off between the two results (Figure 6.13). At  $\lambda_0 = 0.7$  the low velocity zone is sufficiently narrowed, but much scattering remains. Whether this is an improvement or not is judgemental, but for more complicated velocity structures the scattering will increase. For values of  $\lambda_0$  greater than this the result begins to appear much like the ART reconstruction and therefore makes the use of the SVD inversion unnecessary. These findings do very little to encourage the use of an SVD inversion in any manner.

The Stripa data can be inverted using SVD with *a priori* information provided by ART. In inverting the Stripa data, it is desired that the SVD inversion of the ART result will eliminate some of the smearing which occurs, especially in the reconstruction of Stripa Data Set 2. For Stripa Data Set 1 the only room for improvement is to find anomalous zones undetected by ART. The results do show such zones (Figure 6.14), but the reliability of these values is unknown due to the oscillatory nature of the SVD inversions that have been seen. The possibility of low velocity zones to the upper left and lower right of the section is good from the fracture maps, but their appearance does not distinguish them from similar zones in this section. Therefore, they can not be determined real unless every feature is, which is very unlikely. Again, the true image is unknown and the variances and RMS residuals are all comparable, so any comparison of results must be visual and objective as possible.

The results for Data Set 2 are similar (Figure 6.14). In fact, though the central low velocity zone may have tighter bounds, the smearing seems to have increased. There are still the low velocity zones seen in Data Set 1 which supports their existence, but the strong streak seen in the ART reconstruction only becomes stronger in SVD inversions. This probably signifies that the low velocity areas causing this are lower in velocity than the ART reconstructions show. This is very likely since ART has an averaging effect which tends to raise the velocity values in low velocity zones (see Figure 6.2). The results in general indicate little, if any, improvement in the reconstructions.

### **Discussion**

The ART algorithm is supposed to converge mathematically to the least squares solution (Herman *et al.*, 1978; Lakshminarayanan and Lent, 1975; and Chapter 2), but with inconsistencies in the data, primarily due to measurement errors, this convergence may not be realistic. Therefore, it is prudent to compare the two results for a simple model to see if the reconstructions are similar. There are many similarities in the reconstructions produced by the two methods using the test data as well as the Stripa data. However, in the presence of any noise the ART images are generally smoother than the corresponding SVD inversions. On the other hand, the SVD inverted images give a truer representation of the boundaries and values of the anomalous zones, but tend to obscure these zones with oscillatory behavior and other unrealistic features. It was hoped that these two methods could be combined to form an image with positive contributions from each technique. The only realistic method of doing this is to use the ART result as *a priori* information to the SVD inversion. The results showed modest improvement, but perhaps not enough to justify the expense required to produce such an inversion.

The price for an SVD inversion is high. It takes 2 minutes of CPU time on a VAX 11/780 to invert the  $162 \times 81$  matrix needed for the Stripa data. Thirty iterations of ART take about 20 seconds. It becomes worse for larger problems. It takes about 30 minutes of CPU time to invert the  $391 \times 252$  matrix needed for the Retsof data compared to about 30 seconds for ART. Obviously, the CPU time will continue to increase as the matrix becomes larger. There exist libraries of routines for the sparse matrices found in this study, but the amount of CPU time remains high for any large inversions. There may be some faster routines and it is possible to write machine-dependent code to run very quickly, but this study shows that the inversion itself must be improved in some way for this extra effort to become worthwhile.

## VELOCITY MODEL

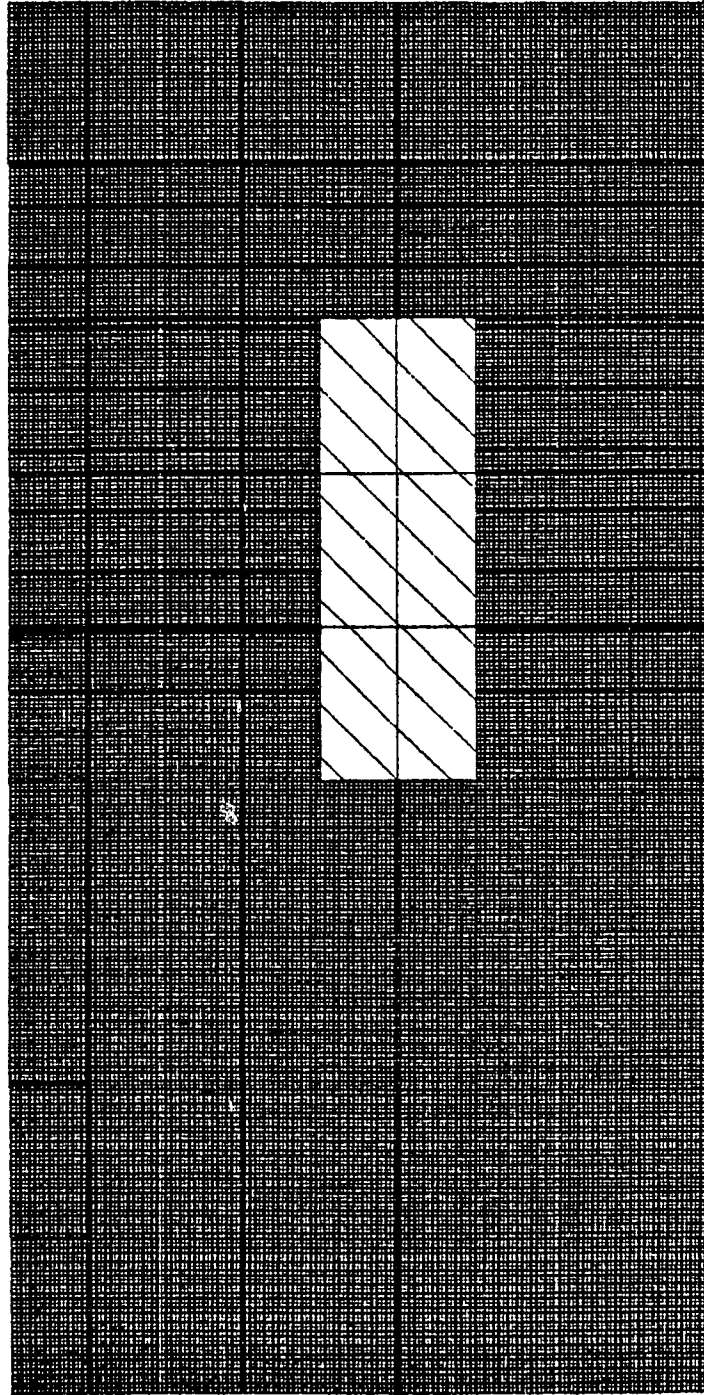
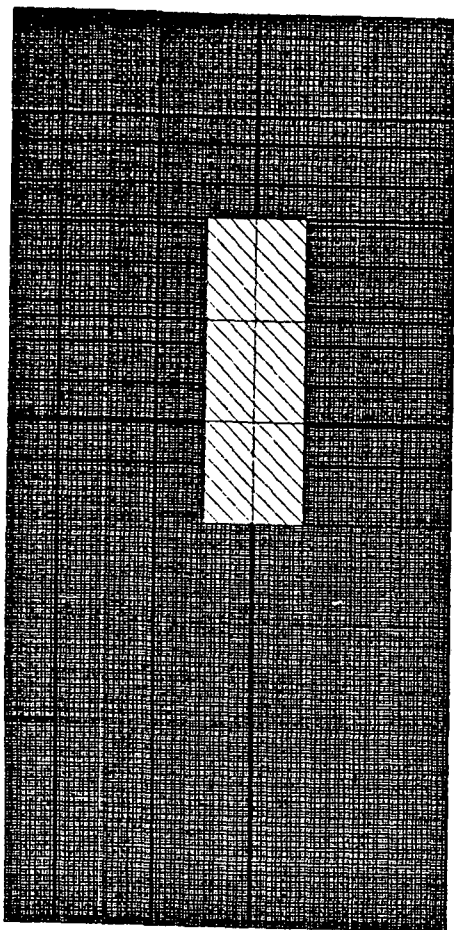


**Figure 6.1.** Velocity model for the synthetic studies. The dimensions are the same as for the Stripa experiment. The dark shade corresponds to 6.0 km/s and the lighter to 5.5 km/s.

## SVD RECONSTRUCTION



## ART2 RECONSTRUCTION

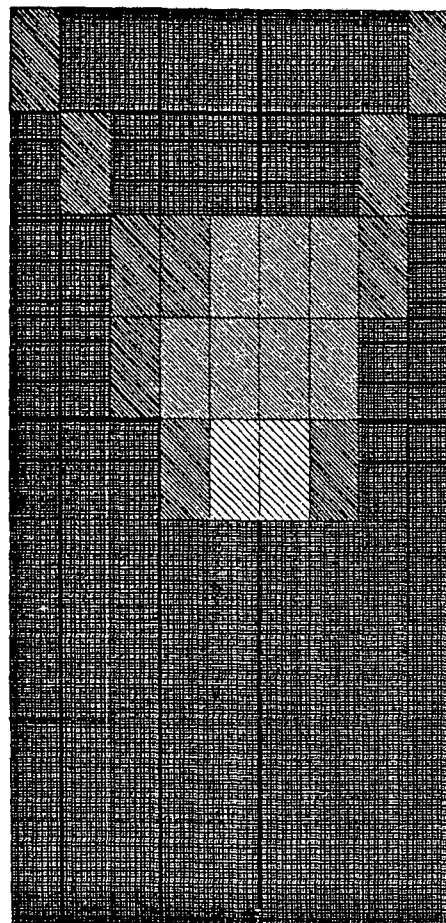
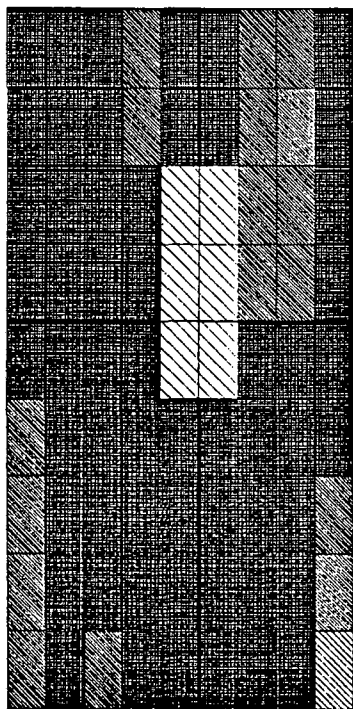
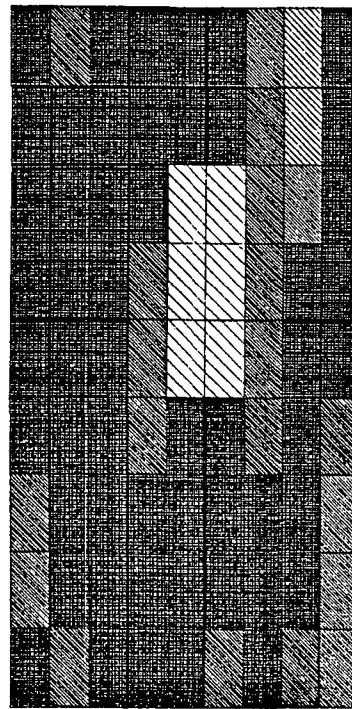


**Figure 6.2.** The results of inverting the travel time data derived from the velocity model in Figure 6.1 with no noise added for singular-value decomposition (SVD) and ART2. The SVD inversion produces a near perfect reconstruction of the model, while ART2 produces a smoothed image.

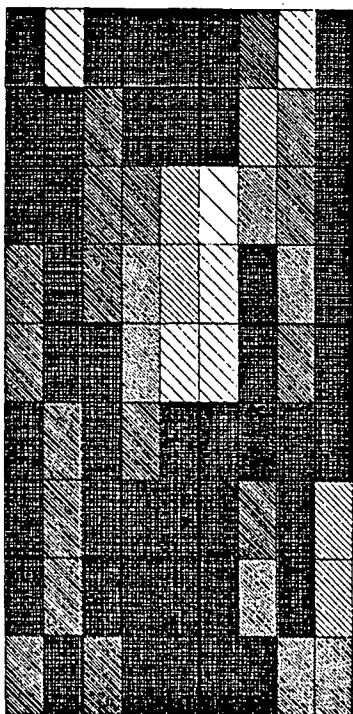
## DAMPED LEAST SQUARES



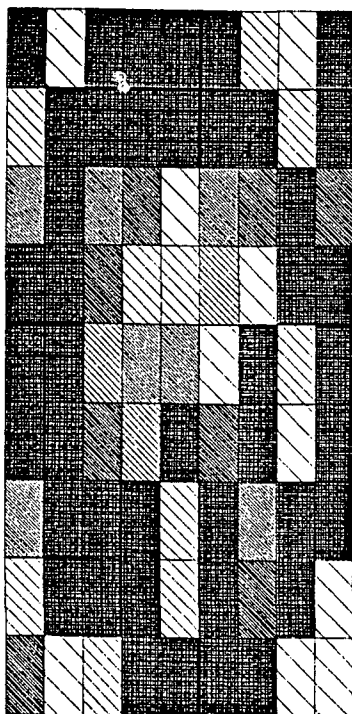
$$\lambda_0 = 0.1$$



$$\lambda_0 = 0.3$$



$$\lambda_0 = 0.5$$

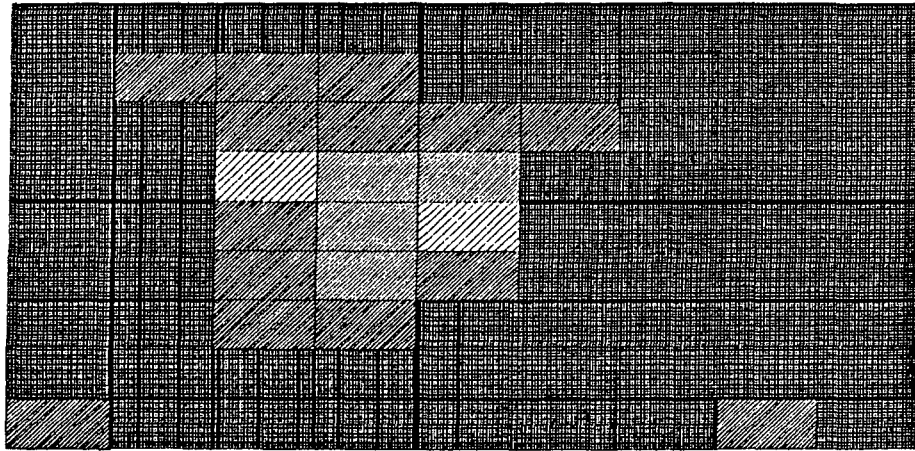


$$\lambda_0 = 0.7$$

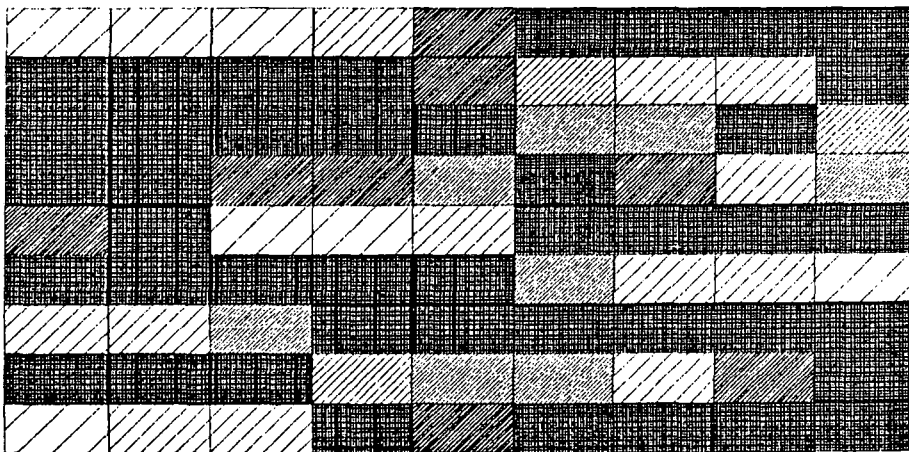
**Figure 6.3.** The results of using a damped least squares inversion of the travel time data of Figure 6.2. The cutoff eigenvalues are  $\lambda_0 = 0.1$ ,  $\lambda_0 = 0.3$ ,  $\lambda_0 = 0.5$  and  $\lambda_0 = 0.7$ . The reconstructions become progressively worse as more eigenvalues are removed.



1% RANDOM GAUSSIAN NOISE



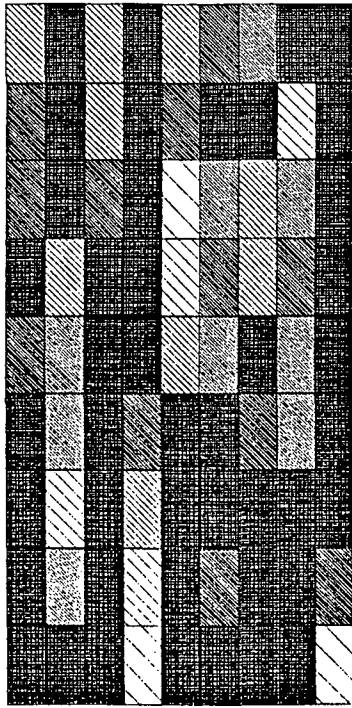
ART2 RECONSTRUCTION



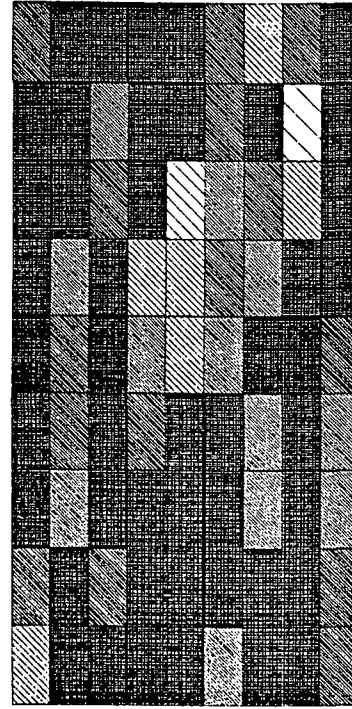
SVD RECONSTRUCTION

**Figure 6.4.** Random Gaussian noise with a standard deviation of 1% of the total travel time is added to the travel times. This produces a great deal of oscillations in the SVD inversion, while the ART2 reconstruction is relatively unaffected.

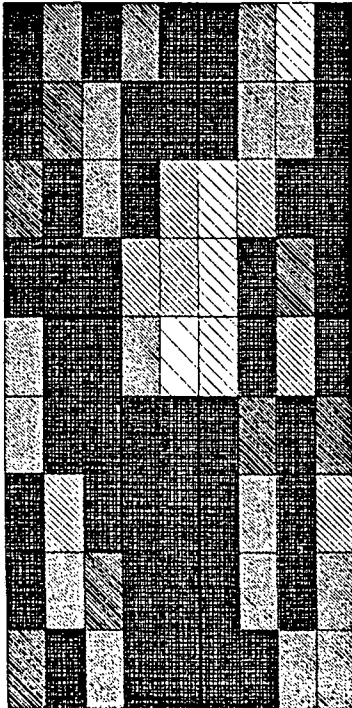
## DAMPED LEAST SQUARES



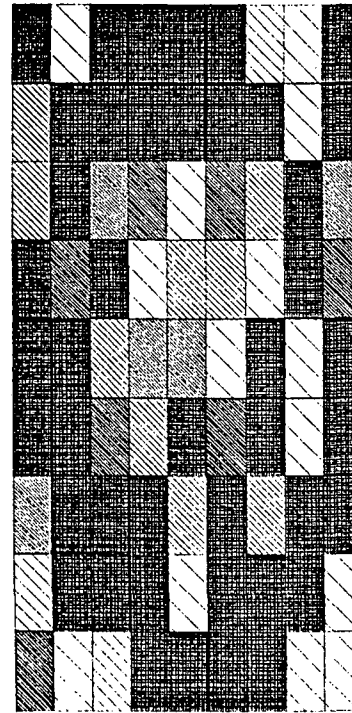
$$\lambda_0 = 0.1$$



$$\lambda_0 = 0.3$$



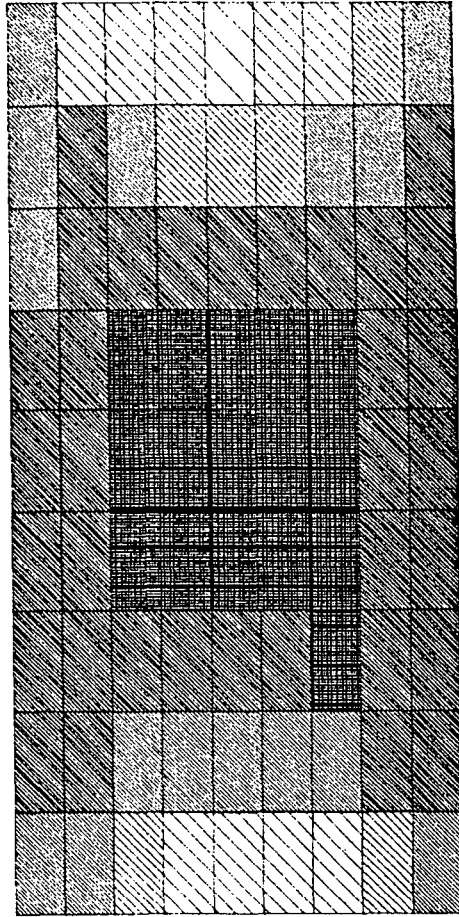
$$\lambda_0 = 0.5$$



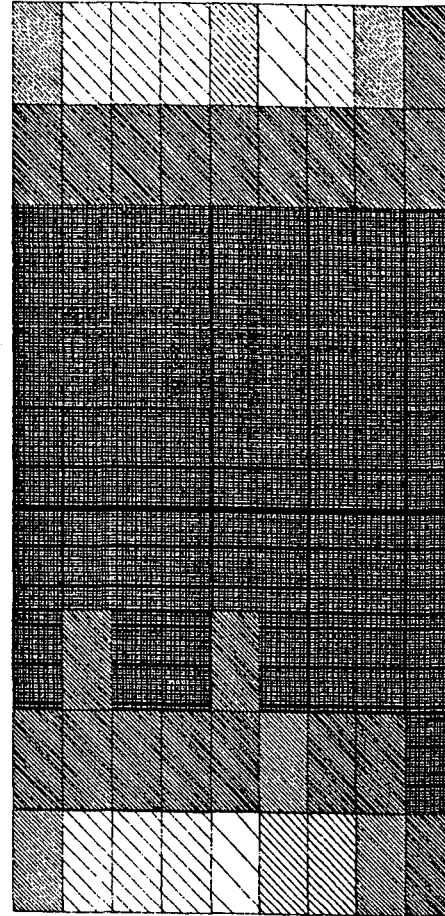
$$\lambda_0 = 0.7$$

**Figure 6.5.** Results using the damped least squares inversion for the noise-added travel time data. The cutoff eigenvalues are  $\lambda_0 = 0.1$ ,  $\lambda_0 = 0.3$ ,  $\lambda_0 = 0.5$  and  $\lambda_0 = 0.7$ , with  $\lambda_0 = 0.5$  producing the greatest improvement.

## RESOLUTION MATRICES FOR STRIPA



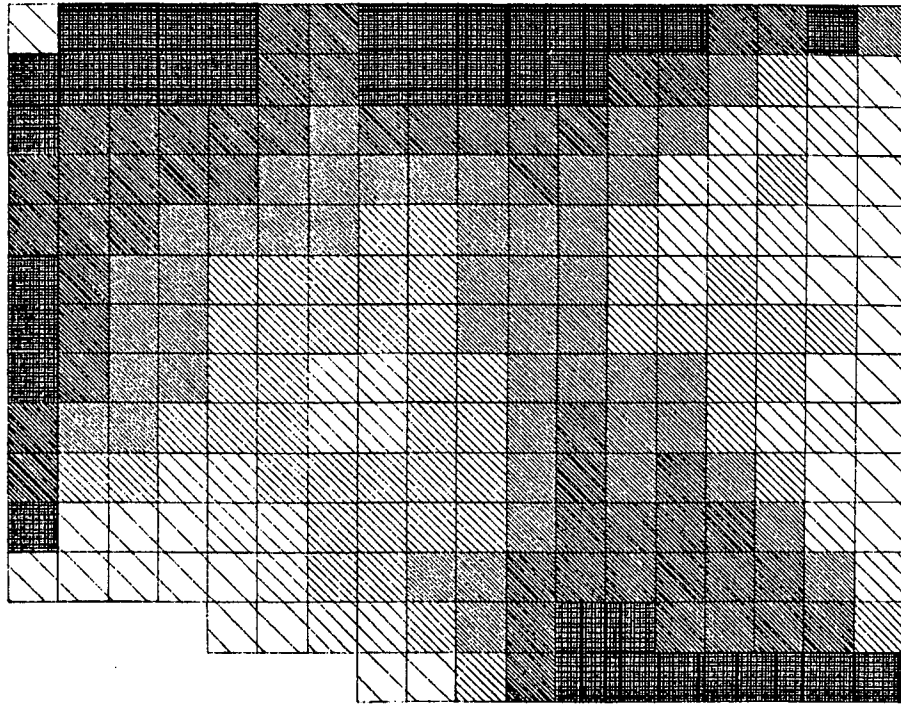
**ART2**



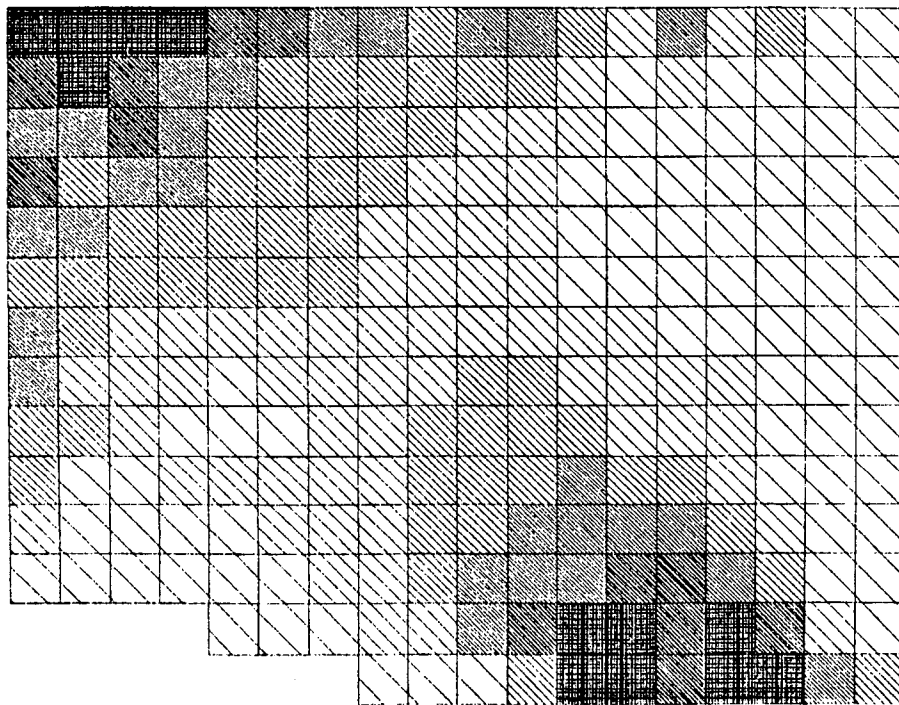
**SVD**

**Figure 6.6.** The diagonals of the resolution matrices for the Stripa geometry. The darker areas are better resolved. The better resolved areas correspond to those of higher ray density (Figure 5.1).

## RESOLUTION MATRICES FOR RETSOFF



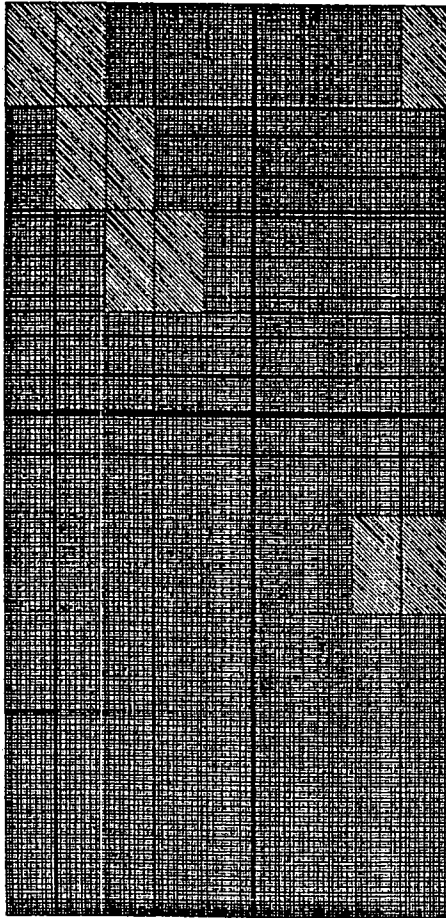
SVD



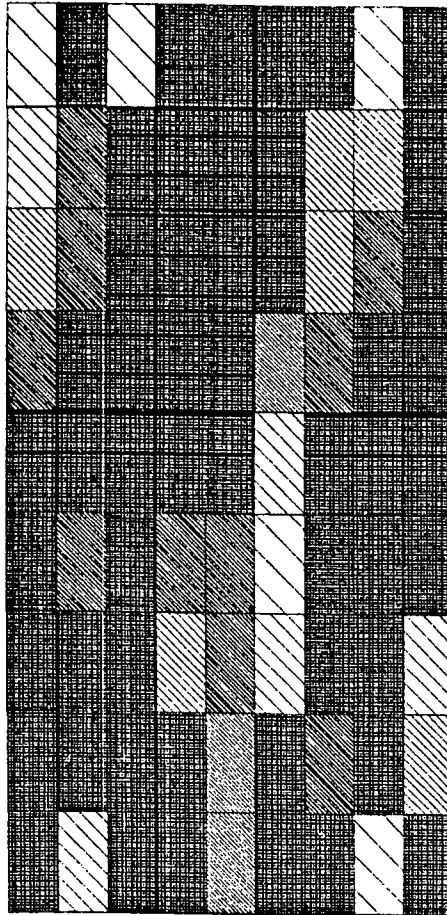
ART2

**Figure 6.7.** The diagonals of the resolution matrix for the Retsoff geometry. The darker areas are better resolved. The better resolved areas again correspond to those areas of higher ray density (Figure 5.5).

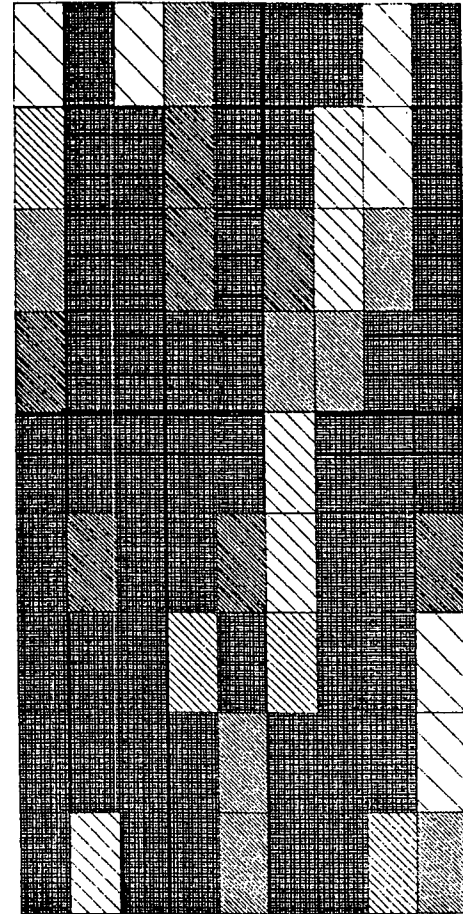
# STRIPA DATA SET 1



ART2



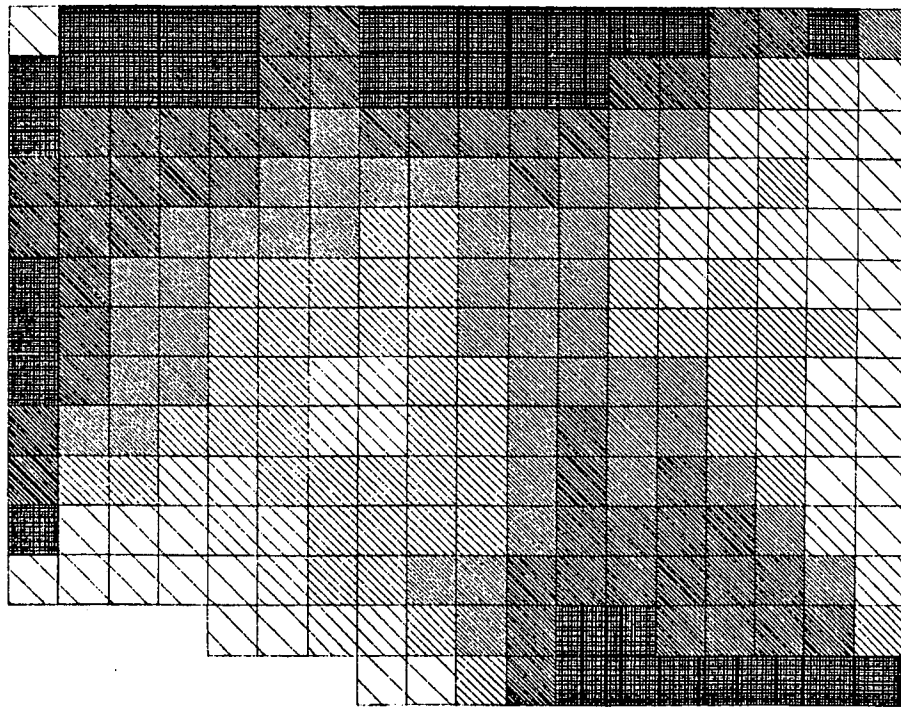
SVD



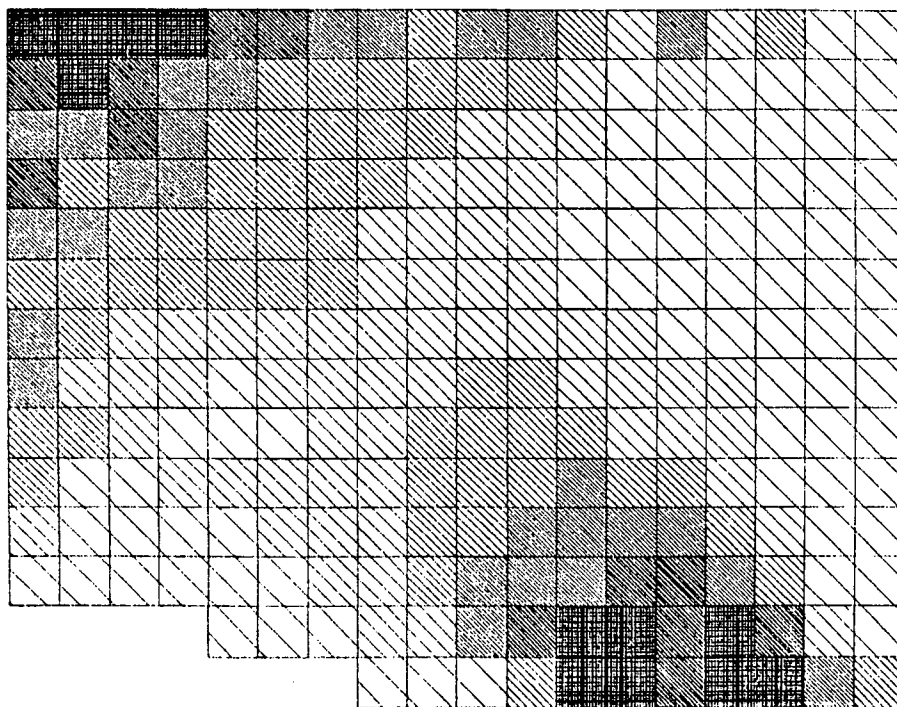
$\lambda_0 = 0.1$

Figure 6.8. Reconstructed images of Stripa Data Set 1 for ART2, SVD, and damped SVD with cutoff eigenvalues  $\lambda_0 = 0.1$ ,  $\lambda_0 = 0.3$ ,  $\lambda_0 = 0.5$  and  $\lambda_0 = 0.7$ . Velocities range from 6.0 km/s (dark) to 5.6 km/s (light).

## RESOLUTION MATRICES FOR RETSOFF



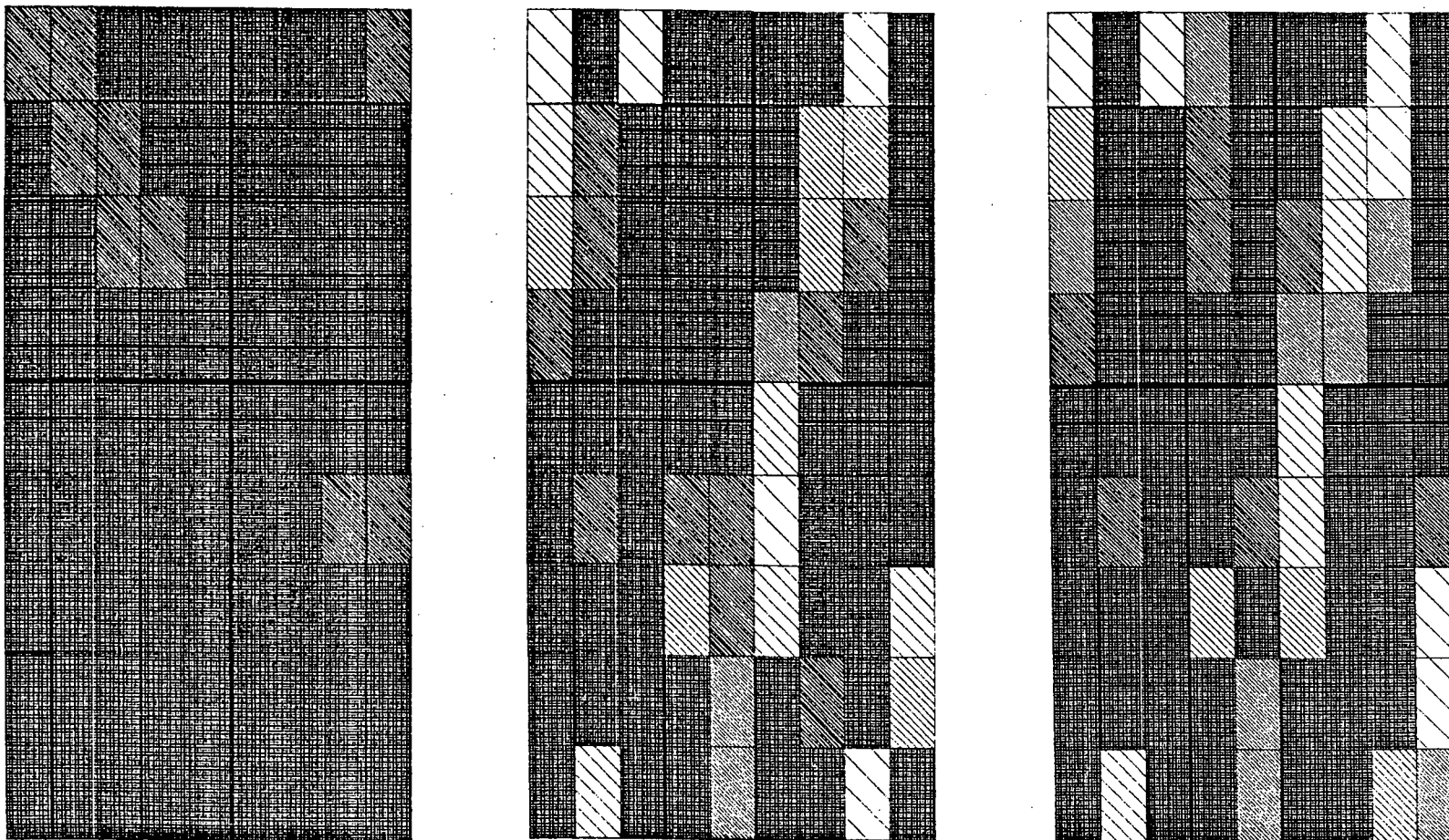
SVD



ART2

**Figure 6.7.** The diagonals of the resolution matrix for the Retsoff geometry. The darker areas are better resolved. The better resolved areas again correspond to those areas of higher ray density (Figure 5.5).

STRIPA DATA SET 1



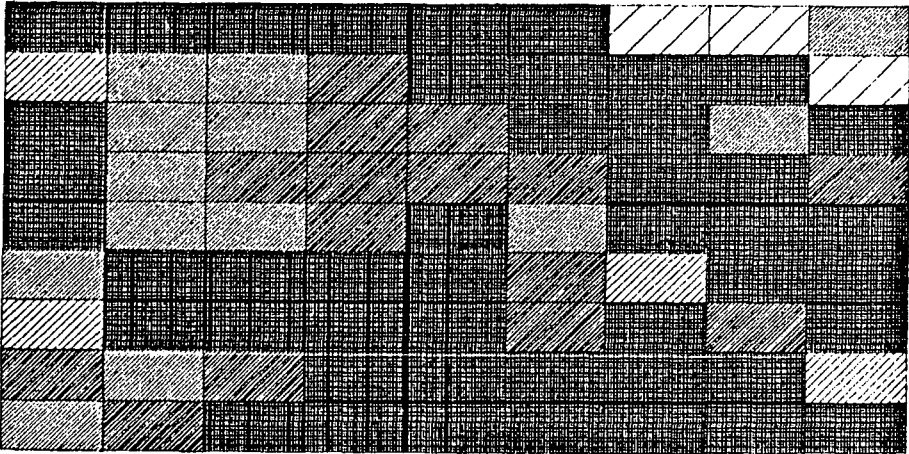
ART2

SVD

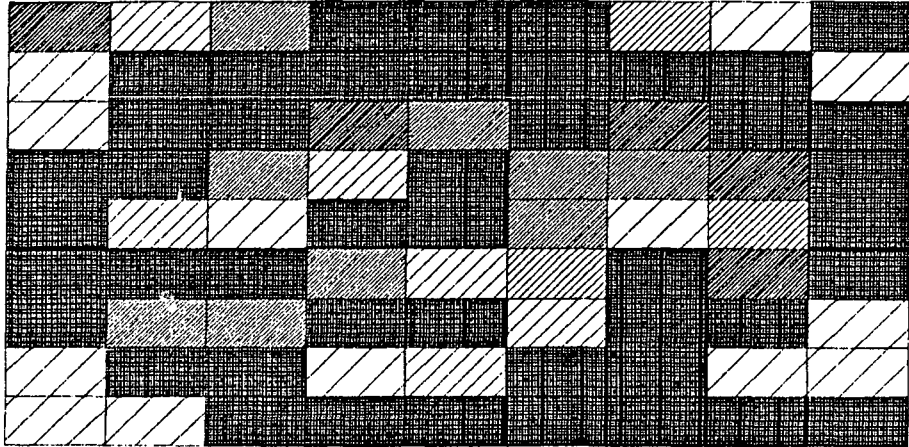
$\lambda_0 = 0.1$

Figure 6.8. Reconstructed images of Stripa Data Set 1 for ART2, SVD, and damped SVD with cutoff eigenvalues  $\lambda_0 = 0.1$ ,  $\lambda_0 = 0.3$ ,  $\lambda_0 = 0.5$  and  $\lambda_0 = 0.7$ . Velocities range from 6.0 km/s (dark) to 5.6 km/s (light).

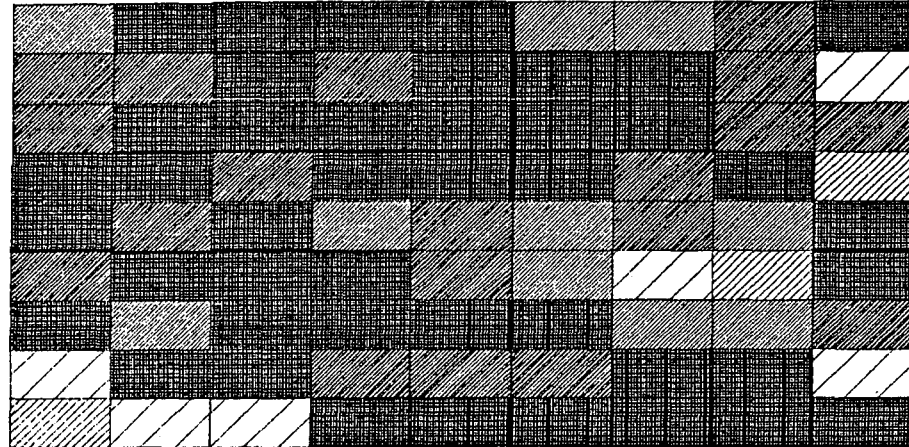
STRIPA DATA SET I



$\lambda_0 = 0.3$



$\lambda_0 = 0.5$

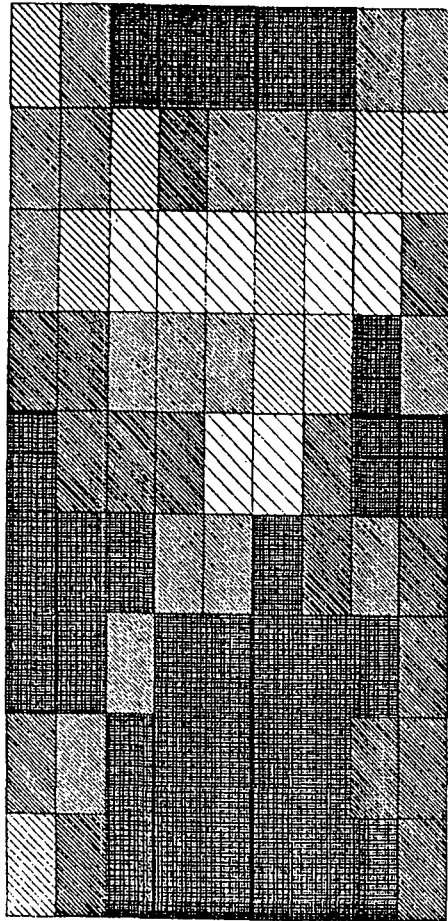


$\lambda_0 = 0.7$

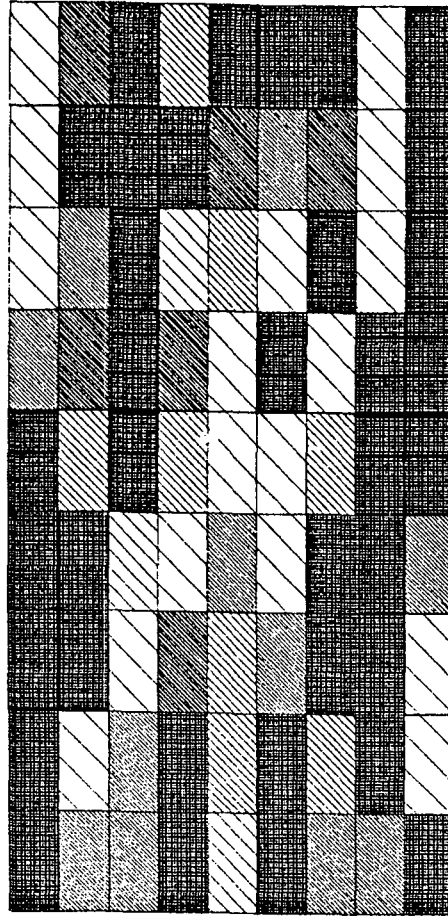
Figure 6.8. (continued).



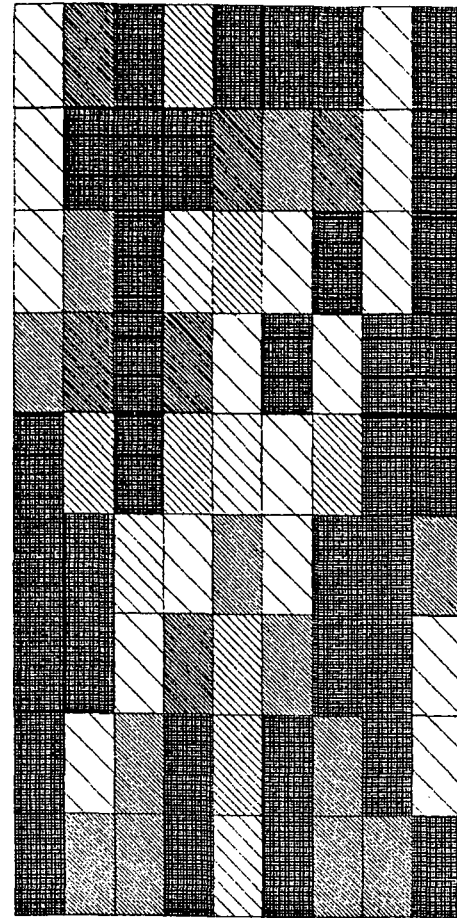
## STRIPA DATA SET 2



ART2



SVD



$\lambda_0 = 0.1$

Figure 6.9. Reconstructed images of Stripa Data Set 2 for ART2, SVD, and damped SVD with cutoff eigenvalues  $\lambda_0 = 0.1$ ,  $\lambda_0 = 0.3$ ,  $\lambda_0 = 0.5$  and  $\lambda_0 = 0.7$ . Velocities range from 6.0 km/s (dark) to 5.6 km/s (light).

## STRIPA DATA SET 2

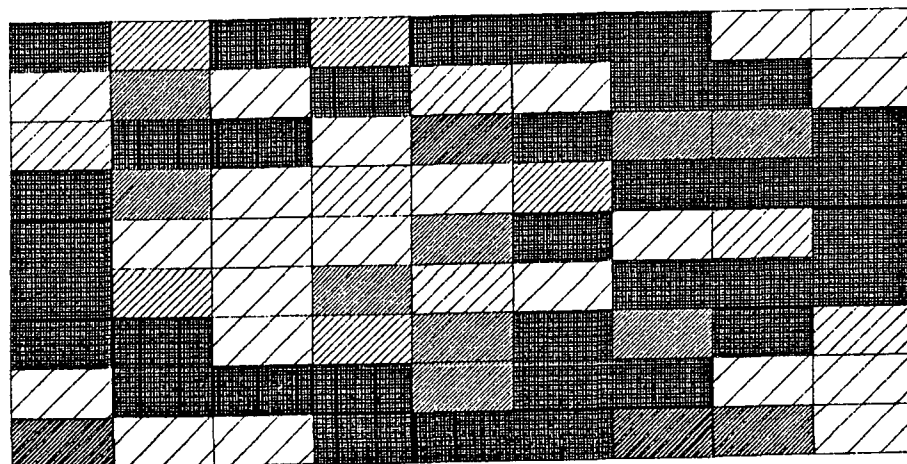
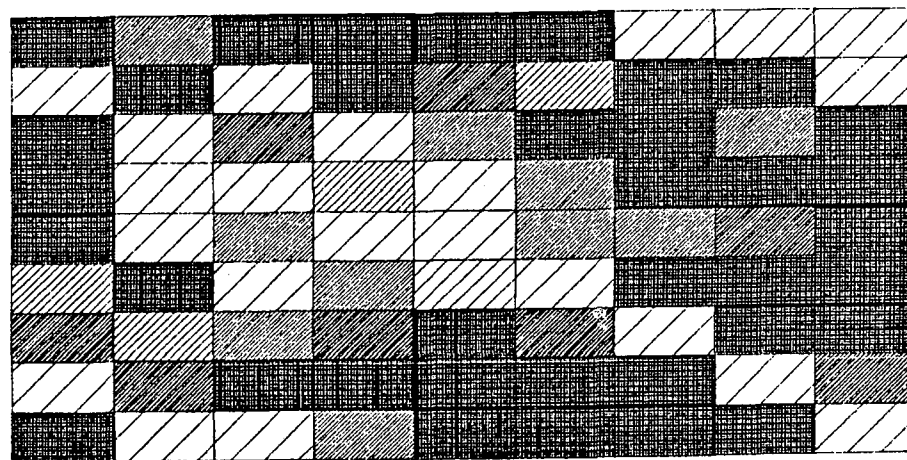
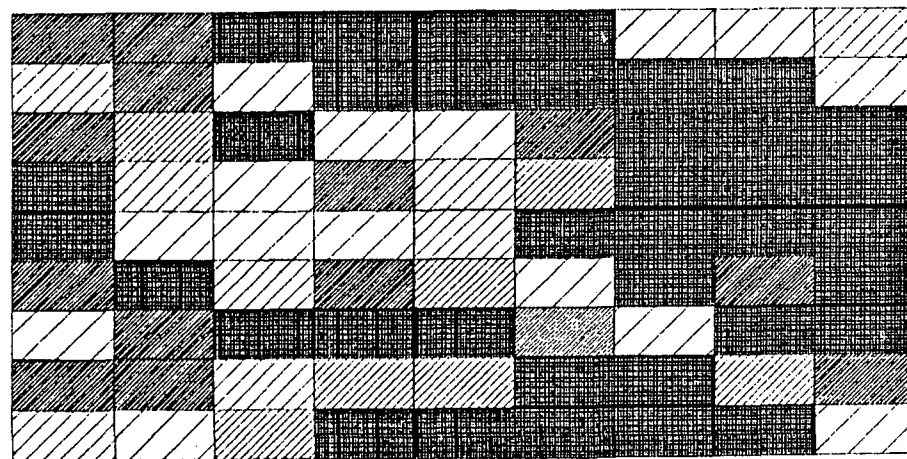
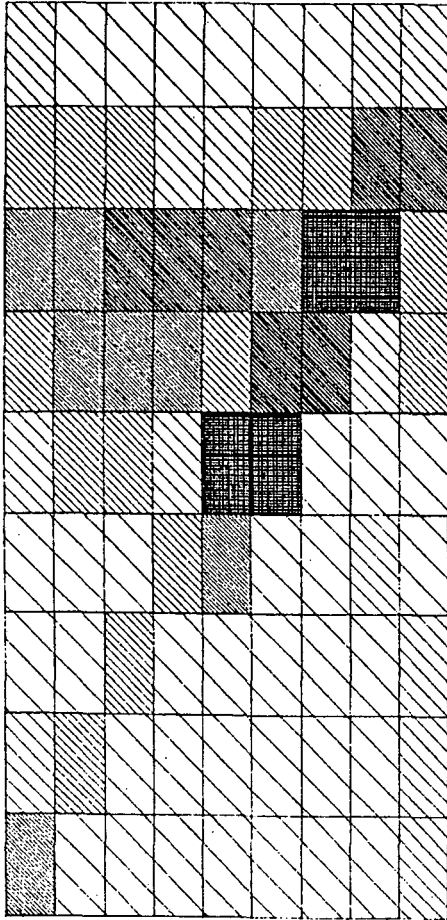
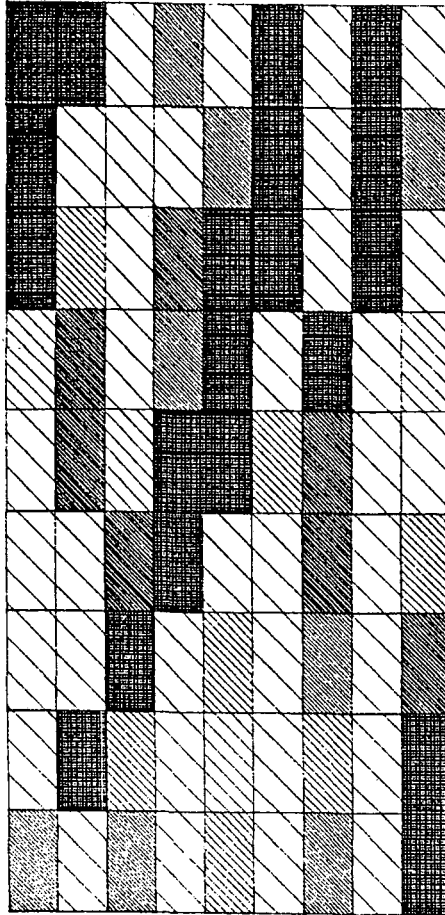
 $\lambda_0 = 0.7$  $\lambda_0 = 0.5$  $\lambda_0 = 0.3$ 

Figure 6.9. (continued).

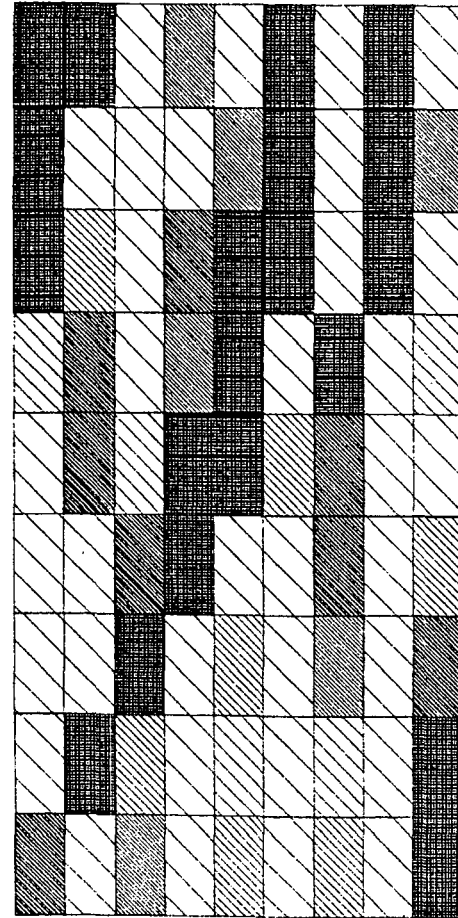
## DIFFERENCES



ART2



SVD



$\lambda_0 = 0.1$

Figure 6.10. The differences are taken between the reconstructions of Data Set 2 (Figure 6.9) and Data Set 1 (Figure 6.8). The differences range from 0.3 km/s (dark) to 0.0 km/s (light).

DIFFERENCES

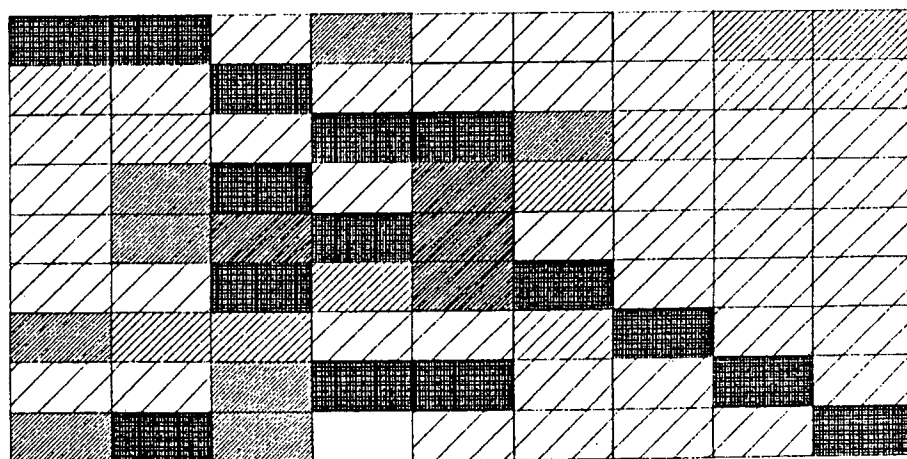
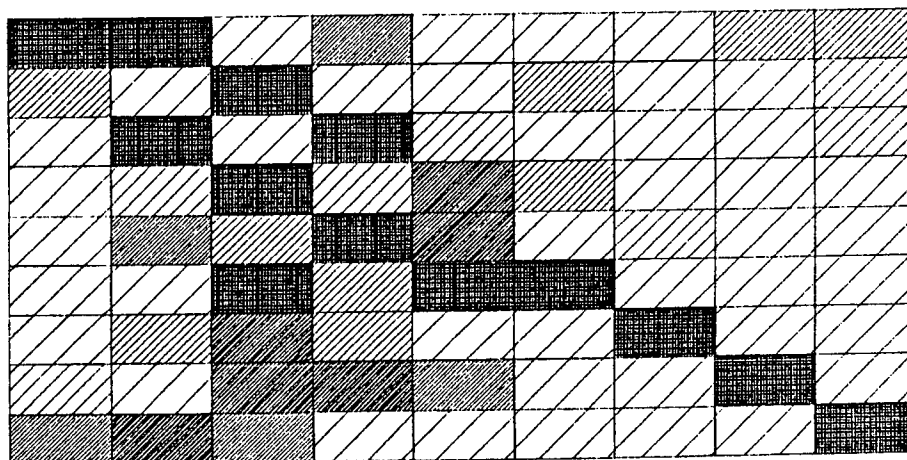
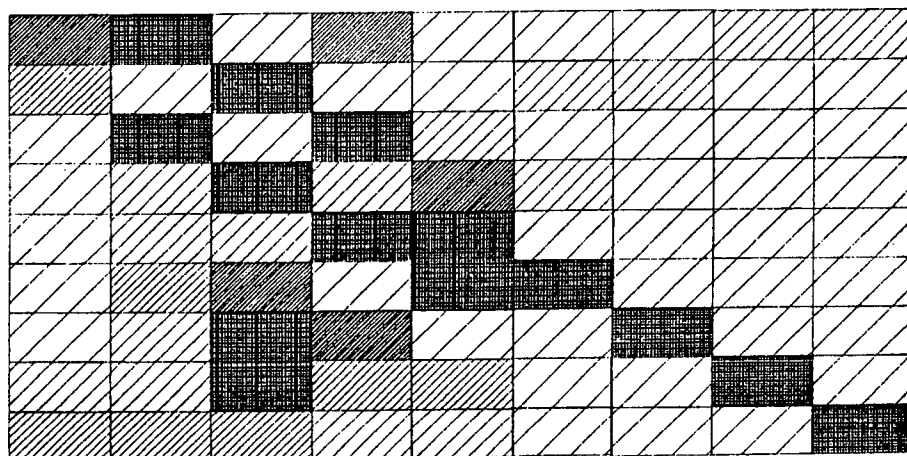
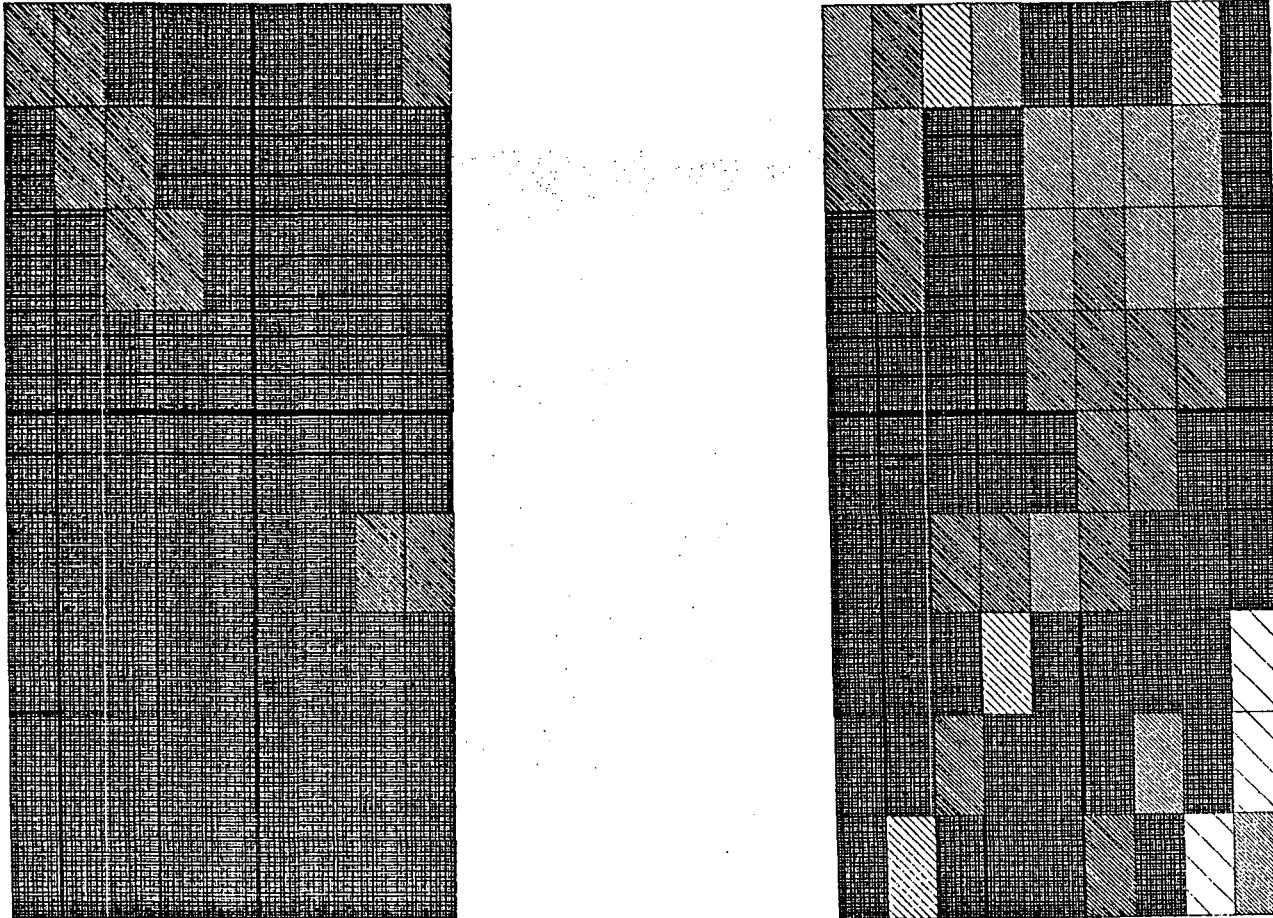


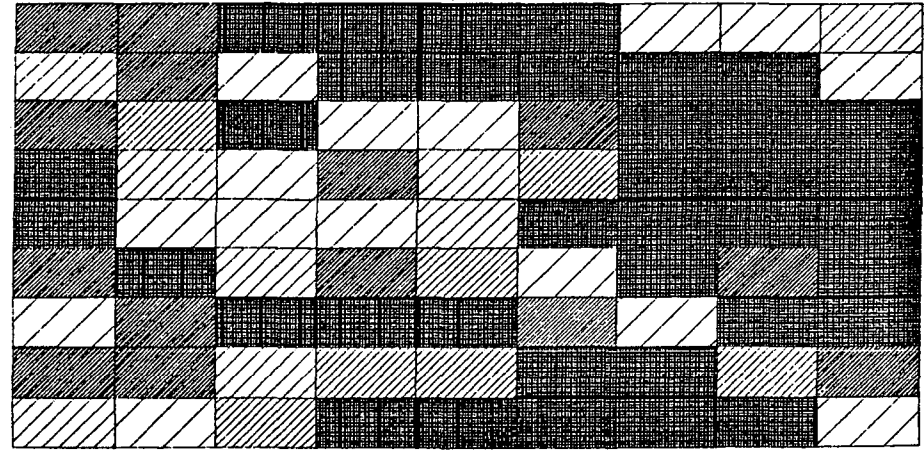
Figure 6.10. (continued).

## STRIPA DATA SET 1

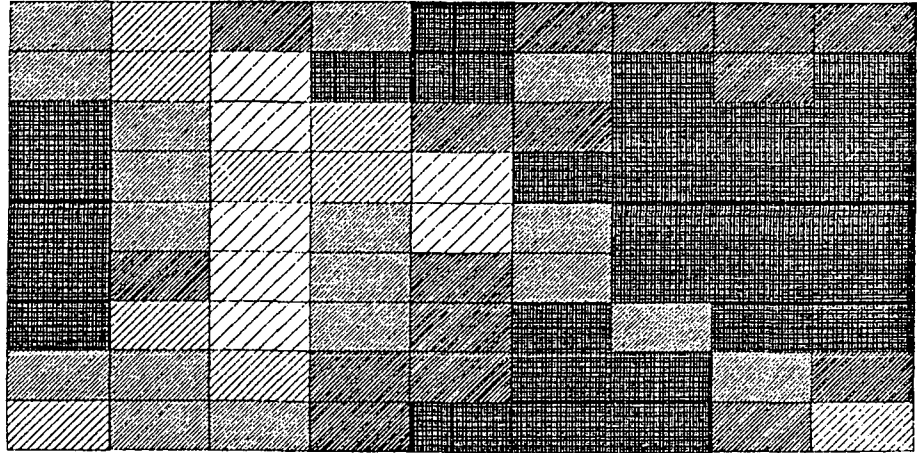


**ART2** **SVD**  
Figure 6.11. A comparison of the ART images with the best SVD reconstructions ( $\lambda_0 = 0.3$ ) for Data Set 1, Data Set 2 and the difference. There are some similarities in the results, but the SVD images remain oscillatory.

STRIPA DATA SET 2



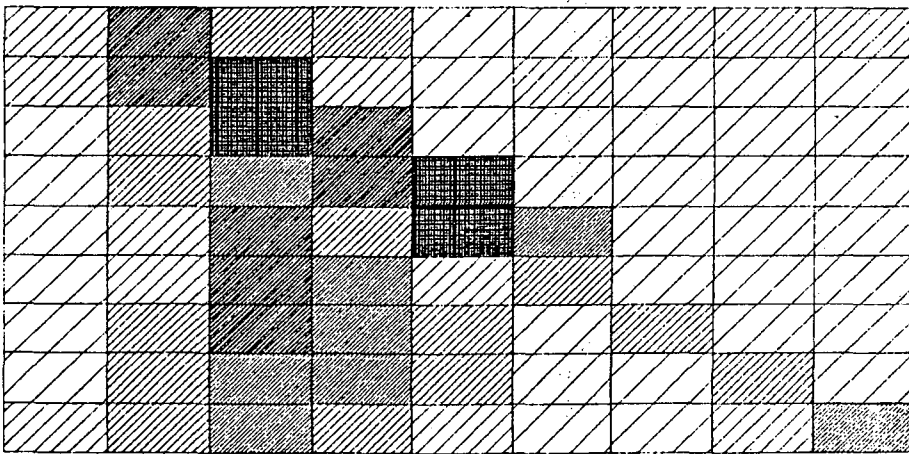
SVD



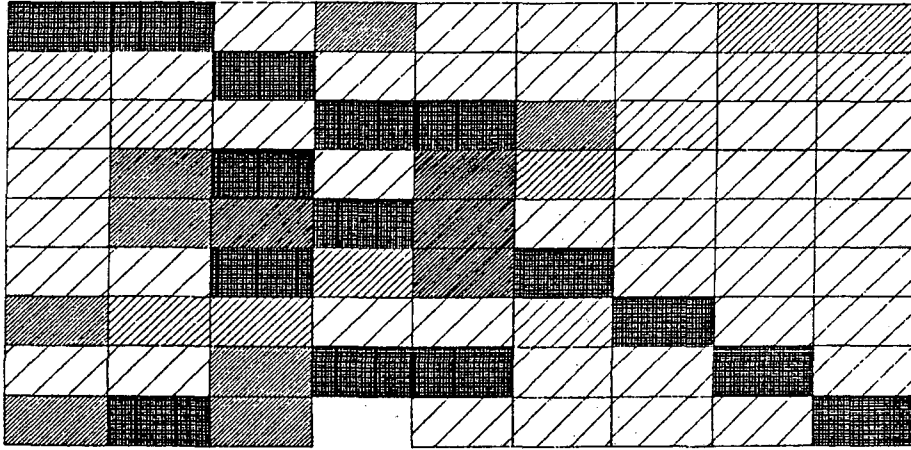
ART2

Figure 6.11. (continued).

DIFFERENCES



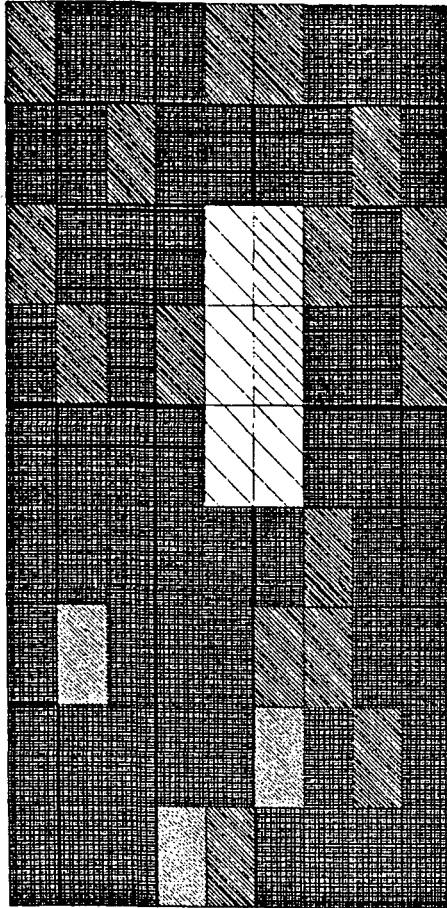
ART2



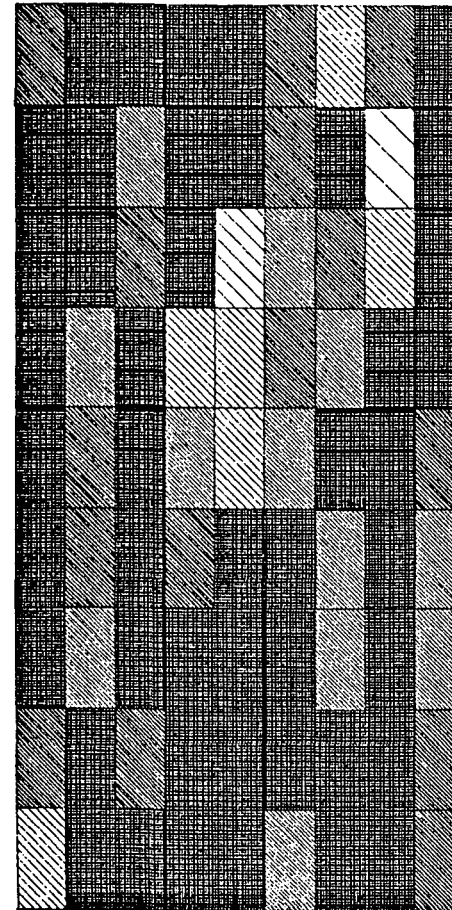
SVD

Figure 6.11. (continued).

## SVD INVERSION



WITH A PRIORI DATA



WITHOUT A PRIORI DATA

Figure 6.12. The SVD inversion of the travel times derived from the model in Figure 6.1 with the model itself used as *a priori* data and  $\lambda_0 = 0.3$ . The improvement is a direct result of using the original model as the *a priori* data.



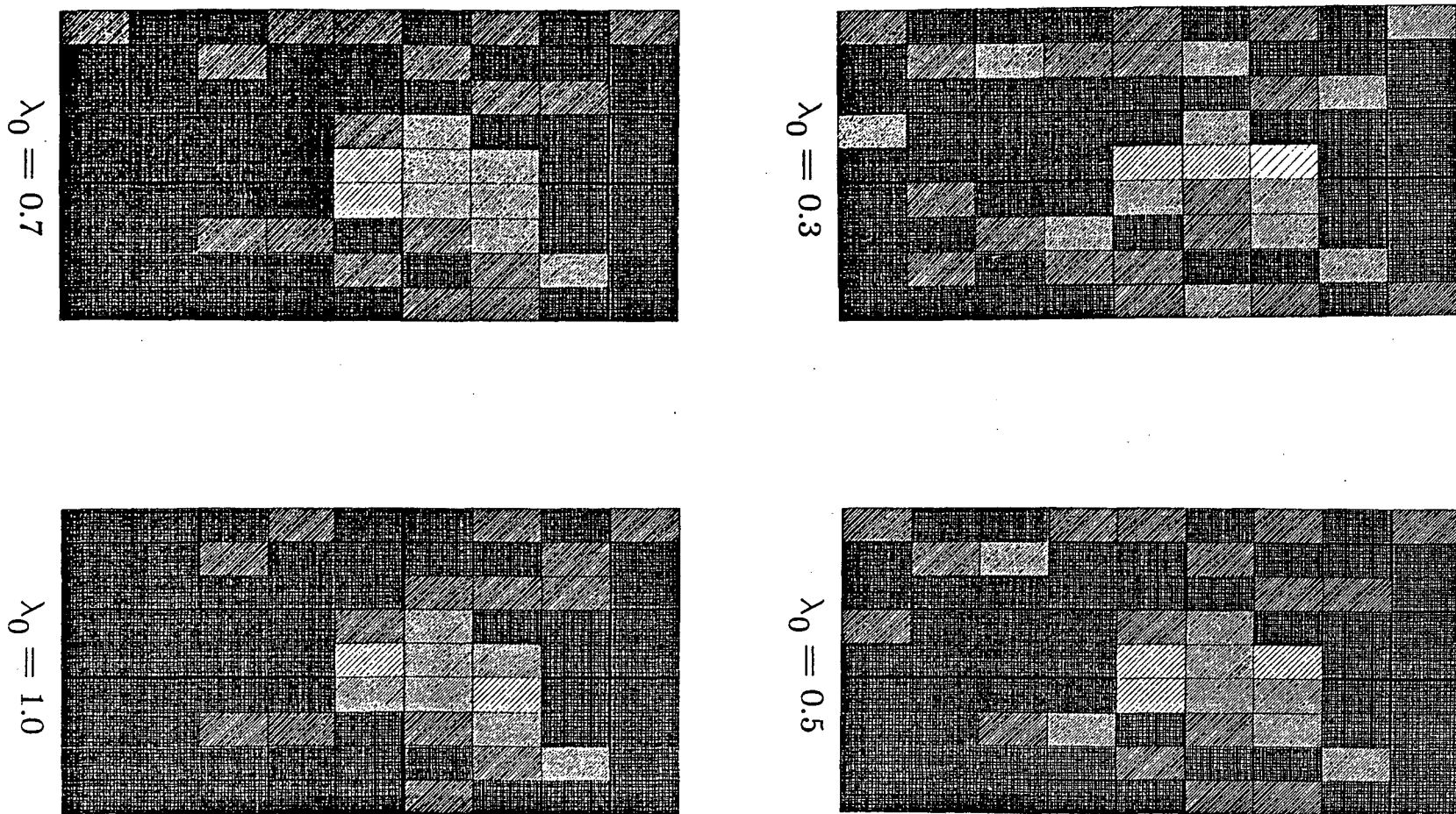
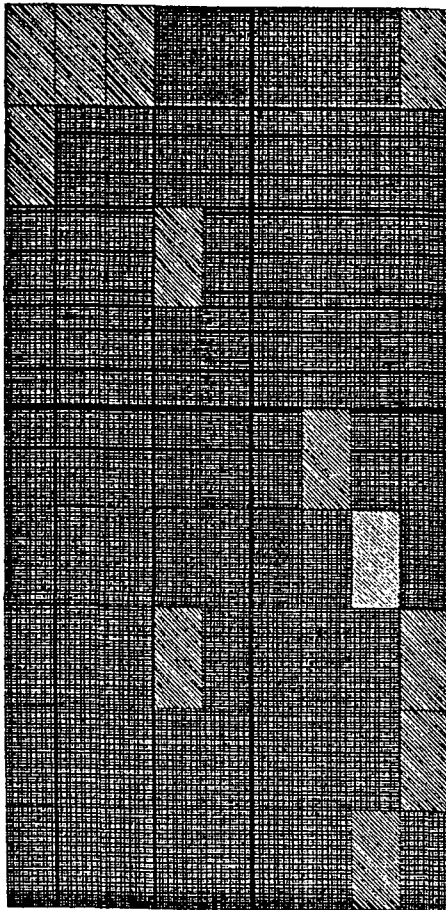
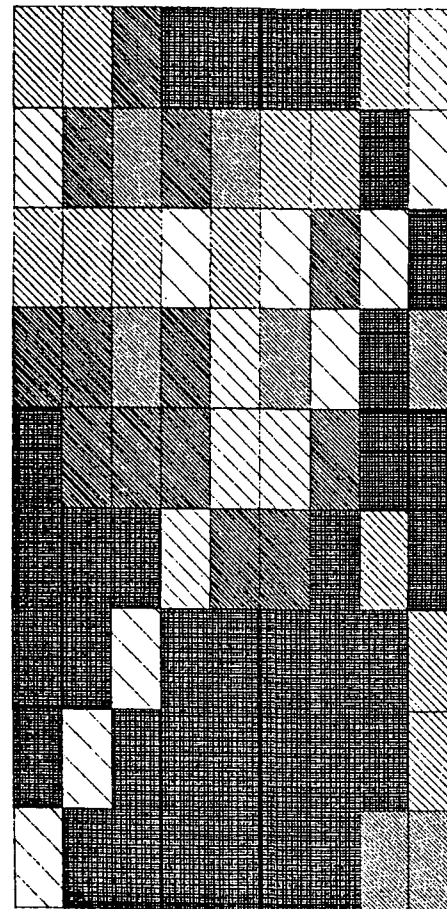


**Figure 6.13.** The damped SVD inversion using ART result as *a priori* data. The cutoff eigenvalues  $\lambda_0 = 0.3$ ,  $\lambda_0 = 0.5$ ,  $\lambda_0 = 0.7$  and  $\lambda_0 = 1.0$ . The images progress toward the ART result as  $\lambda_0$  increases.

## SVD WITH ART AS PRIOR DATA



**STRIPA DATA SET 1**



**STRIPA DATA SET 2**

Figure 6.14. The results of the SVD inversion using the ART result as *a priori* data for Stripa data set 1 and Stripa data set 2. The cutoff eigenvalue is  $\lambda_0 = 0.3$ .

## CHAPTER 7

### Summary, Conclusions and Recommendations

#### Summary

To assess the applicability and reliability of Algebraic Reconstruction Techniques (ART) to geophysical problems, algorithms were developed and applied to several real and synthetic data sets. The ART algorithms were developed for analysis of travel time data to determine the velocity field of a particular medium; such a determination is crucial to the delineation of anomalous zones in media characterized by fractures, non-uniform temperature distributions, compositional variations, and specific hydrological features which may relate to variations in acoustic velocity.

ART was initially applied to a simple velocity model to study the general behavior and reliability of the algorithms themselves. A more complex model was then used to study in greater detail the characteristics of the algorithms and modifications, such as the incorporation of weighting and smoothing functions. This latter, more realistic model produced a more complete account of the expected difficulties in the inversion of real data. Knowledge gained from the studies with synthetics was applied to two high-quality travel-time data sets. The experiments were carried out at the Retsof salt mine in New York and at the underground radioactive waste study site in Sweden (Stripa). The reconstructions of both data sets were consistent with known structures and expected velocity fields.

The ART algorithms can be shown theoretically to converge to the least squares solution. This convergence is not observed in the application of the method. However, synthetic studies show that ART produces a more realistic reconstruction of the original velocity model than does least squares. Hence, in an effort to optimize the effectiveness of the ART algorithms, a combination of these techniques is employed.

### **Conclusions**

Algebraic reconstruction techniques can be an effective means of determining the two-dimensional velocity distribution of a medium. The velocity structure of several models were accurately recovered by the ART inversions. However, these synthetic studies also showed adverse characteristics of the reconstructions, primarily described by oscillating velocity values in adjacent pixels which can result in peppered reconstructions, and the smearing of low or high velocity zones into the surrounding medium. Such velocity oscillations are a manifestation of a general instability associated with improper damping, small pixel size or simply noisy data. The oscillations can be virtually eliminated with the incorporation of a smoothing function into the algorithm. The application of smoothing and raytracing algorithms also served to diminish the effects of smearing, but did not eliminate them. Proper station geometry is essential in reducing smearing.

Analysis of the synthetic data also showed that the iterative process does not ultimately converge to the original model. There are several reasons for this behavior. When straight rays are used in the inversion the algorithm is no longer iterating toward the original model, but to some non-unique solution which fits the travel-time data. This results in the misrepresentation of the distance and RMS residual values which are calculated with respect to curved rays through the original model. The limited effectiveness of the curved ray algorithm is also related to this ultimate divergence. The rays are traced exactly the same for the forward and inverse problems, except the curve

is approximated by straight line segments through the pixels in the inverse problem. Therefore, the results effectively show the non-uniqueness of the problem and an accurate conclusion to the curved ray analysis awaits further studies.

It is necessary to determine the iteration at which the ultimate divergence begins, since reconstructions are overly smoothed before this iteration and peppered after it. This "optimal iteration" is generally not distinct; reconstructions tend to be similar for several iterations before and after. The synthetic travel time data are used to characterize the behavior of the reconstructions around the point closest to the original model. Results of this analysis lead to the choice of two reasonable criteria upon which to identify the optimal iteration in real data studies: the reconstructions are more oscillatory after the optimal iteration, and the optimal iteration occurs just after a sharp bend in the variance and RMS residual curves. The use of these two criteria leads to the determination of a reasonable stopping point for the process.

Two other parameters must be determined for a given data set: the relaxation parameter and the pixel size. The proper values are identified by the same criteria used in the determination of the optimal iteration. The damping should be altered until the bend in the variance or RMS residual curve levels between 10 and 20 iterations (the analysis of real data showed that the bend is more apparent for the RMS residual curve). Less damping will initiate oscillations in the curves and greater damping smooths the bend so that it is no longer easily distinguished. The size of the pixels used in the inversion effectively determines the limiting size of the velocity features which can be recovered. A tradeoff results because the solution becomes more unstable with decreased pixel size. Therefore, the optimal pixel size is that which is small enough to recover the desired velocity features without resulting in peppered reconstructions.

Noise was modeled by adding random Gaussian adjustments to the travel time data. The inversion for the simple velocity model was an underdetermined problem and the addition of noise resulted in an increase in oscillations and smearing effects.

However, the inversion for the complex model was overdetermined and the addition of noise resulted in very little change in the reconstructions for 5% and 10% noise. This surprising result suggests that the artifacts of noise may be deterministic and can possibly be eliminated with the an increase in ray paths or decrease in number of pixels.

The application to real data of the criteria obtained from the analysis of synthetic travel time data demonstrated the efficacy of the method. In the inversion of the Stripa and Retsof data sets, ART-type algorithms were shown to offer a rapid, reliable means of reconstructing the slowness fields. Details in the form of low velocity zones in media with up to 40% velocity contrast were recovered, their location and values apparently determined accurately. The assumption of straight rays caused few problems in the apparent reliability of the results, even in high contrast media, although experiments requiring increased accuracy using a larger number of ray paths and smaller pixels would require curved ray algorithms. Differences in algorithms are minimal, with performance dependent on the specific nature of the data set. Proper relaxation constraints must be applied and the proper number of iterations taken, otherwise very poor reconstructions will result, even though variances and RMS residuals appear acceptable. For real data, this can be especially difficult because non-mathematical methods must be relied upon, in part, to determine the proper parameters. The various weighting schemes and the averaging method of correction (equation 2.10) did not prove useful, but the smoothing algorithm produced great improvements in the Retsof reconstructions, although it proved inappropriate for the Stripa data.

The anomalous Stripa velocities were affected both by thermal variations and the presence of fracture zones, which were accurately reconstructed. These conditions exist in many other situations, including those in geothermal areas and steam injection zones. The monitoring and mapping of these zones is important in studying the productivity of the regions. The Stripa data set shows that both thermal and fracture zones can be accurately identified using ART. The anomalous Retsof velocities were caused

principally by rock failure, and again the reconstructions proved useful in mapping the failure zone. The velocity values of the in-situ rock were as expected, enabling rather simple inversions for absolute determination of arbitrary velocity fields.

### **Recommendations**

In conducting a tomography survey, it is strongly recommended that a complete synthetic study be conducted on prospective velocity models of the area before the data is acquired. The proper geometry of the survey is dependent on the expected velocity distribution, the estimated location of the primary region of interest, and the required resolution and can be more effectively determined by synthetic analysis. A poorly designed station distribution can render a survey virtually worthless. The damping parameter and pixel size are primarily influenced by the station geometry, so reasonable values may be found with these velocity models. The synthetic studies can also help in data interpretation by setting up a catalog of reconstructions for various velocity anomalies and by showing the effect of smearing with a given geometry.

The development of ART in this thesis has focussed on P-wave travel times with a cross-borehole geometry. The techniques may also be applied to S-wave, surface wave and amplitude data in a variety of geometries without changing the algorithms.

#### *A. S-waves and surface waves*

Travel time data from S-waves and surface waves are inverted exactly as P-wave travel times. The lack of clear onset times may produce greater reading errors than for P-waves resulting in noisy reconstructions. Surface wave data are advantageous in that both source and receiver are located at the surface and can be distributed completely around the region of interest. Surface anomalies are recovered and the results are averaged with depth, dependent on the wavelengths involved. The technique is useful in areas where the surface can not be disrupted.

S-wave data should be acquired along with the P-wave data when possible. S-wave surveys use the same geometry as P-waves and can sometimes use the same source so that both data sets may be inverted simultaneously. The S-wave results give additional information about the rock properties and can be combined with P-wave data to produce a map of the Poissons ratio for the region.

### *B. Anisotropy*

For certain media it is highly desirable to include anisotropy in the inversion. Anisotropy may be incorporated into the algorithms in two ways: one can invert directly for the slowness components of anisotropy; alternatively, the anisotropy may be extracted as a correction to the travel time data. The first method involves specifying a functional relationship between the incident angle of the ray and the slowness of each pixel. An elliptical slowness dependence is simplest and requires three components of slowness; hence, three values are assigned to each pixel. The second method requires that an estimate of the general anisotropy of the medium be calculated and the travel times adjusted to remove this anisotropy. The corrected data are then inverted using ART to determine the velocity distribution independent of anisotropy. Each of these methods has advantages in different situations. For example, the second method is optimal for a homogeneous anisotropic medium where the anisotropy is easily estimated.

### *C. Amplitude data*

In the determination of the material properties of an elastic medium, its dissipative characteristics provide an indispensable complement to the velocity structure. These dissipative properties may be understood by analysis of the amplitude of the waveform, and may be parameterized by an intrinsic quality factor,  $Q$ . In addition, filtered data may be studied to determine the frequency dependence of  $Q$ . This frequency dependence is an important indicator of the actual dissipation mechanisms and serves to further illuminate aspects of the material properties of the medium. Some ambiguity will remain owing to non-intrinsic effects such as elastic scattering, noise, geometric effects



and interference phenomena. The geometric effects for a known source spectrum and radiation pattern may be easily accounted for; noise may be expressed in a well-designed study over a spectral band of interest. The resultant apparent attenuation may be further decomposed according to the specific heterogeneous nature of the study area.

#### D. *Reflection and refraction surveys*

ART algorithms can be used with virtually any geometry in which ray paths can be traced. In the context of reflection and refraction surveys, the algorithms are set up as a secondary processing technique: after prominent interfaces have been defined so that the reflected and refracted rays can be traced through the medium. The technique should be helpful in areas with large horizontal velocity variation. The principal ambiguity is related to the choice of interfaces which thus presupposes a degree of confidence in the starting model. Bishop *et al.* (1985) have developed a technique that solves simultaneously for the velocity field and the location of the reflector. Such a technique can also be incorporated in the ART algorithms.

#### E. *Future work*

Extension of this work can take two directions: further studies with real data, and improvements to ART. Real data sets need to be studied to determine if the results found here have a general application to different geometries and wave types. Such studies can also better characterize the behavior of ART. Further analysis with curved ray paths must be undertaken. The effectiveness of curved rays can be studied by using the travel times of ray paths traced through the final solution in the RMS residual. The solution must be smoothed before this can be accomplished. The smoothing can be performed by taking a 2-D spatial Fourier transform with a Nyquist frequency corresponding to the station spacing. An inverse Fourier transform will then result in a reconstruction with the less resolved velocities eliminated. Improvements to ART can begin with the incorporation of *a priori* data and least squares, as studied in Chapter 6.

## References

- Bishop, T. N., K. P. Bube, R. T. Cutler, R. T. Langan, P. L. Love, J. R. Resnick, R. T. Shuey, D. A. Spindler, and H. W. Wyld, 1985. Tomographic determination of velocity and depth in laterally varying media. *Geophysics*, **50**, 903-923.
- Bois, P., M. La Porte, M. Lavergne and G. Thomas, 1972. Well-to-well seismic measurements. *Geophysics*, **37**, 471-480.
- Boyd, D., J. Coonrod, J. Dehnert, D. Chu, C. Lim, B. Macdonald, and V. Perez-Mendez, 1974. A high pressure Xenon proportional chamber for X-ray laminographic reconstruction using fan beam geometry. *IEEE Trans. Nucl. Sci.*, **NS-21**, 184-187.
- Bracewell, R. N., 1956. Strip integration in radioastronomy. *Aust. J. Phys.*, **9**, 198-217.
- Censor, Y., 1983. Finite series-expansion reconstruction methods. *Proc. IEEE*, **71**, 409-419.
- Clayton, R. W. and R. P. Comer, 1983. A tomographic analysis of mantle heterogeneities from body wave travel times (abstract). *EOS Trans. AGU*, **62**, 776.
- Daily, W. D., 1984. Underground oil shale retort monitoring using geotomography. *Geophysics*, **49**, 1701-1707.
- Daily, W. D. and Ramirez, A. L., 1984. Insitu porosity distribution using geophysical tomography. *GRL*, **11**, 614-616.
- Dines, K.A. and R. J. Lytle, 1979. Computerized geophysical tomography. *Proc. IEEE*, **67**, 1065-1073.
- Fawcett, J. A. and R. W. Clayton, 1984. Tomographic reconstruction of velocity anomalies (in print). *BSSA*, **74**.
- Gaardar, N. T. and G. T. Herman, 1972. Algorithms for reproducing objects from their X-rays. *Computer Graphics and Image Processing*, **1**, 97-106.
- Gilbert, P., 1972. Iterative methods for the three-dimensional reconstruction of an object from projections. *J. Theor. Biol.*, **36**, 105-117.
- Gordon, R., 1974. A Tutorial on ART (Algebraic Reconstruction Techniques). *IEEE Trans. Nucl. Sci.*, **NS-21**, 78-93.
- Gordon, R., R. Bender and G. T. Herman, 1970. Algebraic reconstruction techniques (ART) for three-dimensional electron microscopy and X-ray photography. *J. Theor. Biol.*, **29**, 471-481.
- Herman, G. T., 1972. Two direct methods for reconstructing pictures from their projections: A comparative study. *Computer Graphics and Image Processing*, **1**,

123-144.

- Herman, G. T., A. Lent and P. H. Lutz, 1978. relaxation methods for image reconstruction. *Commun. ACM*, **21**, 152-158.
- Herman, G. T., A. Lent and S. W. Rowland, 1973. ART: Mathematics and applications. *J. Theor. Biol.*, **42**, 1-32.
- Herman, G. T., and S. W. Rowland, 1973. Three methods for reconstructing objects from X-rays: A comparative study. *Computer Graphics and Image Processing*, **2**, 151-178.
- Ivansson, S., 1985. A study of methods for tomographic velocity estimation in the presence of low-velocity zones. *Geophysics*, **50**, 969-988.
- King, M. S. and B. N. P. Paulsson, 1981. Acoustic velocities in heated block of granite subjected to uniaxial stress. *GRL*, **8**, 699-702.
- Lancosz, C., 1961: Linear Differential Equations (564 pp.). D. Van Nostrand, London.
- Lakshminarayanan, A. V. and A. Lent, 1979. Method of least squares and SIRT in reconstruction. *J. Theor. Biol.*, **76**, 267-295.
- McMechan, G. A., 1983. Seismic tomography in boreholes. *Geophys. J. R. astr. Soc.*, **74**, 601-612.
- Menke, W., 1984. The resolving power of cross-borehole tomography. *GRL*, **11**, 105-108.
- Paulsson, B. N. P., 1983. Seismic velocities and attenuation in a heated underground granite repository. Ph. D. Thesis, Dept. of Engineering, Univ. of California, Berkeley, CA.
- Paulsson, B. N. P., N. G. W. Cook and T. V. McEvelly, 1985. Elastic-wave velocities and attenuation in an underground granitic repository for nuclear waste. *Geophysics*, **50**, 551-570.
- Radon, J., 1917. (On the determination of functions from their integrals along certain manifolds). *Ber. Saechs. Akad. Wiss. Lipzig, Math Physics Kl.*, **69**, 262-277.
- Scudder, H. J., 1978. Introduction to computer aided tomography. *Proc. IEEE*, **66**, 628-637.
- Shepp, L. A. and B. F. Logan, 1974. The Fourier reconstruction of a head section. *IEEE Trans. Nucl. Sci.*, **NS-21**, 21-43.
- Wong, J., P. Hurley and G. F. West, 1983. Crosshole seismology and seismic imaging in crystalline rocks. *GRL*, **10**, 686-689.

## APPENDIX

A general computer program was developed for this thesis to analyze synthetic and real data sets using any desired algorithm. The program can be easily modified for specific applications or needs. Curved ray paths and smoothing are incorporated by making changes at the appropriate lines described below. If ART2 is used exclusively, the memory allocation can be greatly reduced, since this algorithm does not require that the length of each ray through each pixel be stored.

- 0 - 104     The three input files (parameters, station locations and travel times) are setup and the parameters read into the program.
- 105 - 114   The pixel size and grid are set up by inputting the maximum coordinates of the field and the number of columns and rows of pixels desired.
- 115 - 153   For synthetic analysis the true velocity model can be read in to determine the distance,  $\delta$  (equation 2.25) and random Gaussian noise can be added to the travel time data. The noise is derived using the machine-dependent (VAX 11/780) random number generator RANDU, the function GAUSS and subroutine NOISE.
- 154 - 170   The X (row) and Z (column) coordinate of each grid point is defined.
- 171 - 198   The station locations and travel times are read in and any corrections are applied. The total distance between source and receiver is calculated for each ray path.

199 - 207 The calculation of the ray path through the pixels requires that the ray travel from left to right. The stations are reversed if this is not the case.

238 - 327 In this program listing a straight ray path is assumed and the path lengths through each pixel is calculated. The storage of these pixel lengths takes a tremendous amount of memory so that steps have been taken to reduce the space. Normally, a 3-dimensional array is necessary; an  $I \times J$  array for the pixel numbers, and an  $M$  vector for the number of ray paths. This would quickly exceed the storage capacity of a VAX 11/780 for any reasonably sized data set. The array size can be reduced to two dimensions if each pixel had an individual number. In this algorithm it was more convenient to combine the  $(i, j)$  pixel specification by using integers and multiplying  $j$  by 100 and adding to  $i$ . This results in a single integer value which may be accurately decomposed so long as  $i$  does not exceed 100. This process also splits the array into two one-dimensional vectors; an integer vector, LRBOX, containing the pixel numbers, and a real vector, LR, containing the path lengths through the corresponding pixels. The vectors are compact with each entry filled in sequence as the ray is traced through the field and LRBOX acting as a pointer to the next pixel in the sequence. The number 222222 is used as a marker for the end of each ray. If it is desired, LR may be entirely eliminated by exclusively using ART2, saving valuable computer storage space.

Curved ray paths can be used in place of the straight paths used in this algorithm. To use the curved paths, replace lines 228 - 337 with a ray-tracing subroutine that outputs the  $(X, Z)$  coordinates at some time step. These values are then used to calculate the path length, LR, through each pixel, LRBOX. In this thesis, this calculation was performed

assuming a straight path between the (X,Z) coordinates.

- 328 - 344 In this algorithm, the started model, BOX, is produced by a simple back-projection of the travel times by dividing each by the corresponding path length and assigning each pixel along this path the resulting slowness (equation 2.6). For each pixel, the slownesses produced by the various rays are averaged. If a different starting model is desired, the values are read into BOX at this point. Note that the inverse of BOX, i.e. the velocity, is output.
- 345 - 370 The program now begins to iterate through the specified ART algorithm, a single ray at a time. Before each iteration, any slownesses greater or less than specified values is set back to these values.
- 371 - 391 The travel times are calculated through the updated velocity model and these times subtracted from the observed travel times to produce DELTAG
- 392 - 424 The specified ART algorithm is applied to the corrections. The velocity model can be updated one ray at a time, or the corrections averaged according to equation (2.10).
- 425 - END The model is updated and the distance (if applicable), variance, entropy, and RMS residual are calculated for each iteration. The statistical values are output to UNIT 14 and the updated velocity model output to UNIT 15. A smoothing subroutine can be added before line 435, if desired.

```

0001  CC  ART ALGORITHMS USED FOR CROSS-HOLE TYPE DATA
0002  CC  MODIFIED FOR USE WITH SYNTHETIC DATA
0003  CC  NOISE CAN BE ADDED TO THE DATA
      C
      C  PROGRAM ART
      C
      C  VAX 11/780 VMS VERSION 4.3  APRIL 25, 1986
      C
      C  by JOHN E. PETERSON, JR.
      C  CENTER FOR COMPUTATIONAL SEISMOLOGY
      C  LAWRENCE BERKELEY LABORATORY
      C  UNIVERSITY OF CALIFORNIA
      C  BERKELEY, CA  94704
      C
0004  C
0005  C  COMMAND FILE SETUP: (ART.DAT)
0006  C
0007  C  1  IART  - NUMBER OF ALGORITHM WANTED:
0008  C      1 - ART
0009  C      2 - ART1
0010  C      21- ART2
0011  C      3 - WART (1 WEIGHTED BY LR/RAYPATH)
0012  C      4 - WART1 (2 WEIGHTED BY LR/RAYPATH)
0013  C      5 - WARTA (1 WEIGHTED BY (C/RAYPATH)**4
0014  C      6 - MART
0015  C      7 - SIRT (MUST USE IITER = 2)
0016  C  2  IITER - METHOD OF CHANGING THE PICTURE:
0017  C      1 - EACH TIME A RAY HAS BEEN ANALYZED
0018  C      2 - AFTER ALL RAYS HAVE BEEN ANALYZED
0019  C  3  ITER   - NUMBER OF ITERATIONS WANTED
0020  C  4  RELAX  - RELAXATION PARAMETER
0021  C  5  C D    - TOTAL FIELD DIMENSION - WIDTH (SPACE) HEIGHT
0022  C  6  IMAX JMAX - NUMBER OF COLUMNS (SPACE) ROWS
0023  C  7  NUMMIN  - MINIMUM # OF PIXEL SAMPLES TO OUPUT VALUES
0024  C  8  VMAX VMIN - MAXIMUM AND MINIMUM ALLOWABLE VELOCITIES
0025  C  9  I1 I2 SIGMA TMAX - SEED VALUE FOR RANDU FOR GAUSSIAN NOISE
0026  C      - TMAX IS THE % OF TOTAL TIME
0027  C 10  NORY   - YES OR NO TO READ IN ACTUAL VELOCITY MODEL
0028  C 11- BOXT   - ACTUAL VELOCITY MODEL
0029  C
0030  C  GEOMETRY SETUP:
0031  C
0032  C  THE GEOMETRY IS ASSUMED TO BE A 2-DIMENSIONAL FIELD
0033  C  SOURCE-RECEIVER PAIRS WITH DEPTH (Z) POS DOWNWARD AND
0034  C  THE ORIGIN IN THE UPPER LEFT CORNER (NO NEG VALUES).
0035  C  MOST GEOMETRIES WILL BE OFF-PLANE, A SUGGESTED SET-UP IS:
0036  C      TAKE A BOREHOLE (ASSUMED STRAIGHT) TO THE FAR LEFT AS
0037  C      THE X=0 AXIS WITH THE ORIGIN TAKEN ABOVE THIS, WITH
0038  C      Z=0 TAKEN AS THE SHALLOWEST DEPTH IN THE FIELD.
0039  C      THE X-VALUE OF THE LOCATIONS ARE THEN TAKEN AS THE
0040  C      DISTANCE FROM THE X=0 AXIS AT THE SAME DEPTH.
0041  C
0042  C  SO LOC(X,Z) ARE JUST THE 2-D VALUES OF THE STATION

```

```

0043 C LOCATIONS. THE DATA FILE IS SET UP AS: (UNFORMATTED)
0044 C
0045 C (LOCATION #) (TRUE X) (TRUE Y) (TRUE Z) (LOC(X)) (LOC(Z))
0046 C
0047 C WHERE THE TRUE VALUES (XLOC) ARE THE ACTUAL VALUES OF THE
0048 C DATA COLLECTION GEOMETRY USED TO CALCULATE PATHLENGTHS
0049 C AND LOC(X,Z) ARE USED IN THE ART CALCULATIONS.
0050 C LOCATION #'S ARE JUST IN NUMERICAL ORDER DOWN THE FILE.
0051 C

```

```

0052 C DATA FILE SETUP:

```

```

0053 C
0054 C THE DATA FILE CONTAINS THE STATION NUMBERS AND THE
0055 C TRAVEL TIME BETWEEN THE PAIR (UNFORMATTED). THE
0056 C CORRECTIONS FOR THE PATHLENGTH AND TRAVEL TIME TO
0057 C BE SUBTRACTED FROM THE GIVEN VALUES ARE GIVEN (ONLY
0058 C IF THESE ARE SINGLE NUMBERS FOR THE ENTIRE DAT SET)
0059 C

```

```

0060 C 1 - (DDELAY) (TDELAY)
0061 C 2-NRAY - (SOURCE #) (RECEIVER #) (TRAVEL TIME)
0062 C
0063 C

```

```

0064 C LR(NPTR,K1): LENGTH OF THE K'TH RAY THROUGH PIXEL (J,I)
0065 C BOX(JTEMP,ITEMP): SUM OF THE SLOWNESSES THROUGH (J,I)
0066 C SUMRAY(JTEMP,ITEMP): SUM OF THE LENGTHS THROUGH (J,I)
0067 C

```

```

0068 C UNIT 8 INPUT FILE OF PARAMETERS
0069 C UNIT 10 INPUT FILE OF LOCATIONS
0070 C UNIT 11 INPUT FILE OF TRAVEL TIME DATA
0071 C UNIT 14 OUTPUT FILE FOR STATS: DIST VAR ENTR RMS RES
0072 C UNIT 15 OUTPUT FILE FOR RESULTS
0073 C
0074 C

```

```

0075 REAL LZ,LX,LR1,          !used in geometry of pixels
0076 & Z(150),                !vertical grid values
0077 & X(150),                !horizontal grid values
0078 & XLOC(1000,3),         !field source and receiver locations
0079 & LOC(1000,2),          !converted 2-D locations used in ART
0080 & BOX(150,150),         !slowness values for each pixel
0081 & BOX1(150),            !work space for velocities
0082 & BOXT(150,150),        !true velocity field synthetic analysis
0083 & SUMRAY(150,150),      !work space for summing raylengths
0084 & SUMBOX(150,150),     !work space for summing corrections
0085 & LR(660000),           !length of K'th ray through pixel
0086 & TT(10000),            !travel times
0087 & SLOW(10000),          !calculated average slowness for each ray
0088 & PATH(10000),          !pathlengths
0089 & LRSQR(10000),         !denominator in ART inversion
0090 & NORM1,                 !L1 norm SUM(calc - obs)
0091 & NORM2,                 !L2 norm Sqrt(SUM(calc - obs)**2)
0092 & NORM(150,150),        !L1 norm at each pixel
0093 & YN(500),              !values for calculating Gaussian noise
0094

```



```

0095     INTEGER NUM(150,150),      !number of rays through each pixel
0096     &     LRBOX(660000)        !pixel code that makes LR a 1-D array
0097
0098     CHARACTER*1 NORY           !yes or no if inputting true velocity field
0099
0100     READ(8,*) IART              !algorithm number
0101     READ(8,*) IITER            !correction scheme
0102     READ(8,*) ITER             !number of iterations desired

0103     READ(8,*) RELAX            !value of relaxation parameter
0104
0105     C SET UP PIXEL SIZES AND GRID
0106
0107     READ(8,*) C,D               !maximum field dimensions (horiz) (vert)
0108     READ(8,*) IMAX,JMAX        !number of pixels (column) (row)
0109     A = C/FLOAT(IMAX)          !horizontal dimension of pixel
0110     B = D/FLOAT(JMAX)          !vertical dimension of pixel
0111     READ(8,*) NUMMIN           !min number of rays through pixel to plot
0112     READ(8,*) VMAX,VMIN        !max and min velocities allowed
0113     READ(8,*) I1,I2,SIGMA,TMAX !noise analysis parameters for synthetics
0114
0115     C READ IN TRUE VELOCITY FIELD IF APPLICABLE
0116
0117     READ(8,140) NORY
0118     IF(NORY.EQ.'Y') THEN
0119         DO 34 J = 1,JMAX
0120             READ(8,*) (BOXT(J,I), I = 1,IMAX)
0121             DO 35 I = 1,IMAX
0122                 BOXT(J,I) = 1./BOXT(J,I)
0123             35 CONTINUE
0124         34 CONTINUE
0125     END IF
0126
0127     WRITE(15,*) 'ALGORITHM NUMBER      ',IART
0128     WRITE(15,*) 'CORRECTION METHOD      ',IITER
0129     WRITE(15,*) 'NO. OF ITERATIONS     ',ITER
0130     WRITE(15,*) 'RELAXATION PARAMETER  ',RELAX
0131     WRITE(15,*) 'FIELD DIMENSIONS (X-Z)',C,D
0132     WRITE(15,*) 'NO. OF PIXELS (COL-ROW)',IMAX,JMAX
0133     WRITE(15,*) 'PIXEL SIZE (X-Z)     ',A,B
0134     WRITE(15,*) 'VELOCITY LIMITS      ',VMAX,VMIN
0135
0136     WRITE(14,*) 'ALGORITHM NUMBER      ',IART
0137     WRITE(14,*) 'CORRECTION METHOD      ',IITER
0138     WRITE(14,*) 'NO. OF ITERATIONS     ',ITER
0139     WRITE(14,*) 'RELAXATION PARAMETER  ',RELAX
0140     WRITE(14,*) 'FIELD DIMENSIONS (X-Z)',C,D
0141     WRITE(14,*) 'NO. OF PIXELS (COL-ROW)',IMAX,JMAX
0142     WRITE(14,*) 'PIXEL SIZE (X-Z)     ',A,B
0143     WRITE(14,*) 'VELOCITY LIMITS      ',VMAX,VMIN
0144
0145     C CALCULATE A GAUSSIAN CURVE FOR IF APPLICABLE
0146

```

```

0147     IF(SIGMA.NE.0.) THEN
0148     DO 11 I = 1,151
0149         XN = FLOAT(I-1)/5.
0150         YN(I) = AGAUSS(XN,SIGMA)
0151     11 CONTINUE
0152     END IF
0153
0154 C DEFINE GRID COORDINATES
0155
0156     ZTEMP = 0.
0157     XTEMP = 0.
0158     DO 10 I = 1,150
0159         Z(I) = ZTEMP + B
0160         X(I) = XTEMP + A
0161         ZTEMP = Z(I)
0162         XTEMP = X(I)
0163     DO 20 J = 1,150
0164         SUMRAY(I,J) = 0.
0165         SUMBOX(I,J) = 0.
0166         BOX(I,J) = 0.
0167         NUM(I,J) = 0
0168     20 CONTINUE
0169     10 CONTINUE
0170
0171 C READ IN SOURCE AND RECEIVER LOCATIONS
0172
0173     READ(11,*) DDELAY,TDELAY
0174     DO 30 K2 = 1,1000
0175         READ(10,*,END=31) IDUM,XLOC(K2,1),XLOC(K2,2),XLOC(K2,3),
0176     *         LOC(K2,1),LOC(K2,2)
0177         XLOC(K2,1) = XLOC(K2,1) - DDELAY
0178         LOC(K2,1) = LOC(K2,1) - DDELAY
0179     30 CONTINUE
0180
0181 C READ IN AND ANALYZE ONE RAYPATH AT A TIME
0182
0183     31 NRAYS = 0
0184     NPTR = 0
0185     DMEAN = 0.
0186     DO 2222 K1 = 1,10000
0187         READ(11,*,END=1111) M,N,TT(K1)
0188         PATH(K1) = (XLOC(M,1) - XLOC(N,1))*(XLOC(M,1) - XLOC(N,1))
0189         PATH(K1) = (XLOC(M,2) - XLOC(N,2))*(XLOC(M,2) - XLOC(N,2)) +
0190     *         PATH(K1)
0191         PATH(K1) = (XLOC(M,3) - XLOC(N,3))*(XLOC(M,3) - XLOC(N,3)) +
0192     *         PATH(K1)
0193         PATH(K1) = SQRT(PATH(K1))
0194         TT(K1) = TT(K1) - TDELAY
0195         IF(SIGMA.NE.0.) CALL XNOISE (TT(K1),TT1,TMAX,YN,I1,I2)
0196         TT(K1) = TT(K1) + TT1
0197         NRAYS = NRAYS + 1           !Total number of rays
0198

```

```

0199 C FIND THE RAYPATH THROUGH THE PIXEL GRID
0200 C ALWAYS PROCEED ALONG RAY FROM LEFT TO RIGHT
0201
0202     IF(LOC(M,1).GE.LOC(N,1)) THEN
0203         L = N
0204         N = M

0205     M = L
0206     END IF
0207
0208 C CALCULATE SLOWNESS AND TAKE-OFF ANGLE OF THE K'TH RAY AND
0209 C THE MEAN SLOWNESS OF THE TOTAL FIELD
0210
0211     LRSQR(K1) = 0.
0212     SLOW(K1) = TT(K1)/PATH(K1)
0213     DMEAN = DMEAN + SLOW(K1)
0214     THETA = ATAN((LOC(M,2) - LOC(N,2))/(LOC(N,1) - LOC(M,1)))
0215
0216 C INITIALIZE START AND END POINT VALUES AND CALCULATE INITIAL
0217 C AND ENDPOINT PIXEL NUMBERS
0218
0219     X1 = LOC(M,1)
0220     Z1 = LOC(M,2)
0221     I = INT(X1/A) + 1
0222     J = INT(Z1/B) + 1
0223     X2 = LOC(N,1)
0224     Z2 = LOC(N,2)
0225     IX = INT(X2/A) + 1
0226     JZ = INT(Z2/B) + 1
0227
0228 C START CALCULATIONS OF THE LENGTH OF RAY THROUGH EACH PIXEL
0229 C DIFFERENT ALGORITHMS FOR POS AND NEG TAKE-OFF ANGLES
0230
0231     IF(THETA.GT.0.) THEN
0232         DO 510 K = 1,150
0233             IF(I.GT.IMAX) GOTO 500
0234             NPTR = NPTR + 1
0235             ITEMP = I
0236             JTEMP = J
0237             X4 = X(I)
0238             Z4 = Z(J)
0239             IF(J.EQ.JZ.AND.I.EQ.IX) THEN
0240                 Z4 = Z2
0241                 X4 = X2
0242             END IF
0243             LZ = Z1 - Z4 + B
0244             LX = X4 - X1
0245             ZT = LX*TAN(THETA)
0246             IF(ZT.GT.LZ) THEN
0247                 LR1 = LZ/SIN(THETA)
0248                 X1 = X1 + LZ/TAN(THETA)
0249                 Z1 = Z4 - B
0250                 J = J - 1

```

```

0251         ELSE
0252             LR1 = LX/COS(THETA)
0253             X1 = X4
0254             Z1 = Z1 - ZT
0255             I = I + 1

0256         END IF
0257
0258         NUM(JTEMP,ITEMP) = NUM(JTEMP,ITEMP) + 1
0259         LRBOX(NPTR) = JTEMP*100 + ITEMP
0260         LR(NPTR) = LR1
0261         BOX(JTEMP,ITEMP) = SLOW(K1)*LR1 + BOX(JTEMP,ITEMP)
0262         SUMRAY(JTEMP,ITEMP) = SUMRAY(JTEMP,ITEMP) + LR1
0263         IF(IART.EQ.1.OR.IART.EQ.3.OR.IART.EQ.5)
0264             *           LRSQR(K1) = LRSQR(K1) + LR1*LR1
0265         IF(IART.EQ.2.OR.IART.EQ.21.OR.IART.EQ.4)
0266             *           LRSQR(K1) = LRSQR(K1) + LR1
0267         IF(X4.EQ.X2) I = IMAX + 5
0268
0269         510 CONTINUE
0270         500 CONTINUE
0271         ELSE
0272         DO 511 K = 1,150
0273             IF(J.GT.JMAX) GOTO 501
0274             NPTR = NPTR + 1
0275             ITEMP = I
0276             JTEMP = J
0277             X4 = X(I)
0278             Z4 = Z(J)
0279             IF(J.EQ.JZ.AND.I.EQ.IX) THEN
0280                 Z4 = Z2
0281                 X4 = X2
0282             END IF
0283             LZ = Z4 - Z1
0284             LX = X4 - X1
0285             ZT = LX*TAN(-THETA)
0286             IF(ZT.GT.LZ) THEN
0287                 IF(THETA.EQ.0.) THEN
0288                     LR1 = LX
0289                     X1 = X1 + LX
0290                 ELSE
0291                     LR1 = LZ/SIN(-THETA)
0292                     X1 = X1 + LZ/TAN(-THETA)
0293             END IF
0294             Z1 = Z4
0295             J = J + 1
0296         ELSE
0297             IF(THETA.EQ.0.) THEN
0298                 LR1 = LX
0299             ELSE
0300                 LR1 = ZT/SIN(-THETA)
0301             END IF
0302             X1 = X4

```

```

0303           Z1 = Z1 + ZT
0304           I = I + 1
0305           END IF
0306

0307           NUM(JTEMP,ITEMP) = NUM(JTEMP,ITEMP) + 1
0308           LRBOX(NPTR) = JTEMP*100 + ITEMP
0309           LR(NPTR) = LR1
0310           BOX(JTEMP,ITEMP) = SLOW(K1)*LR1 + BOX(JTEMP,ITEMP)
0311           SUMRAY(JTEMP,ITEMP) = SUMRAY(JTEMP,ITEMP) + LR1
0312           IF(IART.EQ.1.OR.IART.EQ.3.OR.IART.EQ.5)
0313             *           LRSQR(K1) = LRSQR(K1) + LR1*LR1
0314           IF(IART.EQ.2.OR.IART.EQ.21.OR.IART.EQ.4)
0315             *           LRSQR(K1) = LRSQR(K1) + LR1
0316           IF(X4.EQ.X2) J = JMAX + 5
0317
0318           511 CONTINUE
0319           501 CONTINUE
0320           END IF
0321           NPTR = NPTR + 1
0322           LR(NPTR) = 222222.           !The number 222222 signifies
0323           LRBOX(NPTR) = 222222           !the end of a ray
0324           2222 CONTINUE
0325           1111 DMEAN = DMEAN/FLOAT(NRAYS)           !The mean velocity field
0326           PRINT *, NPTR
0327
0328           C CALCULATE THE INITIAL FIELD BY A SIMPLE BACK-PROJECTION
0329
0330           DO 97 J = 1,JMAX
0331             DO 96 I = 1,IMAX
0332               BOX1(I) = 0.
0333               IF(SUMRAY(J,I).EQ.0.) GOTO 96
0334               BOX(J,I) = BOX(J,I)/SUMRAY(J,I)
0335               BOX1(I) = 1./BOX(J,I)
0336               IF(NUM(J,I).LE.NUMMIN) BOX1(I) = 0.
0337             96 CONTINUE
0338             WRITE(15,300) (BOX1(I), I = 1,IMAX)
0339           97 CONTINUE
0340
0341           DO 99 J = 1,JMAX
0342             WRITE(15,301) (NUM(J,I), I = 1,IMAX)
0343           99 CONTINUE
0344
0345           C THE ART ALGORITHMS LOOP THROUGH IFLAG ITERATIONS
0346
0347           IFLAG = 0
0348           1110 IFLAG = IFLAG + 1
0349
0350           DO 77 J = 1,JMAX
0351             DO 78 I = 1,IMAX
0352               NORM(J,I) = 0.
0353             78 CONTINUE
0354           77 CONTINUE

```

```

0355     NORM1 = 0.
0356     NORM2 = 0.
0357     VAR = 0.

0358     NPTR = 0
0359
0360     C IF VELOCITIES ARE LESS THAN VMIN OR GREATER THAN VMAX SET
0361     C EQUAL TO THESE VALUES
0362
0363     DO 89 J = 1,JMAX
0364     DO 88 I = 1,IMAX
0365     IF(BOX(J,I).EQ.0.) GOTO 88
0366     IF(BOX(J,I).LT.1./VMAX) BOX(J,I) = 1./VMAX
0367     IF(BOX(J,I).GT.1./VMIN) BOX(J,I) = 1./VMIN
0368     88 CONTINUE
0369     89 CONTINUE
0370
0371     C CALCULATE THE TIME THROUGH THE CALCULATED VELOCITY
0372     C FIELD AND SUBTRACT FROM THE OBSERVED TRAVEL TIMES
0373
0374     DO 80 K1 = 1,NRAYS
0375     TEMP = 0.
0376     IPTR = NPTR
0377     DO 83 K = 1,300
0378     NPTR = NPTR + 1
0379     IF(LRBOX(NPTR).EQ.222222) GOTO 81
0380     JTEMP = INT(LRBOX(NPTR)/100)
0381     ITEMP = LRBOX(NPTR) - JTEMP*100
0382     TEMP = TEMP + LR(NPTR)*BOX(JTEMP,ITEMP) !Calculated travel times
0383     83 CONTINUE
0384     81 CONTINUE
0385
0386     IF(IART.LT.6.AND.LRSQR(K1).EQ.0.) PRINT *, K1
0387     DELTAG = TT(K1) - TEMP ! (obs - calc) travel times
0388     IF(DELTA.GT.1.) PRINT *, DELTAG
0389     DELTAS = SLOW(K1) - TEMP/PATH(K1)
0390     NORM1 = NORM1 + DELTAG
0391     NORM2 = NORM2 + DELTAG*DELTAS
0392
0393     C APPLY THE SPECIFIED ART ALGORITHM
0394
0395     DO 84 K = 1,300
0396     IPTR = IPTR + 1
0397     IF(LRBOX(IPTR).EQ.222222) GOTO 82
0398     JTEMP = INT(LRBOX(IPTR)/100)
0399     ITEMP = LRBOX(IPTR) - JTEMP*100
0400     WT = 1.
0401     IF(IART.EQ.5) WT = (A/PATH(K1))**2
0402     IF(IART.EQ.1) DELTAF = RELAX*LR(IPTR)*DELTAS/LRSQR(K1)
0403     IF(IART.EQ.2) DELTAF = RELAX*LR(IPTR)*DELTAS/LRSQR(K1)
0404     IF(IART.EQ.21) DELTAF = RELAX*DELTAS/LRSQR(K1)
0405     IF(IART.EQ.3) DELTAF = RELAX*LR(IPTR)*LR(IPTR)*DELTAS/LRSQR(K1)
0406     IF(IART.EQ.4) DELTAF = RELAX*LR(IPTR)*DELTAS/LRSQR(K1)

```

```

0407      IF(IART.EQ.5) DELTAF = RELAX*LR(IPTR)*DELTA/LRSQR(K1)
0408      IF(IART.EQ.6)

0409      *      DELTAF = ((TT(K1)/TEMP)**(RELAX*LR(IPTR)))*BOX(JTEMP,ITEMP)
0410      IF(IART.EQ.7) DELTAF = RELAX*LR(IPTR)*DELTAS
0411
0412      C CORRECT ACCORDING TO THE ITER (1 OR 2) CORRECTION SCHEME
0413
0414      IF(IITER.EQ.1.AND.IART.EQ.6) BOX(JTEMP,ITEMP) = WT*DELTAF
0415      IF(IITER.EQ.1.AND.IART.NE.6)
0416      *      BOX(JTEMP,ITEMP) = BOX(JTEMP,ITEMP) + WT*DELTAF
0417      IF(IITER.EQ.2)
0418      *      SUMBOX(JTEMP,ITEMP) = SUMBOX(JTEMP,ITEMP) + WT*DELTAF
0419
0420      NORM(JTEMP,ITEMP) = NORM(JTEMP,ITEMP) + DELTAG
0421      84 CONTINUE
0422      82 CONTINUE
0423      80 CONTINUE
0424
0425      C IF IITER = 2, SUMBOXY(J,I) SUMS ALL THE CORRECTIONS TO BOX(J,I).
0426      C THESE ARE THEN DIVIDED BY THE NUMBER OF RAYS SAMPLING THE BOX
0427
0428      NNN = ABS(FLOAT(NRAYS-(IMAX*JMAX)))
0429      NORM2 = SQRT(NORM2/NNN)
0430      WRITE(15,*) 'NORM1 =',NORM1
0431      WRITE(15,*) 'NORM2 =',NORM2
0432      WRITE(15,*) 'THE ERROR MATRIX FOR ITERATION',IFLAG - 1
0433      DO 74 J = 1,JMAX
0434      WRITE(15,300) (NORM(J,I), I = 1,IMAX)
0435      74 CONTINUE
0436
0437      ENTR = 0.
0438      VAR1 = 0.
0439      DIST = 0.
0440      DO 87 J = 1,JMAX
0441      DO 86 I = 1,IMAX
0442      BOX1(I) = 0.
0443      IF(NUM(J,I).EQ.0) GOTO 86
0444      IF(IITER.EQ.2.AND.IART.EQ.6)
0445      *      BOX(J,I) = SUMBOX(J,I)/FLOAT(NUM(J,I))
0446      IF(IITER.EQ.2.AND.IART.NE.6.AND.IART.NE.7)
0447      *      BOX(J,I) = BOX(J,I)+SUMBOX(J,I)/FLOAT(NUM(J,I))
0448      IF(IART.EQ.7) BOX(J,I) = BOX(J,I) + SUMBOX(J,I)/SUMRAY(J,I)
0449      BOX1(I) = 1./BOX(J,I)
0450      IF(NUM(J,I).LE.NUMMIN) BOX1(I) = 0.
0451      SUMBOX(J,I) = 0.
0452      DIST = DIST + (BOX(J,I) - BOXT(J,I))*(BOX(J,I) - BOXT(J,I))
0453      VAR1 = VAR1 + (BOX(J,I) - DMEAN)*(BOX(J,I) - DMEAN)
0454      ENTR = ENTR + (BOX(J,I)/DMEAN)*(LOG(BOX(J,I)/DMEAN))
0455      86 CONTINUE
0456      WRITE(15,300) (BOX1(I), I = 1,IMAX)
0457      87 CONTINUE
0458

```

```

0459      DIST = SQRT(DIST/(VAR1))                !Distance to true model

0460      VAR1 = VAR1/FLOAT(IMAX*JMAX)            !Variance
0461      ENTR = - ENTR/LOG(FLOAT(IMAX*JMAX))     !Entropy
0462      WRITE(15,*) 'VARIANCE = ',VAR1
0463      WRITE(14,*) IFLAG,DIST,VAR1,ENTR,NORM2
0464      C   PRINT *, IFLAG,DIST,VAR1,ENTR,NORM2
0465      IF(IFLAG.LT.ITER) GOTO 1110
0466
0467      PRINT *, CHAR(27),CHAR(7)
0468
0469      140 FORMAT(A1)
0470      151 FORMAT(A)
0471      156 FORMAT(5I3,4F6.2)
0472      200 FORMAT(1X,I4,4F15.7)
0473      300 FORMAT(15(F6.3,1X))
0474      301 FORMAT(20(I5,1X))
0475
0476      STOP
0477      END

```

```

0001
0002      SUBROUTINE XNOISE (X,TT1,TMAX,YN,I1,I2)
0003      REAL YN(400),NOISE1
0004      CALL RANDU(I1,I2,NOISE1)
0005      CALL RANDU(I1,I2,SIGN)
0006      DO 202 II = 1,150
0007          IF(NOISE1.GT.YN(II).AND.NOISE1.LT.YN(II+1))
0008              *   TT1=FLOAT(II)*X*TMAX/150.
0009      202 CONTINUE
0010      IF(NOISE1.GT.YN(151)) TT1 = X*TMAX/150.
0011      IF(SIGN.GT.0.5) TT1 = -TT1
0012      RETURN
0013      END

```

```

0001
0002      FUNCTION AGAUSS (X,SIGMA)
0003      REAL Z,Y2,TERM1,SUM1,DENOM
0004      Z = ABS(X)/SIGMA
0005      AGAUSS = 0.
0006      IF(Z.EQ.0.) GOTO 5
0007      TERM1 = 0.7071067812*Z
0008      SUM1 = TERM1
0009      Y2 = (Z**2)/2.

```



```
0010     DENOM = 1.
0011
0012     1 DENOM = DENOM + 2.
0013     TERM1 = TERM1*(Y2*2./DENOM)
0014     SUM1 = SUM1 + TERM1
0015     IF(TERM1/SUM1.GT.1.E-10) GOTO 1
0016     AGAUSS = 1.128379167*SUM1*EXP(-Y2)
0017     5 RETURN
0018     END
```

This report was done with support from the Department of Energy. Any conclusions or opinions expressed in this report represent solely those of the author(s) and not necessarily those of The Regents of the University of California, the Lawrence Berkeley Laboratory or the Department of Energy.

Reference to a company or product name does not imply approval or recommendation of the product by the University of California or the U.S. Department of Energy to the exclusion of others that may be suitable.

*LAWRENCE BERKELEY LABORATORY  
TECHNICAL INFORMATION DEPARTMENT  
UNIVERSITY OF CALIFORNIA  
BERKELEY, CALIFORNIA 94720*